博士論文

Study on High Performance Control of Switched Reluctance Motor for Industrial Servo Drive Application

産業サーボドライブ用 SR モータの高性能制御に関する研究

2019

Shin Sung Yong

Study on High Performance Control of Switched Reluctance Motor for Industrial Servo Drive Application

産業サーボドライブ用 SR モータの高性能制御に関する研究

By

Shin Sung Yong

A thesis submitted for the degree of Doctor of Engineering

Graduate School of Engineering

Department of Electrical and Mechanical Engineering

Nagoya Institute of Technology

Nagoya, Japan

September 2019

Study on High Performance Control of Switched Reluctance Motor for Industrial Servo Drive Application

A thesis submitted to Graduate School of Engineering,

Department of Electrical and Mechanical Engineering,

Nagoya Institute of Technology,

for the degree of Doctor of Engineering.

By

Shin Sung Yong

Supervisor

Professor Kosaka Takashi

Department of Electrical and Mechanical Engineering

September 2019

Declaration of Originality

I hereby declare that the research recorded in this thesis and was composed and originated entirely by myself in the Graduate School of Engineering, Department of Electrical and Mechanical Engineering at the Nagoya Institute of Technology.

Shin Sung Yong

List of Contents

Chapter 1

Introduction

1.1 Development trend of industrial motor

1.1.1 Greenhouse gas and motor development trend

Todays, environment problems become important things to human beings. Especially, the greenhouse gases that cause temperature rise of atmosphere have been big issue. All countries have been making an effort to reduce the greenhouse gases. Of those gases, the carbon dioxide produced from fossil fuels and during industrial processes accounts for 65%. 66% of the carbon dioxide (CO_2) is released from industry, transportation, building and electricity production sectors, as can be seen in figure 1.1[(1)]. To reduce CO_2, in case of the transportation sector, internal combustion vehicles have been being replaced with electric/hybrid electric vehicles (EV/HEV) using electric motors. In other sectors, all electric motors utilized in electric products or equipment have been forced to improve their efficiency. However, CO_2 emission is increasing year by year as can be seen in figure 1.2[(2)]. In this situation, electric motors always have been enforced to have high efficiency.

Although there are so many types of motor, in this paper, representative five motors are compared in order to explain the development trends shown in figure 1.3. Because of CO_2 emission, efficiency has become most important index to motors. PMSM (Permanent Magnet

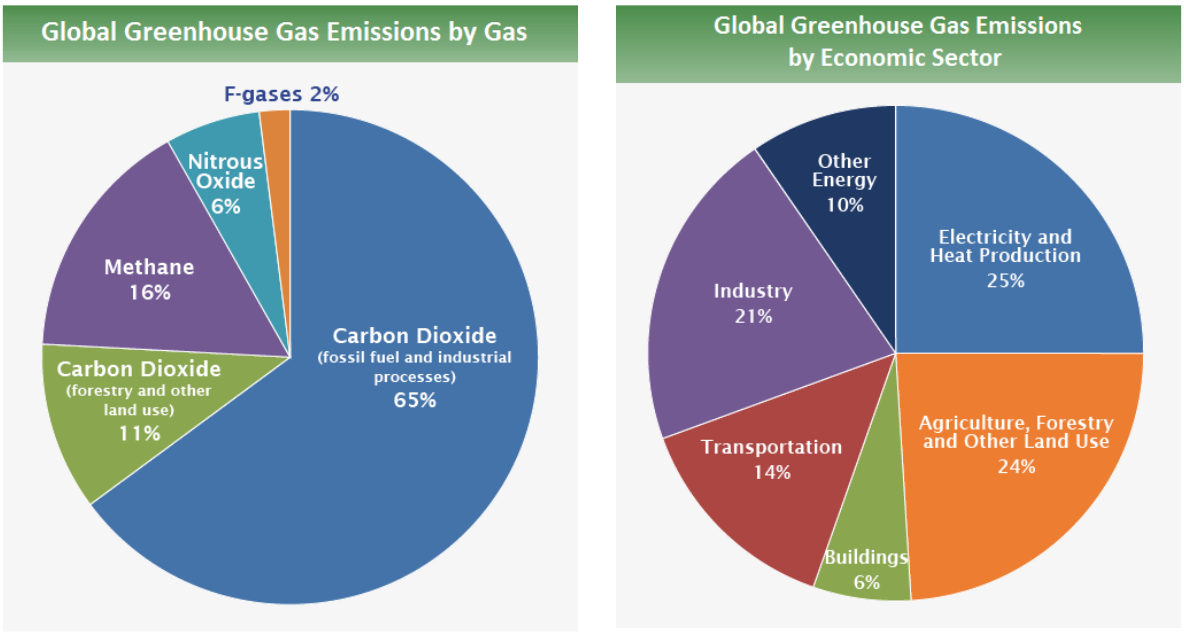

Source : EPA (United States Environmental Protection Agency)

Figure 1.1 Global greenhouse gas emission in 2014

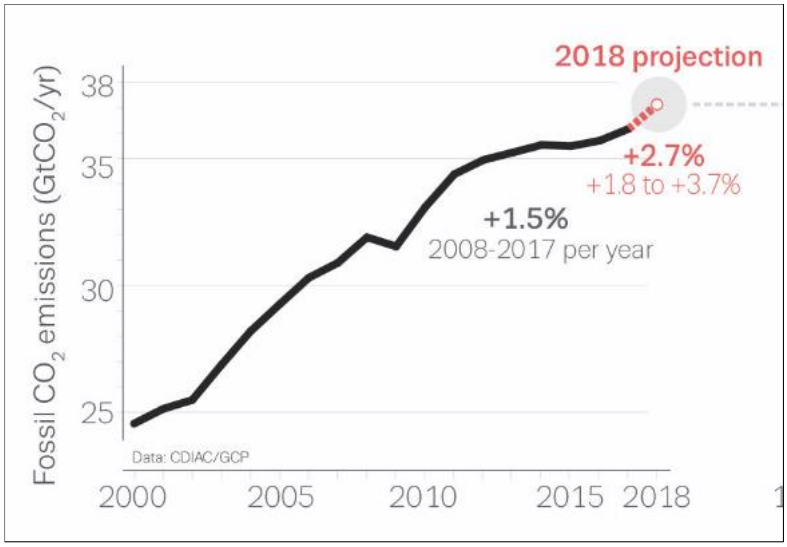

Source : Global Carbon Project.org

Figure 1.2 The trend of global fossil CO_2 emission

Synchronous Motor) has become the most popular motor since 1990s. PMSM is classified into SPMSM (Surface PMSM) and IPMSM (Interior PMSM) accordance with rotor structure. In IPMSM, magnet is inserted into rotor, it has the drawback of large vibration and torque ripple due to high order harmonic of the variance of reluctance compared to SPMSM. However, IPMSM is more popular owing to strong points:

1) IPMSM has both magnet torque and reluctance torque so that higher torque density compared with SPMSM utilizing only magnet torque is achieved.
2) By applying field weakening control for high speed region, speed range becomes wider thanks to reluctance torque.
3) In high speed operation, IPMSM has no magnetic scattering problem by centrifugal force. On the other hand, SPMSM requires a can-shaped structure around magnet to avoid scattering of magnetic.

PMSM has been popular over the past few decades and now also being developed by conjunction with the following technologies. Thickness of magnet can be reduced through the development of rare earth magnets such as neodymium-iron-boron magnet (NdFeB) to increase coercivity and residual flux density. By using this, motor size could be reduced, and copper loss could be decreased by increasing back EMF and by decreasing d-axis current at field weakening control thanks to an increase of d-axis inductance especially in IPMSM. In addition, through increased coil filling factor by employing rectangular copper wire as well as sophisticated winding technology of magnetic wire, copper loss could be reduced. In addition, development of control technology of PMSM including position sensorless control[3][4] and torque ripple minimization control[5] makes PMSM attractive to adapt to

Motor	IM	SPMSM	IPMSM	SynRM	SRM
Structure	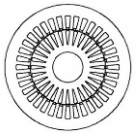	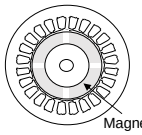	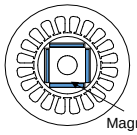	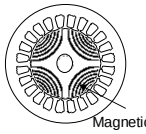	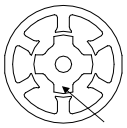
Torque source	 Torque by electromagnetic induction	Magnetic Torque			
			Reluctance Torque		
		※ Magnetic Torque: Suction / repulsive force between permanent magnet and electro magnet ※ Reluctance Torque: Suction force between rotor salient pole and electro magnet			
Strong / Weak point	▪ Rigid structure ▪ Low vibration and noise ▪ Simple control (Line voltage drive) ▪ Rotor copper loss ▪ Low strength of rotor slot bridge	▪ High efficiency, Low noise ▪ High torque density ▪ Easy control by using commercial power module ▪ Demagnetization by temperature ▪ SUS CAN need for protection of magnet scattering of SPM		▪ Low cost ▪ High temperature endurance ▪ Low efficiency ▪ Low strength of rotor flux barrier	▪ Simple and strong rotor structure ▪ Low cost ▪ High temperature endurance ▪ Low efficiency ▪ High vibration and noise
Speed	Not good	Not bad	Good	Not good	Good
Torque	Bad	Good	Good	Not good	Good
Cost	Good	Bad	Not Bad	Good	Good
Efficiency	Bad	Good	Good	Not bad	Not bad
Torque ripple / vibration	Good	Good	Not good	Not good	Bad

Figure 1.3 The characteristics by motor type

many applications. One of major applications of SPMSM is for industrial servo drive system where superior aspects of SPMSM such as high torque, low inertia and precise torque control capability owing to low torque ripple are well matched. On the other hand, IPMSM is favorably used for EV or HEV where wide speed range operation with high efficiency and high power density are required.

1.1.2 Problems of rare earth permanent magnet and SRM as the most promising alternative of PMSM

As mentioned earlier, the development of NdFeB magnet using rare earth materials has

brought about efficiency improvement in PMSM. In conjunction with carbon dioxide emission regulations, the use of PMSM employing NdFeB magnet has been rapidly expanded. Under this circumstance, China, which owns 65% of rare earth material reserves, accounts for 97% of the world's supply of NdFeB magnet. This has raised concern about weaponization of the resources. The concern has become a reality. As shown in figure 1.4, the price of Dy(Dysprosium) and Tb(Terbium) doped to NdFeB magnet to improve coercivity, which provides NdFeB magnet with a capability of high operating temperature, has increased in 2011 rapidly due to the 2008 import restriction measures by China[(6)]. As a result, the price of NdFeB magnet at 2011 also has increased more than 15 times compared with that at 2008[(7)]. In addition, Roskill reported that the price of Nd has risen to 47% in 2019 compared to 2008, and by 2029, demand of NdFeB by drive train (NEV) is expected to grow to 82% compared to 2019 with 15% increase annually in Nd price as shown in figure 1.4 b) and c)[(8)].

To solve the concern above, the development of new technologies that can reduce or get rid of the use of rare earth permanent magnets or apply non-rare earth permanent magnets while keeping motor performance as it is, has been being greatly expanded. As a result, motor development trends have been changed to suppress the usage of rare earth magnet in PMSM as can be seen in figure 1. 5.

As the motor candidates for getting away from the rare earth magnet, there are IM(Induction Motor), SynRM(Synchronous Reluctance Motor), SRM (Switched Reluctance Motor) and so on. SRM has double salient pole structure both in rotor and stator and uses only reluctance torque and therefore, it doesn't use any magnet material. SynRM also produces only

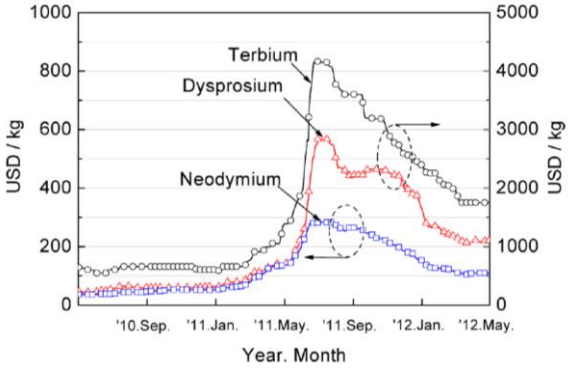

[Charts for rare-earth material price in china][6]

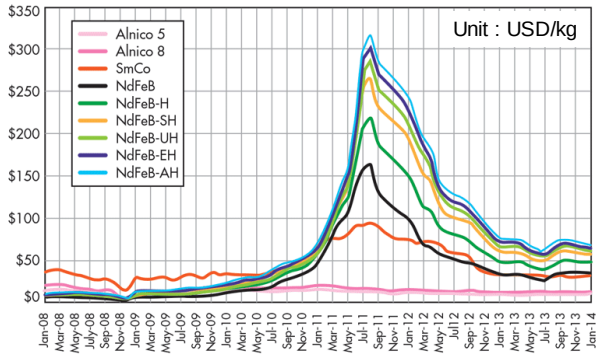

Source : Electronic Design[7]

a) price trends of Dy (Dysprosium), Tb (Terbium), and NdFeB (2008~2014)

b) Nd ask price chart from Roskill (2014~2019)[8]

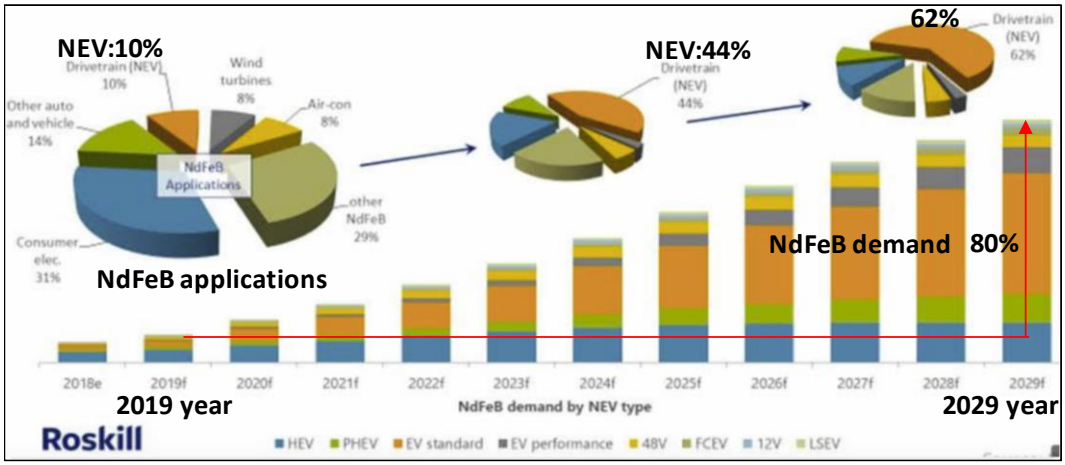

c) application ratio and demand forecast at NEV(HEV, EV, etc.) for NdFeB(2018~2029)[8]

Figure 1.4 Market trends of rare earth magnet materials

reluctance torque, so doesn't need magnet. However, the structure of SynRM is complicate and rotor structure is fragile compared with SRM because it needs distributed winding on stator body and flux barrier on the rotor to change reluctance with sinusoidal waveform with respect to rotor position displacement. The torque of IM is produced by the interaction between the rotating magnetic field produced by AC currents in the stator windings and the induced AC current in the rotor assembly. The general squirrel cage IM using aluminum die-casting as rotor winding doesn't need magnet. However, this motor also has complicate structure and rotor can be easily broken in high speed compared with SRM because it needs distributed winding on stator body and the thickness of rotor slot bridge is thin. Also the copper loss and temperature rise of IM are high compared with SRM because the induced current circulates through the cage winding in the rotor[9]. Above three motors are not good for efficiency, however, if the SRM, which has many advantages among the above three motors, realizes high efficiency, it can be the best candidate as a motor that is rare-earth free. The following describes several ways to improve the efficiency of SRM. Because SRM consists of concentric windings on stator core, the efficiency of SRM can be improved easier than IM and SynRM with distributed windings. Through increasing the slot fill factor by using rectangular magnet wire, the efficiency of SRM can be increased[10][11]. In addition, by using low iron loss electrical steel sheet like amorphous steel sheet[12], efficiency can be increased. The iron loss of amorphous steel sheet is about one tenth of general electrical steel sheet because eddy current loss can be reduced by thin thickness (25μm) and high resistivity. Also, because amorphous steel sheet has high permeability and hence, the current to make same magnetic loading can be reduced compared with the current required when general

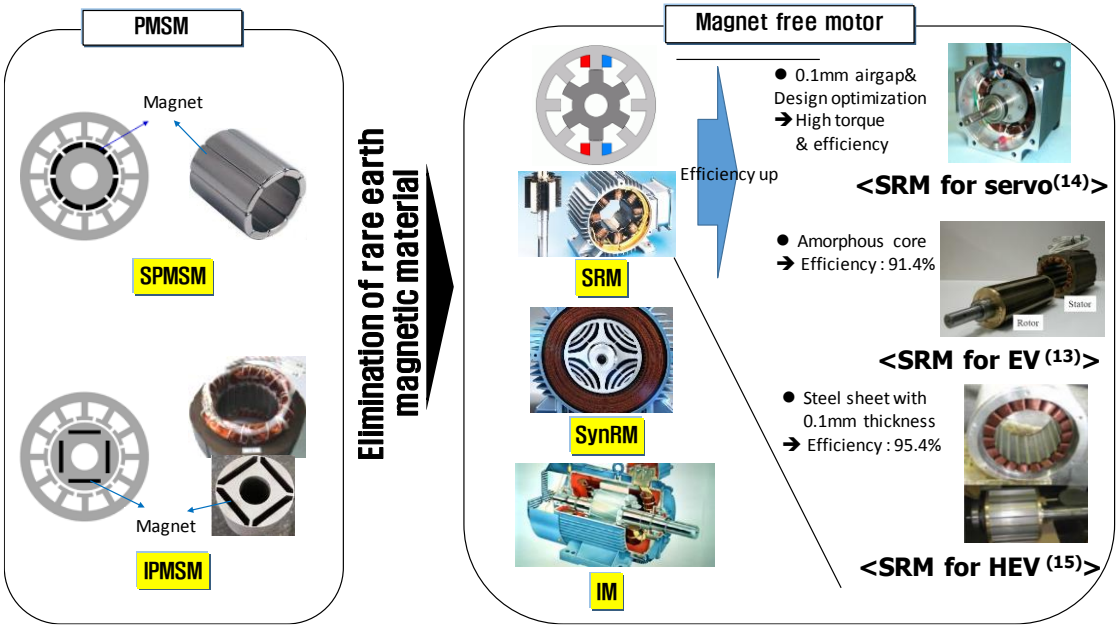

Figure 1.5 Development trend of variable speed driving motor

electrical steel sheet is used and thus, the copper loss reduction is expected by decreasing the current. Actually, by applying amorphous steel sheet to SRM(80kW), efficiency is increased to 91.4% as much as that of PMSM[13]. Besides, to keep the same efficiency with PMSM, the optimal structure design of SRM with 0.1mm airgap for servo drive through GA(Genetic Algorithm) was studied[14]. The SRM, which has similar torque density and efficiency with 400W SPMSM for servo drive, was designed successfully. A design study to improve the efficiency of SRM for HEV(50kW) by 95.4% by minimizing iron loss through a super core (0.1mm thick electrical steel sheet) was also presented[15].

SRM has excellent advantages among alternative rare-earth free motors(IM, SynRM, SRM) and can compete with PMSM in performance and thus, SRM is selected as the most promising rare earth free motor in this paper.

To summarize the content so far, SRM just consists of copper and steel and has

concentrated windings and hence, the structure is simple, rugged and easy to manufacture. Besides, SRM is suitable for high-speed operation and can achieve comparable efficiency with PMSM, resulting in that it is expected to be employed for the applications where durability is required or where high-speed and high output power operations with high efficiency are required. SRM has most proper characteristics as the industrial motor used in severe environment like high temperature and high-speed operation.

SRM, however, has still many problems to be solved compared with PMSM. The driving algorithm for the PMSM that used in industrial application has been developed steadily on the basis of sinusoidal voltage control. As a result, since the motor is controlled by sinusoidal current, the torque ripple and vibration of PMSM are smaller than those of SRM. In addition, for driving in harsh environment, position sensorless algorithm of PMSM have been developed to eliminate a position sensor with low durability. Therefore, many simple sensorless control methods[3][4] for PMSM dives that work well in all speed range also have been in practical use for many applications. On the other hands, SRM produces large vibration and torque ripple due to nature of its unique operating principle. To overcome these issues, many control algorithms for low vibration[19]-[33] and low torque ripple[37]-[54] for precise control in servo system have been studied. However, there are still remaining many problems to be improved. In also sensorless control algorithms[57]-[72], most of them are generally complex and require a large capacity of memory to save the data table used for position estimation because the inductance or flux linkage data has nonlinearity with respect to the current and rotor position. To calculate the inductance or the flux linkage data, current and applied voltage information are required, which are detected by expensive sensors with

high frequency band width. Therefore, simple and economic position estimation algorithms that work well in wide speed range for precise control also must be developed.

As mentioned earlier, SRM has still many problems to be solved so that it competes with PMSM. After reviewing the basic principle of torque generation and general control methods of SRM, the problems are revealed. Then, the target tasks to be solved in this study will be explained.

1.2 Principle of torque generation and drive methods in SRM

1.2.1 Torque generation principle on magnetizing curves

To explain the operating principle, four-phase 8/6 pole 400W SRM shown in figure 1.6 is used as an example. Basically, torque is generated in the direction so that the reluctance between the excited A-phase stator tooth and rotor tooth becomes smaller, i.e. the inductance of the excited A-phase stator winding increases. In other words, torque is produced from unaligned position to aligned position. Rotation direction is assumed as clockwise direction shown in figure 1.6(a). The inductance profile is changed with respect to rotor position as shown in figure 1.6(b). The flux linkage of the excited A-phase winding can be calculated by using equation (1.1) on the assumption that affection of mutual flux linkage is small like equation (1.2). This is because the mutual flux Φ_{AB} and $\Phi_{\bar{A}B}$ can be cancelled each other assuming that the reluctance of the steel core is extremely smaller than one of airgap. However, in real motor, there is an affection by mutual flux. The affection about mutual flux

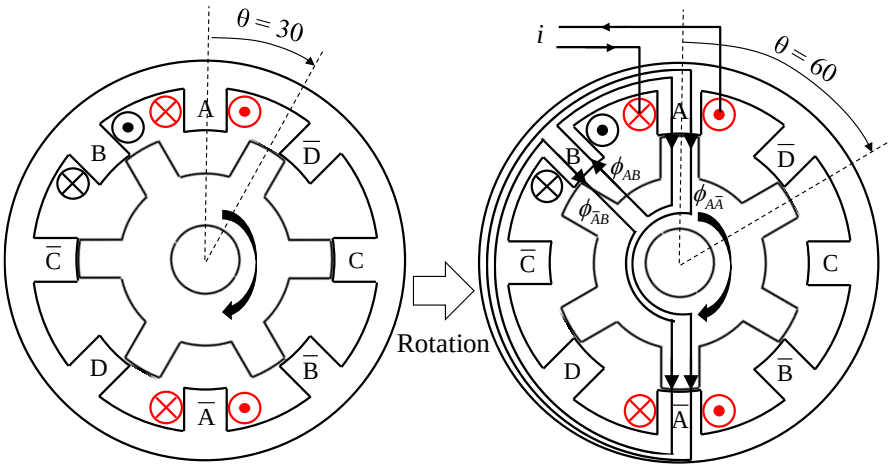

(a) Rotor position change 30→60[deg], and magnetic flux flow when A-phase is turned on at 60 degree

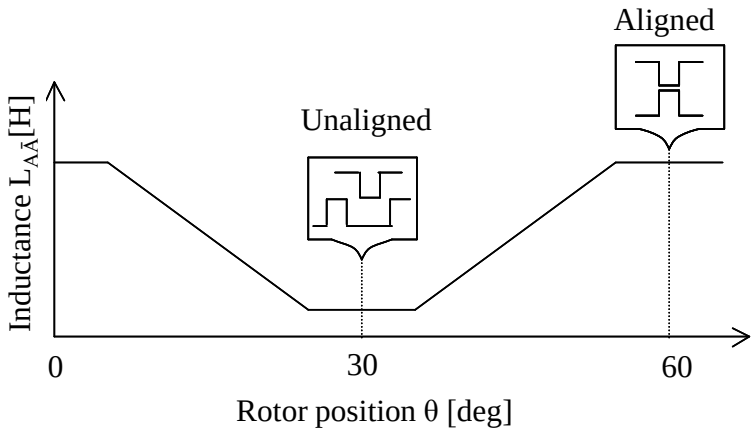

(b) Inductance profile of A phase by rotor position when *i* is constant

Figure 1.6 Inductance profile and magnetic flux flow

will be concerned later in torque ripple control of chapter 4 and 5.

$$\lambda_{A\bar{A}}(i,\theta) = L_{A\bar{A}}(i,\theta)\cdot i = N\cdot\phi_{A\bar{A}} \tag{1.1}$$

$$\phi_{AB} + \phi_{\bar{A}B} \approx 0 \tag{1.2}$$

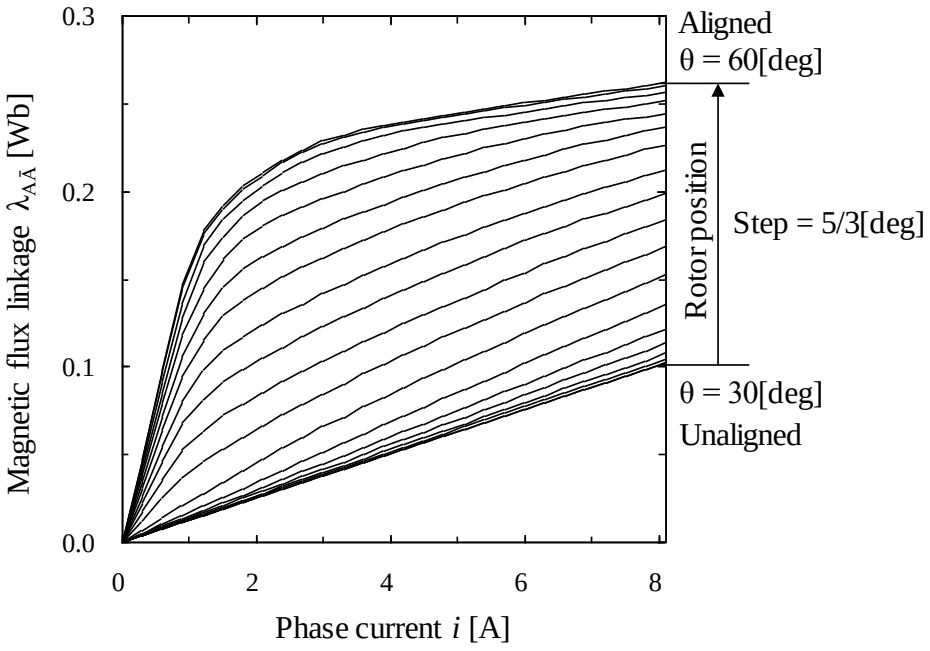

Figure 1.7 Magnetization curve for test motor

In the above equations, $\lambda_{A\bar{A}}$, $L_{A\bar{A}}$, N, i, θ, $\emptyset_{A\bar{A}}$, $\emptyset_{A\bar{B}}$ and $\emptyset_{AB}$ are flux linkage of A-phase, inductance of A-phase, number of turns per A-phase coil, current, rotor position, flux flowing from A tooth to $\overline{\mathrm{A}}$ tooth, flux flowing from A tooth to $\overline{\mathrm{B}}$ tooth and flux flowing from A tooth to B tooth. The flux linkage is changed accordance with rotor position and current as shown in figure 1.7 which is magnetizing curves of A-phase. The flux linkage characteristic has nonlinear shape except one at near unaligned position where magnetic saturation doesn't occur. In contrast, at near aligned position, magnetic saturation easily occurs even if current is small.

In order to calculate the torque characteristic from the magnetizing curves, partial differential of magnetic co-energy with respect to rotor position is used. As can be seen in figure 1.8, electric energy W_e is converted to magnetic energy W_m and mechanical energy

W_{mech}. Assuming that the voltage drop by resistance is small and the instantaneous torque τ in small time variance is constant, input voltage and the differential of mechanical energy can be given in,

$$v = d\lambda / dt, \quad dW_{mech} = \tau d\theta \tag{1.3}$$

From energy balance, the relation between the energies can be expressed as following fashion.

$$\begin{aligned} &dW_e = (iv)dt = dW_m + dW_{mech} \\ &\Rightarrow dW_m = (iv)dt - dW_{mech} = id\lambda - \tau d\theta \end{aligned} \tag{1.4}$$

Generally, magnetic energy W_m and magnetic co-energy W_m' have the relationship,

$$\begin{aligned} &W_m(\lambda,\theta) = \int id\lambda\Big|_{\theta=const}, \;\; W_m'(i,\theta) = \int \lambda di\Big|_{\theta=const}. \\ &\Rightarrow W_m'(i,\theta) = i\cdot\lambda - W_m(\lambda,\theta) \end{aligned} \tag{1.5}$$

The meaning of equation (1.5) can be figured out from the figure 1.9 and equation when $i=i_1$ and $\lambda=\lambda_1$ is given in,

$$W_m'(i_1,\theta) = i_1\cdot\lambda_1 - W_m(\lambda_1,\theta) \tag{1.6}$$

Differentiating the co-energy W_m' in equation (1.5), equation can be rearranged by,

$$dW_m'(i,\theta) = d(i\cdot\lambda) - dW_m(\lambda,\theta) \tag{1.7}$$

By using equation (1.4), equation (1.7) can be like below.

$$\begin{aligned} dW_m'(i,\theta) &= \lambda di + id\lambda - (id\lambda - \tau d\theta) \\ &= \lambda di + \tau d\theta \end{aligned} \tag{1.8}$$

In other way, the differential of co-energy can be expressed as,

$$dW_m'(i,\theta) = \frac{\partial W_m'(i,\theta)}{\partial i} di + \frac{\partial W_m'(i,\theta)}{\partial \theta} d\theta \tag{1.9}$$

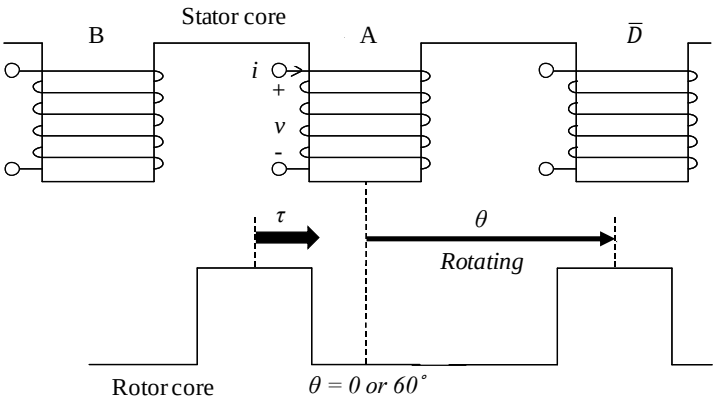

[Torque production and rotating of SRM]

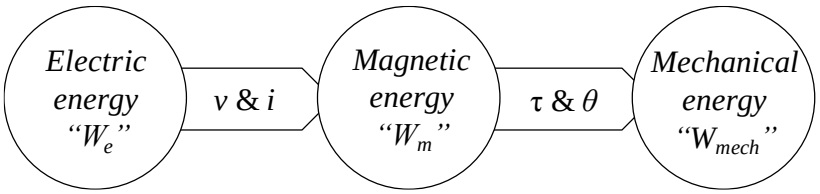

[Energy flow in SRM]

Figure 1.8 Concept of energy flow in SRM

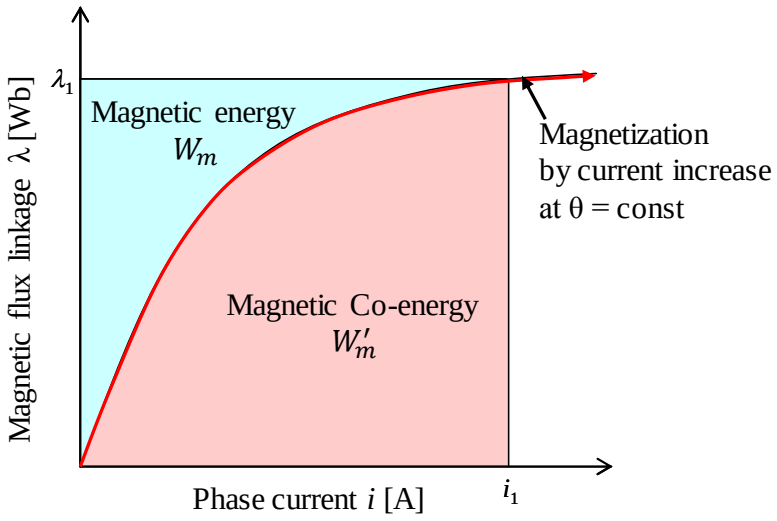

Figure 1.9 Magnetic energy and co-energy at θ = constant

Using the same argument in equations (1.8) and (1.9), torque can be derived as following fashion.

$$\tau = \left.\frac{\partial W_m^{'}(i,\theta)}{\partial \theta}\right|_{i=const} \tag{1.10}$$

Assuming that the inductance is changed by only rotor position, the co-energy of equation (1.5) can be expressed like below.

$$W_m^{'}(i,\theta) = \int \lambda(i,\theta)di = \int L(\theta)idi = \frac{1}{2}L(\theta)i^2 \tag{1.11}$$

Using equation (1.10), torque can be calculated by,

$$\tau = \frac{1}{2}\frac{dL(\theta)}{d\theta}i^2 \tag{1.12}$$

From equation (1.12), if the gradient of inductance variance with respect to position displacement is constant, the constant torque control is possible by controlling the current with constant value. The constant current control method is explained in chapter 1.2.2.

From the equation (1.10), if the co-energy variance $\partial W_m^{'}$ with respect to small position variance $\partial\theta$ is positive, positive torque can be produced. As can be seen in figure 1.10, assuming that the phase current is controlled to be constant value i_2 between 30 and 60 degree and the speed is controlled constant angular speed $\partial\theta/\partial t$, in the energy-conversion loop with trajectory of O→A→B→O, the co-energy variance $\partial W_m^{'}$ of supplied energy is converted to mechanical energy for small position variance $\partial\theta$. In this case, the instantaneous torque τ at each small position variance $\partial\theta$ can be written like below.

$$\tau = \frac{\partial W_m^{'}(i_2,\theta)}{\partial \theta} \tag{1.13}$$

The average torque over one revolution produced in one energy-conversion loop, that is, in

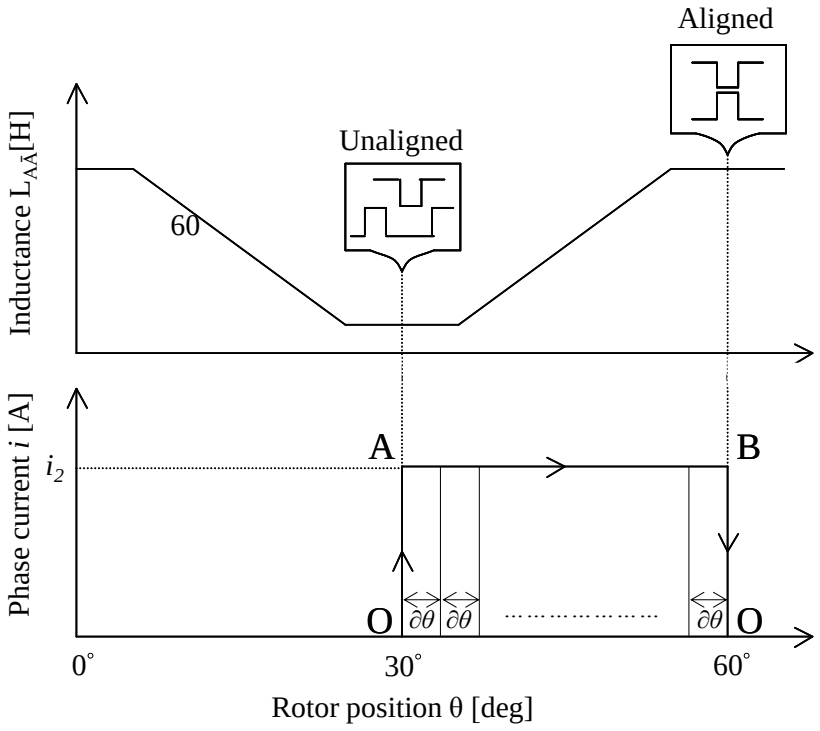

(a) Current variance with respect to position

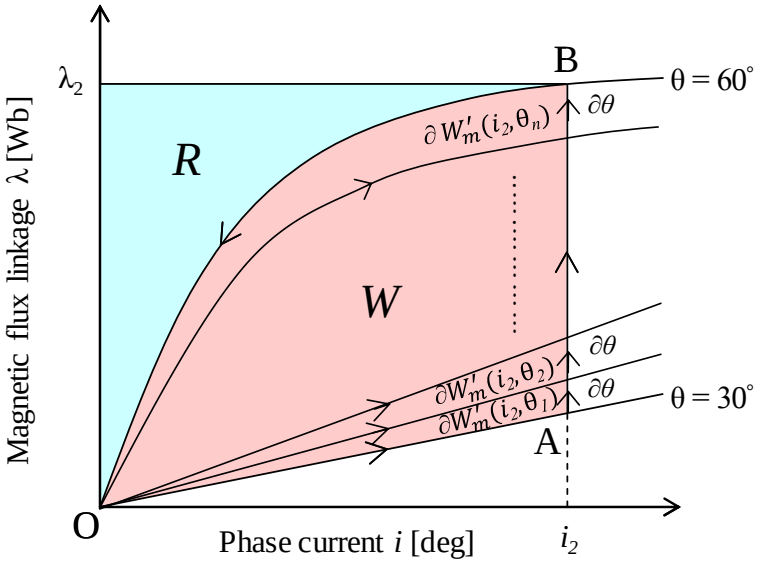

(b)Energy-conversion loop by current change

Figure 1.10 Energy-conversion ratio at constant current

one stroke, can be derived by integrating equation (1.13) like following manner.

$$T_{avg} = \frac{1}{2\pi}\int_0^{2\pi} \tau d\theta = \frac{W}{2\pi}\Big|_{\text{at one stroke}} \tag{1.14}$$

The average torque can be determined from the number of strokes per revolution. Because the all rotor pole N_r is acting on all phase N_p over one revolution, total stroke will be $N_r \times N_p$. Therefore, the average torque can be written like below.

$$T_{avg} = N_r N_p \frac{W}{2\pi} \tag{1.15}$$

In order to design a SRM drive system with high torque density and high efficiency, the area *W* in the figure 1.10 must be larger than the area *R* that is the magnetic energy returned to the supply system. That is a fundamental way to design and control SRM using saturation region effectively. The high permeability of amorphous steel sheet or the increasing of MMF by high slot filling factor also contributes to increasing of the area *W*. Through the control of voltage parameters such as turn-on angle, commutation angle and reference voltage, the current profile is generally controlled so as to maximize the area *W* for resulting copper loss.

1.2.2 General driving method and problems in SRM

From the previous descriptions, to generate positive torque, the change of co-energy with respect to position displacement must be positive. From the equation (1.12), this implies that the inductance variance with position change must be increased. Therefore, the current must be supplied to the region where the inductance variance with respect to the position displacement is positive. For this reason, the current flow discontinuously and rapidly attenuate before reaching at the region where the inductance variance becomes negative.

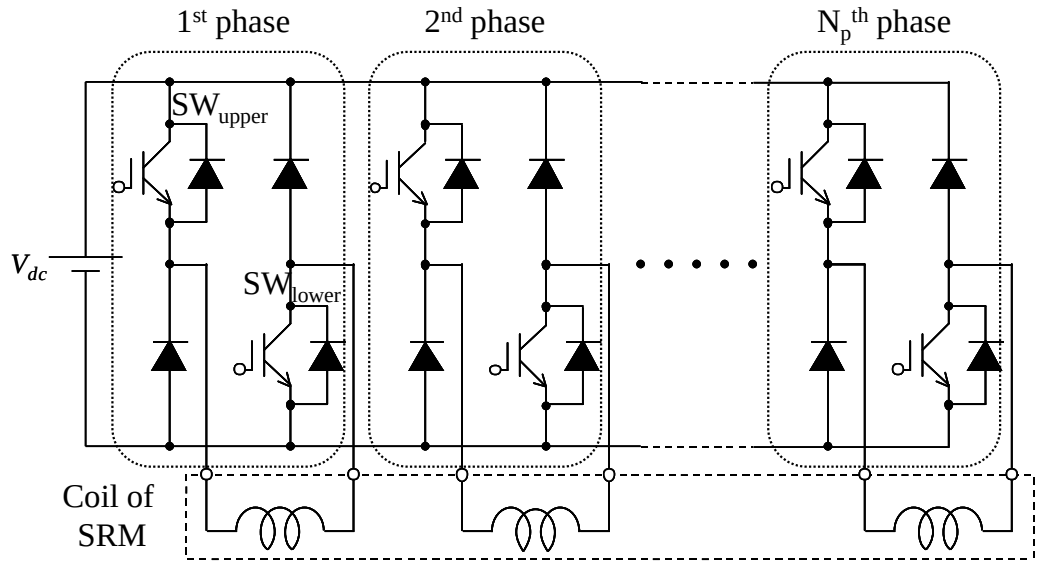

Figure 1.11 Connection of motor coil and asymmetric H-bridge converter

Since the current flows in one direction and each phase is energized independently, drive circuit generally is composed of asymmetric H-bridge converter per phase shown in figure 1.11. The applied voltage per phase varies with the switching state shown in figure 1.12.

Conventional driving methods are classified into three methods as follows.

1) Single pulse voltage control

   Control parameters of this method are just on angle θ_o and commutation angle θ_c as shown in figure 1.13. When both of upper and lower switches are simultaneously turned on at θ_o, the DC bus voltage is applied to the winding per phase. At commutation angle θ_c, negative DC bus voltage is applied because all switches are turned off and the freewheeling diodes are turned on due to the inductance. Generally, this method is suitable for high speed operation. At low speed, this method is unsuitable because of small back EMF, which makes the current increase rapidly

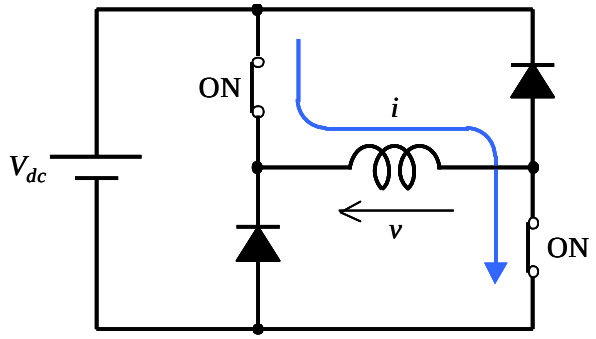

（a） Both switch on, $v=V_{dc}$

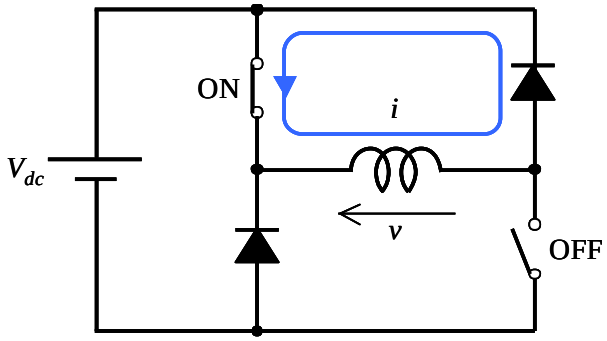

（b） Upper switch on, $v=0$ (current freewheeling)

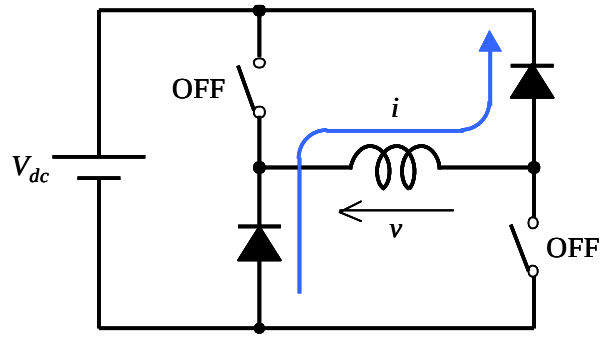

（c） Both switch off, $v=-V_{dc}$ (current freewheeling)

Figure 1.12　voltage and current depending on switching pattern

when the switches are turned on.

2) PWM voltage control

For safe operation in all speed range including low speed region, the average voltage applied to the winding per phase is adjusted by PWM (pulse width modulation) as shown in figure 1.14. The average of applied voltage V_{avg} is controlled by changing duty D for a control interval T and given in,

$$V_{avg} = \frac{D}{T} \times V_{dc\_link} . \tag{1.16}$$

According to the operating torque and speed, the duty D, θ_o, and θ_c can be adjusted. To suppress instantaneous current fluctuation due to PWM, the soft chopping voltage PWM using zero voltage is generally employed.

3) Constant current control

This method is used for relatively ripple less torque control. As shown in figure 1.15, the current is controlled with a target current i^* by using hysteresis control with the soft PWM chopping. After turning on both the switches at θ_o, current control is executed by the hysteresis control, and the both the switches are turned off at θ_c. Assuming the magnetic linearity, instantaneous torque can be expressed by equation (1.12). If the variance of inductance L with respect to rotor position θ and current i are constant, instantaneous torque is controlled to be constant.

Above methods are very simple and basic methods to drive the SRM by producing torque.

However, these methods have problems as follows.

1) Vibration and acoustic noise

In SRM, as can be seen from the current waveform in each method, the current is rapidly changed at θ_o, θ_c and discontinuous in both voltage and current control. As a result, the current waveform contains many high order harmonics. The high order current harmonics generate undesirable electromagnetic force as an exciting force of the stator body, resulting in the stator vibration. If the stator vibration meets the resonant frequency component of the stator body, the large vibration and acoustic noise occur. On the other hand, the vibration of PMSM or IM is smaller than that of SRM because the sinusoidal voltage and current are supplied under vector control for each motor.

2) Torque ripple

For constant torque control, the constant current control can be employed. Even if the current is controlled to be constant value between the turn-on and the commutation angles, high torque ripple, however, can be produced because it is impossible that the rising current after the turn- on angle or tail current after the commutation angle are controlled to be constant. Moreover, in the constant current control region, torque ripple could be observed because the $dL/d\theta$ in equation (1.12) is not constant value due to the nonlinearity of inductance depending on position and current. On the other hand, PMSM has little torque ripple because the phase torque which has sinusoidal waveform is produced by interaction of the rotor flux and the stator flux produced by input phase current with sinusoidal waveform, and the summation of three phase

torques with 120deg shift yields theoretically no pulsation.

3) Position sensing

In SRM, the position sensors such as an encoder or a resolver to detect an exact rotor position is indispensable for precise torque control. However, the position sensors require mounting space and are easy to break in harsh environment where vibration is large and temperature is high. Therefore, the position sensor is an impediment to the advantage of the SRM which is especially suitable for application in severe environments. As a result, the development of position sensorless algorithm is one of important tasks to make the best use of the SRM's advantages.

Many studies on the position sensorless control methods in SRM have been presented[57]-[72]. Most of methods have focused on the position dependency of inductance or flux linkage of the windings. By comparing the value from data table with one calculated from voltage equation using detected currents and detected/commanded voltages, the rotor position can be estimated. For sensorless algorithm of SRM, next is generally required.

(i) For exact position estimation, precise inductance or flux linkage data as function of current and position are needed. These require a huge data memory to save these data as look-up-table(LUT). (ii) To compute the inductance or flux linkage based on the voltage equation using the detected voltage and current per a given phase, an additional circuit like FPGA or a high grade micro processing unit (MPU) is required. (iii) According to operating speed, different algorithm is required because a term in the voltage equation used for the position estimation depends on whether the

rotational speed is low and high. As a result, algorithm tends to be complex, resulting in the system cost-up.

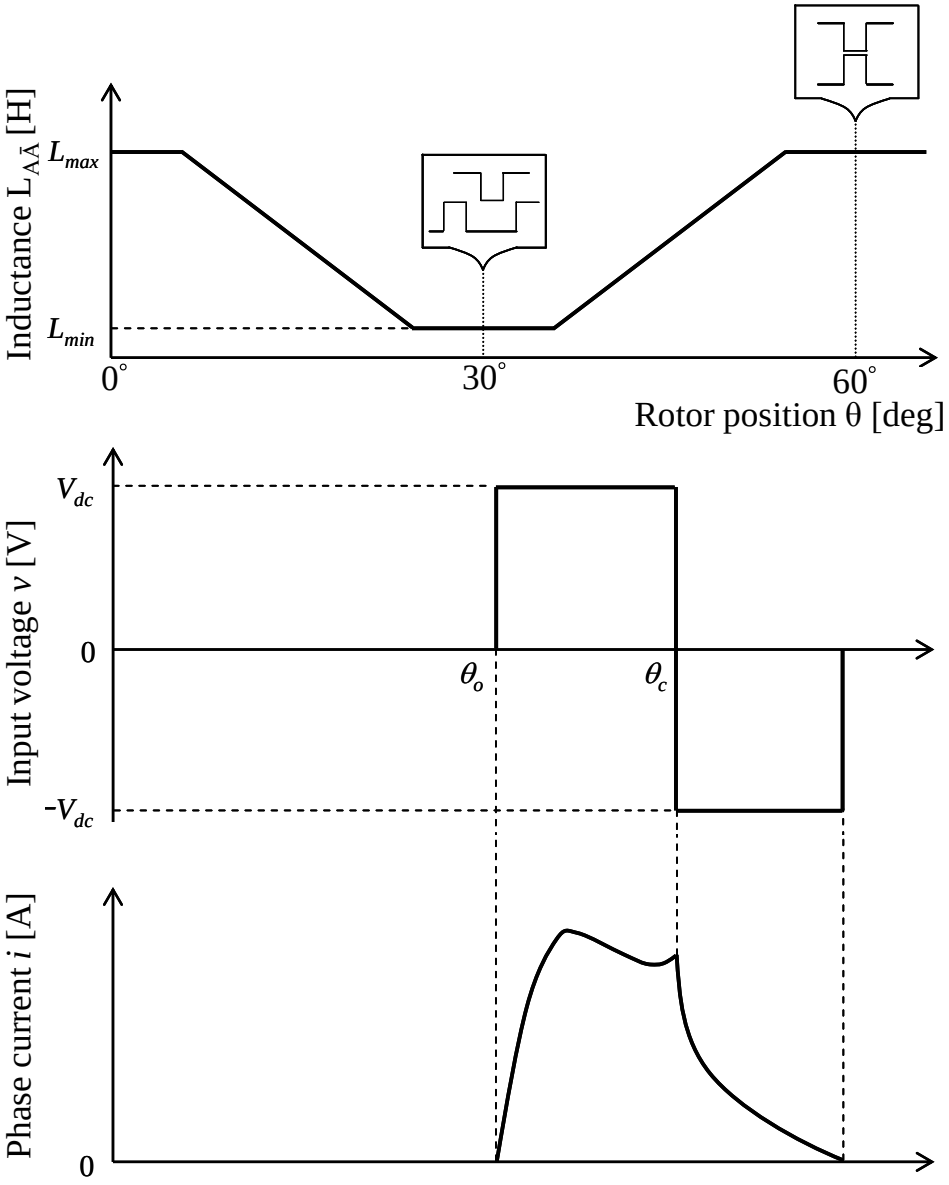

Figure 1.13 Single pulse voltage control

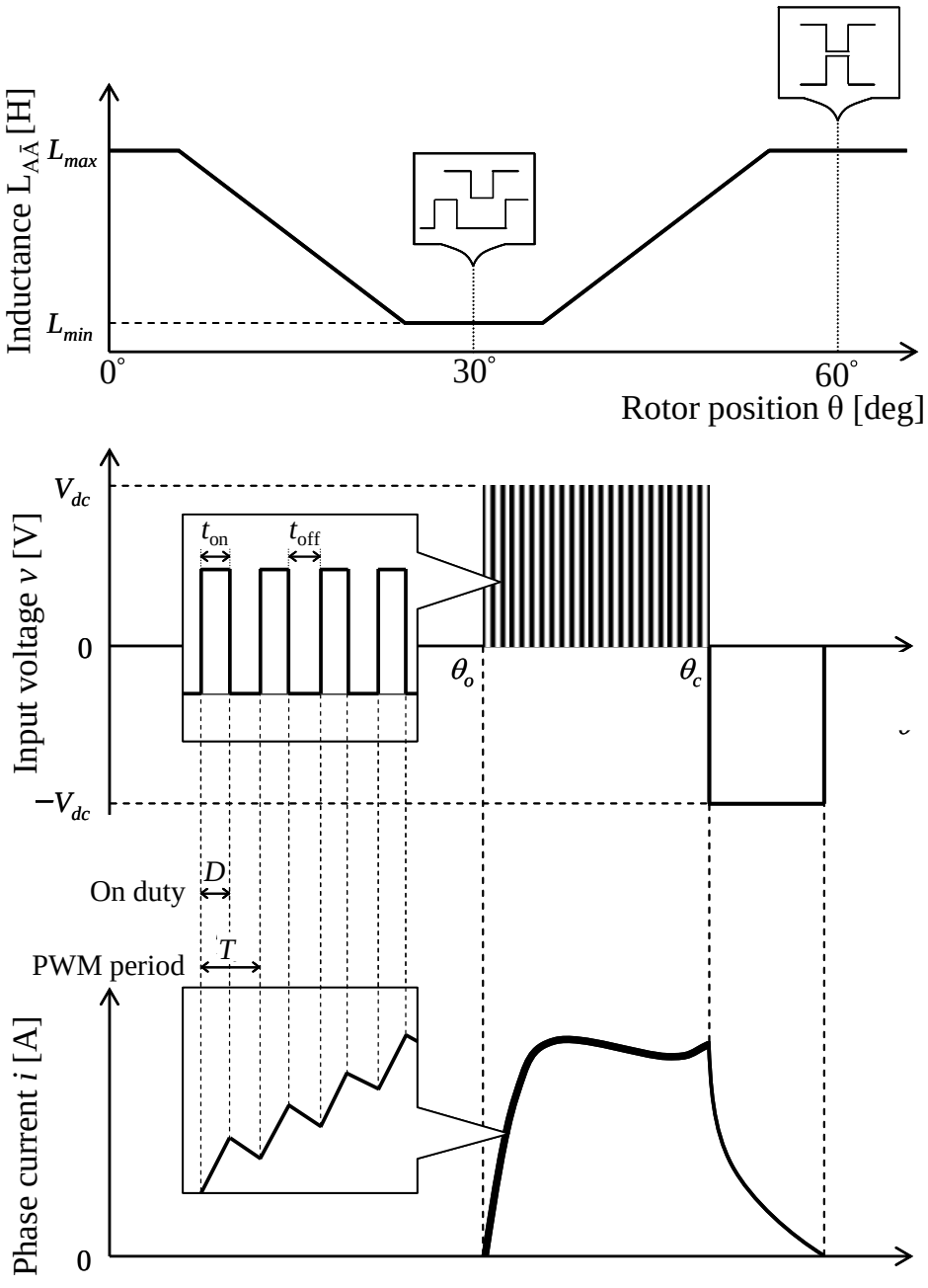

Figure 1.14 PWM voltage control

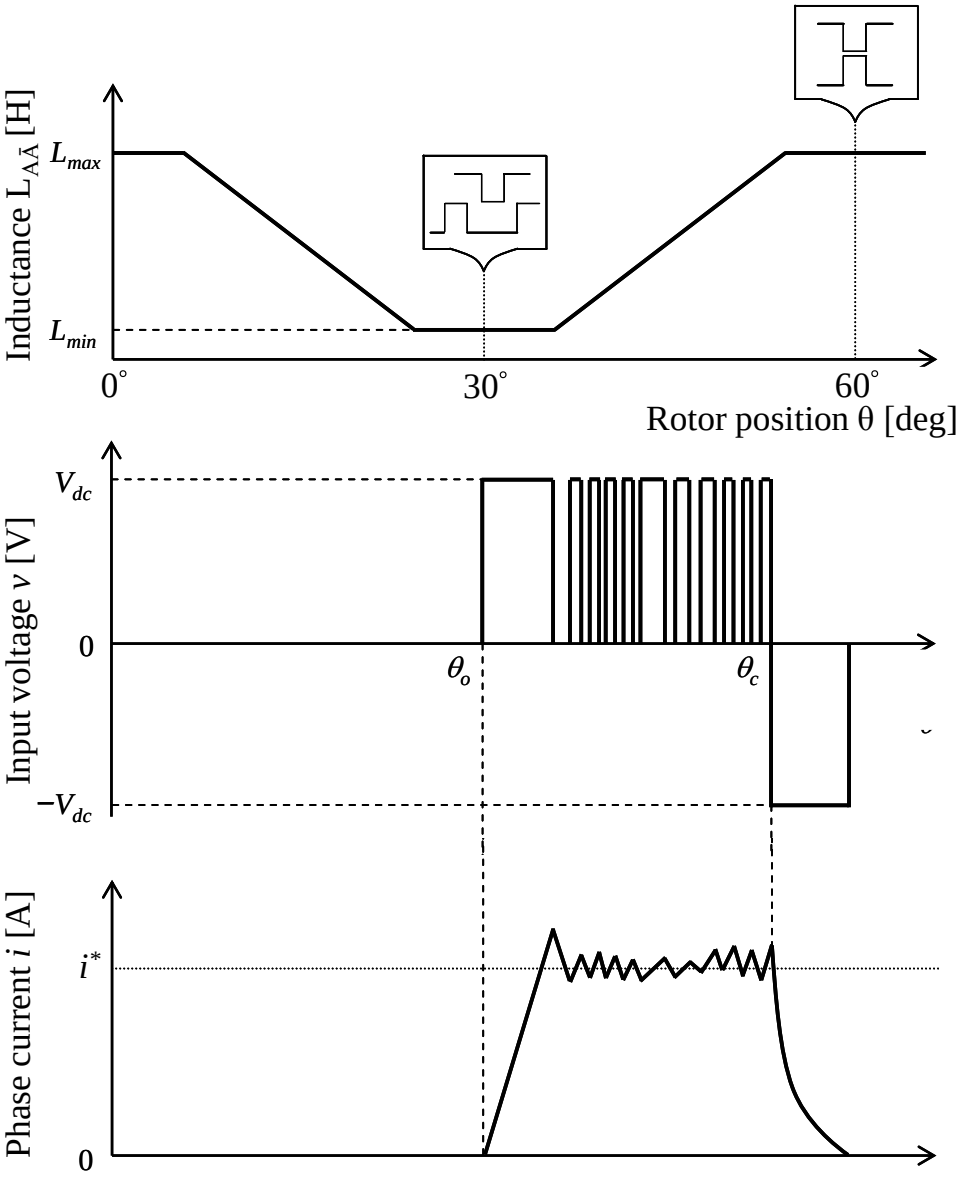

Figure 1.15 Constant current control

1.2.3 Specification of experimental motor

In our laboratory, a SRM for industry servo application was designed to realize the same performances with an existing PMSM (400W) for an industrial servo drive[14]. To replace a motor one-on-one, the SRM considered the design specifications and targets as follows.

1) Motor volume: stator outer diameter 80[mm], stack length 40[mm],
2) Maximum voltage and current of converter : DC link voltage 282.8[V], DC maximum current 8.1[A]
3) Maximum torque and speed: to satisfy the maximum speed and toque curve of figure 1.16.
4) Maximum efficiency: to get the minimum copper loss and iron loss in representative operating points.

To achieve high efficiency and torque density, the four phase 8/6 (stator/rotor) pole SRM with 0.1mm airgap was considered as its basic structure. By optimizing design parameters through GA (genetic algorithm) for the above targets, the design results can be obtained as shown in figure 1.17. Table 1.1 shows the main dimensions and specifications of a test motor fabricated as shown in figure. 1.18.

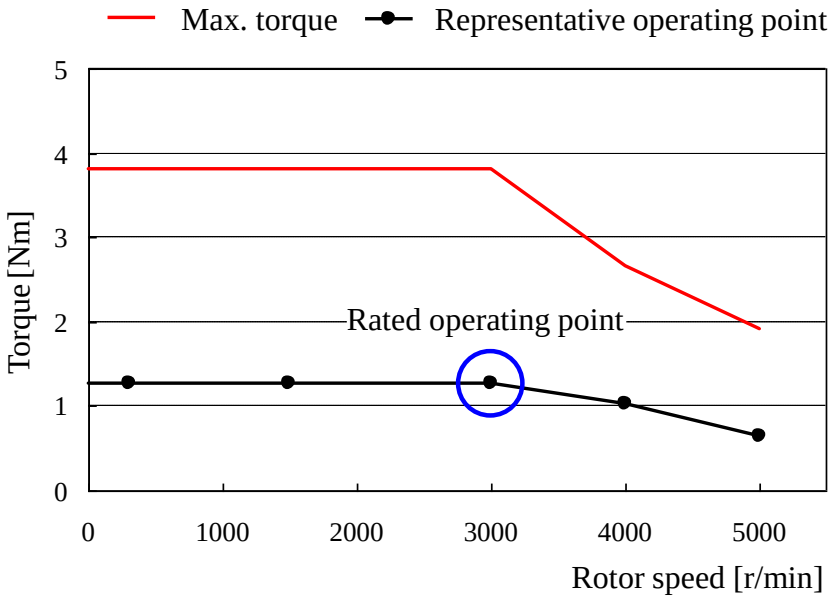

Figure 1.16 Required torque speed characteristics

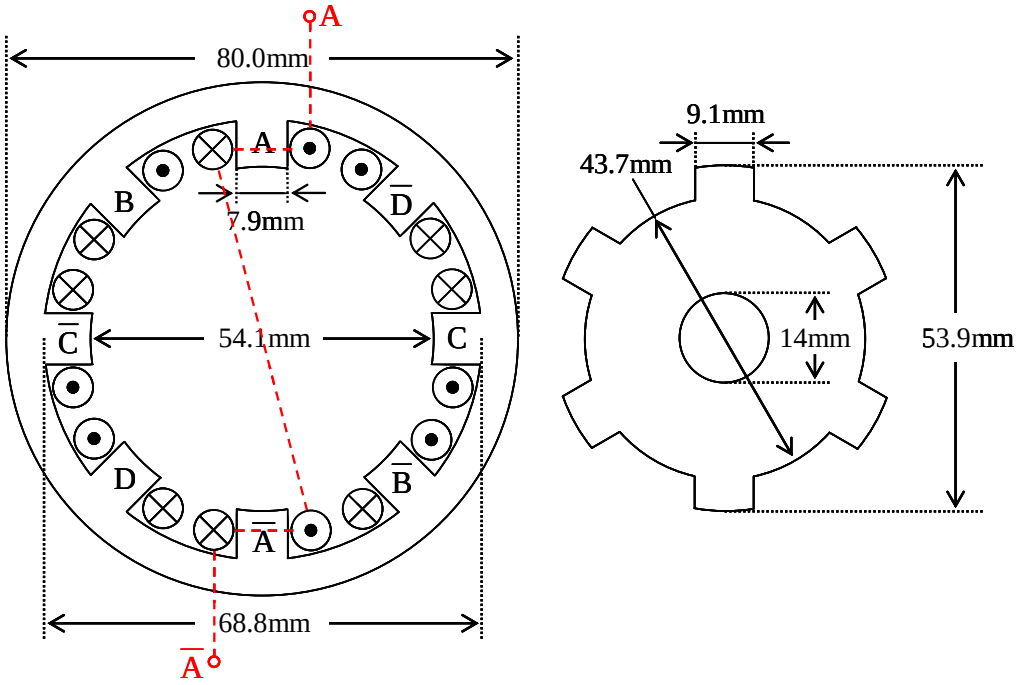

(a) Stator Assembly (b) Rotor Assembly

Figure 1.17 Structure of four phase 8/6 SRM for test

Table 1.1 The specification of 4 phase 8/6 SRM for test

Rated power [W]	400	Stator pole angle [deg]	16.793
Rated torque [Nm]	1.27	Rotor pole angle [deg]	19.440
Rated speed [r/min]	3000	Stator pole height [mm]	7.35
Stator outer diameter [mm]	80	Rotor pole height [mm]	5.1
Stack length [mm]	40	Stator back yoke width [mm]	5.6
Shaft diameter [mm]	14	Rotor yoke width [mm]	14.85
Airgap [mm]	0.1	Number of turn per coil [turn/pole]	185
Stator / rotor core	35H360	Phase resistance[Ω]	5.2

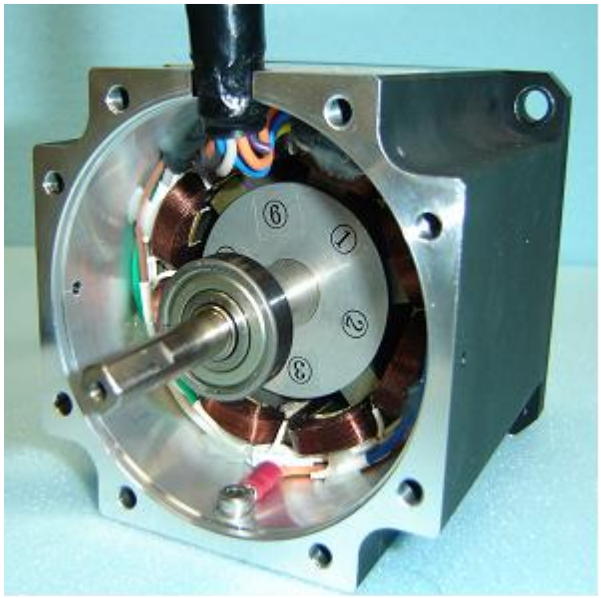

Figure 1.18 Picture of designed four phase 8/6 SRM

1.2.4 Characteristics of Servo drive systems using SRM

Generally, the servo drive system for position control consists of position feedback controller(PC), speed feedback controller(SC) and torque controller(TC) as shown in figure 1.19. PC and SC calculate out the target speed ω^* for the input position error(θ^*-θ), and the target torque T^* for the input speed error(ω^*-ω) respectively. the TC calculates out the target voltage v_x^* about each phase x for input target torque T^*. v_x is controlled by using PWM duty

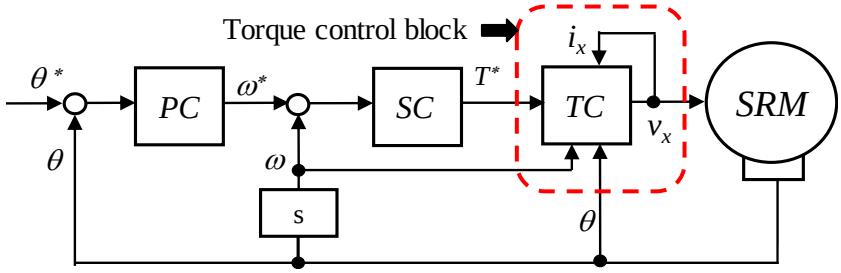

Figure 1.19 Position control block diagram of servo drive system using SRM

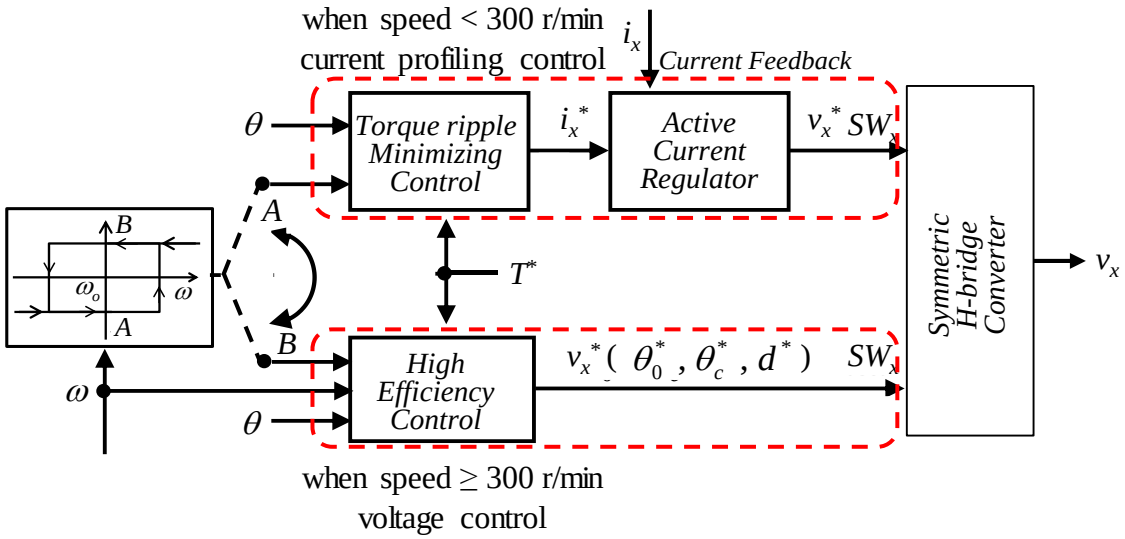

Figure 1.20 Torque control block diagram according to operating speed

control. The TC is divided to current control and voltage control according to operating speed as shown in figure 1.20. Under the condition higher than base speed-300 r/min, the voltage control is performed with voltage parameters (on angle θ_o, commutation angle θ_c, voltage duty d^*) to increase efficiency while making the average torque to be target value. On the other hand, under the condition lower than 300 r/min, the current profiling control that makes the phase current to track with the target current profile for constant torque control is conducted.

When the position error is high, quick position moving is required. At this time that the speed is generally higher than 300 r/min, the voltage control is conducted. However, because the base frequency of voltage is high in high speed, therefore, the voltage contains high order harmonics, the harmonic component of voltage can cause a large vibration near the natural frequency of the motor. On the other hand, when the position error is low, accurate positioning is required. At this time that the speed is generally lower than 300 r/min, the current profiling control for minimization of torque ripple is conducted. However, this method has the problem that as the load increases, the torque ripple in the current overlap area increases. The explanation about this problem and details about current profiling control will be described in chapter 4.

In conclusion, the two issues described above are major obstacles to competing with PMSM, which are large vibration by voltage control at high speed operation and high torque ripple by conventional current profiling control at low speed region. Through the solution of above two problems, the value of SRM as a motor for industrial servo systems can be improved, thus gaining a competitive edge over PMSM.

1.3 The purpose and configuration of paper

The SRM designed for the industrial servo application has still drawbacks caused by control methods as explained in chapter 1.2.2. The control methods to mitigate the problems are proposed, respectively. Firstly, for minimization of vibration, the vibration cancellation method using 2-stage commutation was proposed in advance study. However, this method has the problem that does not work well under high speed and load condition. So, the modified 2-stage commutation method is proposed to mitigate this problem. Secondly, to minimize torque ripple in every position, the current profiling control method was proposed in advance. However, in current overlapping region between two phases, the torque ripple increases with the load torque increase due to an affection of mutual coupling effect. To solve this problem, the modified method considering the mutual coupling effect is proposed. Lastly, in order to solve the problems that can be found in the conventional position estimation algorithms such as complexity and expensiveness to apply, the economic and simple algorithm using gradient of phase voltage and their rate between two phases obtained from three voltage sensor is proposed. The purpose of this paper is to propose the drive system with control methods for minimizing vibration, acoustic noise, and torque ripple, and simple and economic position sensorless algorithm while keeping other performance sufficient for the general-purpose industrial servo motor drive application.

This paper consists of seven chapters. Chapter 1 is concerned with the back ground and the purpose of this study. Chapters 2 and 3 summarize the control method for minimizing

vibration and noise. Chapters 4 and 5 describe the control approach for torque ripple minimization. Chapter 6 presents a newly proposed position sensorless algorithm. Finally, Chapter 7 make a conclusion and discussion about remaining future works. The details will be explained as follows.

Chapter 1 Introduction

The trends of motor development for high efficiency and supply problems about rare earth magnets have been explained. The alternative rare-earth free motors were surveyed. Especially, this paper selects SRM as a promising motor comparable with the PMSM. Many remaining issues of SRM to be overcome have been presented for as the purpose of being comparable with PMSM.

Chapter 2 Mechanism of vibration generation in SRM and active vibration cancellation techniques

The mechanism of vibration generation of general SRM will be explained. To reduce the vibration with resonant frequency, conventional 2-stage commutation method which studied in advance will be explained before clarifying the issues remaining in next chapter.

Chapter 3 A new modified two stage commutation method to achieve better AVC in SR servo motor

The problem that conventional method does not work well in high speed and high load condition firstly will be cleared. The reason of this problem will be investigated through 2D-FEA simulation and theoretical analysis. Finally, modified 2-stage commutation method to mitigate this problem will be proposed and its effectiveness will be proven by experiments.

Chapter 4 Conventional torque ripple minimization control of SRM for servo

The conventional torque control method using current profiling control will be explained. The target current profile derived from current-torque-position model and target torque contour function are controlled by using active current regulator called as current tracking controller. However, the torque ripple in current overlapping region between two phases is increased by an affection of mutual coupling effect between the energized two adjacent phases. The reason of this problem is investigated through 2D- FEA simulation.

Chapter 5 Torque ripple minimization control based on magnetizing curves model considering mutual coupling

To minimize torque ripple in the current overlapping region, the modified method considering the mutual coupling effect will be proposed. The process to obtain the magnetizing curves and the current-torque-position model considering the mutual coupling effect will be explained. Finally, it will be demonstrated that the torque ripple is minimized

by using the target current profile derived from the modified current-torque-position model.

Chapter 6 Sensorless position estimation for SRM using phase voltage and voltage rate

A survey of general position sensorless algorithms that have been proposed up to now will be given. The problems of conventional method will be clarified based on analyses of strong and weak points of the existing methods and then, the aim of this paper will be presented. To develop a simple and economic sensorless algorithm, this study focuses on linear gradients of phase voltage and voltage rate between two phases detected by three voltage sensors will be proposed. Through experiments, an accuracy of the algorithm proposed will be verified.

Chapter7 Conclusion

The contents done by this thesis and the tasks to be addressed in the future will be summarized.

Chapter2
Mechanism of vibration generation in SRM and active vibration cancellation techniques

2.1 Prologue

In this chapter, the mechanism of vibration generation in SRM is overviewed. Firstly, Electromagnetic (EM) impact pulse is defined as an exciting source of vibration. This EM impact pulse is analyzed mathematically and the mechanism of vibration generation in SRM is investigated from a viewpoint of harmonics involved in the EM impact pulse. Secondly, two-stage commutation control method proposed by Pollock. C is explained as one of active vibration cancellation techniques to reduce the vibration[30]. Finally, two-stage commutation control method employing negative PWM voltage control proposed in advance research[32] is reviewed.

2.2 Basics of vibration generation mechanism[16]

Basically, the principle of vibration production from a single degree of freedom (SDOF) system to multi-degree of freedom (MDOF) system is described. Then, of the vibration mode $\{\varphi_m\}$ and force mode$\{F\}$ described in MDOF system, the force mode $\{F\}$, i.e. the spatial harmonic of the radial force in test motor being a source of vibration is analyzed.

2.2.1 Vibration in a single degree of freedom system

In this subsection, a free and a forced dynamic responses in a single degree of freedom system (SDOF) are examined. The SDOF system in the mechanical system consists of mass, spring, and damper as can be seen in figure 2.1. The mass is allowed to move in only one direction by force. In this system, the equation of motion is obtained from the balance of forces against the mass. The forces against the mass consist of elastic restoring force f_{spring}, damping force $f_{damping}$, and external force $f_{external}$. Through Newton's second raw, the relationship between the forces is given in,

$$f = f_{spring} + f_{damping} + f_{external} = m\ddot{x}(t)\left(= m\frac{d^2x(t)}{dt^2} \right) \tag{2.1}$$

$$m\ddot{x}(t) = f_{spring} + f_{damping} + f_{external} = -k\dot{x}(t) - cx(t) + f(t). \tag{2.2}$$

As a result, the equation of motion will be derived as,

$$m\ddot{x}(t) + c\dot{x}(t) + kx(t) = f(t) \tag{2.3}$$

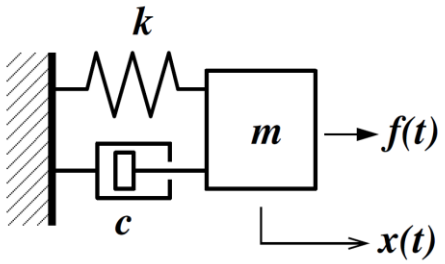

Figure 2.1 Single degree of freedom system

where, x, m, c and k are displacement [m], mass [kg], viscous damping coefficient [N·s/m] and elastic stiffness coefficient [N/m], respectively. To solve this differential equation for displacement x, Laplace transform is introduced and given in,

$$\begin{aligned} &m(s^2X(s)-sx(0^-)-\frac{dx(0^-)}{dt})+c(sX(s)-x(0^-))+kX(s)=F(s) \\ &x(0^-)=x_0,\ \frac{dx(0^-)}{dt}=v_0 \end{aligned} \tag{2.4}$$

where x_0 and v_0 are an initial position and an initial velocity, respectively. From the equation (2.4), the equation can be derived in following manner.

$$\begin{aligned} X(s) &= \frac{1}{m}\frac{1}{s^2+\frac{c}{m}s+\frac{k}{m}}F(s)+\frac{sx_0+v_0+\frac{c}{m}x_0}{s^2+\frac{c}{m}s+\frac{k}{m}} \\ &= \frac{1}{m}\frac{1}{s^2+2\omega_n\xi s+\omega_n^2}F(s)+\frac{sx_0+v_0+2\omega_n\xi x_0}{s^2+2\omega_n\xi s+\omega_n^2} \end{aligned} \tag{2.5}$$

The first term is the forced response and the second term is the free response. ω_n and ξ are a natural angular frequency and a damping ratio, respectively, and can be expressed by following fashion.

$$\omega_n=\sqrt{\frac{k}{m}} \quad , \quad \xi=\frac{c}{2\sqrt{mk}} \tag{2.6}$$

Assuming that the system is under-damping ($0<\xi<1$) and taking inverse Laplace transform of the free response component in equation (2.5), one can be obtained as,

$$\begin{aligned} x(t) &= \frac{1}{2}\left(x_0 + j\frac{\omega_n \xi x_0 + v_0}{\omega_d} \right) e^{-(\omega_n \xi + j\omega_d)t} + \frac{1}{2}\left(x_0 - j\frac{\omega_n \xi x_0 + v_0}{\omega_d} \right) e^{-(\omega_n \xi - j\omega_d)t} \\ &= \frac{1}{2}\sqrt{{x_0}^2 + \left(\frac{\omega_n \xi x_0 + v_0}{\omega_d} \right)^2} \cdot e^{-\omega_n \xi t} \cos(\omega_d t + \theta_0) \\ &= \mathrm{X} e^{-\omega_n \xi t} \cos(\omega_d t + \theta_0) \end{aligned} \tag{2.7}$$

where, ω_d *and* θ_0 is a damped natural angular frequency and an initial phase, which is expressed as following manner.

$$\theta_0 = \tan^{-1}\left(\frac{\omega_n \xi x_0 + v_0}{x_0 \omega_d} \right),\ \omega_d = \omega_n \sqrt{1-\xi^2} \tag{2.8}$$

Figure 2.2 shows free response in time domain under the condition that the initial position and velocity are set to x_0 and v_0, respectively. If the external force is set to be $f(t) = \delta(t)$ (impulse function), the forced response, which is derived as $F(s)$=1 in the first term of equation (2.5), is given in,

$$x(t) = \frac{m^{-1}}{\omega_d} \cdot e^{-\omega_n \xi t} \sin(\omega_d t) \tag{2.9}$$

On the other hand, if the second order differential of the external force is set to be $d^2f(t)/dt^2 = \delta(t)$, the acceleration a(t) as a result of the forced response, which is derived as $s^2F(s)$=1 in the first term of equation (2.5), can be obtained as,

$$a(t) = \frac{m^{-1}}{\omega_d} \cdot e^{-\omega_n \xi t} \sin(\omega_d t) \tag{2.10}$$

As can be seen in figure 2.3, when $d^2f(t)/dt^2$ is equal to $\delta(t)$, the time response of acceleration becomes damped oscillating waveform. Besides, if the external force varies sinusoidal like $f(t) = F_0 \cdot \cos(\omega_{dr} t)$, the displacement $x(t)$ can be deduced by,

$$x(t) = \frac{1}{m\sqrt{(\omega_n^2 - \omega_{dr}^2)^2 + (2\omega_n\omega_{dr}\xi)^2}} F_0 \cos\left(\omega_{dr}t - \tan^{-1}\left(\frac{2\omega_n\omega_{dr}\xi}{\omega_n^2 - \omega_{dr}^2}\right)\right) \quad (2.11)$$
$$= G_0 F_0 \cos(\omega_{dr}t - \theta_d)$$

where, F_0 and ω_{dr} are a magnitude and an angular frequency of the sinusoidal external force and G_0 is a transfer gain, θ_d is a phase delay. As a result, the displacement x varies with sinusoidal waveform. For frequency analysis of the transfer gain G_0, dynamic amplification factor $M = kG_0$ is defined as,

$$M = kG_0 = \frac{1}{\sqrt{(1-r^2)^2 + (2\xi r)^2}} \quad (2.12)$$

where $r = \omega_{dr}/\omega_n$ is frequency ratio. As can be seen in figure 2.4, the dynamic amplification factor M varies with the frequency ratio. When the angular frequency ω_{dr} is same as the the damped angular frequency ω_d, the gain takes its maximum and the maximum magnitude at this frequency depends on the damping factor ξ. It is reasonable to suppose that the force component with the damped natural angular frequency yields the maximum vibration.

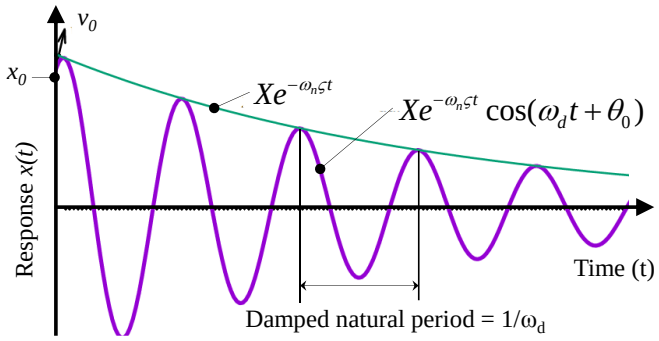

Figure 2.2 Free response of under-damping system in time domain.

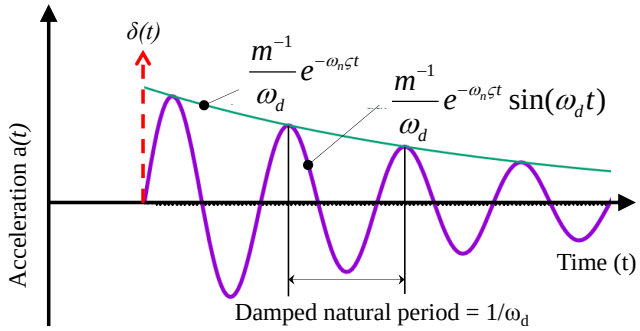

Figure 2.3 Impulse response of SDOF system in time domain.

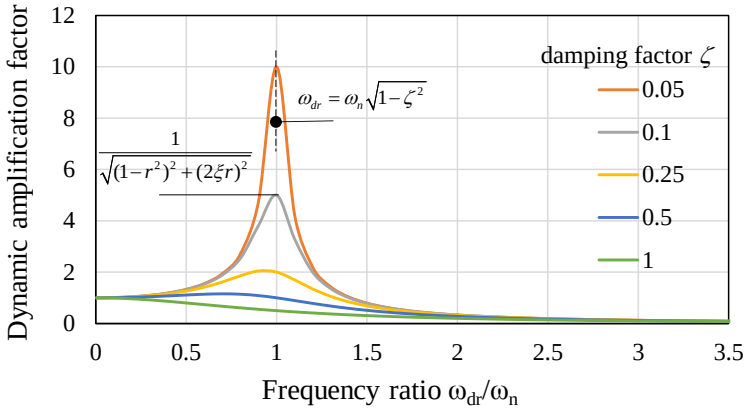

Figure 2.4 Dynamic amplification factor when an external sinusoidal force is applied.

2.2.2 Vibration in multi-degree of freedom system[16]

Actually, the real system like an electric machine is composed of mechanical system with multi-degree of freedom (MDOF), in which multiple SDOF systems are connected. In a SDOF system, it has a single natural frequency and a single vibration mode. However, in an MDOF system consisting of *m* set of SDOFs, the different *m* vibration modes with individual natural frequency exist. For an ease of explanation, the two degrees of freedom (2DOF) system is introduced in figure 2.5 as an example. In this system, the equation of motion will be given in following manner.

$$\begin{aligned} m_1\ddot{x}_1 + c_1\dot{x}_1 + c_2\{\dot{x}_1 - \dot{x}_2\} + k_1x_1 + k_2\{x_1 - x_2\} &= f_1 \\ m_2\ddot{x}_2 + c_2\{\dot{x}_2 - \dot{x}_1\} + k_2\{x_2 - x_1\} &= f_2 \end{aligned} \tag{2.13}$$

By using matrix expression, equation (2.13) is expressed as,

$$\begin{bmatrix} m_1 & 0 \\ 0 & m_2 \end{bmatrix}\begin{bmatrix} \ddot{x}_1 \\ \ddot{x}_2 \end{bmatrix} + \begin{bmatrix} c_1 + c_2 & -c_2 \\ -c_2 & c_2 \end{bmatrix}\begin{bmatrix} \dot{x}_1 \\ \dot{x}_2 \end{bmatrix} + \begin{bmatrix} k_1 + k_2 & -k_2 \\ -k_2 & k_2 \end{bmatrix}\begin{bmatrix} x_1 \\ x_2 \end{bmatrix} = \begin{bmatrix} f_1 \\ f_2 \end{bmatrix}. \tag{2.14}$$

To obtain natural frequency, zero input force and zero damping coefficient are assumed and then, natural frequency can be calculated from the equation below.

$$\begin{bmatrix} m_1 & 0 \\ 0 & m_2 \end{bmatrix}\begin{bmatrix} \ddot{x}_1 \\ \ddot{x}_2 \end{bmatrix} + \begin{bmatrix} k_1 + k_2 & -k_2 \\ -k_2 & k_2 \end{bmatrix}\begin{bmatrix} x_1 \\ x_2 \end{bmatrix} = \begin{bmatrix} 0 \\ 0 \end{bmatrix} \tag{2.15}$$

Assuming that the free response is represented by harmonic in nature, $x_n = X_n e^{j\omega t}$ with a complex value X_n, equation (2.15) can be rewritten as following fashion.

$$-\omega^2\begin{bmatrix} m_1 & 0 \\ 0 & m_2 \end{bmatrix}\begin{bmatrix} x_1 \\ x_2 \end{bmatrix} + j\omega\begin{bmatrix} k_1+k_2 & -k_2 \\ -k_2 & k_2 \end{bmatrix}\begin{bmatrix} x_1 \\ x_2 \end{bmatrix} = \begin{bmatrix} 0 \\ 0 \end{bmatrix} \tag{2.16}$$

Assuming that the x_1 and x_2 are not zero, to satisfy equation (2.15) the equation below must be satisfied.

$$\det\left|-\omega^2\begin{bmatrix} m_1 & 0 \\ 0 & m_2 \end{bmatrix} + j\omega\begin{bmatrix} k_1+k_2 & -k_2 \\ -k_2 & k_2 \end{bmatrix}\right| = 0 \tag{2.17}$$

Then, the natural frequency of 2DOF system will be derived as,

$$\omega_{n1},\omega_{n2} = \sqrt{\frac{1}{2}\left[\left(\frac{k_1}{m_1}+\frac{k_1+k_2}{m_2}\right) \pm \sqrt{\left(\frac{k_1}{m_1}+\frac{k_1+k_2}{m_2}\right)^2 - 4\frac{k_1k_2}{m_1m_2}}\right]} \quad . \tag{2.18}$$

If two natural frequencies are inputted to equation (2.16), then x_1 and x_2 for each natural frequency are calculated. Eigenvector [x_1, x_2] for each natural frequency ω_{n1}, ω_{n2} are called as vibration mode $\{\varphi_1\}$, $\{\varphi_2\}$. As a result, a shape of vibration by the displacements x_1 and x_2 distributed in space will be different depending on the natural frequencies. Figure 2.6 illustrates typical vibration modes in the 2DOF system.

Generally, in the *m*-DOF system, *m* natural frequencies $\{\omega_{n1}, \omega_{n2}, \ldots, \omega_{nm}\}$ and *m* vibration modes $\{\{\varphi_1\},\{\varphi_2\},\ldots\ldots,\{\varphi_m\}\}$ for the individual natural frequency are existed. In *m*-DOF system, the equation of moving can be written as,

$$[\boldsymbol{M}]\{\ddot{\boldsymbol{x}}\} + [\boldsymbol{C}]\{\dot{\boldsymbol{x}}\} + [\boldsymbol{K}]\{\boldsymbol{x}\} = \{\boldsymbol{f}\} \tag{2.19}$$

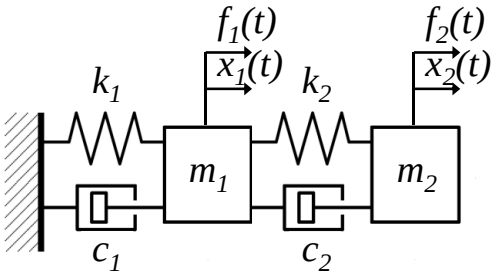

Figure 2.5 Two degrees of freedom system

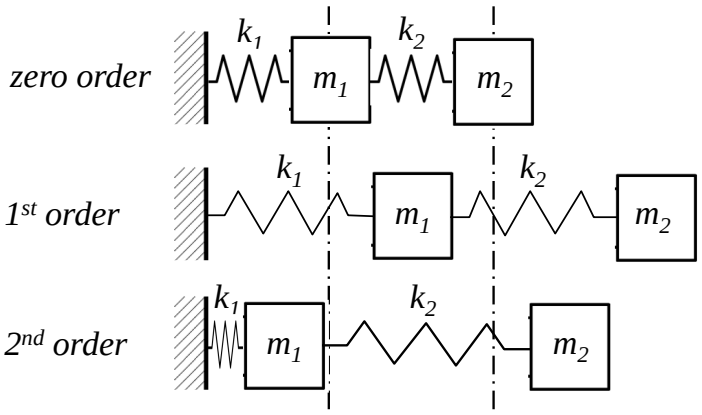

Figure 2.6 Vibration mode in 2DOF(dampers are omitted)

where, [$\boldsymbol{M}$], [$\boldsymbol{C}$], and [$\boldsymbol{K}$] are the matrix of mass, damping, and stiffness respectively.

On the assumption that the displacement is $\{\boldsymbol{x}\}=\{\boldsymbol{X}\}e^{j\omega t}$ and the force is $\{\boldsymbol{f}\}=\{\boldsymbol{F}\}e^{j\omega t}$, the displacement at a certain point can be expressed by superimposition of spatially distributed vibration modes with a corresponding gain G_k and given in,

$$\{\boldsymbol{X}\}=\sum_{k=1}^{m} G_k\{\boldsymbol{\varphi_k}\} \tag{2.20}$$

By utilizing that eigenvector $\{\boldsymbol{\varphi_m}\}$ has orthogonality with mass matrix and stiffness matrix,

the gain G_k will be obtained from following manner[16].

$$\begin{aligned} G_k &= \frac{\{\boldsymbol{\varphi_k}\}^T \{\boldsymbol{F}\}}{\{\boldsymbol{\varphi_k}\}^T [\boldsymbol{K}]\{\boldsymbol{\varphi_k}\} - \omega^2 \{\boldsymbol{\varphi_k}\}^T [\boldsymbol{M}]\{\boldsymbol{\varphi_k}\} + j\omega \{\boldsymbol{\varphi_k}\}^T [\boldsymbol{C}]\{\boldsymbol{\varphi_k}\}} \\ &= \frac{\{\boldsymbol{\varphi_k}\}^T \{\boldsymbol{F}\}}{k_k - \omega^2 m_k + j\omega c_k} \end{aligned} \tag{2.21}$$

k_k, m_k and c_k are modal stiffness, modal mass and modal damping coefficient, respectively, and they are expressed as following fashions.

$$k_k = \{\boldsymbol{\varphi_k}\}^T [\boldsymbol{K}]\{\boldsymbol{\varphi_k}\},\ m_k = \{\boldsymbol{\varphi_k}\}^T [\boldsymbol{M}]\{\boldsymbol{\varphi_k}\},\ c_k = \{\boldsymbol{\varphi_k}\}^T [\boldsymbol{C}]\{\boldsymbol{\varphi_k}\} \tag{2.22}$$

Eventually, the gain of k^{th} vibration mode is concerned with the vibration mode $\{\boldsymbol{\varphi_k}\}^T$, the force mode $\{\boldsymbol{F}\}$ at each position and its angular frequency ω. Consequently, (2.20) will be rearranged and given in,

$$\{\boldsymbol{X}\} = \sum_{k=1}^{m} \frac{\{\boldsymbol{\varphi_k}\}^T \{\boldsymbol{F}\}\{\boldsymbol{\varphi_k}\}}{k_k - \omega^2 m_k + j\omega c_k} = \sum_{k=1}^{m} \frac{\{\boldsymbol{\varphi_k}\}^T \{\boldsymbol{F}\}\{\boldsymbol{\varphi_k}\}}{k_k \left[1 - \left(\frac{\omega}{\omega_k} \right)^2 m_k + 2j\xi_k \left(\frac{\omega}{\omega_k} \right) \right]} \tag{2.23}$$

where, ξ_k is k^{th} damping coefficient and can be defined as,

$$\xi_k = c_k \Big/ 2\sqrt{m_k c_k} \quad . \tag{2.24}$$

As can be known through (2.23), if the vibration mode shape coincides with the mode shape of the external force distributed in space, $\{\boldsymbol{\varphi_k}\}^T \{\boldsymbol{F}\}$ takes its maximum value and the denominator takes its minimum when the angular frequency ω of the external force meets to

the natural frequency ω_k, resulting in the maximum amplification of $\{\boldsymbol{\varphi}_k\}^T\{\boldsymbol{F}\}$.

2.3 Analysis of electromagnetic force in SRM

Based on the contents in section 2.2.2, it is investigated how the vibration source of SRM is produced in this chapter. As is well known, the total electric magnetic force F_t consists of tangential force F_θ and radial force F_r as shown in the left side of Figure 2.7. Most of the tangential force contributes to production of shaft torque T through the equation, $T = F_\theta \times r$[N·m], where r is a radius of the rotor. On the other hand, the radial force F_r acts as a source to produce motor vibration by pulling both stator and rotor in radial direction. To examine the space distribution of electromagnetic radial force (hereafter, called as EM force) in 4-phase 8/6 SRM as an example, it is assumed that the current is commutated in order of A→B→C→D-phase with a phase shift of π/2 degrees electrically (mechanical 15 degrees). In this case, the EM forces F_A, F_B, F_C and F_D acting on stator tooth in each phase are also shifted with the same phase shift as shown in the right side of figure 2.7. By FFT analysis, the EM force of each phase can be expressed by Fourier cosine series expansion containing DC component F_{dc} and time harmonic components and are given in,

$$\begin{aligned}
&EM\ force\ of\ A\ \text{phase} = F_A(t) = F_{dc} + \sum_{n=1}^{\infty} F_n \cdot \cos\left(n\omega_{dr}t + \phi_n\right) \\
&EM\ force\ of\ B\ \text{phase} = F_B(t) = F_{dc} + \sum_{n=1}^{\infty} F_n \cdot \cos\left(n\omega_{dr}t + \phi_n - n\frac{\pi}{2}\right) \\
&EM\ force\ of\ C\ \text{phase} = F_C(t) = F_{dc} + \sum_{n=1}^{\infty} F_n \cdot \cos\left(n\omega_{dr}t + \phi_n - n\pi\right) \\
&EM\ force\ of\ D\ \text{phase} = F_D(t) = F_{dc} + \sum_{n=1}^{\infty} F_n \cdot \cos\left(n\omega_{dr}t + \phi_n - n\frac{3\pi}{2}\right)
\end{aligned} \tag{2.25}$$

where, F_n is the magnitude of n^{th} order time harmonic, ω_{dr} is electrical angular rotor speed, ϕ_n is a phase angle of n^{th} order time harmonic. As the EM forces act as just pulling force for the stator teeth, the space distribution of EM forces on stational frame defined on the stator body at a certain instant can be displayed as shown in the right side of figure 2.8. As can be seen from the figure, θ is defined as an angle on the stational frame whose origin is the center of A-phase stator tooth located at north. The spatial distribution of the EM force on the stational frame can be expressed by using Fourier cosine expansion and as,

$$F_s(\theta) = \sum_{k=0}^{N/2} F_{s\_k} \cdot \cos\left(k\theta - \theta_k\right) \tag{2.26}$$

where, N is a number of stator tooth. F_{s_k} and θ_k are force amplitude and phase angle of k^{th} order component, respectively, and derived from Discrete Fourier Transfrom (DFT) as follows.

$$\begin{aligned} F_{s\_0} &= \frac{1}{N}\sum_{m=1}^{N} F\big|_{\theta=\theta_m} \\ F_{s\_k} &= \frac{2}{N}\sqrt{\left(\sum_{m=1}^{N} F\big|_{\theta=\theta_m}\cos k\theta_m\right)^2 + \left(\sum_{m=1}^{N} F\big|_{\theta=\theta_m}\sin k\theta_m\right)^2} \\ \theta_k &= \tan^{-1}\frac{\sum_{m=1}^{N} F\big|_{\theta=\theta_m}\sin k\theta_m}{\sum_{m=1}^{N} F\big|_{\theta=\theta_m}\cos k\theta_m} \end{aligned} \tag{2.27}$$

where θ_m is the angle of the center of each stator tooth from the origin of θ and m is an number assigned to each stator tooth as shown in figure 2.8. A relationship between θ_m and N and m is given in $\theta_m = 2\pi(m\text{-}1)/N$. $F|_{\theta=\theta_m}$ is defined as the EM force at each position θ_m on the stational frame at a certain instant. The spatial distribution of each harmonic component is

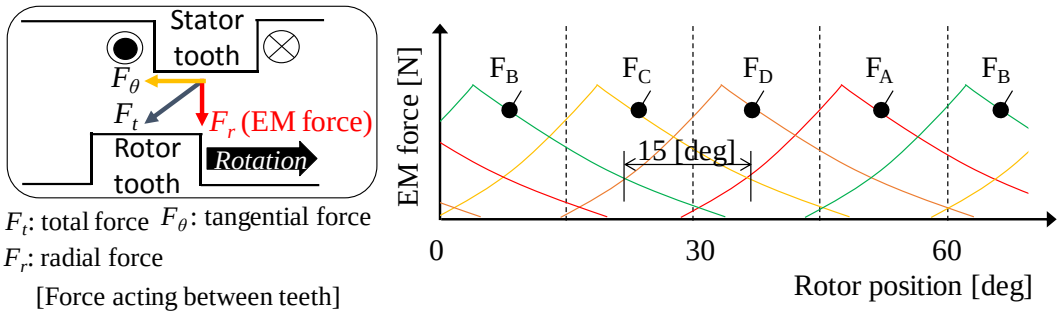

Figure 2.7 Forces acting on stator tooth and EM force variation of each phase.

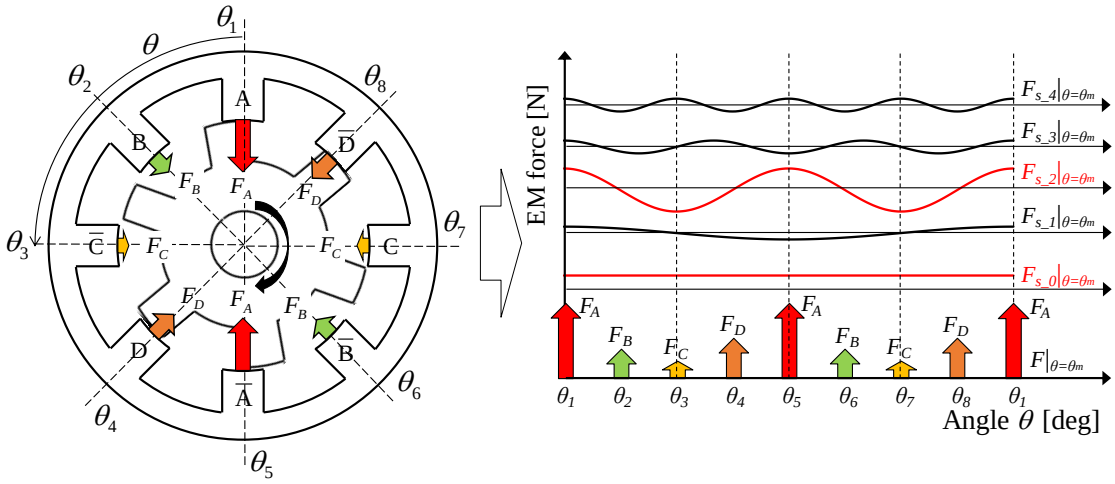

Figure 2.8 Space distribution of EM force at certain instant.

illustrated in the right side of figure 2.8. From the figure, it is easy to identify that the dominant space distribution of the EM force is the second order space harmonic F_{s_2}. From now on, it will be founded out which time harmonic components containing the EM forces are related to the second-order space harmonics.

In equation (2.27), $F|_{\theta=\theta m}$ that is the EM force at each position θ_m on the stational frame

can be replaced with the EM force acting on each stator tooth as can be seen from figure 2.8 and thus,

$$\begin{aligned} F\big|_{\theta=\theta_1} &= F\big|_{\theta=\theta_5} = F_A, \;\; F\big|_{\theta=\theta_2} = F\big|_{\theta=\theta_6} = F_B \\ F\big|_{\theta=\theta_3} &= F\big|_{\theta=\theta_7} = F_C, \;\; F\big|_{\theta=\theta_4} = F\big|_{\theta=\theta_8} = F_D \end{aligned} \tag{2.28}$$

The magnitude of second-order spatial harmonic F_{s_2} of equation (2.27) will be expressed like equation (2.29) to analyze after calculating the cosine and sine series in the root respectively.

$$\begin{aligned} F_{s\_2} &= \frac{2}{N}\sqrt{\left(\sum_{m=1}^{N} F\big|_{\theta=\theta_m}\cos 2\theta_m\right)^2 + \left(\sum_{m=1}^{N} F\big|_{\theta=\theta_m}\sin 2\theta_m\right)^2} \\ &= \frac{2}{N}\sqrt{\left(F_{s\_2\_\cos}\right)^2 + \left(F_{s\_2\_\sin}\right)^2} \end{aligned} \tag{2.29}$$

Substituting equation (2.28), $\theta_m = \pi(m\text{-}1)/4$ and equation (2.25) into equation (2.29), two terms $F_{s\_2\_\cos}$ and $F_{s\_2\_\sin}$ can be rearranged as follows.

$$\begin{aligned} F_{s\_2\_\cos} &= \sum_{m=1}^{8} F\big|_{\theta=\theta_m}\cos\left(2\theta_m\right) \\ &= 2\left\{F_A\cos(0) + F_B\cos\left(\frac{\pi}{2}\right) + F_C\cos(\pi) + F_D\cos\left(\frac{3\pi}{2}\right)\right\} \\ &= 2\sum_{n=1}^{\infty} F_n\left\{\cos\left(n\omega_{dr}t + \phi_n\right) - \cos\left(n\omega_{dr}t + \phi_n - n\pi\right)\right\} \end{aligned} \tag{2.30}$$

$$
\begin{aligned}
F_{s\_2\_\sin} &= \sum_{m=1}^{8} F\big|_{\theta=\theta_m} \sin(2\theta_m) \\
&= 2\left\{ F_A \sin(0) + F_B \sin\left(\frac{\pi}{2}\right) + F_C \sin\left(\frac{2\pi}{2}\right) + F_D \sin\left(\frac{3\pi}{2}\right) \right\} \\
&= 2\sum_{n=1}^{\infty} F_n \left\{ \cos\left(n\omega_{dr} t + \phi_n - \frac{n\pi}{2} \right) - \cos\left(n\omega_{dr} t + \phi_n - \frac{3n\pi}{2} \right) \right\}
\end{aligned}
\tag{2.31}
$$

According to equations (2.30) and (2.31), if n is an even number, the second order space harmonic disappears because both of $F_{s\_2\_\cos}$ and $F_{s\_2\_\sin}$ become zero. Therefore, only odd order time harmonics containing the EM force contribute to producing the second order space harmonic. Now, if we define a base frequency as f_{base}, a relationship between the electrical angular rotor speed ω_{dr} and f_{base} can be expressed as $\omega_{dr} = 2\pi f_{base}$. As another expression, the base frequency f_{base} is given in,

$$
f_{base} = \frac{N_{r/\min}}{60} N_r \tag{2.32}
$$

where $N_{r/min}$ and N_r are motor rotational speed and the rotor pole number, respectively. N_r of test motor is six. For an example, assuming that the test motor has circular second order mode as its main vibration mode whose natural frequency is 4.4[kHz], the base frequency is 300[Hz] at $N_{r/min}$ =3000[r/min]. If the 13th, 15th and 17th order time harmonics whose frequencies are near the natural frequency of motor are invloled in the EM force, will yield the second order space harmonic, that is, the circular second order vibration mode and will result large stator vibration due to mechanical resonance.

2.4 Vibration mode and hammering test result in test motor

In this section, the vibration mode of the test motor is investigated through 2D-FEA and the vibration transfer characteristic hammering test is carried out to obtain the vibration transfer characteristic of the test motor.

Figure 2.9 shows the models of test motor for 2D-FEA. Figure 2.9(a) is the full model for electromagnetic analysis. (b) is the simplified model for modal analysis, which consists of only a bracket and stator core. The vibration modes and their natural frequency can be computed by 2D-FEA-based modal analysis. The Poisson's ratio and Young's modulus obtained from the catalog are used. According to the modal analysis, the major vibration mode of test motor is the circular second order mode with natural frequency f_n = 4038[Hz] as shown in figure 2.10.

To clarify experimentally the vibration modes and their natural frequency of test motor, hammering test has been conducted. For the test, the impulse hammer (Ono-Sokki, GK-3100, bandwidth 8[kHz]) has been used. For measurement of acceleration, the accelerometer (ENDEVCO, 7250-A) is attached on the test motor surface. Frequency analysis of acceleration and impact force inputted by the impulse hammer is processed by FFT analyzer (A&D company, AD-3651). Through the analyzer the frequency analysis of transfer characteristic of vibration [m/sec^2] for an exciting impact force [N/sec^2] for the test motor is executed. The accelerometers are attached at 6 points on the top surface of the motor as shown in figure 2.11. The impact force is applied to the surface H by using the impulse

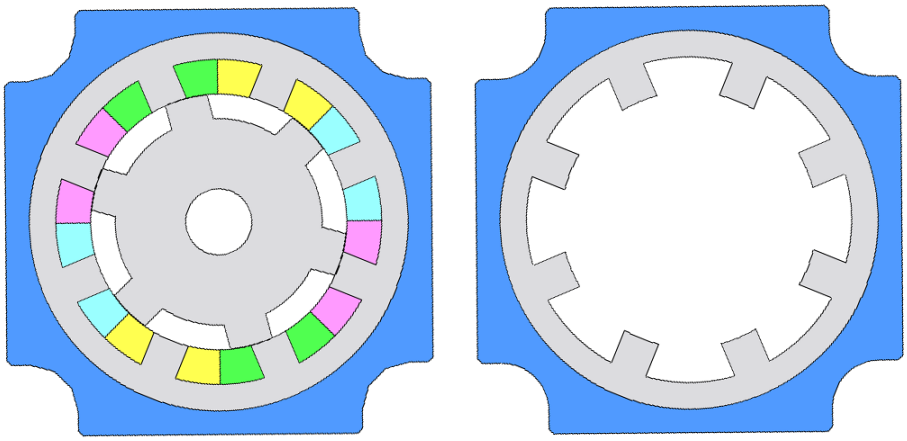

(a) model for electromagnetic analysis (b) model for modal analysis

Figure 2.9 Models of test motor for 2D-FEA simulation.

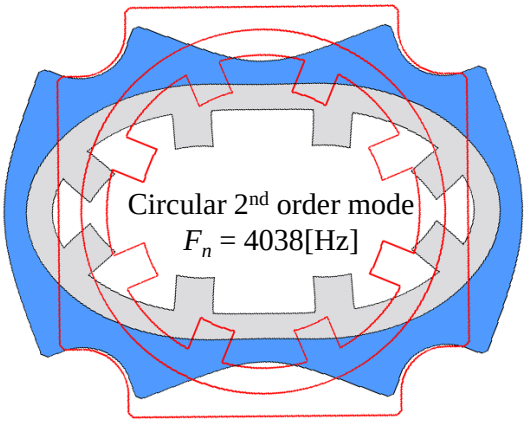

Figure 2.10 Analyzed main vibration mode of test motor.

hammer. Figure 2.12 demonstrates the frequency analysis results of input force and measured acceleration at the accelerometer assigned as the number 3. From the figure, the natural frequency of the main vibration is 4.4[kHz]. In addition, accordance with the sensing position with the assigned numbers from 1 to 6, the gains of transfer function (acceleration/impact force [$(m/s^2)/(N/s^2)$]) at the natural frequency can be calculated as shown in figure 2.13. From

this test result, it is clear that the main vibration mode of the test motor is the circular second order mode, and the accelerometers with the assigned number 3 and 4 show maximum vibration gain. In this study, therefore, the middle point between the number 3 and 4 is selected as a representative position to measure and evaluate vibration due to the circular second order mode as the main vibration mode of test motor

In the mechanical system having the circular second order vibration mode like the test motor, if the frequency of second order space harmonic as the main mode included in excitation force meets to the natural frequency, a large vibration occurs. At 3000[r/min], 15^{th} order EM force component with respect to the base frequency 300[Hz] becomes a main source of vibration at the system having 4.4[kHz] natural frequency. To reveal the production of the high-frequency component of EM force, in the next chapter, we will examine the EM force under single pulse voltage control.

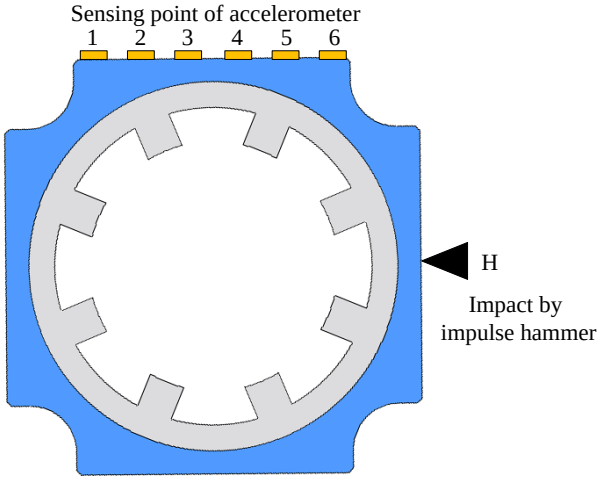

Figure 2.11 Set up of impulse hammer test.

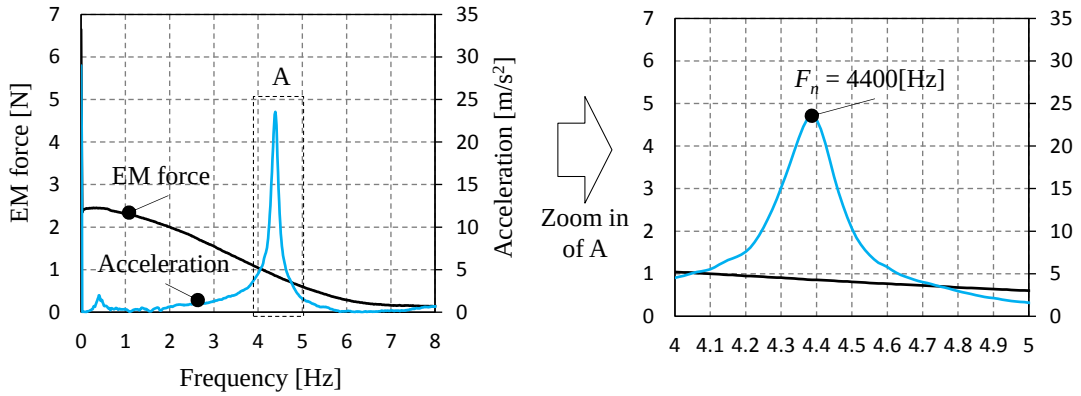

Figure 2.12 Vibration response at sensing point 3 when hammer impact on point H

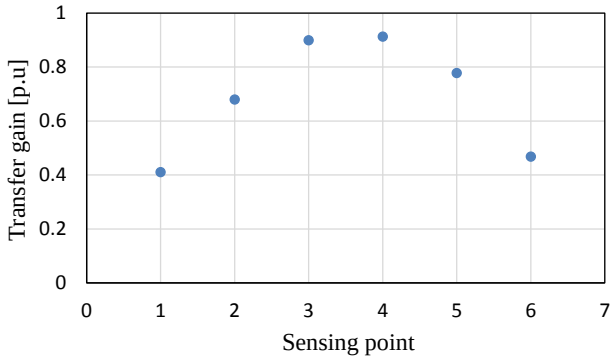

Figure 2.13 Transfer gain of natural frequency (4.4 kHz) component on 6 point

2.5 Vibration generation and its reduction method at commutation in SRM

2.5.1 Vibration arising from EM impact pulse[17]

To investigate a source of vibration, the EM force of A phase in the test motor is analyzed mathematically as an example. Generally, in a single pulse voltage control, the applied voltage at the commutation angle θ_0 is changed rapidly from $+V_{dc}$ to $-V_{dc}$ and the rotor position at the commutation stays at near around the aligned position as shown in Fig. 1.13.

At near around the aligned position, the EM force is generally high and rapidly decrease with the voltage change as shown in figure. 2.7. Since the vibration transfer function can be represented as the function between acceleration A and second order differential of F_r with respect to time as mentioned later, it can be supposed that the vibration is produced due to the second order differential of EM force with respect to time (Hereafter called as EM impact pulse) at the commutation, which has high order harmonics. Therefore, we focus on analysis of EM impact pulse that is a source of vibration.

From Maxwell's stress tensor method, radial force component f_r of local stress[18][19] acting on a part of the stator tooth surface is given in,

$$f_r = \frac{B_r^2 - B_\theta^2}{2\mu_0} \tag{2.33}$$

where B_r, B_θ and μ_0 are radial and tangential flux densities at the excited tooth surface, and vacuum permeability, respectively. As the commutation in the SRM is executed near the aligned position, it is reasonable to suppose that the relationship between the radial and tangential flux densities can be approximated as $B_r^2 \gg B_\theta^2$ and B_r is uniform on the excited tooth surface [19]. To calculate the total EM force, closed surface integration is also applied along closed surface line S, which corresponds to the outlines of the stator and rotor teeth shown in figure 2.14. Therefore, the total EM force F_r acting on the stator tooth surface is given by the below equation.

$$F_r = \oint_S f_r ds \approx \frac{B_r^2}{2\mu_0} S_{align} \tag{2.34}$$

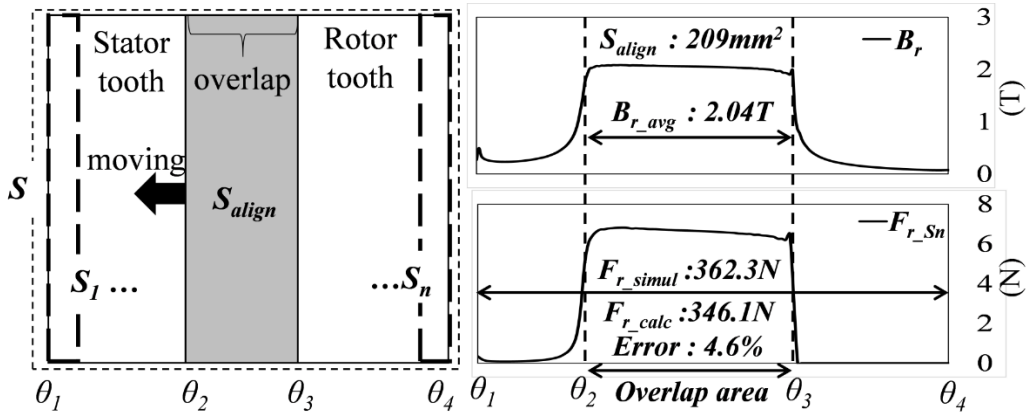

Figure 2.14 2D-FEM simulation and calculation result of radial force and magnetic flux linkage through the Maxwell stress tensor method under the rotor position 53deg. and current with 2.5[A]

S_{align} is the overlap area between the rotor and stator teeth. Although radial force F_{r_Sn} at local closed surface S_n is not strictly same with respect to the position in area S as can be seen in figure 2.14, B_r and F_{r_Sn} in the overlap area have uniform magnitudes with little differences[19]. Consequently, there is only a 4.6% difference between the total EM force F_{r_calc} calculated by equation (2.34) using the average magnetic flux density B_{r_avg} at S_{align} and the FEA-simulated total EM force F_{r_simul} as shown in figure 2.14. In addition, assuming that most of the magnetic flux flows through overlap area of the rotor and stator teeth and the flux density is distributed uniformly, the following approximation can be introduced.

$$B_r \approx \frac{\lambda_r}{nS_{align}} \tag{2.35}$$

Where, λ_r, n is the flux linkage of one phase coil and a number of turn per coil of one phase, respectively. As a result, substituting (2.35) into (2.34), the following equation can be obtained.

$$F_r(\lambda_r,\theta) \approx \frac{\lambda_r^2}{2\mu_0 n^2 S_{align}} \tag{2.36}$$

The radial force can be expressed by the equation above concerned with flux linkage and rotor position θ because the flux linkage and overlap area is the function of rotor position. Both the flux linkage and the rotor position are the functions of time. As a result, the EM impact pulse will be obtained as below fashion.

$$\begin{aligned}\frac{d^2F_r}{dt^2} &= \frac{d^2\lambda_r}{dt^2}\cdot\frac{\partial F_r}{\partial \lambda_r}+\left(\frac{d\lambda_r}{dt}\right)^2\cdot\frac{\partial^2 F_r}{\partial {\lambda_r}^2}\\ &+\frac{d^2\theta}{dt^2}\cdot\frac{\partial F_r}{\partial \theta}+\left(\frac{d\theta}{dt}\right)^2\cdot\frac{\partial^2 F_r}{\partial \theta^2}\\ &+\frac{d\lambda_r}{dt}\cdot\frac{d\theta}{dt}\left\{\frac{\partial}{\partial \lambda_r}\cdot\frac{\partial F_r}{\partial \theta}+\frac{\partial}{\partial \theta}\cdot\frac{\partial F_r}{\partial \lambda_r}\right\}\end{aligned} \tag{2.37}$$

Generally, at commutation instant, the phase inductance is high and easily can be saturated because the rotor position is located at near the aligned position. Therefore, the time constant of phase winding is high and the variance of current is very small compared to the variance of inductance with respect to position variance. For example, In the time variance Δt of 1[μsec] under the case of 6000[r/min] running state, position variance is 0.036[deg] and current variance is a few [mA]. So generally, the variance of magnetic flux linkage is mainly affected by the variance of rotor position. However, in this small step, generally, the variance of flux linkage $\Delta\lambda_r$ by low inductance variance is lower than the variance of rotor position $\Delta\theta$. By using the relations from 1) to 5) introducing below, the terms in equation (2.37) can be reduced like equation (2.43).

1) Generally $\Delta\lambda_r \ll \Delta\theta$ at small time step Δt. (e.g. $\Delta\theta$ is over 63 times of $\Delta\lambda_r$ during $\Delta t = 1\mu sec$ at commutation instant under rated power condition from 2D-FEA)

2) The differential terms of 2nd, 4th, 5th, 6th in equation (2.37) are expressed as following fashion.

$$\left(\frac{d\lambda_r}{dt}\right)^2 \approx {V_{dc}}^2, \quad \left(\frac{d\theta}{dt}\right)^2 \approx \omega^2, \quad \frac{d\lambda_r}{dt}\cdot\frac{d\theta}{dt} \approx V_{dc}\cdot\omega \quad \because v \approx V_{dc} \tag{2.38}$$

Generally, V_{dc} is less than 1000[V]. when the mechanical angular speed ω is 104~628[radian/sec] that a speed is between 1000 and 6000[r/min], V_{dc}^2 and $V_{dc}\cdot\omega$ of the above values are higher than, and within maximum ten times of $V_{dc}\cdot\omega$ and ω^2 respectively.

3) The partial differential terms appeared as 2nd and 6th terms in equation (2.37) have a relation like below, using the relation of 1).

$$\frac{\partial}{\partial\lambda_r}\cdot\frac{\partial F_r}{\partial\lambda_r} \gg \frac{\partial}{\partial\theta}\cdot\frac{\partial F_r}{\partial\lambda_r} \qquad \because \partial\lambda_r \ll \partial\theta \tag{2.39}$$

4) The partial differential terms appeared as 4th and 5th terms in equation (2.37) have a relation like below, using the relation of 1).

$$\frac{\partial}{\partial\theta}\cdot\frac{\partial F_r}{\partial\theta} \ll \frac{\partial}{\partial\lambda_r}\cdot\frac{\partial F_r}{\partial\theta} \qquad \because \partial\lambda_r \ll \partial\theta \tag{2.40}$$

5) The partial differential terms appeared as 2nd and 5th terms in equation (2.37) have a relation like below, using the relation of 1).

$$\frac{\partial}{\partial\lambda_r}\cdot\frac{\partial F_r}{\partial\lambda_r} \gg \frac{\partial}{\partial\lambda_r}\cdot\frac{\partial F_r}{\partial\theta} \qquad \because \frac{\partial F_r}{\partial\lambda_r} \gg \frac{\partial F_r}{\partial\theta} \tag{2.41}$$

By using the relations from 2) to 5), equation (2.37) will be approximated as follows.

$$\frac{d^2F_r}{dt^2} \approx \frac{d^2\lambda_r}{dt^2}\cdot\frac{\partial F_r}{\partial \lambda_r} + \left(\frac{d\lambda_r}{dt}\right)^2 \cdot \frac{\partial^2 F_r}{\partial \lambda_r^{\,2}} + \frac{d^2\theta}{dt^2}\cdot\frac{\partial F_r}{\partial \theta} \tag{2.42}$$

As constant speed operation of the motor makes $d^2\theta/dt^2=0$, the above equation will be approximated by,

$$\frac{d^2F_r}{dt^2} \approx \frac{d^2\lambda_r}{dt^2}\cdot\frac{\partial F_r}{\partial \lambda_r} + \left(\frac{d\lambda_r}{dt}\right)^2 \cdot \frac{\partial^2 F_r}{\partial \lambda_r^{\,2}} \,. \tag{2.43}$$

Next, assuming that the resistive voltage drop is negligible under middle or high speed operation, the voltage equation of SRM will be approximated as follows

$$v = Ri + \frac{d\lambda}{dt} \approx \frac{d\lambda}{dt} \tag{2.44}$$

The applied voltage when it is changed from $+V_{dc}$ to $-V_{dc}$ at the commutation instant can be expressed as following manner.

$$v = -V_{dc} + 2V_{dc}\cdot e^{-\frac{t}{\tau}} \tag{2.45}$$

Where τ is time constant at the turn off of the switch, normally τ is one-fifth of the switch turn off time. By using the above equation, the differential of input voltage v with respect to time t will be given in ,

$$\frac{dv}{dt} \approx \frac{d^2\lambda}{dt^2} \approx -\frac{2V_{dc}}{\tau}\cdot e^{-\frac{t}{\tau}}. \tag{2.46}$$

By using equation (2.46) and equation (2.36), 1st and 2nd terms iu equation (2.43) can be

written as following expressions.

$$\frac{d^2\lambda_r}{dt^2}\cdot\frac{\partial F_r}{\partial \lambda_r}\approx -\frac{2\lambda_r}{\tau}\cdot\frac{V_{dc}}{\mu_0 n^2 S_{align}}e^{-\frac{t}{\tau}}$$
$$\left(\frac{d\lambda_r}{dt}\right)^2\cdot\frac{\partial^2 F_r}{\partial {\lambda_r}^2}\approx V_{dc}\cdot\frac{V_{dc}}{\mu_0 n^2 S_{align}} \tag{2.47}$$

In the experimental system for the test motor, switch turn off time is lower than 1[μsec], so τ is lower than one-fifth of 1[μsec]. And the flux linkage of test motor at rated operating condition is about 0.2[Wb]. Generally, V_{dc} is lower than 1000[V]. Therefore, equation (2.47) can be rewritten as following fashion at the commutation instant ($t \fallingdotseq 0$).

$$\frac{d^2\lambda_r}{dt^2}\cdot\frac{\partial F_r}{\partial \lambda_r}\approx -\frac{2\lambda_r}{\tau}\cdot\frac{V_{dc}}{\mu_0 n^2 S_{align}}e^{-\frac{t}{\tau}}\approx 2\cdot 10^6\cdot\frac{V_{dc}}{\mu_0 n^2 S_{align}}$$
$$\left(\frac{d\lambda_r}{dt}\right)^2\cdot\frac{\partial^2 F_r}{\partial {\lambda_r}^2}\approx V_{dc}\cdot\frac{V_{dc}}{\mu_0 n^2 S_{align}}\approx 10^3\cdot\frac{V_{dc}}{\mu_0 n^2 S_{align}} \tag{2.48}$$

As a result, equation (2.37) can be reduced as folloing expression.

$$\frac{d^2F_r}{dt^2}\approx\frac{d^2\lambda_r}{dt^2}\cdot\frac{\partial F_r}{\partial\lambda_r}\approx\frac{dv}{dt}\cdot\frac{\partial F_r}{\partial\lambda_r} \tag{2.49}$$

The equation (2.49) can be expressed by using unit impulse function $\delta(t)$ and voltage variation ΔV at commutation.

$$\frac{d^2F_r}{dt^2}=F_{impulse}\cdot\delta(t)$$
$$F_{impulse}=\Delta V\frac{\partial F_r}{\partial\lambda_r} \tag{2.50}$$

The magnitude of EM impact pulse is proportional to voltage variation ΔV and partial differential of EM force with respect to flux linkage. As a result, substituting (2.50) into (2.10), vibration as acceleration can be obtained like below.

$$a(t) = F_{impulse} \frac{m^{-1}}{\omega_d} \cdot e^{-\omega_n \xi t} \sin(\omega_d t) \tag{2.51}$$

From the equation above, it is observed that the vibration is produced by EM impact pulse with the shape of impulse function. The magnitude is proportional to the voltage variance if the variance of $\delta F_r/\delta \lambda_r$ is small. Vibration becomes the damped oscillation with the damped natural frequency as shown in figure 2.15. The natural frequency component of EM impact pulse is transferred to vibration at the commutation.

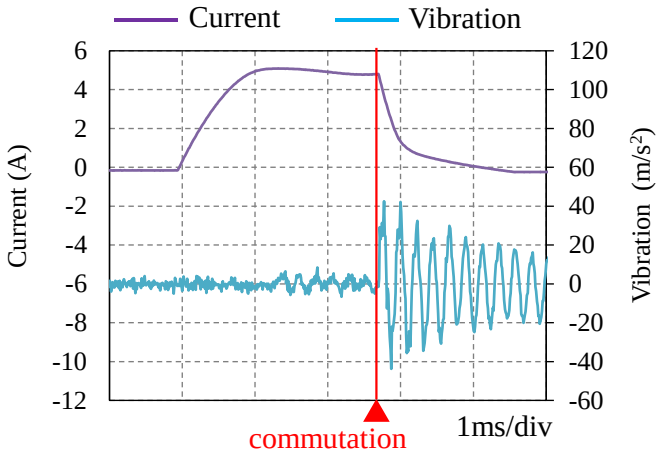

Figure 2.15 Vibration production at commutation under single pulse voltage control.

2.5.2 Vibration reduction methods

As described in the preceding subsection, the stator vibration occurs at the commutation due to the EM impact pulse which is produced by the rapid change of voltage. In the general single pulse voltage control, at the commutation angle θ_c, the vibration with the damped natural frequency is generated as shown in figure 2.16.

To reduce the vibration caused by the EM force variation, many kinds of methods have been proposed. These reduction methods can be classified into structural design approach of motor[19)-(22)] and control approach without changing the motor structure[23)-(32)]. The First category includes the design of a number of rotor poles[20)], the application of a cylindrical cage in rotor[21)] and double stator with a segmented rotor to decrease the radial force that is a source of vibration and noise[19)(22)]. However, the design modification is basically out of our studies because other drive performances such as the maximum torque and realizing the required torque-speed range must be kept as it is. Therefore, our studies mainly focus on reducing the vibration based on the control method. Of them, the voltage smoothing method has been studied to minimize the variance of radial force at the commutation[28)]. Also, the method using dithers into turn-on and -off angles has been proposed[23)(29)]. Through the switching at random turn-on and -off angles, the degree of excitation in resonance frequency is reduced and as a result, the spectrum of vibration spreads broadly. This method is more proper for the system with multiple natural frequencies. On the contrary, active vibration cancellation (AVC) technique to eliminate the vibration occurring at the commutation by generating another vibration with out of phase has been proposed[30)(31)]. In this method,

another vibration with a delay of half cycle of dominant resonant frequency is produced under a fixed commutation angle, not random like dithering methods[23][29]. Dithering methods were more difficult to attenuate enough the vibration occurring at the commutation than AVC method. In a case of the test motor in this study which has just one dominant natural frequency, the AVC methods seem to be working better.

2.5.3 Vibration reduction by two stage commutation method

In this study, the AVC method through two stage commutation method has been focused on to minimize the vibration[30]. For wide speed range control, however, single pulse voltage drive has been not appropriate because PWM control has been usually necessary for variable speed drive. For the AVC under PWM control, a modified two stage commutation method employing negative voltage PWM has been proposed [32]. In this method, the negative PWM voltage has been applied to a test motor after zero voltage period with a half period (T_n/2) of natural frequency, in which PWM duty has been set to be equal with that for positive PWM voltage before the zero voltage period as can be seen in figure 2.17.

At each commutation, the vibration of equation (2.51) is produced by each EM impact pulse. Through equation (2.50), the EM impact pulse at each commutation can be expressed as following fashion.

$$\begin{aligned} &\text{At } 1^{st} \text{ commutation}: \frac{d^2F_r}{dt^2} = F_{impulse\_1}\cdot\delta(t), \qquad F_{impulse\_1} = (V_{ref} - 0)\frac{\partial F_r}{\partial \lambda_r} \\ &\text{At } 2^{nd} \text{commutation}: \frac{d^2F_r}{dt^2} = F_{impulse\_2}\cdot\delta(t - T_n/2), \quad F_{impulse\_2} = (0-(-V_{ref}))\frac{\partial F_r}{\partial \lambda_r} \end{aligned} \tag{2.52}$$

Assuming that the value of $\delta F_r/\delta\lambda_r$ at the first commutation is identical with that at the second

commutation, the EM impact pulse produced at each commutation is equal and then, the acceleration of vibration by using expression (2.51) can be derives as,

$$\begin{aligned} &\text{After } 1^{st}\text{commutation} \ : a_1(t) = F_{impulse\_1}\frac{m^{-1}}{\omega_d}\cdot e^{-\omega_n\xi t}\sin(\omega_d t) \\ &\text{After } 2^{nd}\text{commutation} : a_2(t) = F_{impulse\_2}\frac{m^{-1}}{\omega_d}\cdot e^{-\omega_n\xi (t-T_n/2)}\sin(\omega_d (t-T_n/2)) \end{aligned} \quad . \tag{2.53}$$

Assuming that the decay of exponential term of the first vibration during the time delay $T_n/2$ is small, the vibration after the 2nd commutation will be canceled each other as can be seen in figure 2.17. This is the principle of two stage commutation method.

For the effective operation of this method, the necessary conditions must be satisfied and are:

1) There must be no vibration except when the first commutation is executed,
2) The phase shift between the 1st vibration a_1 and the 2nd vibration a_2 must be 180 degree, and
3) The amplitudes of a_1 and a_2 must be the same.

For 2), the zero-voltage period inserted between the 1st and 2nd commutations must be equal to half the period $T_n/2$ of the natural frequency of the stator body. For 3), the phase voltage magnitudes applied before and after the zero-voltage period must be equal. Assuming that the amplitudes of the EM impact pulse at the 1st and the 2nd commutations are identical, two vibrations with the same amplitude can be generated.

As for a better execution of the two stage commutation method, special switching technique that has been proposed in prior research is employed[32]. By changing switching patterns, the two voltage pulses that have a separate duty in one PWM period are produced.

In other words, the switching count in one PWM period is same, however, the number of ON pulse inputted into the winding of the motor is doubled and therefore, the actual PWM voltage frequency applied to the motor can be doubled although the switching frequency is kept as it is. For example, in the case of 10kHz switching frequency, the voltage PWM frequency becomes 20kHz by using this switching pattern. This special switching technique

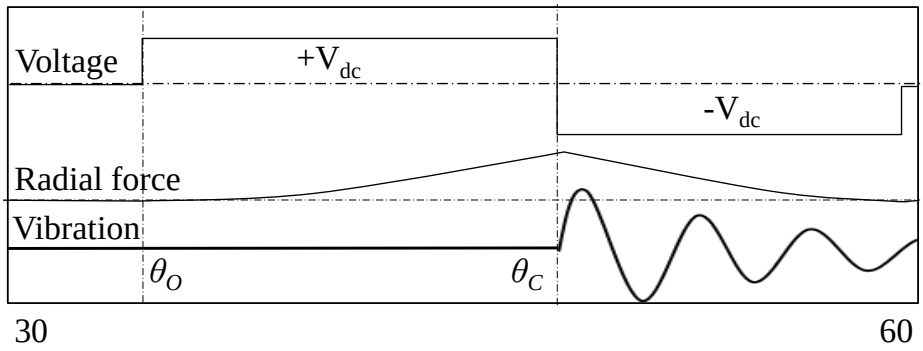

Figure 2.16 Vibration arising at commutation under single voltage pulse control.

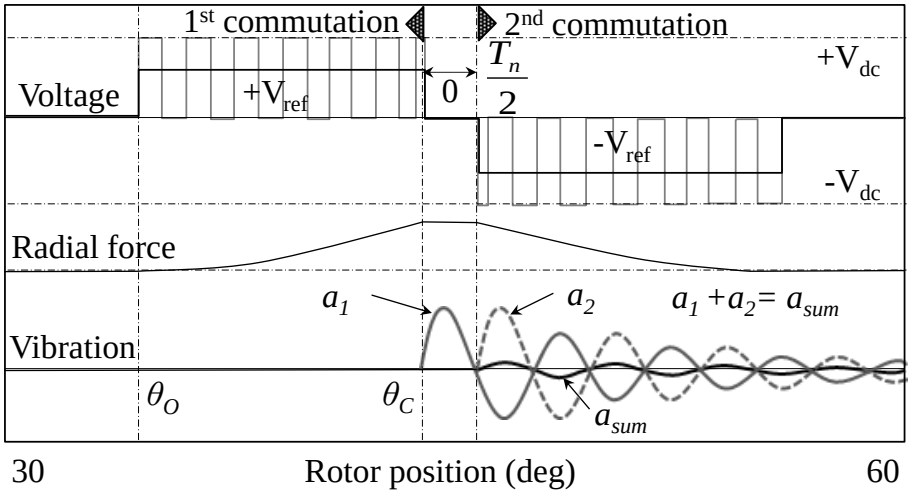

Figure 2.17 Vibration suppression by AVC under a modified two stage commutation method.

offers not only an accurate controllability of the zero-voltage period which is the most important in this method, but also reduced noise and vibration due to PWM switching.

2.6 Epilogue

In this chapter, the principle of vibration generation was firstly introduced based on the SDOF and MDOF systems. The second order mode of spatial harmonic distribution of EM force and the harmonic components of instantaneous EM force generating the vibration of the motor were described. It was revealed that if the spatial harmonic component and frequency of EM force matched to vibration mode with the natural frequency of the test motor, the large vibration occured. In practice, the vibration in SRM was produced by the harmonic component of EM impact pulse produced at the commutation. The two stage communication method to eliminate this vibration was explained. The necessary conditions for executing this control algorithm effectively were explained.

Chapter3
A new modified two stage commutation method to achieve better AVC in SR servo motor

3.1 Prologue

The modified two stage commutation method employing negative PWM voltage control (hereafter, named as conventional method), which was already proposed as AVC of SRM, was described in chapter 2. Although this conventional method can be applied to general SRMs, the problems that why the conventional method does not work well are firstly revealed in this chapter. There are two problems. The first problem is that the large vibration is remained even after two-stage commutation because an unexpected vibration before the commutation exists. The second problem is that the vibration cancelation is not effective when an SRM is operated under the high speed and high load condition even if the first problem is solved. This study investigated why above problems occur through an electromagnetic structural coupled analysis using a finite element method and mathematical analysis of the EM impact pulse. Eventually, the reason of the first problem has been the vibration produced by EM impact pulse at the teeth overlapping point. The reason of the second problem has been the unbalance of the EM impact pulses produced at each commutation due to magnetic saturation. In order to solve the first problem, fillet shape pole

rotor will be designed and employed. To solve the second problem, a modified two-stage commutation method will be proposed. Through experiments and simulations, the vibration reduction performance of the modified two-stage commutation method using the test motor with the designed fillet shape pole rotor will be revealed.

3.2 Problem of the conventional method for SRM with rectangular rotor pole and its solution employing a rotor with newly designed pole shape

In this section, the problems of unsatisfying of the first necessary condition for effective control of the conventional method described in chapter 2, are dealt with. The first necessary condition is that "There must be no vibration except when the first commutation is executed". In real, however, except the vibration at the first commutation, another vibration exists. The reason for this is investigated and the solution will be also proposed[34].

3.2.1 Vibration production at starting point of teeth overlap

In general SRMs, rotor pole shape is rectangular as shown in figure 1.17. When the single voltage pulse is applied to the test motor at the rated speed of 3000[r/min], the vibration at the area "A" before at the commutation θ_c is already produced as can be seen in figure 3.1. Despite that the DC-bus voltage V_{dc} and the turn-on angle θ_o are changed, the amplitude of the vibration before at the commutation rarely changes. In addition, no change of the position at which the vibration occurs is also observed. The reason of this vibration is due to sudden

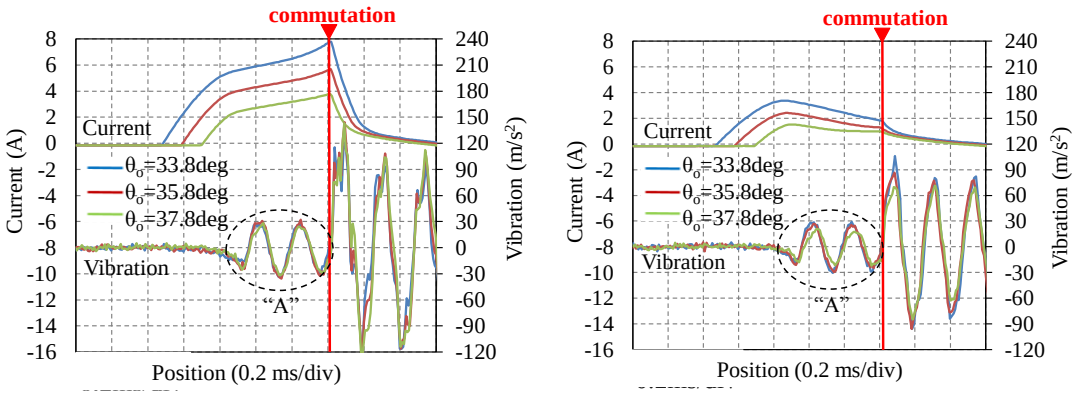

(a) V_{dc}=180[V] (b) V_{dc}= 282[V]

Figure 3.1 Vibration and current waveforms with respect to the changes of turn-on angle θ_0 and applied voltage at 3000[r/min] under a fixed commutation angle θ_C = 51[deg.].

change of magnetic flux at the position where the energized stator tooth just starts to overlap with the rotor tooth as shown in figure 3.2(a). This results in the EM impact pulse generation at "b" becomes the source of the unexpected vibration as can be seen in figure 3.2(b). The EM impact pulses found at "B" and "C" are produced by the two stage commutation. Generally, at "b", in spite of current differences with respect to the DC-bus voltage V_{dc} differences, magnetic saturation at the tooth corner is quite high due to just corner of stator and rotor teeth overlapping. Therefore, the amplitude of EM impact pulse is dependent from neither the DC-bus voltage V_{dc} or the turn-on angle θ_o, but only proportional to motor speed[(34)]. As the rotation speed increases, the unexpected vibration before at the commutation increases. As a result, even if the conventional method is employed, vibration after at the commutation is not minimized well due to the vibration produced before at the commutation as can be seen in figure 3.2(b).

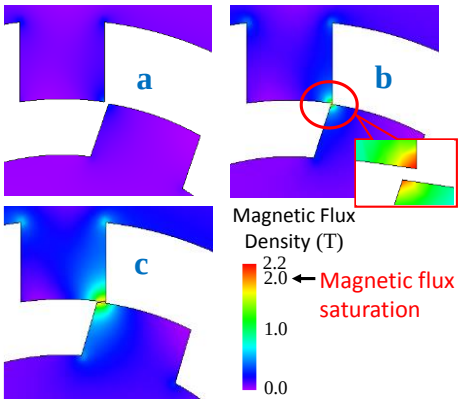

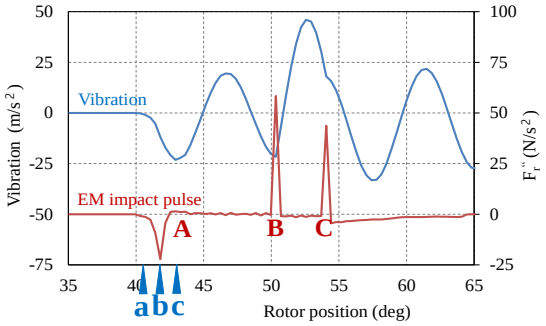

(a) contour plot of magnetic flux density (b) vibration and EM impact pulse

Figure 3.2 Simulation result of unexpected vibration under the conventional method at the rated power and the maximum speed 5000 r/min.

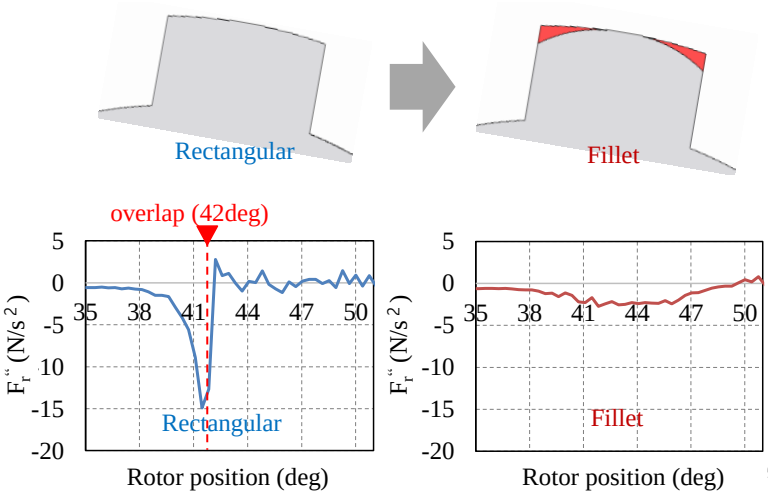

Figure 3.3 Simulation result of EM impact pulse with respect to the rotor pole shape at the rated power and the maximum speed 5000 r/min.

3.2.2 Design of a rotor with fillet shape pole to reduce vibration at starting point of teeth overlap

To minimize the unexpected vibration, a rotor with fillet shape pole shown in figure 3.3 is considered. This rotor pole shape enables to eliminate the EM impact pulse at the teeth overlap point as shown in figure 3.3. However, the maximum torque under the maximum current limitation will be decreased because the saliency will be reduced by the fillet shape. For minimization of the unexpected vibration produced at the teeth overlap point while keeping the maximum torque under the maximum current limitation, the design optimization about five parameters (R, x, L, r_1, r_2) depicted in figure 3.4 is conducted. Finally, the test motor with the designed rotor with fillet shape is fabricated as can be seen in figure 3.5(a). Figure 3.5(b) demonstrates the maximum torque-speed characteristic measured by using the test motor under PWM voltage control with the optimized voltage control parameters. Figure 3.6 illustrates the results simulated under the conventional two stage commutation at 5000

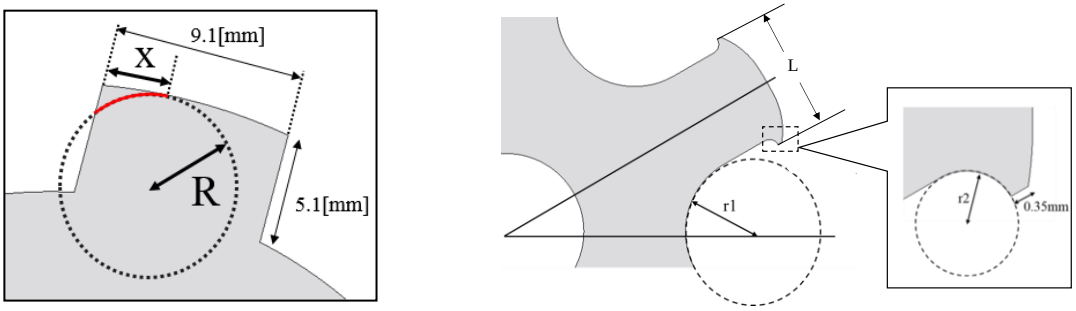

Figure 3.4 Dimensional parameters of rotor with fillet shape pole for optimization.

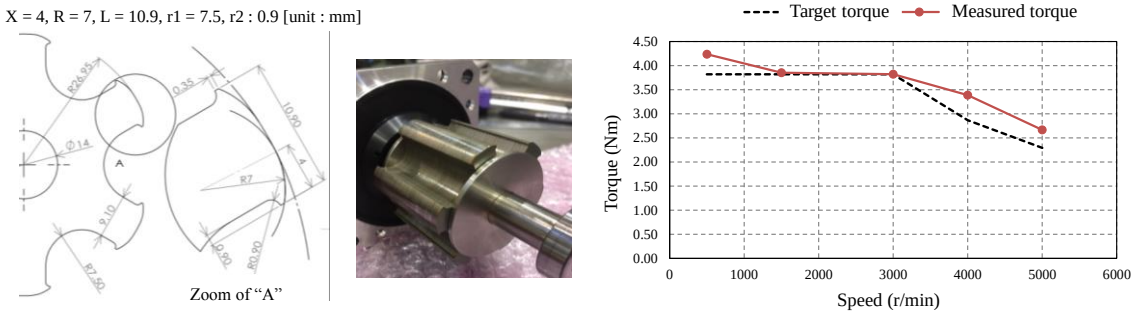

(a) optimized rotor dimensions (b) measured torque-speed curve

Figure 3.5 Optimized rotor shape and measured torque-speed characteristic.

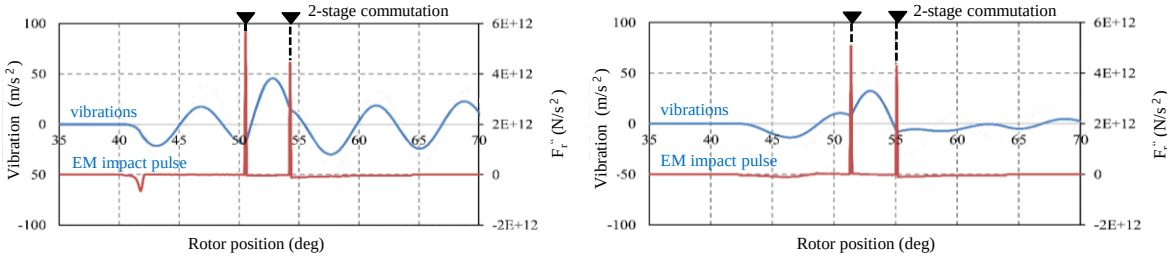

(a) with rectangular shape pole (b) with fillet shape pole

Figure 3.6 Simulation of vibration and EM impact pulse with respect to two rotors at 20% of the rated torque and the maximum speed 5000 [r/min].

[r/min] and 20% of the rated torque. It is found from the figure that the test motor employing the designed rotor with fillet shape pole is more effective in vibration minimization than the test motor coupled with the rectangular shape rotor. From now on, the test motor employing the designed rotor is used for a new modified two stage commutation method studied in this chapter.

3.3 Investigations into a drawback of the conventional method and its reason through mathematical analysis and 2D-FEA simulation

The conventional two stage commutation method has still has a problem to be solved after employing the rotor with fillet shape pole. In this chapter, the problem and its reason are investigated and revealed through mathematical analysis and 2D-FEA simulation.

3.3.1 Problem of the conventional method

In the conventional two stage commutation method, if the voltage variance ΔV at each commutation is same, each vibration a_1 and a_2 which is produced by same EM impact pulse ($F_{impulse\_1} = F_{impulse\_2}$) in equation (2.53) can be canceled each other theoretically after the second commutation. However, in a real system, it has different results depending on the operating condition. For an example, figure 3.7 shows simulation results of vibration in the test motor under 20% and 60% load of the rated torque, respectively, at 3000[r/min] running speed. In this simulation, we set the zero voltage period $T_n/2 = 1/(2f_n) = 1/(2\times4043)\fallingdotseq125$[μsec]. As can be seen in this figure, the vibration cancelation does not work well under relatively heavy load condition (60%) compared with that under light load condition (20%). From figure 3.7(b), it is reasonable to suppose that the amplitude of the vibration occurring at the 2nd commutation is larger than that occurring at the 1st commutation. The reason for this phenomenon is investigated in next subsection.

3.3.2 Reason for the problem

For mathematical analysis, the amplitude of EM impact pulse is considered. The amplitude of EM impact pulse at each commutation can be represented by substituting equation (2.36) into (2.52) and given in,

$$\begin{aligned} &\text{At } 1^{st} \text{ commutation}: F_{impulse\_1} = \Delta V_1 \frac{\partial F_{r1}}{\partial \lambda_{r1}}, \qquad F_{impulse\_1} = \Delta V_1 \frac{\lambda_{r1}}{\mu_0 n^2 S_{align1}} \\ &\text{At } 2^{nd} \text{commutation}: F_{impulse\_2} = \Delta V_2 \frac{\partial F_{r2}}{\partial \lambda_{r2}}, \qquad F_{impulse\_2} = \Delta V_2 \frac{\lambda_{r2}}{\mu_0 n^2 S_{align2}} \end{aligned} \tag{3.1}$$

where ΔV_1 and ΔV_2 are the voltage variance at the 1st and the 2nd commutations, respectively.In both operating conditions, the voltage variance at each commutation is set to be identical, that is, $\Delta V_1 = \Delta V_2$. In the conventional method, it was assumed that the $\delta F_r/\delta \lambda_r$ is similar at the first and the second commutation. However, in 60% load condition, it is reasonable to suppose that the amplitude of the EM impact pulse $F_{impluse\_2}$ occurring at the 2nd commutation is larger than the EM impact pulse $F_{impluse\_1}$ occurring at the 1st commutation because a_2 is larger than a_1. As a result, in 60% load condition, the next relationship about $\delta F_r/\delta \lambda_r$ is obtained as following fashion.

$$\frac{\partial F_{r1}}{\partial \lambda_{r1}} < \frac{\partial F_{r2}}{\partial \lambda_{r2}} \quad \Rightarrow \quad \frac{\lambda_{r1}}{\mu_0 n^2 S_{align1}} < \frac{\lambda_{r2}}{\mu_0 n^2 S_{align2}} \tag{3.2}$$

In a real system, teeth overlap area S_{align} has the following relations: S_{align1} at the 1st commutation < S_{align2} at the second commutation. From the relations of the teeth overlap area and equation (3.2), we can derive the following relationship.

$$\because\ S_{align1} < S_{align2} \quad \Rightarrow \quad 1 < \frac{S_{align2}}{S_{align1}} < \frac{\lambda_{r2}}{\lambda_{r1}},\ \lambda_{r1} < \lambda_{r2} \tag{3.3}$$

This means that the increase in magnetic flux linkage is higher than the increase in the overlap area at 2nd commutation. From another simulation result shown in figure 3.8, it is assured

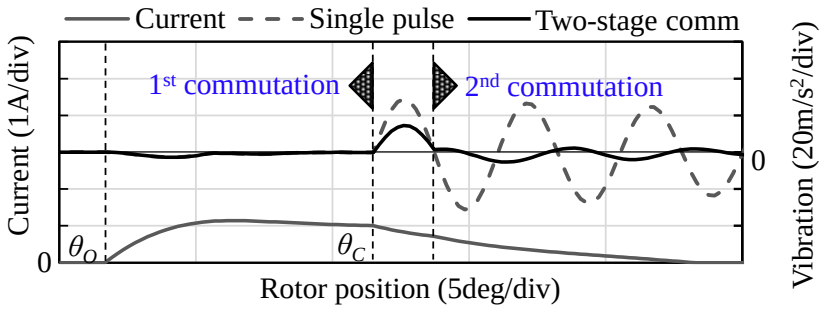

(a) speed: 3000 [r/min], torque: 20% of the rated torque

(θ_O: 41.6[deg], θ_C: 51.5[deg], voltage: +197→0→-197 [V])

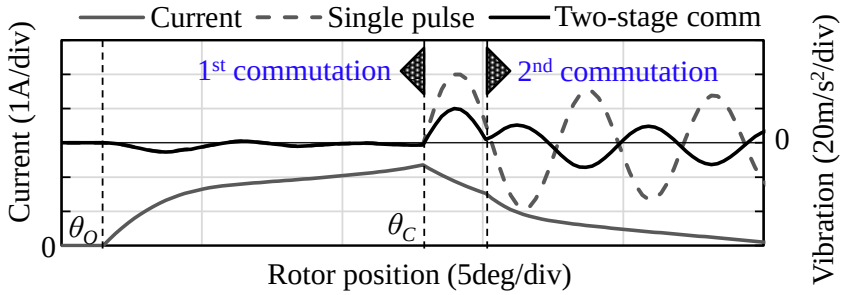

(b) speed: 3000 [r/min], torque: 60% of rated torque

(θ_O: 41.3[deg], θ_C: 53.0[deg], voltage: +283→0→-283 [V])

Figure 3.7 Simulation results of vibration under the conventional method.

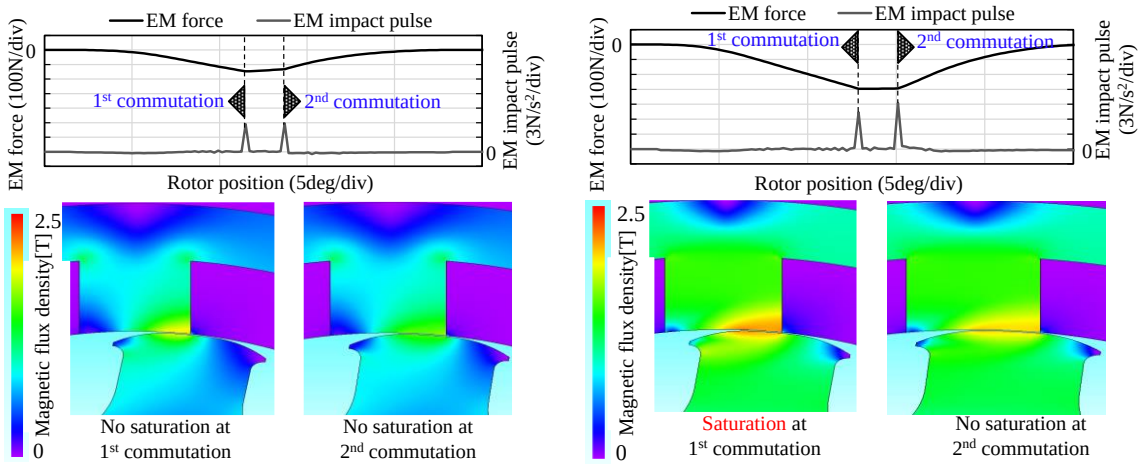

(a) speed: 3000 [r/min], torque: 20% of the rated torque

(b) speed: 3000 [r/min], torque: 60% of the rated torque

Figure 3.8 EM force, EM impact pulse and contour plot of magnetic flux density operating under the conventional method.

that at 20% load condition, the EM impact pulse at each commutation is almost same. However, at 60% load condition, the EM impact pulse at the 2nd commutation is higher than that at 1st commutation. Also from the magnetic flux density contour diagram, the magnetic saturation which can be found at the 1st commutation is disappeared at the 2nd commutation. Thus, it is reasonable to say that the flux linkage at the 2nd commutation is increased as the saturation is disappeared.

In conclusion, the reason why the problem arises is that the EM impact pulse at each commutation is not same because of the variance of magnetic saturation especially at heavy load condition despite that the voltage variance at each commutation is controlled with the same quantity.

3.4 A new modified two stage commutation method

In order to solve the unbalance of EM impact pulse at each commutation which was explained in the former section, a new method to control positive and negative reference voltage before after the commutation separately is proposed. For the satisfaction of both the vibration minimization and the target performance (target torque, low copper loss), the necessity of optimization of voltage parameters is explained.

3.4.1 Basic operation of the new modified method

In the conventional method, the positive and negative reference voltage must be controlled with the same amplitude for achieving the same voltage variation at each commutation. That is the method to obtain the same EM impact pulse under the assumption which $\delta F_r/\delta\lambda_r$ at each commutation is same. However, at heavy load condition, the method to control the EM impact pulse by compensating the variance of $\delta F_r/\delta\lambda_r$ is necessary because $\delta F_r/\delta\lambda_r$ at each commutation is varied with the effect of magnetic saturation. It is possible to compensate by independently controlling the negative reference voltage and the positive reference voltage in accordance with following expression.

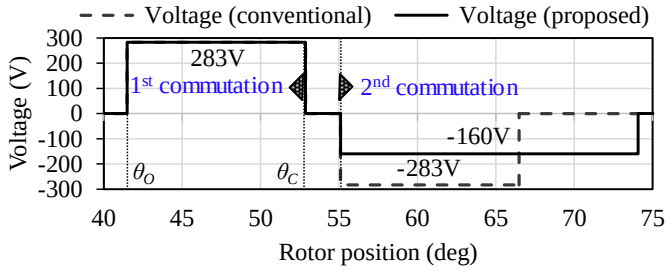

(a) applied voltage waveforms (θ_O: 41.5[deg], θ_C: 53[deg], proposed : +283 →0 →-160 [V] , conventional: +283 →0 → -283 [V]).

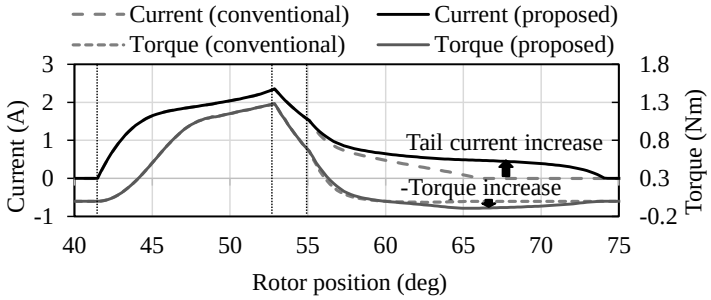

(b) phase current and torque

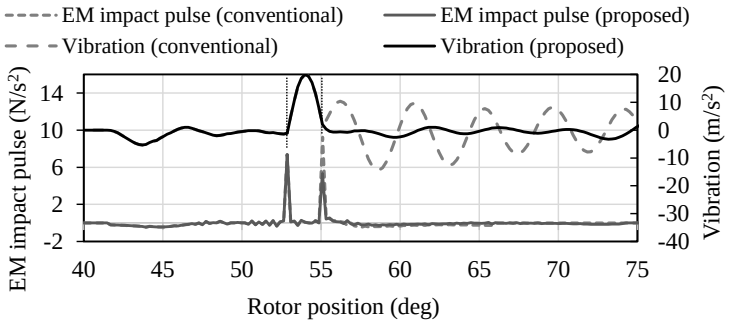

(c) EM impact pulse and vibration

Figure 3.9 Vibration reduction results when employing a new modified two stage commutation at 60% of the rated torque and speed of 3000 [r/min].

$$\begin{cases} \text{At } 1^{st} \text{ commutation} : F_{impulse\_1} = \Delta V_1 \dfrac{\partial F_{r1}}{\partial \lambda_{r1}} \\ \text{At } 2^{nd} \text{commutation} : F_{impulse\_2} = \Delta V_2 \dfrac{\partial F_{r2}}{\partial \lambda_{r2}} \end{cases} \tag{3.4}$$

$$\Rightarrow \begin{cases} if \quad \dfrac{\partial F_{r1}}{\partial \lambda_{r1}} < \dfrac{\partial F_{r2}}{\partial \lambda_{r2}}, \quad \text{then control to become } \Delta V_1 > \Delta V_2 \\ else \dfrac{\partial F_{r1}}{\partial \lambda_{r1}} > \dfrac{\partial F_{r2}}{\partial \lambda_{r2}}, \quad \text{then control to become } \Delta V_1 < \Delta V_2 \end{cases}$$

As can be seen in equation (3.4), through separate control of positive and negative reference voltage, $F_{impulse\_1}$ and $F_{impulse\_2}$ can be controlled separately although $\delta F_r/\delta \lambda_r$ varies. For an example, to protect the increase in the EM impact pulse at the 2nd commutation which occurs at 60% load condition, the negative reference voltage is changed from 283V to 160V as shown in figure 3.9. The EM impact pulse at the 2nd commutation is decreased and the effectiveness of vibration minimization becomes better. This is called a new modified two stage commutation method as proposal in this study.

3.4.2 Necessity of voltage parameter optimization

The new modified two stage commutation method makes it possible to achieve better vibration reduction performance. However, as can be seen in figure 3.9(b), the decrease of the negative reference voltage yields a long tail current that causes an average torque reduction and an increase in copper loss. Although an advanced turn-on angle control can be applied to maintain the average torque, it will impose a further increase in copper loss by an increase in initial current at the turn-on angle. Therefore, to reduce the vibration while minimizing copper loss and producing demanded average torque, the optimization of a set of

control parameters is an indispensable task. The set of control parameters to be optimized in this method are turn-on angle θ_o, commutation angle θ_c, positive reference voltage amplitude $+V_{ref}$ before the 1st commutation, and negative reference voltage amplitude $-V_{ref}$ after the 2nd commutation.

3.5 Optimization of voltage parameters based on GA(Genetic Algorithm)

A dynamic simulator combined with the GA proposed in reference[35] was also used to optimize the set of control parameters in this study. About both of simulation model and test motor, the optimization is conducted for vibration minimization while keeping the target performances such as commanded average torque and less copper loss.

3.5.1 Introduction of GA

Before the introduction of GA, the evaluation method for assurance of vibration minimization is needed at first. Until now, the EM impact pulse at each commutation that is derived from 2nd order differential of EM force with respect to time must have the same amplitude for perfect vibration cancellation theoretically. However, as the EM impact pulse obtained from the real test motor has high-frequency noise by 2nd order differential of EM force, it's very difficult to evaluate the EM impact pulse directly as vibration minimization factor. In this study, to overcome this disturbance the harmonic component of the EM force near natural frequency is considered as the evaluation factor. Ideally, the EM impact pulse is the impulse function including infinite frequency components. The impulse function at time

domain is represented as the following form.

$$\delta(t)=\int_{-\infty}^{+\infty}\cos(2\pi ft)df \Rightarrow \delta(t)=\begin{cases}+\infty & t=0\\ 0 & t\neq 0\end{cases} \tag{3.5}$$

Through the Fourier transform of the impulse function, it is informed that each frequency component has unity gain through equation (3.6).

$$\Im\{\delta(t)\}=F(j\omega)=\int_{-\infty}^{+\infty}\delta(t)e^{-j\omega t}dt=1 \tag{3.6}$$

The characteristic of the impulse function at time and frequency domain are shown in figure 3.10. Considering that the impulse function with the time delay of half period of natural frequency (T_n/2), it can be described as following fashion.

$$\delta(t-(T_n/2))=\int_{-\infty}^{+\infty}\cos(2\pi f(t-(T_n/2)))df \Rightarrow \delta(t-(T_n/2))=\begin{cases}+\infty & t=T_n/2\\ 0 & t\neq T_n/2\end{cases} \tag{3.7}$$

The Fourier transform of the impulse function above is like below.

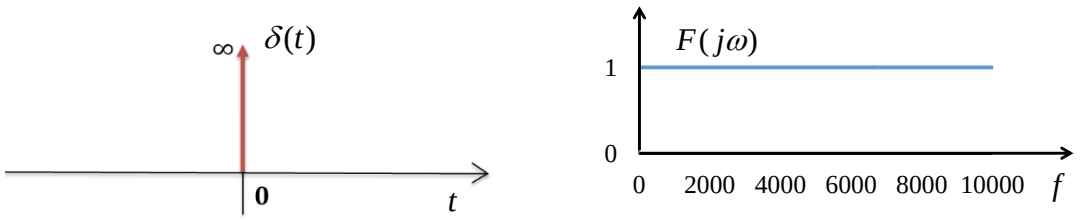

(a) time domain (b) frequency domain

Figure 3.10 Impulse function.

$$\because \int_{-\infty}^{+\infty} \delta(t-(T_n/2))\,f(t)dt = f(T_n/2)$$
$$\Im\{\delta(t-(T_n/2))\} = F(j\omega) = \int_{-\infty}^{+\infty} \delta(t-(T_n/2))e^{-j\omega t}dt = e^{-j\omega(T_n/2)} \tag{3.8}$$

Considering that the impulse function with time delays such as equation (3.7) and the general impulse function such as equation (3.5) exist in the time domain at the same time, the Fourier transform of the summation of each impulse function is given in ,

$$\Im\{\delta(t)+\delta(t-(T_n/2))\} = F(j\omega) = 1+e^{-j\omega(T_n/2)}$$
$$|F(j\omega)| = |F(j2\pi f)| = \sqrt{2+2\cos(2\pi f(T_n/2))} \tag{3.9}$$

Then, in the frequency domain, the value at the natural frequency is decreased to zero as shown in figure 3.11(b). This means that through the two-stage commutation control having EM impact pulses of the same magnitude at each commutation, the harmonic component close to the natural frequency can be reduced. As a result, if the perfect cancellation of harmonic component near the natural frequency of the EM impact pulse is achieved, the harmonic component at the natural frequency of vibration can be eliminated. In order words, the harmonic component near the natural frequency of EM force must be minimized for the

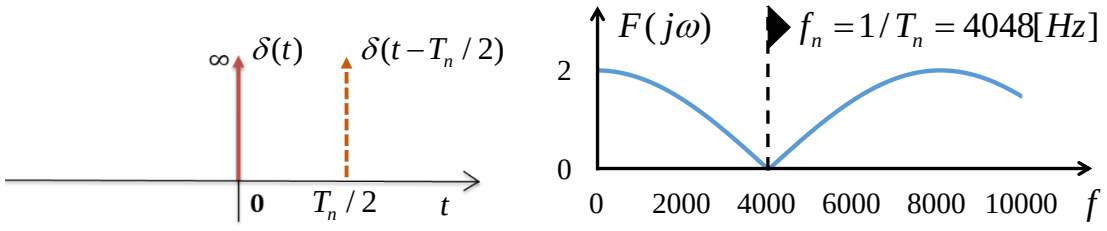

(a) time domain (b) frequency domain

Figure 3.11 Superimposing impulse function and time delayed impulse function (when using natural frequency 4048[Hz] of 2D-FEA model).

minimization of the vibration. This is only because there is a relationship that the harmonic component of EM impact pulse is $(n\omega_b)^2$ times of the harmonic component of EM force from following equation.

$$\begin{aligned} &DFT\ of\ EM\_force && : F = f_0 + \sum_{n=1}^{\infty}\{f_n \cos(n\omega_b t + \theta_n)\} \\ &DFT\ of\ EM\_impact\_pulse && : F'' = d^2F/dt^2 = -\sum_{n=1}^{\infty}\left\{(n\omega_b)^2 f_n \cos(n\omega_b t + \theta_n)\right\} \end{aligned} \tag{3.10}$$

The minimization of n^{th} order harmonic component $(n\omega_b)^2 f_n$ near the natural frequency of EM impact pulse has the same meaning with the minimization of n^{th} order harmonic component f_n near the natural frequency of the EM force. For this reason, for evaluation of vibration minimization explained later, the minimization of the harmonic component near the natural frequency of the EM force is evaluated as the alterative to that of the EM impact pulse.

Next is the explanation of genetic algorism (GA). As can be seen in figure 3.12, one generation consists of fifty individuals. An individual is a set of the four control parameters mentioned earlier. To evaluate the fitness of all fifty individuals for every generation loop of the GA, a dynamic simulator based on a model of nonlinear magnetizing curves is employed to compute instantaneous current, flux linkage and torque profiles for a given set of control parameters as shown in figure 3.13. The dynamic simulator firstly computes the instantaneous current profiles based on the voltage equation of motor for inputted voltage profile and rotor position. Subsequently, corresponding flux linkages, torque profiles and EM force are also computed using the calculated instantaneous current profiles. By using these current, torque, flux linkage and EM force, copper loss, average torque and harmonic component of EM force through DFT analysis are computed and evaluated as performance

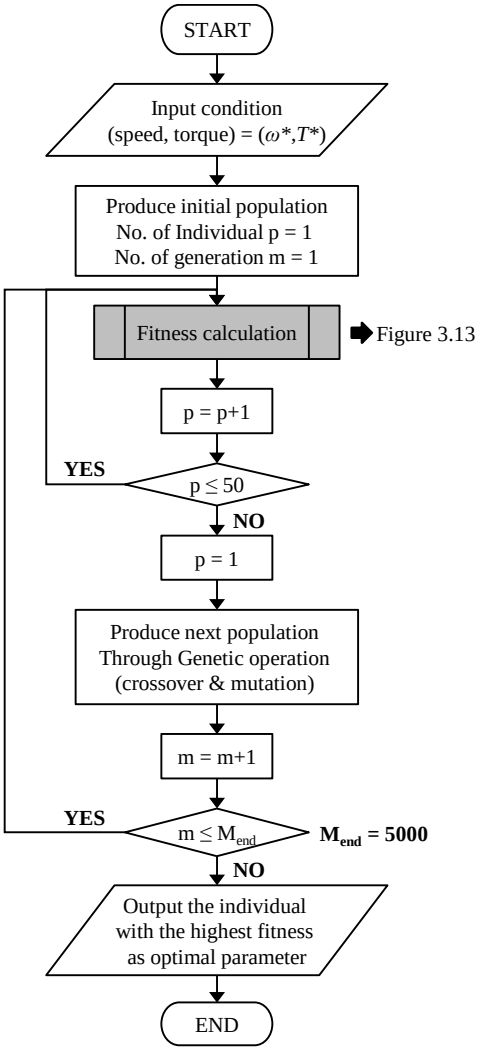

Figure 3.12 Flowchart of GA.

indices for each individual. After finishing the fitness evaluations for all fifty individuals, next population with 50 individuals is created through genetic operations (uniform crossover, adaptive mutation, and elite preserving)[35]. Table 3.1 appears the ranges and resolutions of the parameters employed in this optimization. After repeating the genetic operations through 5000 generations, an optimum set of control parameters can be determined.

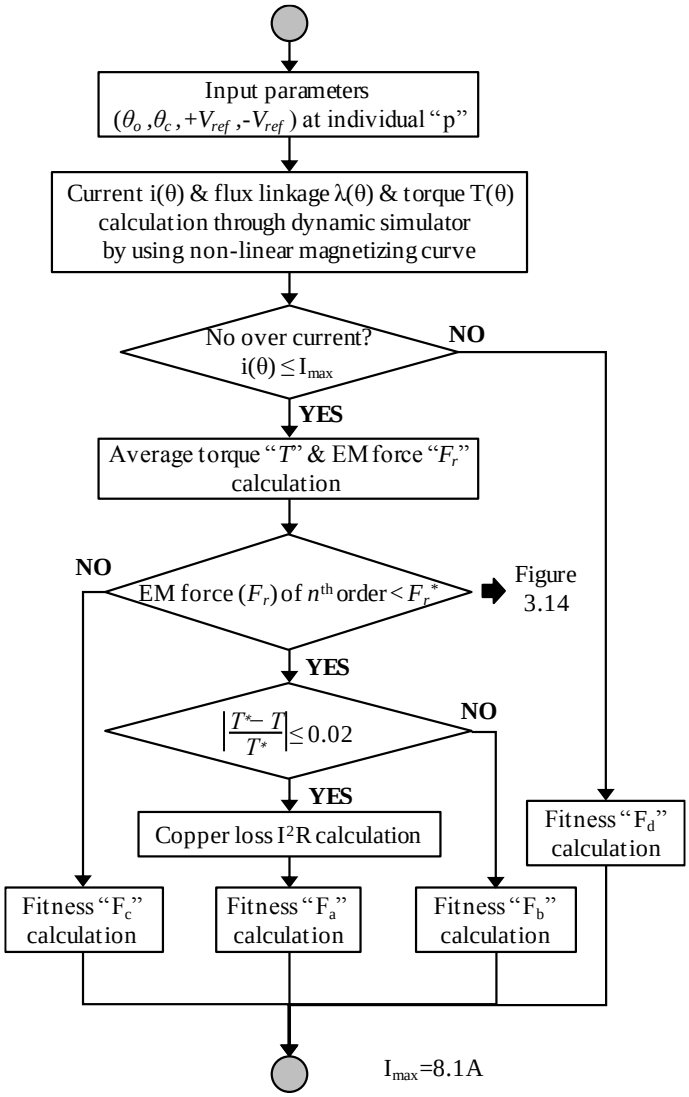

Figure 3.13 Flowchart for fitness calculation.

The first performance index is the average torque T_{ave}. The criterion is whether the computed average torque T_{ave} meets a given target torque T^* with a 2% tolerance, i.e. the torque error T_{err} is lower than 2% as described by following equation.

Table 3.1 GA specifications searching for optimal control parameters

Parameters & Range/Assigned bit	Turn-on angle, θ_o	35 to 42 / 7bit
	Commutation angle, θ_c	42 to 60 / 8bit
	PWM duty of +V	0 to V_{dc} / 8bit
	PWM duty of -V	0 to V_{dc} / 8bit
Execution number of GA	No. of individuals	50
	No. of generations	5000

$$Criterion1:\ \text{average torque } T_{ave} \Rightarrow T_{err} = \left| \frac{T^* - T_{ave}}{T^*} \right| \times 100 \le 2[\%] \tag{3.11}$$

The second performance index is the amplitude of the n^{th} harmonic component near the natural frequency included in the EM force. The criterion is whether this amplitude of the harmonic component is lower than that obtained under the conventional method and given in,

$$Criterion2:\ \text{EM force } F_r \Rightarrow \left| x^{th} \text{ order of } F_r \right| \le F_r^* . \tag{3.12}$$

The amplitude of harmonic component near the natural frequency obtained under the conventional method is defined as the target value F_r^*. Figure 3.14 shows the target value of the EM force obtained from the FEA model of the test motor and that obtained in the real test motor, respectively.

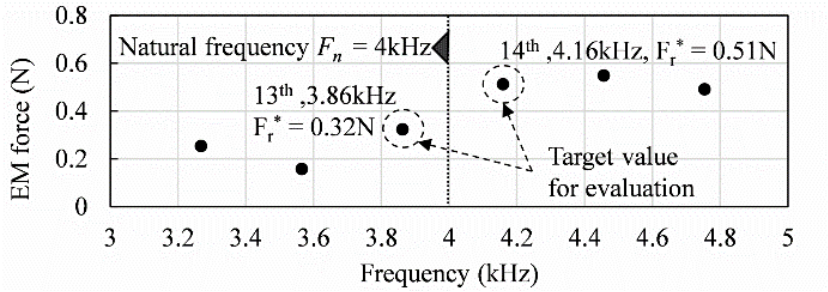

(a) target value of EM force on FEA model of the test motor

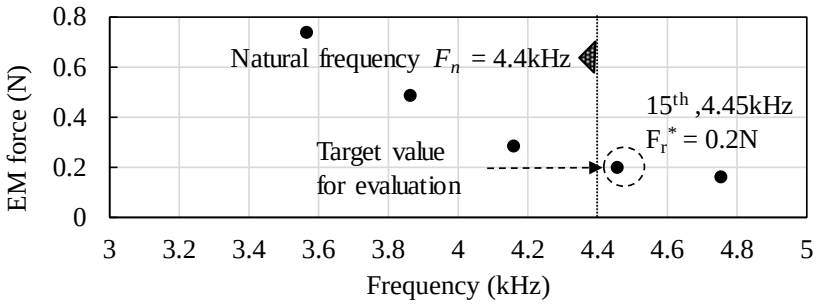

(b) target value of EM force in real test motor

Figure 3.14 Frequency analysis of EM force optimized through the conventional method under the rated torque and speed conditions.

The dominant natural frequency of the motor on FEA model and the real test motor are different due to, for an example, differences between mechanical properties of electromagnetic steel on catalog and those in the real test motor. To demonstrate the validity of the optimization of the control parameters for the FEA model as well as for the test motor, the control parameters for both the FEA model and test motor are optimized separately.

The target values of the EM force for the FEA model are set to 0.32[N] as the 13th component and 0.51[N] as the 14th component. On the other hand, the target values for the

test motor is set to 0.2[N] as the 15th component of the DFT base frequency f_{base} at the motor speed of 3000[r/min] under the rated torque condition. The base frequency f_{base} of DFT in one electrical period is changed by speed N_{rpm} and rotor pole number according to equation (2.32) . When the motor is running at 3000[r/min], the base frequency f_{base} is 300[Hz]. However, in GA, the period of calculation step must be considered for the base frequency calculation because the EM force harmonic is obtained from the DFT using the EM force data obtained at each calculation step in one electric period. For an example, when the period T_{calc} of one calculation step is 33.33[μsec], the calculation steps N_{calc} in one electrical period under the 3000[r/min] driving condition are 101 steps ($60/(N_{rpm}\times N_r)/33.33$[μsec]=100.01). Then, the 101 calculation steps are used for DFT and therefore, the base frequency is 297[Hz]=1/(101×33.33[μsec]). The equation for recalculation of the base frequency considering calculation step in GA is given in,

$$\begin{aligned} N_{calc} &= 60/(N_{rpm}\cdot N_r)/T_{calc} \\ f_{base} &= 1/(N_{calc}\times T_{calc}) \end{aligned} \tag{3.13}$$

At 5000[r/min], the base frequency is 492[Hz]=1/(61×33.33[μsec]). Before executing DFT for the EM force, the calculation of the EM force in one electrical period is important. In the FEA model, the EM force model is obtained by using the polynomial equation and DFT for the EM force data with respect to the variance of current and rotor position and therefore, the EM force data can be easily calculated from the EM force model. However, in case of the real test motor, since the EM force cannot be obtained experimentally, the calculation based on the equation (2.36) is approximately used. To calculate the EM force, the flux linkage and overlap area S_{align} are necessary. The flux linkage can be obtained from the dynamic simulator

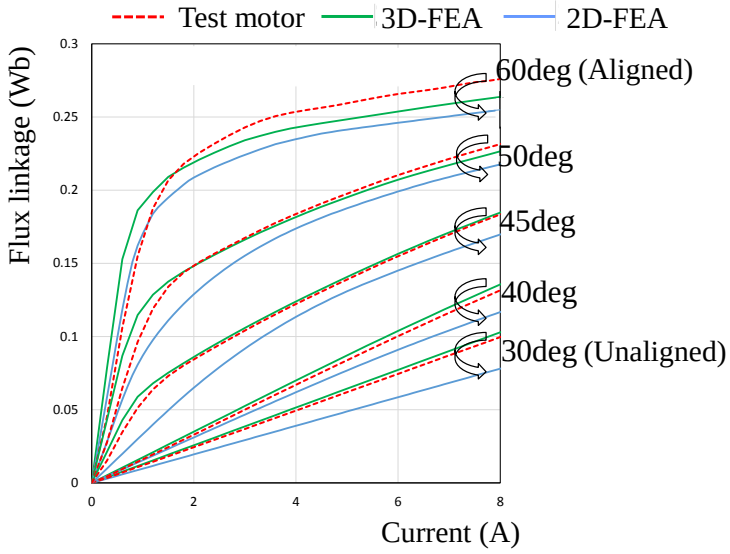

Figure 3.15 Comparison of magnetizing characteristic

in GA and S_{align} can be calculated by the dimension of motor structure and rotor position.

However, the EM force F_{r_calc} calculated from this method has some error compared with the EM force F_{r_simul} computed by the FEA because the total flux linkage λ_r and flux linkage component ($B_{r\_avg} \times S_{align}$) flowing into S_{align} is different. The total flux linkage λ_r flows through an area larger than S_{align} by fringing flux as shown in figure 2.14. Thus, for a more accurate EM force calculation, the S_{align} obtained from the FEA considering the fringing effect and magnetic saturation in the teeth is modeled and alternatively utilized. For more exact S_{align} data, the 3D-FEA results having similar magnetizing characteristic with the real motor are selected as the data for modeling of S_{align} after comparing the magnetizing characteristic of the real motor in 2D-FEA and 3D-FEA as shown in figure 3.15. This overlap area is called the effective overlap area $S_{align\text{-}eff}$ and is given by the following form.

$$S_{align-eff}(\lambda_r,\theta)=\left.\frac{\lambda_r^2}{2\mu_0 n^2 F_r}\right|_{From\ 3D-FEA} \tag{3.14}$$

Where λ_r and F_r are the values calculated in the 3D-FEA. As a result, the following equation can be used to calculate the EM force more accurately using the λ_r computed in the dynamic simulator in the fitness calculation process.

$$F_r(\lambda_r,\theta)\approx\frac{\lambda_r^2}{2\mu_0 n^2 S_{align-eff}} \tag{3.15}$$

Finally, the natural frequency component of the calculated EM force is obtained using the DFT (Discrete Fourier transform).

The third performance index is the copper loss. The copper loss is a net performance index only calculated for the individual that satisfies both two criteria mentioned above.

$$Criterion3:\ \text{copper loss}\ \mathrm{P}_c=i^2R \quad \Rightarrow \text{As low as possible!} \tag{3.16}$$

The individual with less copper loss among the individuals that satisfy both two criteria of the torque and EM force becomes better one. To find the optimal parameters satisfying the above criteria, the fitness F_a, F_b, F_c, and F_d are calculated. Each fitness is calculated like below $\mathrm{F_b} = -T_{err}\times10^2$, $F_c = -29\times10^5$, $F_d = -(+V_{ref})/V_{dc}\times255\times10^4$, $F_a = 100/P_c$. After finishing the genetic operations, the set of control parameters with the highest fitness values of F_a while the magnitude of target harmonics of EM force is less than that of the target value and T_{err} is satisfied, is selected as the optimal set.

3.5.2 Optimized voltage parameters accordance with the driving condition

The optimization of control parameters is conducted for the FEA model and the real test motor using the previously mentioned GA. Table 3.2 and 3.3 show the optimization results of the FEA model and test motor respectively. Table 3.2 summarizes the optimal set of control parameters determined by the GA for the FEA model of the test motor based on two kinds of commutation methods under the given operating conditions. And the simulation results (copper loss and average torque) obtained by the FEA for the optimal voltage parameters are listed. Table 3.3 summarizes the optimal set of control parameters determined by the GA for the real test motor and the experimental result (copper loss and average torque) for the optimal voltage parameters.

In all cases, the average torque meets the target value and the difference between the copper losses from the conventional method and the new modified method is small.

Table 3.2 Optimal parameters and simulation results for average torque and copper loss for FEA model of test motor

Condition (ω^*,T^*)	Methods	Optimal parameters				Simulation results	
		+ V_{ref} [V]	- V_{ref} [V]	θ_O [deg]	θ_C [deg]	T_{ave} [Nm]	P_c [W]
3000 [r/min] 1.27 [Nm]	Conventional	280	-280	39.60	52.39	1.27	37.47
	Proposed	280	-239	39.82	53.17	1.27	38.29
5000 [r/min] 0.76 [Nm]	Conventional	282	-282	36.85	52.00	0.76	22.61
	Proposed	282	-270	36.92	53.80	0.76	23.21

Table 3.3 Optimal parameters and experimental results for average torque and copper loss for the real test motor

Condition (ω^*,T^*)	Methods	Optimal parameters				Experimental results	
		+ V_{ref} [V]	- V_{ref} [V]	θ_O [deg]	θ_C [deg]	T_{ave} [Nm]	P_c [W]
3000 [r/min] 1.27 [Nm]	Conventional	277	-277	38.93	52.16	1.27	44.15
	Proposed	283	-221	38.6	51.51	1.27	48.22
5000 [r/min] 0.76 [Nm]	Conventional	281	-281	36.10	51.51	0.76	29.49
	Proposed	281	-216	35.43	48.78	0.76	32.08

3.6 Experiment and simulation result

With the optimal voltage parameters obtained from the simulation model and the real test motor, the vibration simulation on FEA model under the conventional control method and the new modified control method is conducted. In addition, the vibration and acoustic noise measurement tests using the real test motor are also conducted.

3.6.1 Comparison of vibration reduction in the FEA model

The vibration is compared through 2D-FEM electromagnetic structural coupled analysis using the optimized control parameters obtained from the FEA model appeared in Table 3.2. As can be seen in figure 3.16, under the rated speed 3000[r/min] and the rated torque 1.27[Nm] condition, the optimal voltage is changed from 280→0→-280[V] (θ_o=39.6[deg], θ_c=52.39[deg]) to 280→0→-239[V] (θ_o=39.82[deg], θ_c=53.17[deg]) for the new modified method. As a result, owing to the reduction of 13^{th} and 14^{th} order harmonic components of the EM force near the natural frequency, the vibration is suppressed compared with the single voltage pulse control and the conventional method. Moreover, as can be seen in figure 3.17, under the maximum speed 5000[r/min] and the torque of 0.76[Nm] condition resulting in the rated power output, the optimal voltage is changed from 282→0→-282[V] (θ_o=36.85[deg], θ_c=52.00[deg]) to 282→0→-270[V] (θ_o=36.92[deg], θ_c=53.80[deg]) for the new modified method. As a result, thanks to the reduction of 8^{th} order harmonic component of the EM force near the natural frequency, the vibration is suppressed compared with the single voltage pulse control and the conventional method.

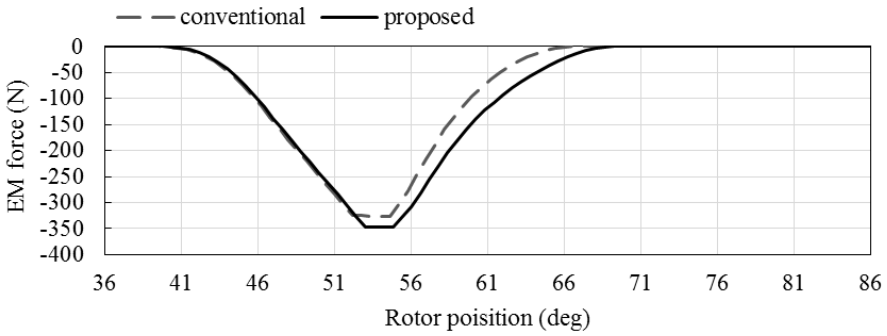

(a) EM force

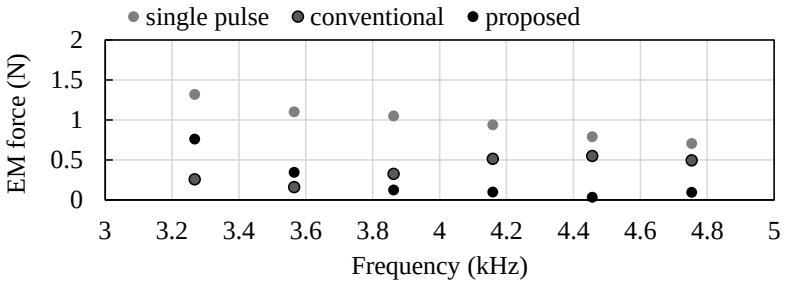

(b) DFT analysis of EM force

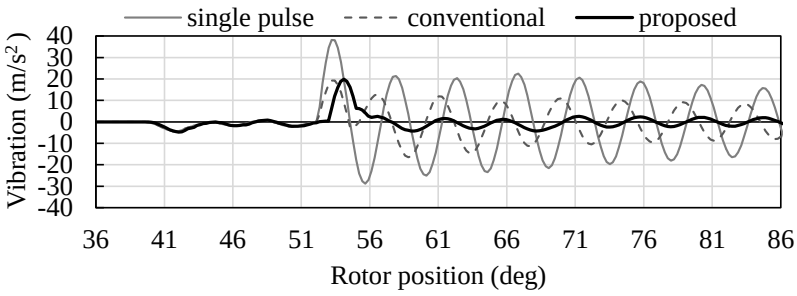

(c) vibration result

Figure 3.16 Simulation results for different commutation methods using the optimum control parameters under the rated torque at the rated speed condition.

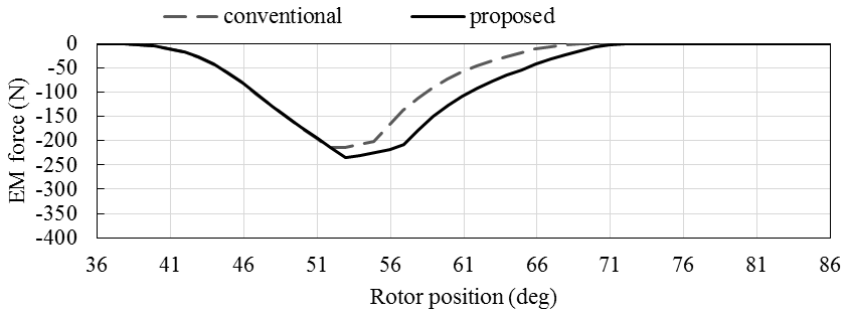

(a) EM force

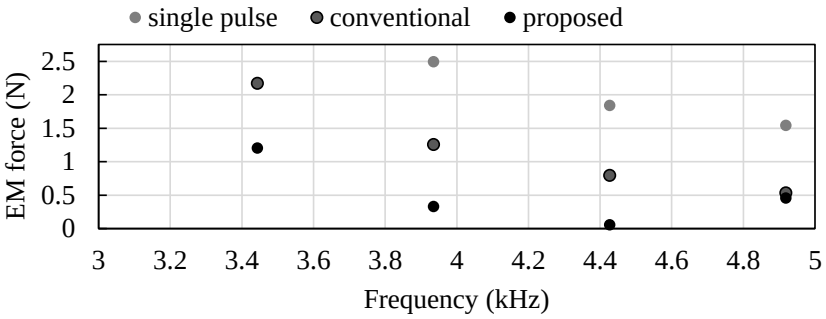

(b) DFT analysis of EM force

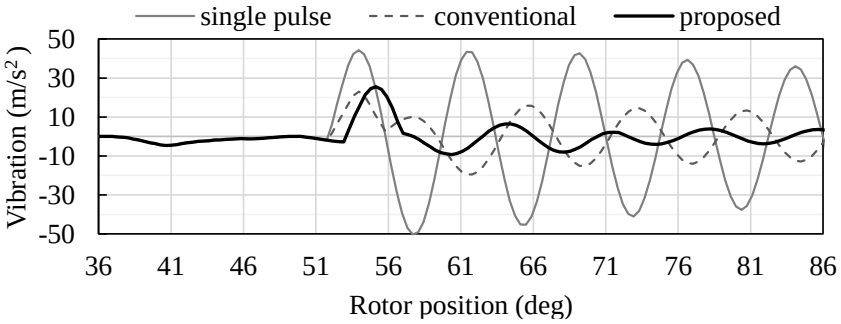

(c) vibration

Figure 3.17 Simulation results for different commutation methods using the optimum control parameters under the rated power at the maximum speed condition.

3.6.2 Comparison of vibration and acoustic noise reduction in real test motor

The vibration and acoustic noise are compared through experiments employing the optimized control parameters for the real test motor appeared in Table 3.3. For the experiment, the equipment is set up as shown in figure 3.18. The PE-Expert III (Myway Plus Corporation) is used as a controller to generate gate signals for asymmetric H-bridge converter with a PWM frequency of 20[kHz]. For position sensing, a 4000[ppr] incremental encoder (OM corporation) is attached. As a load, a servo motor (Yaskawa Electric Corporation, SGMSH-15A) is coupled with the test SRM and used as a constant speed dynamo. An accelerometer (ENDEVCO corporation, 7250A-2) and sound level meter (RION corporation, NL-31) are used to measure the vibration and acoustic noise, respectively. A noise and vibration analyzer (AND company, AD-3651) is used to record and analyze the noise and vibration results.

Under single phase excitation test with one voltage pulse, vibration is compared as shown in figures 3.19 and 3.20. The voltage parameter of table 3.3 is used as the different commutation methods. At the condition of 3000[r/min] and the rated torque of 1.27[Nm], the vibration under the new modified method is minimized to 30% at the natural frequency of 4.4[kHz] comparing with the conventional method. At the condition of 5000[r/min] and the torque of 0.76[Nm] resulting in the rated power, the vibration under the new modified method is suppressed to 60% at the natural frequency comparing with the conventional method.

Through the continuous all phase excitation, the vibration and acoustic noise are compared as shown in figures 3.21, 3.22, 3.23 and 3.24. The optimized control parameters appeared in

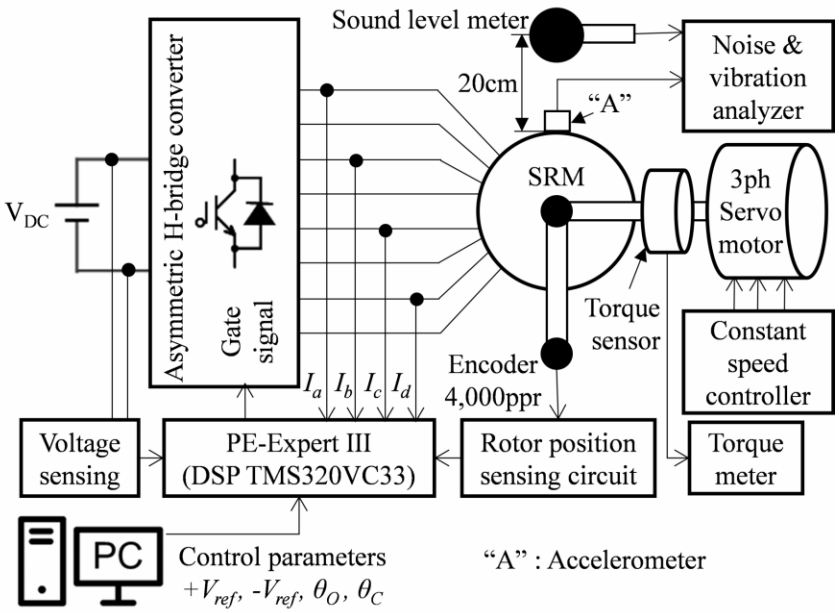

(a) block diagram of experimental system

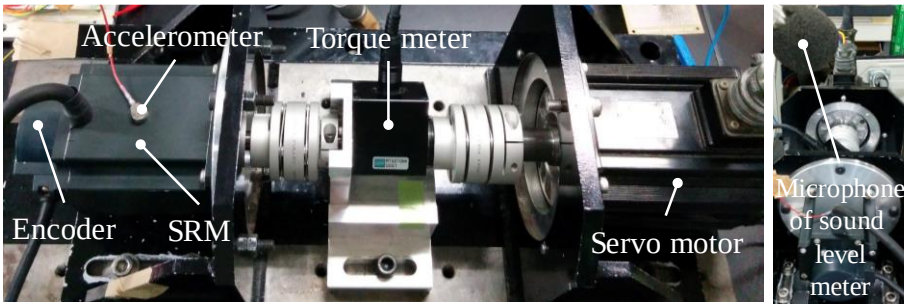

(b) external view of experimental setup

Figure 3.18 Experimental setup.

table 3.3 are used.

As can be seen in figure 3.21, under the rated speed and torque condition, the vibration at the natural frequency is reduced by 35% compared to the conventional method. As shown in

figure 3.22, under the rated power at the maximum speed of 5000[r/min], the vibration at the natural frequency is reduced by 80% compared to the conventional method. Acoustic noise is also reduced overall and at the natural frequency as shown in figures 3.23 and 3.24. Table 3.4 is the measurement results of vibration and acoustic noise, copper loss and average torque under the different commutation methods. It can be seen from the table that the vibration and the acoustic noise at the natural frequency and the overall acoustic noise are attenuated by employing the proposed new modified commutation method while keeping the average target torque and suppressing the increase in copper loss.

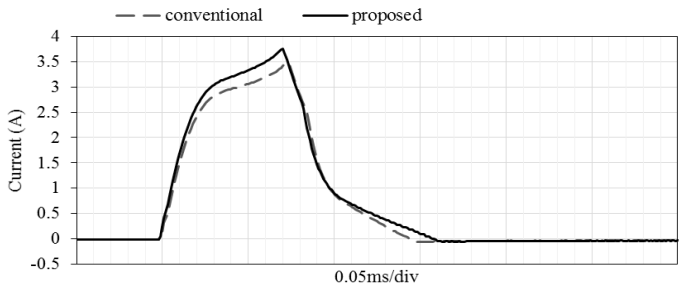

(a) current waveform

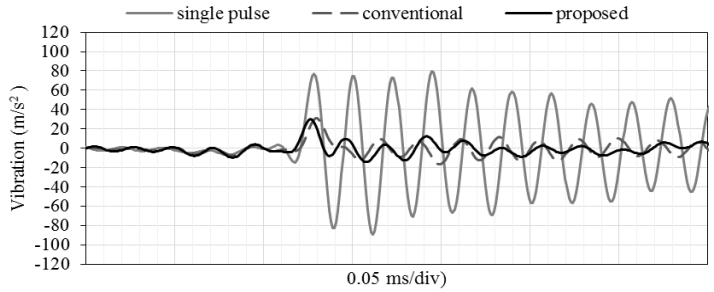

(b) vibration

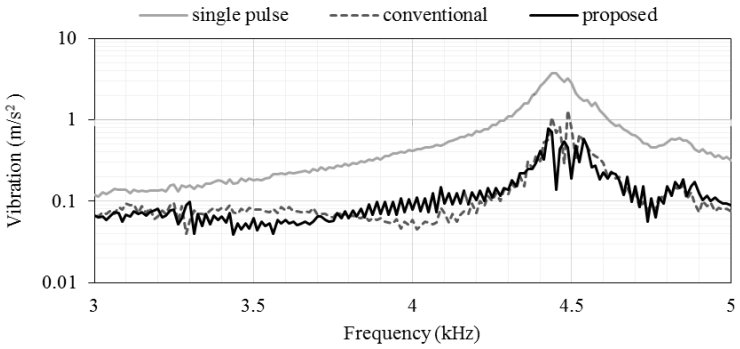

(c) DFT analysis of vibrations

Figure 3.19 One voltage pulse excitation test results for different commutation methods using the optimum parameters under the rated torque and speed condition.

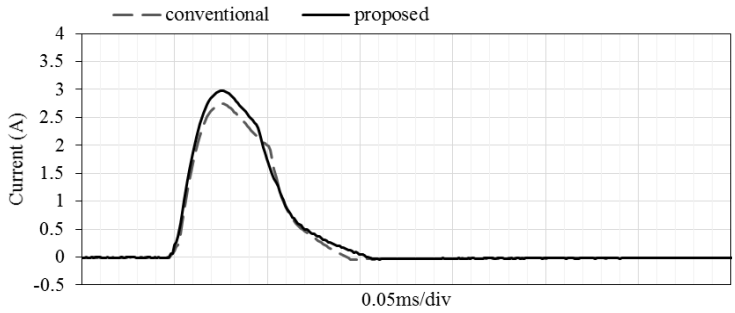

(a) current waveform

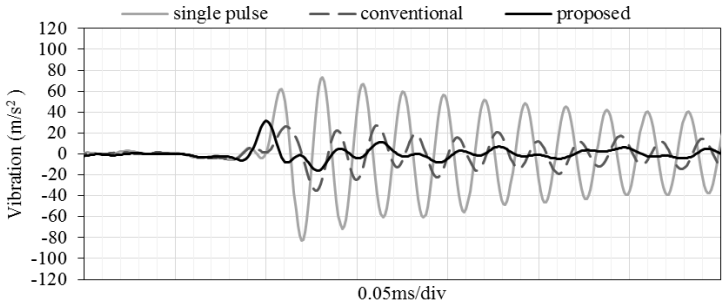

(b) vibration

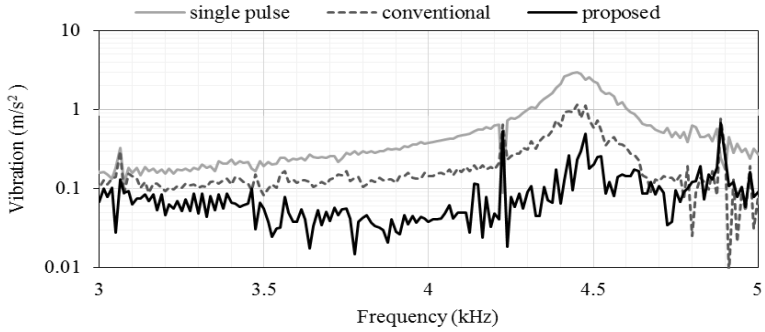

(c) DFT analysis of vibration

Figure 3.20 One voltage pulse excitation test results for different commutation methods using the optimum parameters under the rated power at the maximum speed.

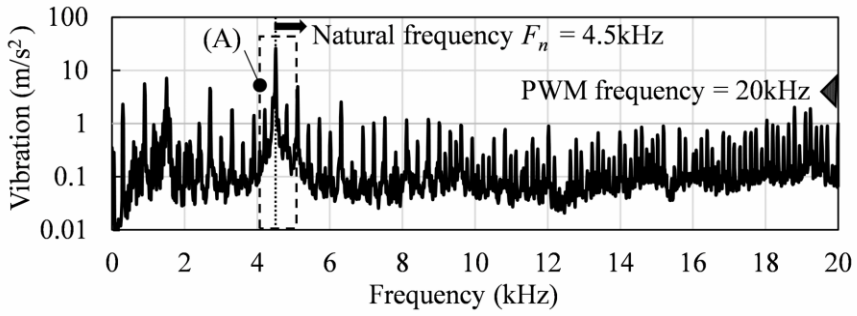

(a) conventional commutation method

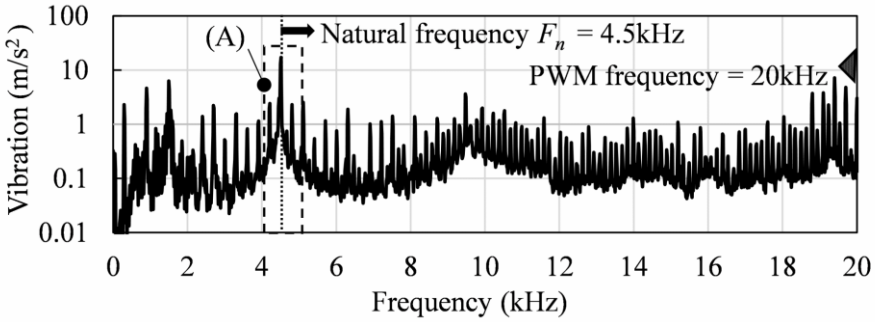

(b) proposed new modified commutation method

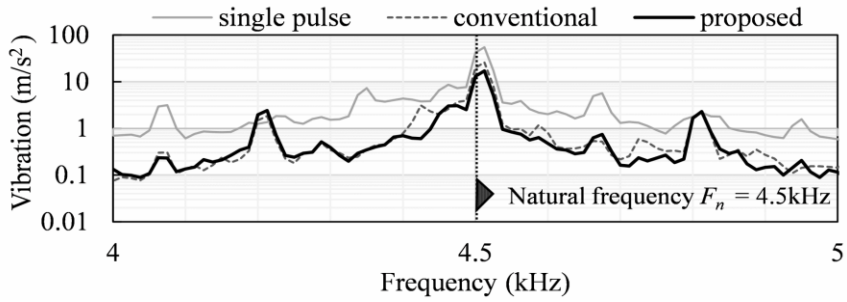

(c) comparison of results at (A) enlarging around the natural frequency

Figure 3.21 Measured vibration spectra for different commutation methods using the optimal control parameters under the rated torque and speed condition.

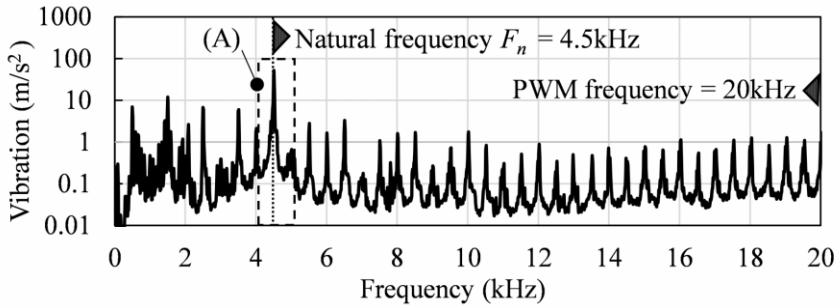

(a) conventional commutation method

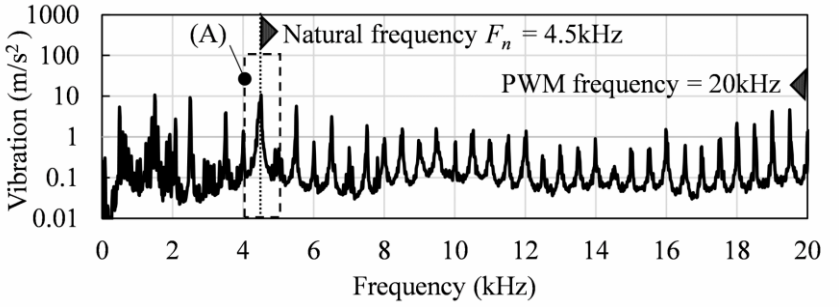

(b) proposed new modified commutation method

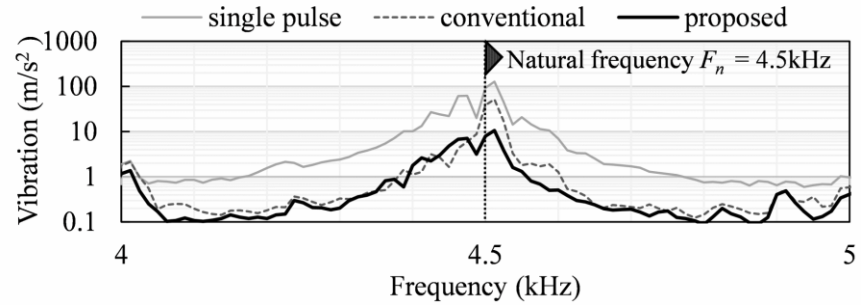

(c) comparison of results at (A) enlarging around the natural frequency

Figure 3.22 Measured vibration spectra for different commutation methods using the optimal control parameters under the rated power at the maximum speed.

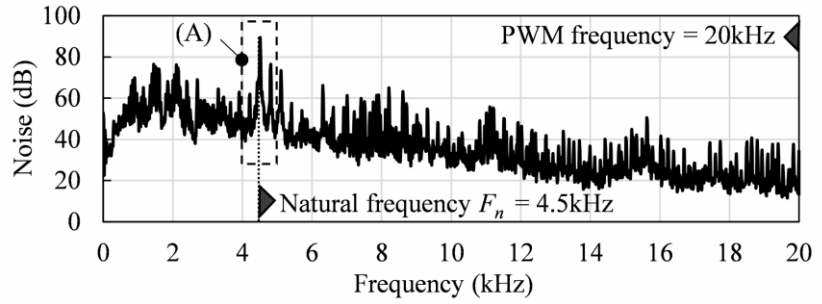

(a) conventional commutation method

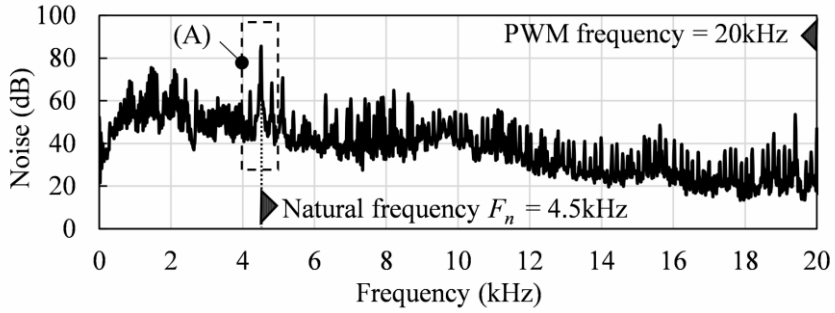

(b) proposed new modified commutation method

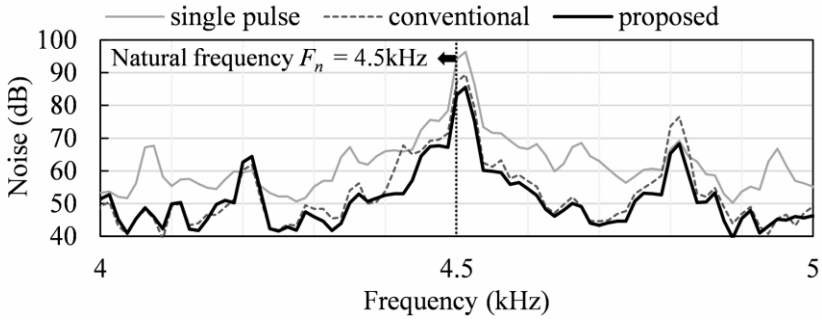

(c) comparison of results at (A) enlarging around the natural frequency

Figure 3.23 Measured noise spectra for different commutation methods using the optimal control parameters under the rated torque and speed condition.

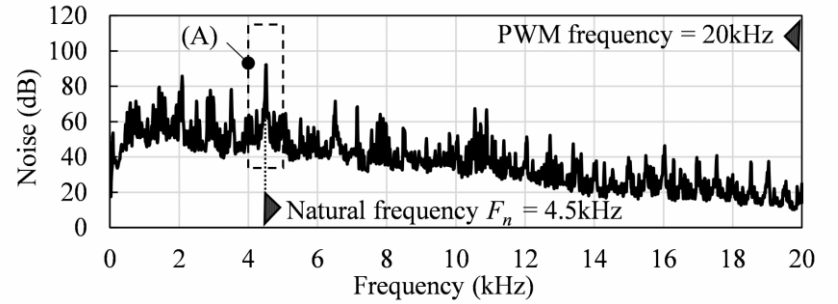

(a) conventional commutation method

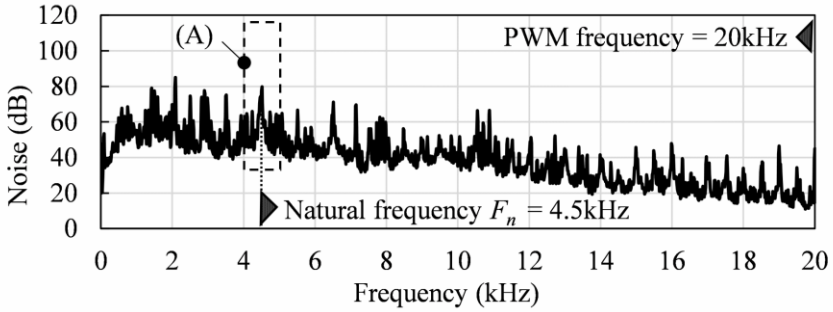

(b) proposed new modified commutation method

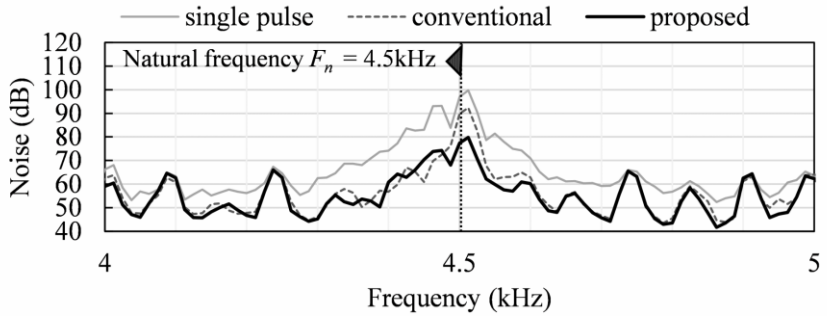

(c) comparison of results at (A) enlarging around the natural frequency

Figure 3.24 Measured noise spectra for different commutation methods using the optimal control parameters under the rated power at the maximum speed.

Table 3.4 Summary of experimental results.

method	Speed [r/min]	T_{ave} [Nm]	P_c [W]	Vibration reduction [%]	Noise (at F_n) [dB]	Noise (over all) [dB]
Conventional	3000	1.27	44.15	-	89.4	93.5
Proposed	3000	1.27	48.22	35	85.5	90.6
Conventional	5000	0.76	29.49	-	92.0	96.5
Proposed	5000	0.76	32.08	80	79.8	92.0

3.7 Epilogue

Through this chapter, the problem why the conventional two stage commutation method did not work effectively at heavy load and high-speed condition was revealed and the reason also was investigated theoretically. To overcome this problem, the new modified two stage commutation method was proposed. As a result, it was revealed that the proposed method was more effective than the conventional method concerning the vibration and acoustic noise reduction while keeping the target torque and avoiding copper loss.

In the future, 1) optimization of control parameters to achieve further high efficiency control considering both copper loss and iron loss in the proposed method and 2) study of control method to have the same vibration reduction performance without changing the rotor pole shape, i.e. with the motor using conventional rectangular pole shape rotor, will be required.

Chapter4
Conventional torque ripple minimization control of SRM for servo

4.1 Prologue

In chapter 1, the importance of torque ripple minimization control especially in the servo drive system which requires exact position control in low speed region has been described. In view of the importance, various approaches for minimizing torque ripple have been presented up to now. In this chapter, these earlier studies are firstly surveyed. Among various approaches, this study focuses on the current profiling control method. Through the description of control block for servo drive application, a basic principle of the current profiling control method based on magnetizing curves under single phase excitation is explained (hereafter, named as conventional method). In addition, the current profile generator and current profile tracking controller that make the conventional method up are briefly described. The conventional method, however, has a problem of large torque ripple at current overlapping region due to mutual coupling effect. Theoretical analysis for and investigation into the problem through 2D-FEA are conducted. Finally, the reason why the problem arises is revealed.

4.2 Survey of earlier studies on torque ripple minimization control of SRM

To minimize torque ripple, many kinds of control methods had been proposed[37)-(50)]. In order to realize flat torque control in SRM, direct torque control (DTC) and/or current control (CC) were generally employed as stated in Ref. (37). DTC was a method to determine switching signals through torque hysteresis controller after comparing a target torque with an estimated torque obtained from torque estimator under predefined *dwell angle*[(36)]. This method was difficult to achieve high-efficiency control because there was no attention about torque sharing between adjacent phases[(37)]. In addition, DTC was difficult to eliminate torque ripple perfectly due to limitation of band width of hysteresis controller as its nature. Whereas, CC was classified roughly into two methods. One was *chopping-current regulation*[(36)], in which phase current was controlled with a constant amplitude over the *dwell angle*[(36)(37)]. The other was an instantaneous current profiling control with respect to target torque and rotor position. The former had a problem of large torque ripple at commutation from one phase to next phase, while the latter was possible to minimize the torque ripple in entire region[(39)-(50)]. For this reason, this study focused on the instantaneous current profiling control.

The instantaneous current profiling control roughly consisted of two parts: (i) current profile generator and (ii) current profile tracking controller. To generate the current profile for achieving flat torque control in the part (i), many modeling approaches were proposed[(39)-(50)]. One of them used torque-rotor position-current (here-after, named as T-θ-i) model obtained from measured self-inductance profile[(40)(41)]. Another employed T-θ-i model

computed by finite element analysis (FEA)[42)-(44)] or direct torque measurement[45)]. However, these methods had essentially some error due to missing of consideration of magnetic saturation[40)(41)], difference between real motor and ideal one on FEA[42)-(44)], and torque measurement error existing[45)]. In order to overcome these modeling problems, current profiling techniques based on *T*-θ-*i* model derived from measured magnetizing curves were also reported[46)-(50)]. Although these current profiling control methods basically worked well, they failed to operate properly during current overlapping region. The reason was that mutual coupling effect between adjacent phases was not considered in the case of that the magnetizing curves of single phase were only measured and taken into account. It was investigated and revealed that the flux linkage of energized main phase was affected by the mutual coupling effect[51)(52)]. In Ref. (51), through the voltage equation which was able to be expressed by using self and mutual inductances obtained from FEA considering magnetic non-linearity, torque variation due to the mutual coupling effect was proved. In Ref. (52), through the torque component separation by using self and mutual fluxes computed by frozen permeability method on FEA, it was reported that the affection of torque variation by the mutual coupling effect was not able to be ignored.

To suppress the torque ripple produced by the mutual coupling effect, the torque control algorithm taking the mutual coupling effect into account was proposed[53)(54)]. One was a method using motor model formulated by self and mutual inductances obtained from FEA[53)], the other was based on flux linkage-current-position (hereafter, named as λ-*i*-θ) model obtained from FEA[54)]. In Ref. (53), only FEA simulation-based current profiling under the *chopping-current regulation* was studied, in which just a little suppression effect on torque

ripple was found. In Ref. (54), the *chopping-current regulation* with a little current profile optimization was proposed and tested. In the simulation, although the torque ripple was reduced well compared with the conventional *chopping-current regulation* more than 45% of torque ripple remained in the experimental test. The authors of Ref. (54) noticed that *"the accuracy of this method for practical SRM, depends on how close to the FEA data, matches with the real SRM"*[54]. Moreover, these methods resulted in a large torque ripple remaining that seemed to be unacceptable for industrial servo drive applications.

In this study, a modified current profiling control based on two phase model considering the mutual coupling effect is proposed, which is built on the current profiling control method based on single phase model[48] (hereafter, named as conventional method). The conventional method has employed current-torque-position (hereafter, named as *i*-*T*-θ) model derived from *T*-θ-*i* model that has been calculated from the measured magnetizing curves under single phase excitation. From *i*-*T*-θ model, the target current profile for target torque has been determined. In addition, for a fast and precise instantaneous current tracking control, PWM voltage control based on voltage equation using λ-θ-*i* model that has been also derived from the measured magnetizing curves has been built. Before introducing the two phases model, the reason why the conventional method has not worked at heavy load condition is reviewed by way of FEA for a 400W 4-phase 8/6 SRM shown in subsection 1.2.3.

4.3 Controller configuration of SR servo motor drive

To describe the operation principle of the conventional method, a servo motor controller for SRM used in the conventional method is explained. Figure 4.1 shows the servo motor controller for positioning control[48]. The controller consists of position feedback controller (*PC*), speed feedback controller(*SC*) and torque controller(*TC*). The PC produces the target speed ω^* from the position error between the position reference θ^* and the detected actual position θ. The *SC* generates the torque command T^* from the speed error between the speed

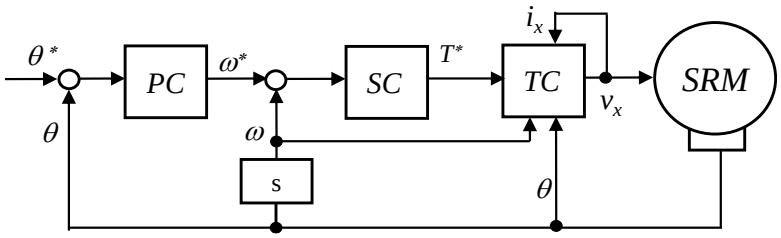

Figure 4.1 Block diagram of controller for SR servo motor drive[48].

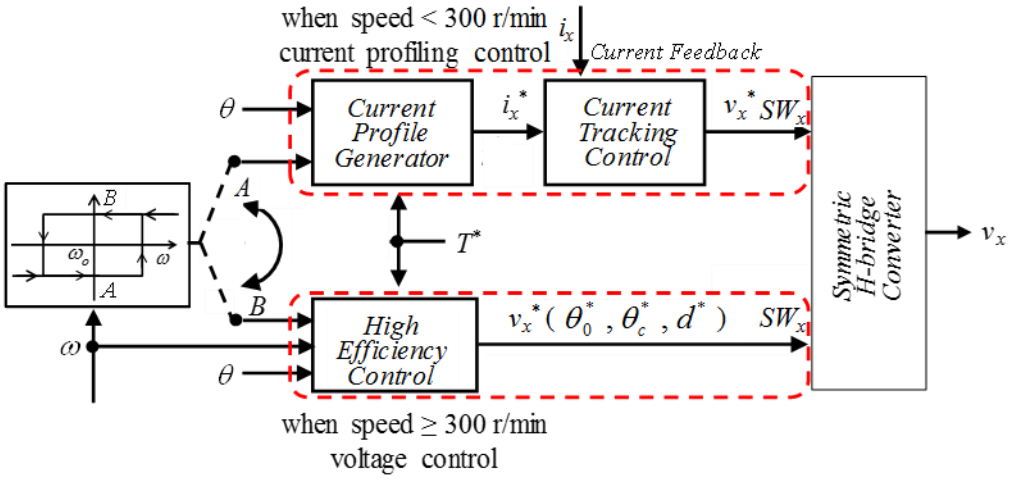

Figure 4.2 Block diagram of torque controller[48].

reference ω^* and the detected actual speed ω. The *PC* and *SC* are composed of P(proportional)-controller and PI(proportional-integral)-controller, respectively. On the contrary, the torque is controlled by the *TC* that does not any of P- or PI-controller as shown in figure 4.2. In the *TC*, for exact position control in the low speed region less than the base speed of 300[r/min], the *current profiling control* for torque ripple minimization is employed. In the middle and high speed region beyond the base speed of 300 [r/min], the average torque is controlled to be identical with the reference while maintaining maximum efficiency, which is called as *"high efficiency control"*.

The current profiling control is executed in accordance with following procedures. Firstly, the rotor position θ and the target torque T^* are inputted into the current profile generator and then, instantaneous current profile reference of X-phase i_x^* is calculated from i-θ-T model and torque contour function, which will be explained in detail later. Secondly, the current tracking controller based on voltage equation of SRM achieves that the instantaneous real motor current follows the current reference, which is also explained in detail later. In the high efficiency control for the middle and high speed region, the PWM voltage control is employed by using the voltage parameters (on angle θ_o, commutation angle θ_c, duty of phase voltage d^*) that are optimized for a given torque and speed condition. In this study, the torque ripple minimization for accurate position control in low speed region is focused on.

4.4 Brief explanation about conventional method

In this section, the conventional method is briefly explained. Firstly, an instantaneous reference torque per a phase for a given average torque command at a detected rotor position

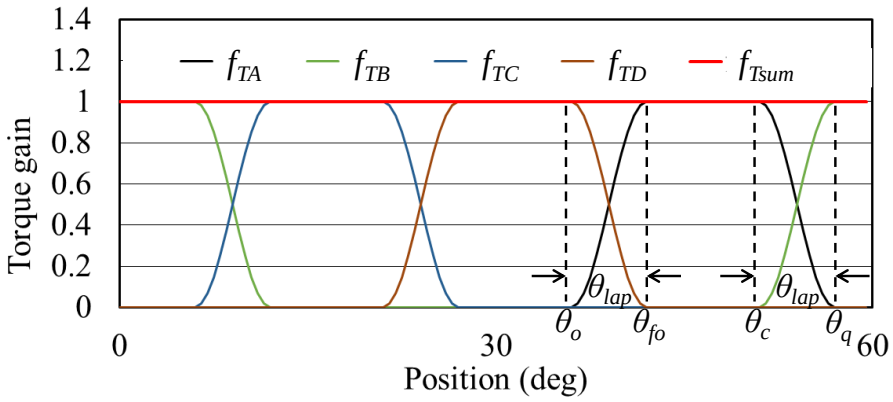

Figure 4.3 Torque contour function used in the conventional method[48]

is determined via the torque contour function[40][48] shown in figure 4.3. Subsequently, the corresponding instantaneous current profile is computed through *i*-*T*-θ model[48]-[50]. Finally, the instantaneous current tracking control is executed under PWM voltage control based on the voltage equation[48]-[50].

4.4.1 Torque contour function[40][48]

The torque contour function can be selected from many kinds of possible functions[40]. As an example, figure 4.3 illustrates the torque contour function employed in this study for the 4-phase test motor. The torque contour function per phase is expressed as $f_{Tx}(\theta)$ with generalized form. The total sum of the torque contour function per phase with respect to 4-phase machine is given in,

$$f_{Tsum} = \sum_{x=A}^{D} f_{Tx}(\theta) = 1 \tag{4.1}$$

where, x denotes the phase number. The instantaneous reference torque per a phase τ_x^* with respect to a given average torque command T_t^* and the rotor position θ is expressed by,

$$\tau_x^*(\theta) = T_t^* \times f_{Tx}(\theta) \tag{4.2}$$

Then, the total torque is controlled to be flat shape according to following equation.

$$\sum_{x=A}^{D} \tau_x^*(\theta) = T_t^* \tag{4.3}$$

In this torque contour function, two angles θ_{fo} and θ_{lap} are free parameters. The former represents a start angle of non-overlapping conduction period and the latter is overlapping conduction angle, respectively. Since the test motor has a symmetric structure and the phase shift between adjacent phases is 15 degrees, other angle parameters become dependent variables on θ_{fo} and θ_{lap} and are given in,

$$\theta_o = \theta_{fo} - \theta_{lap},\ \theta_c = \theta_o + 15,\ \theta_q = \theta_{fo} + 15 \tag{4.4}$$

where, θ_o is turn-on angle, θ_c is a commutation angle and θ_q is an extinction angle, respectively[36]. To get unity gain at the overlapping region, the torque contour function of A-phase can be expressed in following manner.

$$f_{TA}(\theta) = \frac{1}{2}\left[\cos\left(\frac{\theta - \theta_{f0}}{\theta_{lap}}\pi\right) + 1\right] \tag{4.5}$$

In the conventional method previously studied[48], θ_{f0} was set to 42 degree that the overlap of stator and rotor teeth in A-phase starts and θ_{lap} was set to 6 degree, respectively.

4.4.2 *i-θ-T* model and target current computation[48]-[50]

In the conventional method, an assumption usually used in SRM is introduced, that is, the mutual inductance has been negligible small compared with the self-inductance. In this case, *T-θ-i* model obtained from the measured magnetizing curves under only single phase

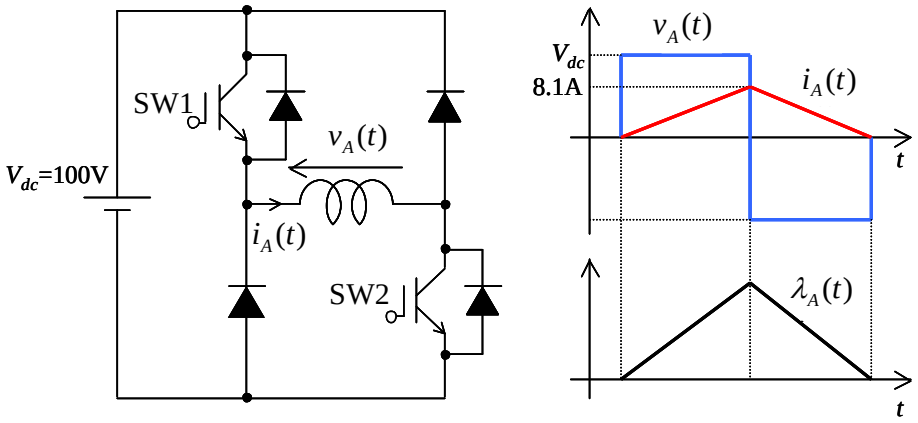

Figure 4.4 Voltage, current and magnetic flux linkage waveforms under measurement of magnetizing curve at a certain fixed rotor position.

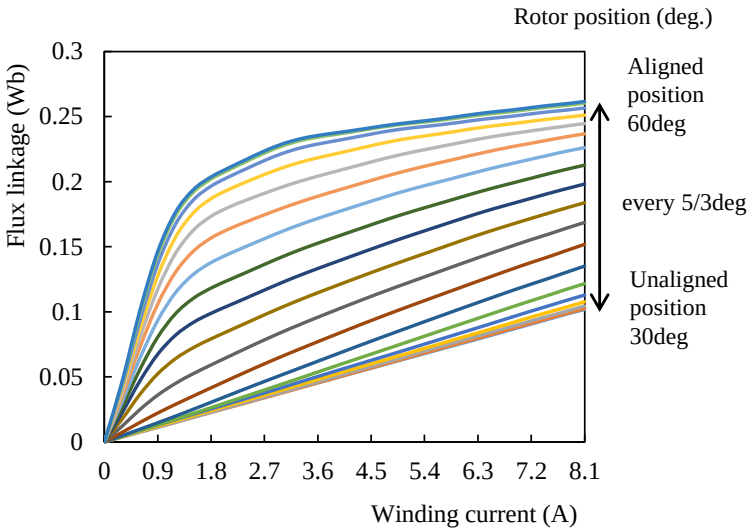

Figure 4.5 Measured magnetizing curve of A-phase used in the conventional method[48].

excitation can be used as a base model to calculate the instantaneous current profile. As shown in figure 4.4, if the both switches SW1 and SW2 are turned on and turned off after reaching the maximum current 8.1[A] at a certain fixed rotor position, phase voltage v_A and

current i_A vary with respect to time as shown in the figure, respectively. Then through the voltage equation of SRM, the flux linkage of excited phase can be calculated by,

$$\lambda_A = \int (v_A - R \cdot i_A) dt \,. \tag{4.6}$$

By changing every fixed position with a position interval, the magnetizing curves between the unaligned and the aligned position can be obtained by repeating the same measurement. Figure. 4.5 shows the measured magnetizing curves of A-phase in the test motor. The flux linkage λ_A can be expressed by a polynomial equation of A-phase current i_A at every fixed rotor position θ_x and given in,

$$\lambda_A(i_A)\Big|_{\theta=\theta_x} = \sum_{n=1}^{n_{\max}} L_n \Big|_{\theta=\theta_x} \cdot i_A^n \tag{4.7}$$

where, n_{max} denotes the highest order of polynomial equation. The coefficients L_n can be obtained by curve fitting for the magnetizing curve at every fixed rotor position θ_x. The corresponding spatial coefficient distribution of each current order is modeled by Discrete Fourier Transform (DFT) and given in,

$$L_n(\theta) = \sum_{k=0}^{k_{\max}} L_{nk} \cos(k\alpha\theta) \tag{4.8}$$

where, L_{nk} and k_{max} denote the coefficients and the highest order of cosine series expansion. α is the number of rotor poles. As a result, the magnetizing curves model can be derived as,

$$\lambda_A(i_A, \theta) = \sum_{n=1}^{n_{\max}} L_n(\theta) \cdot i_A^n \tag{4.9}$$

By using the magnetic co-energy W_{mA}' expression, the instantaneous torque expression under only A-phase excitation can be deduced as,

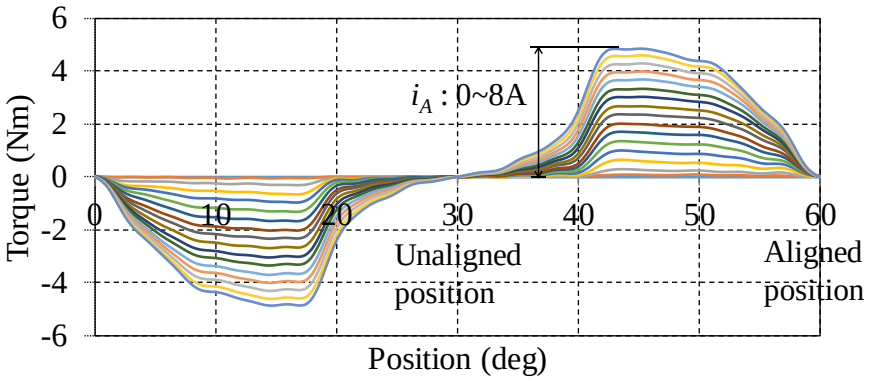

Figure 4.6 *T-θ-i* model of A-phase employed in the conventional method.

$$W_{mA}{}' = \int_0^{i_A} \lambda_A(i_A, \theta) di_A \tag{4.10}$$

$$\tau_A(i_A, \theta) = \frac{\partial W_{mA}{}'}{\partial \theta} \tag{4.11}$$

Figure 4.6 depicts the *T-θ-i* characteristic of A-phase calculated from equation (4.11). Through this *T-θ-i* model, *i-T-θ* model can be also expressed as a polynomial equation and given in following fashion.

$$i_A^*(\tau_A^*, \theta) = \sum_{m=1}^{m_{\max}} K_m(\theta) \cdot \tau_A^{*m} \tag{4.12}$$

where, $K_m(\theta)$ is the spatial coefficient distribution with respect to each torque order m stored in memory space. $m_{\max}$ denotes the highest order of the polynomial equation. Thus, once the instantaneous torque reference in A-phase $\tau_A{}^*$ at the detected rotor position is determined by equation (4.2), the instantaneous current profile $i_A{}^*$ can be computed by equation (4.12). Assuming that the stator and rotor structures are symmetric, the same procedures can be applied to other phases *B*, *C* and *D* to compute the instantaneous current profile just considering 15degrees phase shift. Figure 4.7 illustrates the instantaneous torque

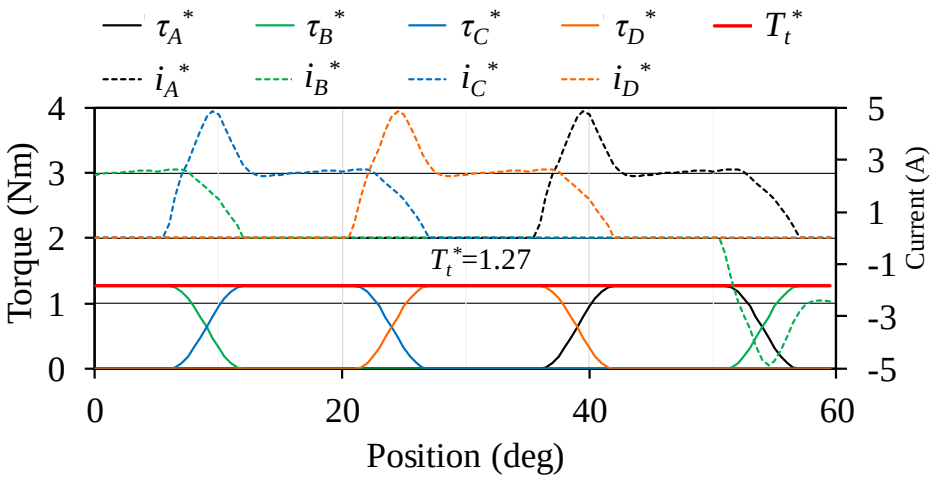

Figure 4.7 Instantaneous torque reference and corresponding current profile of each phase in the conventional method.

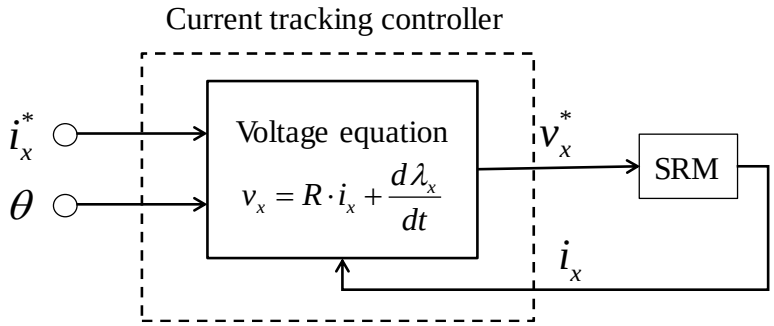

Figure 4.8 Block diagram of voltage reference generation for current tracking control[48].

reference in each phase and the corresponding current profiles under the rated torque command as an example.

4.4.3 Current profile tracking control[48]

The important thing for flat torque control is to control precisely to follow the target current

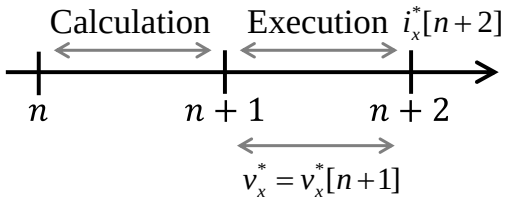

Figure 4.9 Target voltage control timming[48].

profile obtained in subsection 4.4.2. In the prior study, for rapid and precise current control, the current tracking control based on voltage equation of SRM has been proposed[48]. Figure 4.8 shows the block diagram of the inside of current tracking control shown in figure 4.2. Assuming again that the mutual inductance in SRM is negligible small compared with the self-inductance, an applied voltage to A-phase can be computed by following voltage equation.

$$v_A = Ri_A^* + \frac{d\lambda_A^*}{dt} \tag{4.13}$$

In digital system, as shown in figure 4.9, to control the current to the target value after *n+2* sampling point, the voltage reference at *n+1* sampling point can be estimated at *n* sampling point and calculated from following equation.

$$v_A^*[n+1] = R\frac{i_A^*[n+2]+i_A[n+1]}{2} + \frac{\lambda_A^*[n+2]-\lambda_A[n+1]}{T_s} \tag{4.14}$$

The calculated voltage reference is realized at *n+1* sampling point. In equation (4.14), T_s is a cycle of PWM carrier signal. Each term of equation (4.14) is calculated in accordance with following steps.

1) instantaneous current reference at *n+2* sampling point $i_A^*[n+2]$: through equation (4.2) and (4.12), the torque reference of A-phase $T_A^*[n+2]$ and $i_A^*[n+2]$ at θ_{est} $[n+2]$

estimated from running speed ω_{drv} can be calculated.

$$\begin{aligned} &\theta_{est}[n+2]=\theta[n]+\omega_{drv}\cdot 2\cdot T_s, \quad \tau_A^*[n+2]=\tau_A^*(\theta_{est}[n+2]) \\ &\Rightarrow i_A^*[n+2]=i_A^*(\tau_A^*[n+2],\theta_{est}[n+2]) \end{aligned} \tag{4.15}$$

2) current at $n+1$ sampling point $i_A[n+1]$: assuming that the real current at $n+1$ is following well the reference current $i_A^*[n+1]$, it can be obtained by,

$$i_A[n+1]\approx i_A^*[n+1] \tag{4.16}$$

3) the flux linkage reference at $n+2$ sampling point $\lambda_A^*[n+2]$: by using equation (4.9) and the current reference obtained from equation (4.15), it can be given in,

$$\lambda_A^*[n+2]=\lambda_A(i_A^*[n+2],\theta_{est}[n+2]) \tag{4.17}$$

4) the flux linkage at $n+1$ sampling point $\lambda_A[n+1]$: by using the flux linkage at n sampling point $\lambda_A[n]$ and the flux linkage calculation by equation (4.6), it can be computed by,

$$\lambda_A[n+1]=\lambda_A[n]+T_s\left(v_A^*[n]-R\frac{i_A^*[n+1]+i_A[n]}{2}\right). \tag{4.18}$$

Through PWM voltage control with the reference applied voltage calculated by equation (4.13) and the magnetizing curves model in equation (4.9)[38][48][49], the real phase current can track the reference profile. The RMS current control error is minimized to 0.189[A_{rms}], which is about one fourth of the error when hysteresis controller is used[38].

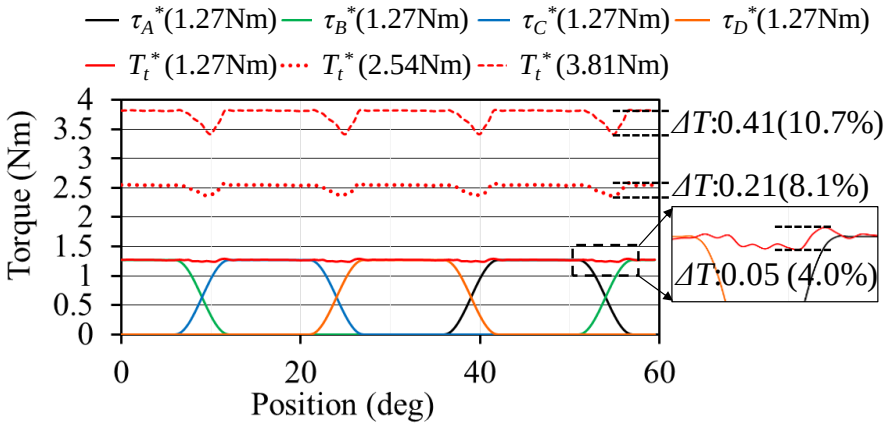

Figure 4.10 Torque ripple ΔT in different load conditions, 1.27Nm (100%), 2.54Nm (200%) and 3.81Nm (300%) at 100r/min.

4.5 Review of torque ripple minimization results in the conventional method

In this section, through the 2D-FEA, the problem that the torque ripple increases with the increase in the load torque, and its reason is examined.

4.5.1 Problem in the conventional method

As a weak point, the conventional method did not work well in some operating condition. As an example, experimental studies using a three-phase SRM with 12/8 poles configuration demonstrated that torque ripple under high load condition increased at the overlapping region in which adjacent two phases were simultaneously energized [49].

Similar simulation studies using the four-phase test motor used in this study are conducted. Figure 4.10 illustrates instantaneous torque waveforms under the conventional method computed by 2D-FEA (JMAG-Designer, ver. 17.0). The value in the bracket ( ) means a

torque ripple factor defined by the ration between a torque fluctuation ΔT and an average torque command T_t^*. In common with the behavior mentioned above, it can be found that the torque ripple at 200% load condition (2 times of the rated torque 1.27Nm) is much bigger than that at 100% load condition.

4.5.2 Detailed analysis of the reason of the problem

In order to reveal the reason of the increase in torque ripple mentioned above, theoretical considerations and further magnetic field analysis using 2D-FEA are conducted. At the overlapping region, the magnetic flux linkage of one phase is affected by mutual flux induced by adjacent exciting phase. In the case that the *D*- and *A*-phase are simultaneously energized in the overlapping region, the total flux linkage can be expressed as,

$$\lambda_A(i_A, i_D, \theta) = \lambda_{AA}(i_A, i_D, \theta) + \lambda_{AD}(i_A, i_D, \theta) \tag{4.19}$$

where, λ_{AA} is self-induced flux linkage in A-phase, λ_{AD} is flux linkage in *A*-phase mutually-induced by *D*-phase. The reason why λ_{AA} and λ_{AD} are function of i_D and i_A, respectively, is because of cross coupling effect arising from magnetic saturation. This results in that the magnetic co-energy of *A*-phase W_{mA}' is affected by λ_{AD}. By rearranging equation (4.10), the magnetic co-energy W_{mA}' considering the mutual coupling effect is given in following fashion.

$$W_{mA}' = \int_0^{i_A} \lambda_{AA}(i_A, i_D, \theta) di_A + \frac{1}{2}\int_0^{i_A} \lambda_{AD}(i_A, i_D, \theta) di_A \tag{4.20}$$

Since the conventional method has no consideration on the mutual coupling effect, *T*-θ-*i* model as well as the magnetic co-energy calculation include errors for those in the real machine. Figure 4.11 shows the simulated magnetizing curves of A-phase without/with D-phase current as the adjacent phase excitation. It can be seen from the figure that the

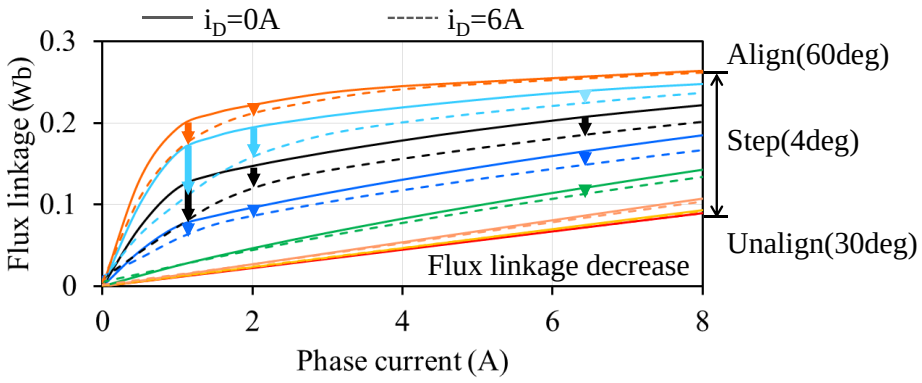

Figure 4.11 Magnetizing curves of A-phase considering mutual coupling effect by D-phase through 2D-FEA

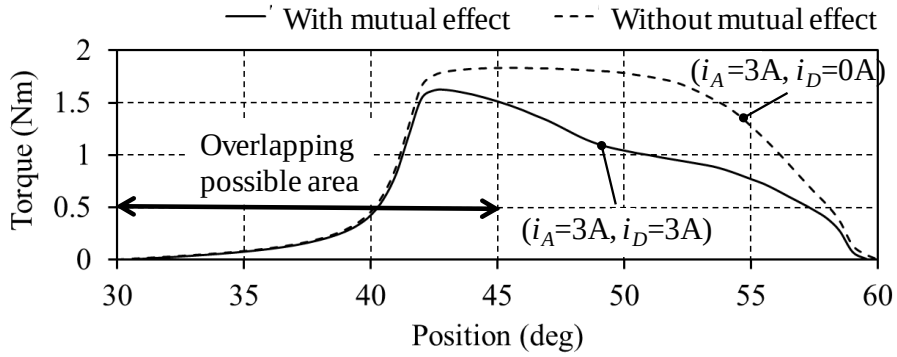

Figure 4.12 Stiffness characteristic of A-phase with and without considering mutual coupling effect by D-phase.

magnetizing curves of A-phase under D-phase excitation with 6Amps are obviously affected by the mutual coupling effect. As a consequence, the variance of the magnetic co-energy for the position displacement $\Delta\theta$ at a certain rotor position decreases due to the mutual coupling effect, resulting in torque reduction. Figure 4.12 demonstrates the stiffness characteristic of A-phase with/without taking into account of the mutual coupling computed by 2D-FEA. To

consider the mutual coupling effect on the produced torque, both A- and D-phase currents are simultaneously fed and set to 3Amps as an example. As can be seen from the figure, the torque produced by A-phase in the possible overlapping region from 30 to 45degrees decreases due to the influence of the mutual coupling effect by D-phase. This decrease in the torque is found in figure 4.10 as the torque dip around 40degrees.

4.6 Epilogue

In this chapter, the conventional current profiling control method for torque ripple minimization was explained. It was revealed that the torque ripple in the current overlapping region increased at high load condition. Through 2D-FEA, it was also revealed that the torque ripple occurred because the phase torque was affected by the mutual magnetic flux produced by adjacent phase. To overcome this issue, the torque ripple minimization method considering mutual coupling effect will be proposed in next chapter.

Chapter5
Torque ripple minimization control based on magnetizing curves model considering mutual coupling

5.1 Prologue

In this chapter, a modified current profiling control taking into account of mutual coupling is proposed. This control is based on the current tracking control of target current profile obtained from modified i-T-θ model and torque contour function considering mutual coupling. Firstly, modified λ-i-θ and modified T-i-θ models considering mutual coupling effect are derived from magnetizing curves data computed by 2D-FEA. By using the modified T-i-θ model, modified i-T-θ model can be obtained. The modified current profile generator that is composed of the modified i-T-θ model and the torque contour function produces instantaneous current reference profile. The validity of the modified current profiling control is demonstrated by comparison with calculation results and simulation results by 2D-FEA. In order to prove the validity of this modified current profiling control by experiment, a way how to measure the magnetizing curves taking account of mutual coupling effect is explained. Finally, experimental studies using the test motor demonstrate that the resultant torque ripple factor under the proposed control are minimized less than 5% at any load conditions up to 200% of the rated torque.

5.2 Torque ripple minimization by using *T-θ-i* model considering mutual coupling effect

In this section, how to derive *T-i-θ* model and modified *i-T-θ* model from the magnetizing curves data considering mutual coupling computed by 2D-FEA is described. Then, how to obtain modified torque contour function taking account of mutual coupling is explained. By using modified *i-T-θ* model and modified torque contour function, calculation process of target current profile for achieving flat torque is mentioned. Through 2D-FEA, the validity of the modified current profile generator is simulated and evaluated from a viewpoint of torque ripple minimization control.

5.2.1 *T-θ-i* model considering mutual coupling effect

In order to minimize torque ripple, modified *T-θ-i* model taking account of mutual coupling effect is derived. For that, at first the magnetizing curves data containing the mutual coupling effect is needed. Figure 5.1 shows the magnetizing curves of A-phase including the mutual flux linkage induced by D-phase computed by 2D-FEA. For ease of seeing the figure, although only four cases of D-phase current with 0, 3, 6 and 8A are depicted, actually the computed data of D-phase current every 0.5A(=ΔI) step from 0 to the maximum 8A (=I_{max}) are used to derive the *T-θ-i* model. In addition, although the magnetizing curves data are computed for the different rotor position every interval $\Delta\theta$=0.5deg. from the aligned positon θ =0deg. to the next aligned position θ =60deg., only those for every 5deg. are shown in the

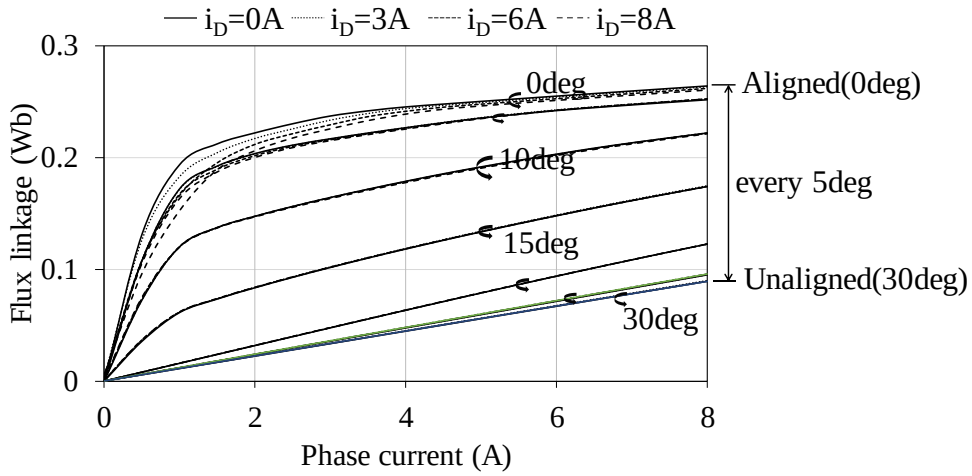

a) Magnetizing curves from 0 to 30 [deg]

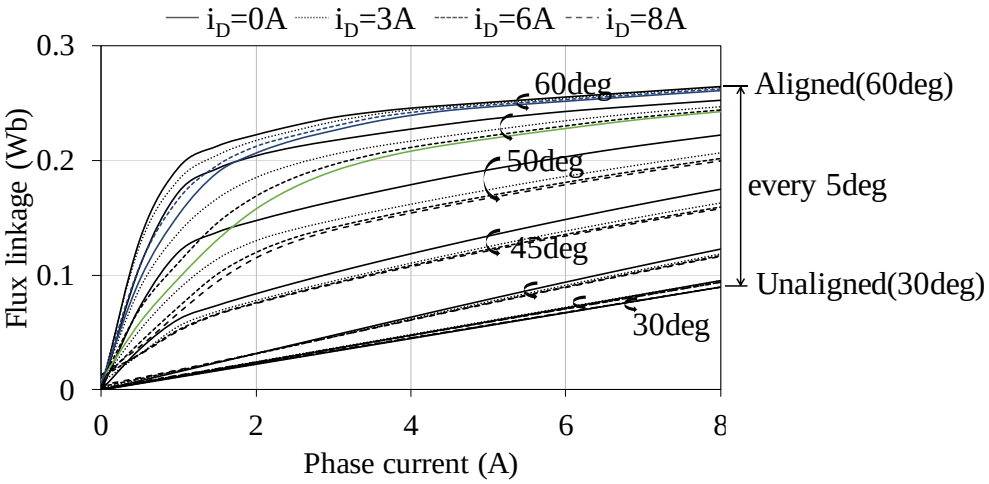

b) Magnetizing curves from 30 to 60 [deg]

Figure 5.1 Magnetizing curves of A-phase considering mutual coupling effect by D-phase excitation computed by 2D-FEA.

figure for an ease to see. As other additional explanation, A-phase current resolution is same with D-phase current.

By using curve fitting for the magnetizing curve under a given constant D-phase current i_{Dj} at a given fixed rotor position θ_x, the flux linkage λ_A can be expressed by a polynomial equation of A-phase current i_A and given in,

$$\lambda_A(i_A)\Big|_{\theta=\theta_x,\, i_D=I_{Dj}(\text{const.})} = \sum_{n=0}^{n_{\max}} L_n(I_{Dj})\Big|_{\theta=\theta_x} \cdot i_A^n \tag{5.1}$$

where, n_{max} again denotes the highest order of polynomial equation. Note that different from equation (4.7) the current order n starts from zero. $L_0(i_{Dj})$ means a mutual flux linkage induced by D-phase current i_{Dj} under no A-phase current excitation. Repeating this process for different level of D-phase current every ΔI from 0 to I_{max}, one can obtain a set of following equations.

$$\left.\begin{aligned}
\lambda_A(i_A)\Big|_{\theta=\theta_x,\, i_D=0(\text{const.})} &= \sum_{n=0}^{n_{\max}} L_n(0)\Big|_{\theta=\theta_x} \cdot i_A^n \\
\lambda_A(i_A)\Big|_{\theta=\theta_x,\, i_D=\Delta I(\text{const.})} &= \sum_{n=0}^{n_{\max}} L_n(\Delta I)\Big|_{\theta=\theta_x} \cdot i_A^n \\
&\vdots \\
\lambda_A(i_A)\Big|_{\theta=\theta_x,\, i_D=I_{\max}(\text{const.})} &= \sum_{n=0}^{n_{\max}} L_n(I_{\max})\Big|_{\theta=\theta_x} \cdot i_A^n
\end{aligned}\right\} \tag{5.2}$$

Taking notice of coefficients appeared as the first terms in equation (5.2) such as $L_0(0)$, $L_0(\Delta I)$, …, and $L_0(I_{max})$ and plotting them with respect to the D-phase current, the curve can be obtained, which draws a relationship between the coefficient L_0 and the D-phase current i_D. Applying a curve fitting to this curve, the following equation can be derived.

$$L_0(i_D)\Big|_{\theta=\theta_x} = \sum_{m=0}^{m_{\max}} L_{0m}\Big|_{\theta=\theta_x} \cdot i_D^m \tag{5.3}$$

Next, repeating the same process above for different rotor position every interval $\Delta\theta$ from the aligned to the next aligned positions, one can obtain a set of following equations.

$$\left.\begin{aligned} L_0(i_D)\Big|_{\theta=\theta_{aligned}} &= \sum_{m=0}^{m_{\max}} L_{0m}\Big|_{\theta=\theta_{aligned}} \cdot i_D^m \\ L_0(i_D)\Big|_{\theta=\theta_{aligned}+\Delta\theta} &= \sum_{m=0}^{m_{\max}} L_{0m}\Big|_{\theta=\theta_{aligned}+\Delta\theta} \cdot i_D^m \\ &\vdots \\ L_0(i_D)\Big|_{\theta=\theta_{unaligned}} &= \sum_{m=0}^{m_{\max}} L_{0m}\Big|_{\theta=\theta_{unaligned}} \cdot i_D^m \\ &\vdots \\ L_0(i_D)\Big|_{\theta=\theta_{aligned}} &= \sum_{m=0}^{m_{\max}} L_{0m}\Big|_{\theta=\theta_{aligned}} \cdot i_D^m \end{aligned}\right\} \tag{5.4}$$

Taking notice of coefficients appeared as the first terms in equation (5.4) such as $L_{00}|_{\theta=\theta aligned}$, $L_{00}|_{\theta=\theta aligned+\Delta\theta}$, …, $L_{00}|_{\theta=\theta unaligned}$, …, and $L_{00}|_{\theta=\theta aligned}$ and plotting them with respect to the rotor position, one can obtain the spatial distribution of coefficient L_{00} is modeled by DFT and given in

$$L_{00}(\theta) = \sum_{k=0}^{k_{\max}} L_{00k} \cos(k\alpha\theta + \phi_k) \tag{5.5}$$

where, L_{00k} and $k_{\max}$ denote the coefficients and the highest order of Fourier cosine series expansion. The difference from equation (4.8) can be recognized that the phase angle ϕ_k exists. Repeating the same process above for the different level of D-phase current every ΔI from 0 to I_{max} and the different rotor position every interval $\Delta\theta$ from the aligned to the next aligned

positions, the magnetizing curves model considering the mutual coupling effect can be derived as,

$$\lambda_A(i_A,i_D,\theta)=\sum_{n=0}^{n_{\max}}\left[\sum_{m=0}^{m_{\max}}\left[\sum_{k=0}^{k_{\max}}L_{nmk}\cos(k\alpha\theta+\phi_k)\right]\cdot i_D^m\right]\cdot i_A^n \tag{5.6}$$

This equation is λ-i-θ model considering the mutual coupling effect (here after, named as modified λ-i-θ model). The order n_{max}, m_{max}, and k_{max} used in the polynomial equation are set to 10, 10, and 60, respectively. In order to calculate phase torque model, an expression of magnetic co-energy taking account of the mutual coupling effect has to be derived using the modified λ-i-θ model. Magnetic co-energy of A phase can be calculated by using equation (4.20). For that, however, self and mutual components of total flux linkage per phase must be separated. In this study, self and mutual components of total flux linkage per phase can be separated by using following equation(53).

$$\lambda_A(i_A,i_D,\theta)=\lambda_A(i_A,0,\theta)+\lambda_{AD}(i_A,i_D,\theta) \tag{5.7}$$

In this equation, assuming that A-phase magnetic flux linkage $\lambda_A(i_A,0,\theta)$ under single phase excitation of A-phase can be regarded as self-flux linkage $\lambda_{AA}(i_A, i_D, \theta)$, mutual flux linkage-$\lambda_{AD}$ is calculated by using the equation $\lambda_{AD}(i_A, i_D, \theta)=\lambda_A(i_A, i_D, \theta)-\lambda_A(i_A, 0, \theta)$. Then, the magnetic co-energy can be derived as following fashion(55).

$$\begin{aligned}W_{mA}'(i_A,i_D,\theta)&=\int_0^{i_A}\lambda_{AA}(i_A,i_D,\theta)di_A+\frac{1}{2}\int_0^{i_A}\lambda_{AD}(i_A,i_D,\theta)di_A\\&=\int_0^{i_A}\lambda_A(i_A,0,\theta)di_A+\frac{1}{2}\int_0^{i_A}\left(\lambda_A(i_A,i_D,\theta)-\lambda_A(i_A,0,\theta)\right)di_A\end{aligned} \tag{5.8}$$

By using the magnetic co-energy W_{mA}' expression above, the instantaneous torque expression of A-phase under D- and A-phase simultaneous excitation can be deduced as,

$$\tau_A(i_A, i_D, \theta) = \frac{\partial w'_{mA}(i_A, i_D, \theta)}{\partial \theta}. \tag{5.9}$$

The *T-θ-i* model of A-phase under two-phase excitation is calculated from equation (5.9). Similarly, the *T-θ-i* model of D-phase under two-phase excitation is calculated from following equation.

$$\tau_D(i_D, i_A, \theta) = \frac{\partial w'_{mD}(i_D, i_A, \theta)}{\partial \theta} \tag{5.10}$$

Based on the *T-θ-i* model, *i-T-θ* model can be expressed as a polynomial equation with two variables using same procedure for deriving the modified *λ-i-θ* model. For example, the *i-T-θ* model of A-phase is given in following fashion.

$$i_A(\tau_A, i_D, \theta) = \sum_{n=0}^{n_{\max}} \left[\sum_{m=0}^{m_{\max}} K_{nm}(\theta) \cdot {i_D}^m \right] \cdot {\tau_A}^n \tag{5.11}$$

Where, $K_{nm}(\theta)$ is the spatial coefficient distribution with respect to torque order n and D-phase current order m. $n_{\max}$ and $m_{\max}$ denote the highest order of torque order n and D-phase current order m. Thus, once the instantaneous torque reference in A-phase τ_A^* at the detected rotor position is determined by equation (4.2), the instantaneous current profile i_A^* considering the mutual coupling effect by D-phase current can be computed by equation (5.11). Assuming that the stator and rotor structures are symmetric, the same procedure can be applied to other phases B, C and D to compute instantaneous current profile for each phase just considering 15degrees phase shift.

However, as can be easily supposed, there is also a coupling in the calculation of the target current profile per phase in the current overlapping region, which causes a problem how to individually determine the target current profiles for adjacent two phases. Take the case of

the current overlapping region with D- and A-phase. The current profiles of adjacent two phases i_D^* and i_A^* for the given target torque per phase τ_A^* and τ_D^* can be calculated from,

$$i_D^* = i_D\left(\tau_D^*, i_A^*, \theta\right) \quad , \quad i_A^* = i_A\left(\tau_A^*, i_D^*, \theta\right) \quad . \tag{5.12}$$

Needless to say, the A-phase current reference profile is required for determining the D-phase current reference profile and vice versa. Therefore, one phase current profile of two-phase current profiles has to be fixed prior to determine the other. In this study, the D-phase current profile is preferentially determined by using the conventional method. This is because the D-phase is outgoing phase in accordance with commutation sequence from D-phase to A-phase for normal rotation (clockwise direction). The D-phase current profile can be temporarily calculated under no excitation in A-phase and given in,

$$i_D^* = i_D\left(\tau_D^*, 0, \theta\right). \tag{5.13}$$

On the other hand, the total torque τ_t, which is expressed as a sum of torque produced from the A-phase and that produced from the D-phase in the overlapping region, can be expressed by using equations (5.9) and (5.10) and as in following expression.

$$\tau_t\left(i_A, i_D, \theta\right) = \tau_A\left(i_A, i_D, \theta\right) + \tau_D\left(i_D, i_A, \theta\right) \tag{5.14}$$

In this study, this is called as modified *T*-θ-*i* model. Figure 5.2(a) shows the calculated curves that presents the total torque τ_t with respect to i_A, i_D and θ under two-phase excitation. For an ease to see, although only five cases of D-phase current with 0, 2, 4, 6 and 8A are dealt with, actually the computed data of D-phase current every ΔI=0.5A from 0 to the maximum 8A (=I_{max}) are used to derive the modified *i*-*T*-θ model as explained later. Figure 5.2(b) demonstrates a comparison of between the total torque τ_t calculated by the modified

T-θ-i model and that computed by 2D-FEA under two-phase excitation with $i_A = i_D = 3A$ as an example. From this figure, it is found that the total torque τ_t calculated from the

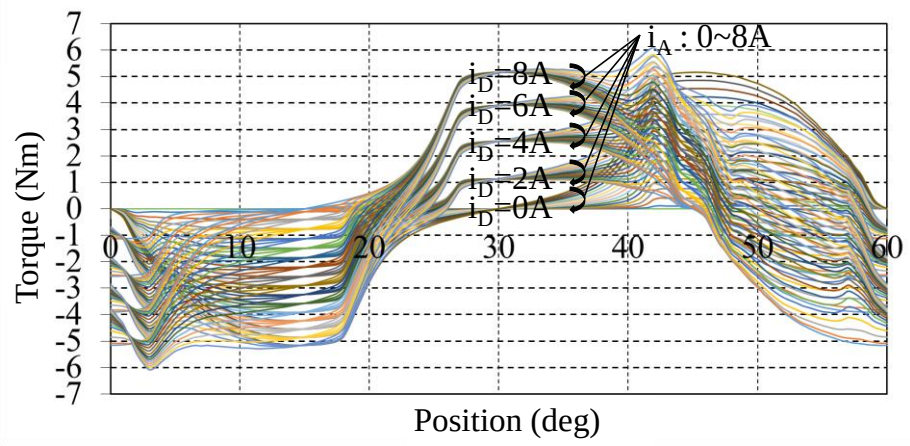

(a) calculated total torque curves from the modified *T-θ-i* model

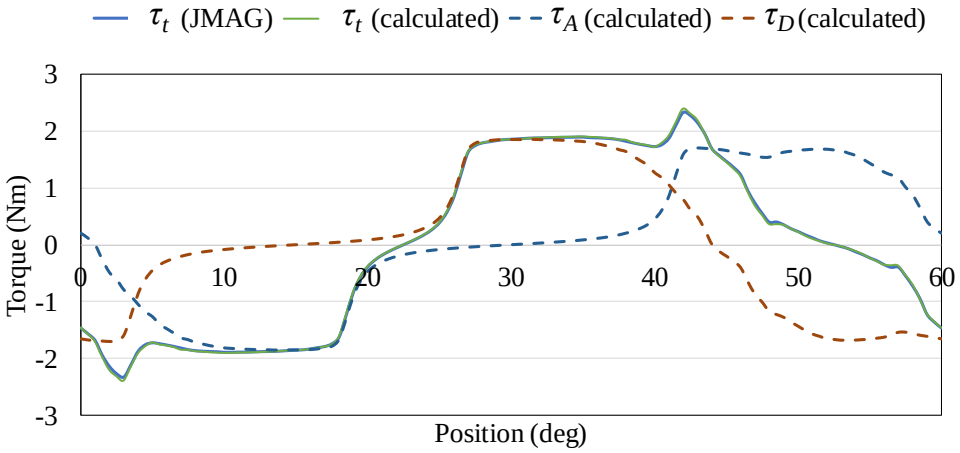

(b) torque calculated from the modified *T-θ-i* model and computed by 2D-FEA at $i_A = i_D = 3A$.

Figure 5.2 *T-θ-i* curves considering mutual coupling effect between A- and D-phase obtained from the modified *T-θ-i* model.

modified *i-T-θ* model agrees well with that computed by 2D-FEA. Moreover, the validation of equation (5.14) is also confirmed by the fact that the sum of torque produced from the A-phase and that produced from the D-phase in the overlapping region is good agreement with the total torque τ_t computed by 2D-FEA.

By using curve fitting and DFT, the A-phase current i_A as modified *i-T-θ* model can be expressed by a polynomial equation of D-phase current i_D and total torque τ_t and given in,

$$i_A(\tau_t, i_D, \theta) = \sum_{n=0}^{n_{\max}} \left[\sum_{m=0}^{m_{\max}} K_{nm}(\theta) \cdot {i_D}^m \right] \cdot {\tau_t}^n . \tag{5.15}$$

In this study, n_{max} and m_{max} as the order of the polynomial equation (5.15) are set 7 and 10, respectively. Once determine the D-phase current profile i_D^* in the overlapping region from equation (5.13), the A-phase current profile, which can produce a given average torque command T_t^* in the overlapping region, can be determined from equation (5.15) using $i_D = i_D^*$ and $\tau_t = T_t^*$.

5.2.2 Simulation of torque ripple minimization control employing the modified *i-T-θ* model

Through the modified *i-T-θ* model and the torque contour function, instantaneous current profile for each phase can be calculated. Now, take the case of the rated torque condition. As mentioned section 5.2.1, in current overlapping region I shown in figure 5.3, the D-phase current profile is firstly determined by employing the conventional method. On the contrary,

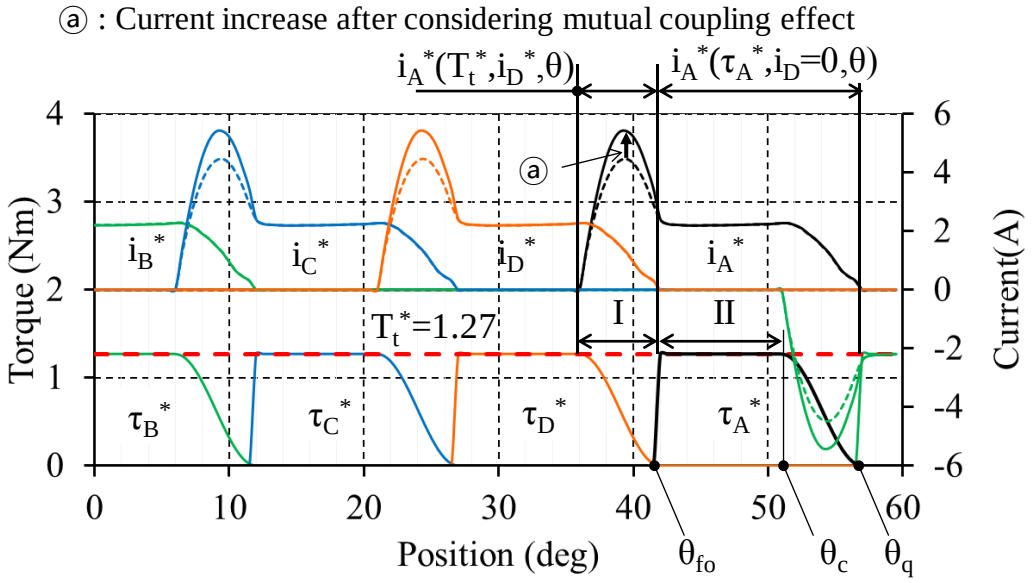

Figure 5.3 Current profile produced via torque contour function in the proposed method.

the A-phase current profile is determined from equation (5.15), which results in the total torque T_t^* considering the mutual coupling effect from the D-phase current at detected rotor position. Compared with the conventional method, the A-phase current i_A^* is modified as shown in ⓐ for torque ripple minimization taking into account of mutual coupling effect. In single phase excitation region II from θ_{fo} to θ_c shown in the figure, the A-phase current reference profile i_A^* can be calculated so as to produce the total torque T_t^* by only A phase. Subsequently, at next commutation from A-phase to B-phase, the same procedures above are repeated by replacing D-phase with A-phase and A-phase to B-phase including current polarity change to avoid instantaneous torque dip[56].

Figure 5.4 demonstrates the 2D-FEA simulation results of torque ripple minimization under 100%, 200% and 300% reference torque conditions at the motor speed 100[r/min]. In

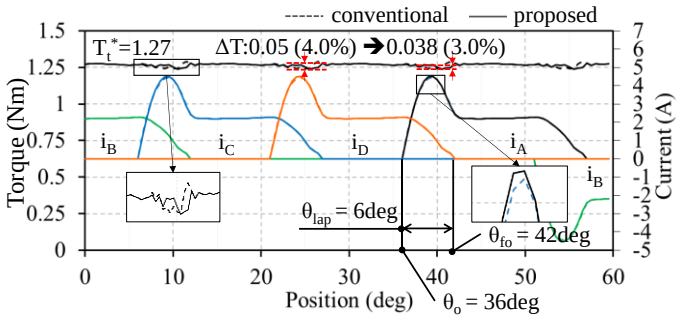

(a) 100% (1.27Nm) load

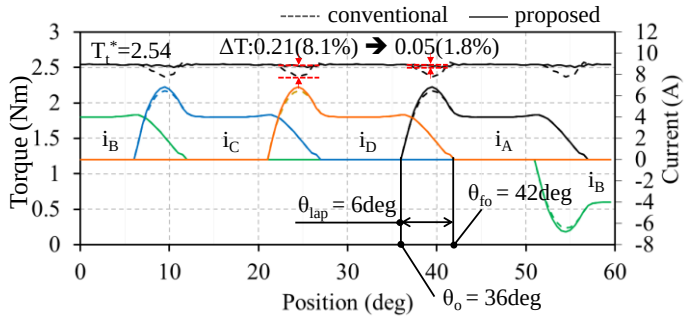

(b) 200% (2.54Nm) load

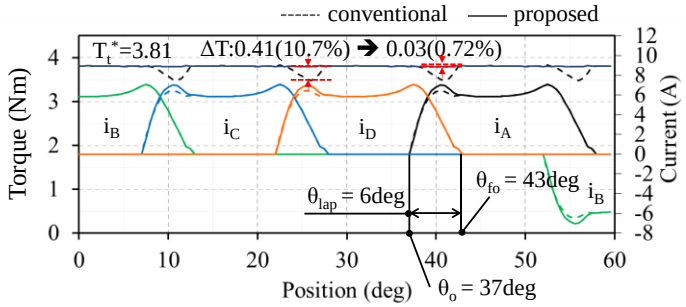

(c) 300% (3.81Nm) load

Figure 5.4 Comparisons of current reference profiles and instantaneous total torque under the conventional control method and the proposed control method.

the proposed method, all phase current reference profiles obtained from modified *i*-*T*-θ model and the torque contour function are used for the inputs to 2D-FEA. It is found from the figure that the proposed method well suppresses torque ripple in the current overlapping region I compared with the conventional method.

5.3 Measurement of magnetizing curves including mutual coupling effect and corresponding modified *i*-*T*-θ model

In this section, a procedure to measure magnetizing curves of the test motor considering the mutual coupling is described. For generating the current reference profile in accordance with the procedure explained in section 5.2, the modified *T*-θ-*i* model and *i*-*T*-θ model based on the measured magnetizing curves are derived. Simulations are conducted, in which the current reference profiles determined by them are applied to the real test motor, so that the effectiveness of the proposed control method is verified.

5.3.1 Procedure for magnetizing curves measurement

In order to apply the proposed current reference profile determination to the real test motor, measurement of the magnetizing curves is needed. Basically, the magnetic flux linkage under single phase excitation can be measured through pulsewise voltage excitation test shown in figure 4.4. However, the mutual coupling effect by adjacent phase excitation in the overlapping region have to be considered for minimizing torque ripple and therefore, other

measurement approach under two-phase excitation has to be come up with. To measure total flux linkage of A-phase taking into account of mutual flux produced by D-phase as an example, two kinds of measurements are required. One is to measure currents and voltages of both in A- and D-phase when applying pulsewise voltage to A-phase while D-phase current is controlled to be nonzero constant value. The other is to measure induced voltage of A-phase when applying pulsewise voltage to D-phase while keeping A-phase current to be zero. The reason why two measurements are needed is theoretically explained.

When both the A-phase current i_A and the D-phase current i_D are fed to the motor simultaneously, the total flux linkage of A-phase is divided into two terms as shown in equation (4.19) and can be rewritten in,

$$\lambda_A(i_A, i_D, \theta) = \lambda_{AA}(i_A, i_D, \theta) + M_{AD}(i_A, i_D, \theta) i_d \tag{5.16}$$

where M_{AD} is the mutual inductance between A-and D-phase. In this case, the voltage equation (4.6) of SRM is rewritten in following fashion.

$$v_A = Ri_A + \frac{d\lambda_{AA}}{dt} + \frac{dM_{AD}(i_A, i_D, \theta)}{dt} i_D + M_{AD}(i_A, i_D, \theta) \frac{di_D}{dt} \tag{5.17}$$

In the measurements, when the pulsewise voltage is applied to A-phase while keeping D-phase current i_D to be a given nonzero constant value, equation (5.17) can be rewritten in following fashion as di_D/dt=0.

$$v_A - Ri_A = \frac{d\lambda_{AA}}{dt} + \frac{dM_{AD}(i_A, i_D, \theta)}{dt} i_D \tag{5.18}$$

Taking integration of equation (5.18), following equation is obtained.

$$\int_0^t \left(v_A - Ri_A\right) dt = \lambda_{AA} + \int_0^t \left(\frac{dM_{AD}(i_A, i_D, \theta)}{dt} i_D \right) dt \tag{5.19}$$

By using a product rule of differential and di_D/dt=0, the integral term of equation (5.19) can be rewritten as following fashion.

$$\begin{aligned}\int_0^t (v_A - Ri_A)dt &= \lambda_{AA}(i_A, i_D, \theta) + \left[M_{AD}(i_A, i_D, \theta) i_D\right]_0^t - \int_0^t \left(M_{AD}(i_A, i_D, \theta) \frac{di_D}{dt} \right) dt \\ &= \lambda_{AA}(i_A, i_D, \theta) + \left[M_{AD}(i_A, i_D, \theta) i_D\right]_0^t \\ &= \lambda_{AA}(i_A, i_D, \theta) + M_{AD}(i_A, i_D, \theta) i_D - M_{AD}(0, i_D, \theta) i_D \\ &= \lambda_{AA}(i_A, i_D, \theta) + \lambda_{AD}(i_A, i_D, \theta) - M_{AD}(0, i_D, \theta) i_D \\ &= \lambda_A(i_A, i_D, \theta) - M_{AD}(0, i_D, \theta) i_D\end{aligned} \tag{5.20}$$

Now, the second term of the last row in equation (5.20) can be calculated from an equation below.

$$M_{AD}(0, i_D, \theta) i_D = \int_0^t v_A dt \Big|_{i_A=0} \tag{5.21}$$

As a result, the total flux linkage of A-phase taking into account of the mutual coupling can be obtained from equations (5.20) and (5.21) and given in,

$$\lambda_A(i_A, i_D, \theta) = \int_0^t (v_A - Ri_A)dt + \int_0^t v_A dt \Big|_{i_A=0} \tag{5.22}$$

According to equation (5.21), the magnetizing curves of A-phase considering the mutual coupling is derived via two step measurements as follows.

(1) First step measurement

At a given fixed rotor position θ, the pulsewise voltage v_A is applied to A-phase while keeping the D-phase current to be nonzero constant value. In this measurement, the D-phase current is controlled to be nonzero constant value by DC chopper with PI regulator. With the measurement of time responses of the pulsewise voltage v_A and resultant A-phase current i_A, one can calculate an integration of (v_A-Ri_A) and thus, the first term of equation (5.22) can be

obtained as a function of the A–phase current under the given constant D-phase current at the given fixed rotor position. Repeating the same measurement for a different level of constant value of the D-phase current and a different fixed rotor position from the aligned to the next aligned positions, one can obtain the first term of equation (5.22) as the function of i_A, i_D and θ, that is, $\lambda_A(i_A, i_D, \theta) - M_{AD}(0, i_D, \theta)i_D$.

(2) Second step measurement

At a given fixed rotor position θ, the pulsewise voltage v_D is applied to D-phase while keeping the A-phase to be zero. In this measurement, the A-phase is just in open circuit. As the A-phase current is zero, with the measurement of time responses of resultant D-phase current i_D and A-phase induced voltage v_A induced by the mutual flux flowing from D-phase, one can calculate an integration of v_A and thus, the second term of equation (5.22) can be obtained as a function of the D–phase current at the given fixed rotor position. Repeating the same measurement for a different fixed rotor position from the aligned to the next aligned positions, one can obtain the second term of equation (5.22) as the function of i_D and θ, that is, $M_{AD}(0, i_D, \theta)\, i_D$.

Finally, a sum of $\lambda_A(i_A, i_D, \theta) - M_{AD}(0, i_D, \theta)i_D$ obtained by the first step measurement and $M_{AD}(0, i_D, \theta)i_D$ obtained by the second step measurement provides us with $\lambda_A(i_A, i_D, \theta)$ as the magnetizing curves of A-phase considering the mutual coupling from the D-phase.

Now, take the case of the magnetizing curves of D-phase considering the mutual coupling from the A-phase. In this case, the equation corresponding to equation (5.16) can be rearranged as,

$$\lambda_D(i_D, i_A, \theta) = L_{DD}(i_D, i_A, \theta) + \lambda_{DA}(i_D, i_A, \theta) \tag{5.23}$$

where L_{DD} is the self-inductance of D-phase and λ_{DA} is flux linkage in D-phase mutually-induced by A-phase. the corresponding voltage equation in D-phase is given in following manner.

$$v_D - Ri_D = \frac{d\lambda_{DA}}{dt} + \frac{dL_{DD}(i_D, i_A, \theta)}{dt} i_D + L_{DD}(i_D, i_A, \theta) \frac{di_D}{dt} \tag{5.24}$$

If the same measurements mentioned above are conducted, that is, when the pulsewise voltage is applied to A-phase while keeping D-phase current i_D to be a given nonzero constant value, equation (5.24) can be rewritten in following fashion as di_D/dt=0.

$$v_D - Ri_D = \frac{d\lambda_{DA}}{dt} + \frac{dL_{DD}(i_D, i_A, \theta)}{dt} i_D \tag{5.25}$$

Taking integration of equation (5.25), following equation is obtained.

$$\int_0^t \left(v_D - Ri_D\right)dt = \lambda_{DA} + \int_0^t \left(\frac{dL_{DD}(i_D, i_A, \theta)}{dt} i_D \right)dt \tag{5.26}$$

Based on a product rule of differential and di_D/dt=0, the integral term of equation (5.26) can be rewritten as following fashion.

$$\int_0^t \left(v_D - Ri_D\right)dt = \lambda_D(i_D, i_A, \theta) - L_{DD}(i_D, 0, \theta) i_D \tag{5.27}$$

The second term of equation (5.27) can be calculated from an equation below.

$$L_{DD}(i_D, 0, \theta) i_D = \int_0^t \left(v_D - Ri_D\right)dt \Big|_{i_A=0} \tag{5.28}$$

As a result, the total flux linkage of D-phase taking into account of the mutual coupling can be obtained from equations (5.27) and (5.28) and given in,

$$\lambda_D(i_D, i_A, \theta) = \int_0^t \left(v_D - Ri_D\right)dt + \int_0^t \left(v_D - Ri_D\right)dt \Big|_{i_A=0} \tag{5.29}$$

From the equation above, it can be seen that with only an addition of a time response of the applied voltage in D-phase v_D as another measurement parameter to the first and the second steps in the measurement of the magnetizing curves of A-phase mentioned earlier, one can obtain $\lambda_D(i_D, i_A, \theta)$ as the magnetizing curves of D-phase considering the mutual coupling from the D-phase. This enables namely to measure simultaneously both the magnetizing curves of A- and D-phase under the two-step measurement. Moreover, this fact contributes to a reduction of a repeating number of the measurements as explained in next subsection.

5.3.2 Reduction of a repeating number of the measurements based on magnetic circuit symmetry

fBoth the first and second measurements have to be repeated for a different rotor position fixed every an interval $\Delta\theta$ from the aligned to the next aligned position. In order to ensure enough accuracy of DFT, the interval $\Delta\theta$ has to be as small as possible so that a repeating number of the measurements increases, resulting in increases of the measurement tasks and time. To reduce the repeating number of the measurements, a minimum range of rotor position to be measured for obtaining the magnetizing curves of A-phase considering the mutual coupling from the A-phase is examined considering magnetic circuit symmetry.

Figure 5.5 depicts cross sections of the test motor at distinctive two rotor positions from a viewpoint of magnetic circuit symmetry. In this figure, an origin of the rotor position, θ=0deg., is defined as the aligned position at which the center of rotor pole is aligned with the center of A-phase stator tooth. The two rotor positions for stator teeth of A- and D-phase are at line symmetry position with respect to an additional line drawn by red line in the figure.

At these two rotor position, one at 22.5 deg. and the other at 52.5deg., the following relationship between the A-phase and the D-phase flux linkages can be found.

$$\begin{aligned}\lambda_A(i_A = I_x, i_D = I_y, \theta = 22.5) &= \lambda_D(i_D = I_x, i_A = I_y, \theta = 22.5)\\ \lambda_D(i_D = I_x, i_A = I_y, \theta = 52.5) &= \lambda_A(i_A = I_x, i_D = I_y, \theta = 52.5)\end{aligned} \tag{5.30}$$

Where I_x and I_y are arbitrary current values. Figure 5.6 shows cross sections of the test motor at two rotor positions θ=52.5±$\Delta\theta$. In figure 5.6(a), ϕ_{AA} and ϕ_{AD} are self-induced flux of A-phase and mutual flux induced by D-phase. In figure 5.6(b), ϕ_{DD} and ϕ_{DA} are self-induced flux of D-phase and mutual flux induced by A-phase. With a line symmetry of magnetic circuit at the two rotor positions θ=52.5±$\Delta\theta$, the following relationship between the A-phase and the D-phase flux linkages can be observed.

$$\begin{aligned}\lambda_A(i_A = I_x, i_D = I_y, \theta = 52.5\text{-}\Delta\theta) &= \lambda_D(i_D = I_x, i_A = I_y, \theta = 52.5\text{+}\Delta\theta)\\ \lambda_D(i_D = I_y, i_A = I_x, \theta = 52.5\text{-}\Delta\theta) &= \lambda_A(i_A = I_y, i_D = I_x, \theta = 52.5\text{+}\Delta\theta)\end{aligned} \tag{5.31}$$

Similarly, at the two rotor positions θ=22.5±$\Delta\theta$, the following relationship between the A-phase and the D-phase flux linkages can be derived.

$$\begin{aligned}\lambda_A(i_A = I_x, i_D = I_y, \theta = 22.5\text{-}\Delta\theta) &= \lambda_D(i_D = I_x, i_A = I_y, \theta = 22.5\text{+}\Delta\theta)\\ \lambda_D(i_D = I_y, i_A = I_x, \theta = 22.5\text{-}\Delta\theta) &= \lambda_A(i_A = I_y, i_D = I_x, \theta = 22.5\text{+}\Delta\theta)\end{aligned} \tag{5.32}$$

As a result, the magnetic flux linkages of A- and D-phase are symmetric each other with respect to θ=22.5deg. and θ=52.5deg. For example, figure 5.7 illustrates the flux linkage distribution of A- and D-phases under their excitation with $i_A = i_D$ =3A with respect to the rotor position θ from the aligned to the next aligned positions. According to the symmetry of

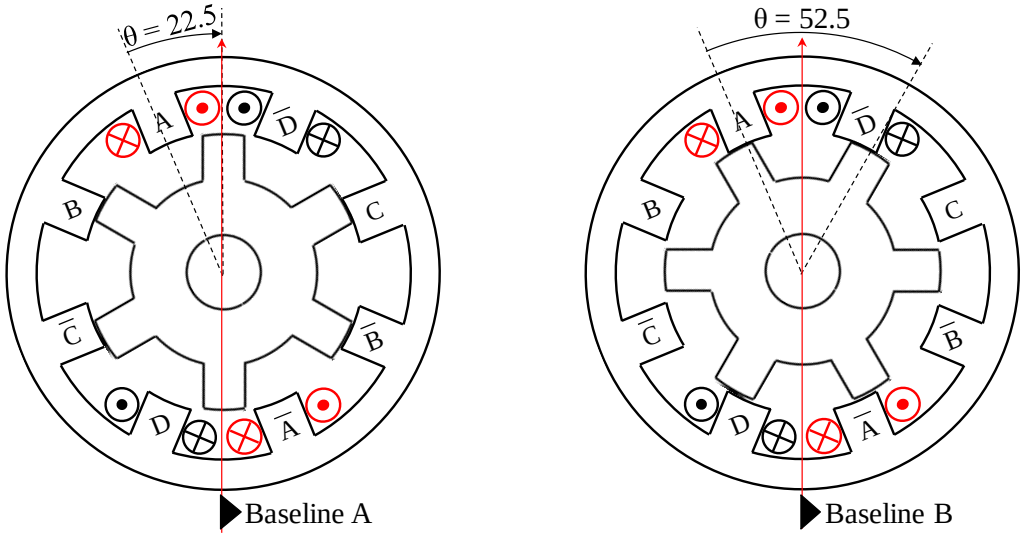

Figure 5.5 Sectional views of the test motor at rotor positions θ=22.5deg. and 52.5deg..

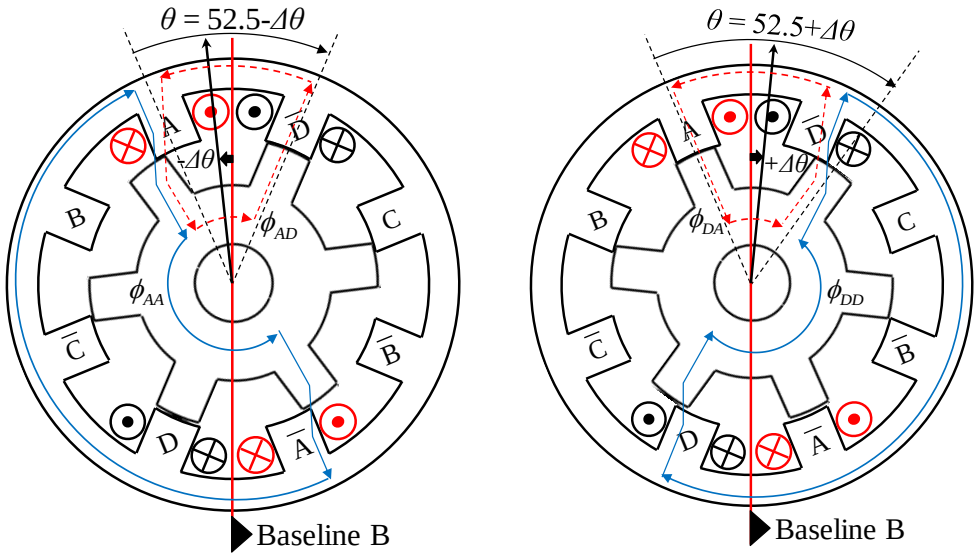

(a) -$\Delta\theta$ moving from 52.5 deg. (b) +$\Delta\theta$ moving from 52.5 deg.

Figure 5.6 Sectional views of the test motor at rotor positions θ=52.5±Δθdeg.

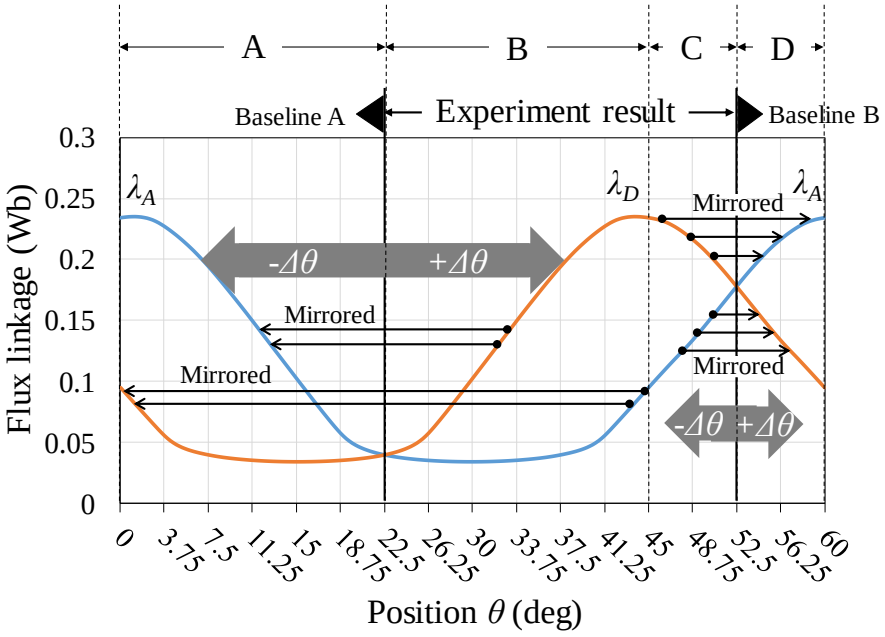

Figure 5.7 Flux linkage distributions of A-and D-phases under excitations in A- and D-phases with 3A.

flux linkage distribution shown in the figure, measured data of the D-phase flux linkages in the position range "B" from θ=22.5 to 45deg. can be mirrored as data of the A-phase flux linkages in the position range "A" from θ=22.5 to 0deg. in accordance with following relation.

$$\lambda_A(i_A = I_x, i_D = I_y, \theta) = \lambda_D(i_D = I_x, i_A = I_y, 45 - \theta) \tag{5.33}$$

Similarly, measured data of the D-phase flux linkages in the position range "C" from θ=52.5 to 45deg. can be mirrored as data of the A-phase flux linkages in the position range "D" from θ=52.5 to 60deg.(=0deg.) in accordance with following relations.

$$\lambda_A(i_A = I_x, i_D = I_y, \theta) = \lambda_D(i_D = I_x, i_A = I_y, 105 - \theta) \tag{5.34}$$

Consequently, from the measured magnetizing curves of A-and D-phase for the minimum range of rotor position between 22.5deg. to 52.5deg. the full magnetizing curves of A-phase from the aligned to the next aligned positions (0~60degrees) can be obtained. As it turned out, the measurement tasks and time can be successfully reduced.

5.3.3 Magnetizing curves measurements

For the measurements, test equipment is set up as shown in figure 5.8. To avoid position fluctuation when the pulsewise voltage is applied to the test motor at a given fixed position, the test motor is coupled with a stepping motor (Oriental Motors, UPH599HG2-B2, 0.0072deg/pulse) with a harmonic gear (Oriental Motors, gear ratio 1:100). In addition, a rigid direct coupling between the test motor shaft and the geared stepping motor shaft is employed. An high resolution rotary encoder (Tamagawa Seiki, TS5667N420, 131072 ppr, 0.0027deg/pulse) is attached to detect the rotor position. PE-Expert III (Myway Plus Corporation) is used as a controller to generate gate signals for the symmetric full bridge

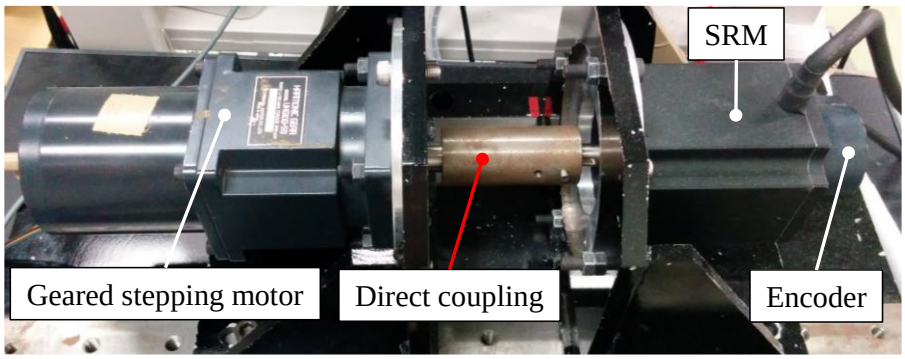

Figure 5.8 Experimental set up for magnetizing curves measurements.

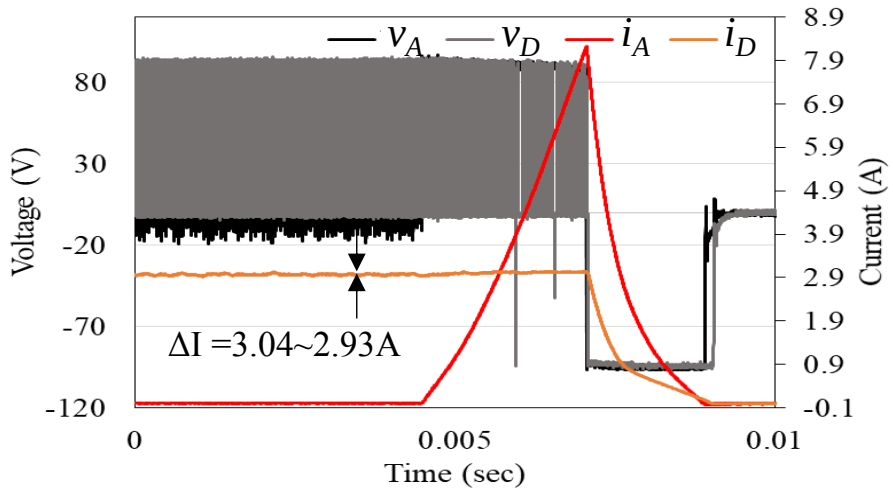

Figure 5.9 Measured voltages and currents in the first measurement under D-phase current with 3A constant.

converter with PWM frequency of 30kHz. Through the control of gate signals, the pulsewise voltage excitation and constant current control are executed. For the constant current control, two kinds of methods are considered. First one is hysteresis control. Other is feedback PI (proportional integral) control. One of them, PI control method is selected as constant current controller because the current variation is well suppressed less than 0.1[A] with respect to the reference value even though the pulseiwse voltage is applied as can be seen in figure 5.9. DC-link voltage is selected as 100V because the D-phase current fluctuates every PWM cycle when the rated DC-link voltage of 283V is used. According to the fixed position change, PI gain is tuned because inductance of the energizing phase varies with rotor position. In addition, to minimize measurement error of magnetizing curves due to residual flux of electromagnetic steel, degaussing processes for A- and D-phase are executed for every curve

measurement as shown in figure 5.10. From the experiment, it can be found that degaussing of D-phase after degaussing of A-phase is sequentially effective and it is efficient to finish with a small current lower than 0.1[A] at the end of the degaussing process. Figure 5.11 shows magnetizing curves with/without the degaussing process. From the figure, it is found that the magnetizing curve with the degaussing is larger than that without the degaussing. It is theoretically true because the magnetizing curve without the degaussing is affected by more severe magnetic saturation because the residual flux acts as an additional offset flux.

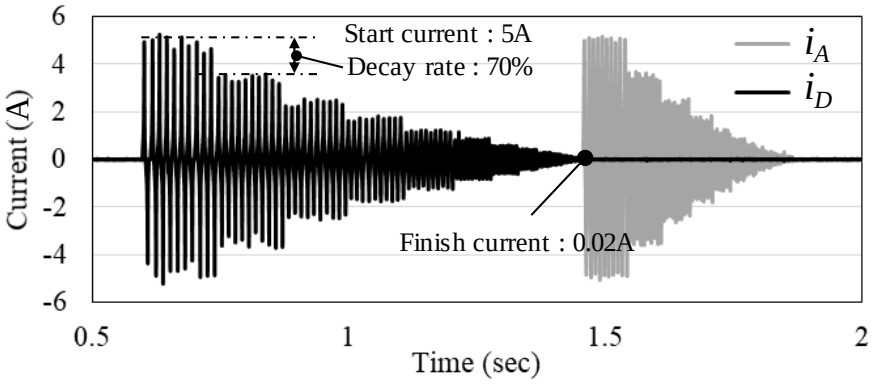

Figure 5.10 Degaussing process for A- and D-phase.

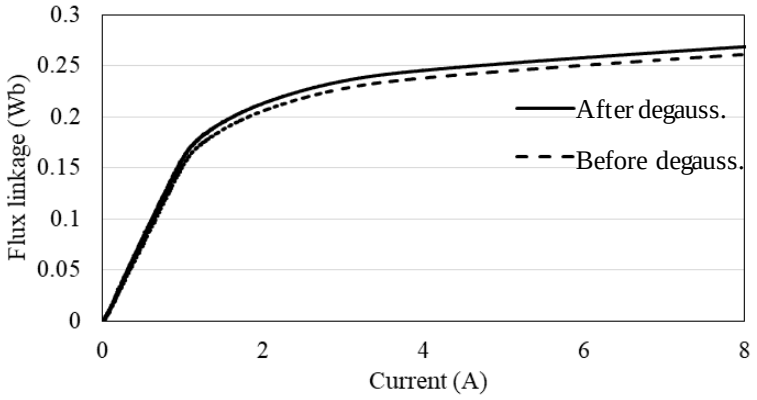

Figure 5.11 Variance of magnetizing curve with/without the degaussing.

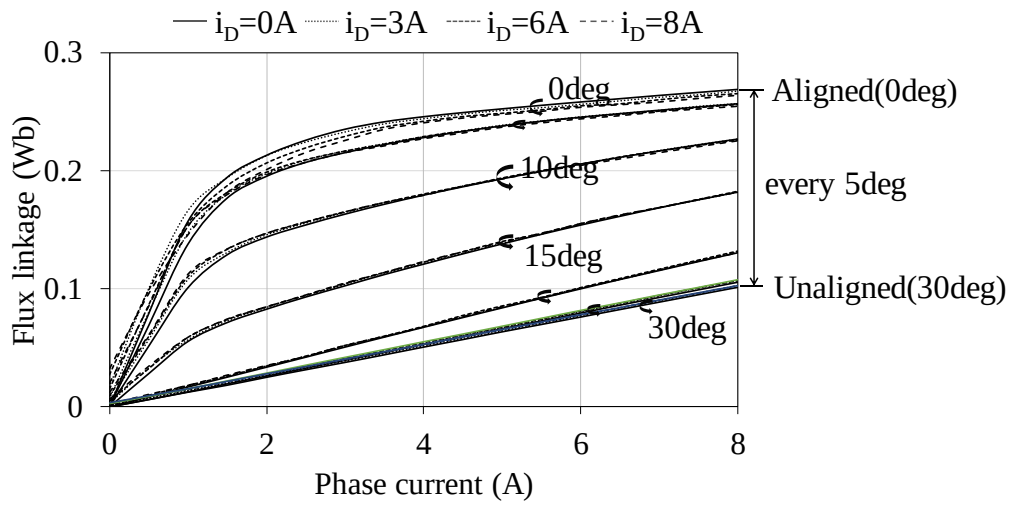

c) Magnetizing curve from 0 to 30 [deg]

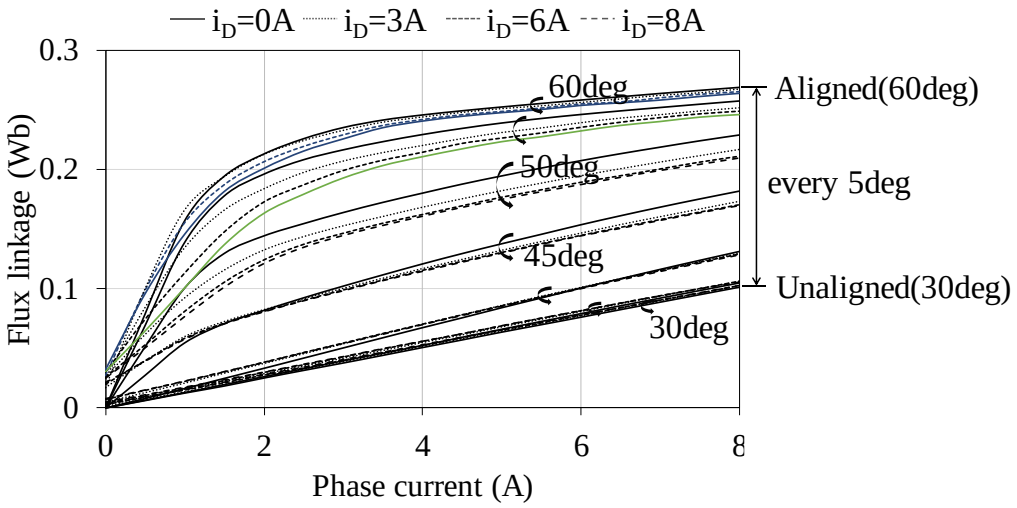

d) Magnetizing curve from 30 to 60 [deg]

Figure 5.12 Measured magnetizing curves of A-phase considering mutual coupling effect of D-phase.

Figure 5.12 demonstrates the measured magnetizing curves of A-phase considering mutual coupling effect from D-phase. As the orders in the polynomial equation (5.6), n_{max} , m_{max} and k_{max} are determined as 10, 10 and 19, respectively. By using these magnetizing curves and equations (5.6), (5.8), (5.9), (5.10) and (5.14), the modified *T-θ-i* model of the real test motor is obtained and show in figure 5.13.

5.3.4 *i-T-θ* model obtained from the measurements and simulation results of torque ripple minimization

From the modified *T-θ-i* model of the real test motor, the *i-T-θ* model based on the measurement results can be derived by using equation (5.15). Through this *i-T-θ* model, the target current profiles to produce the total target torque are calculated based on the torque

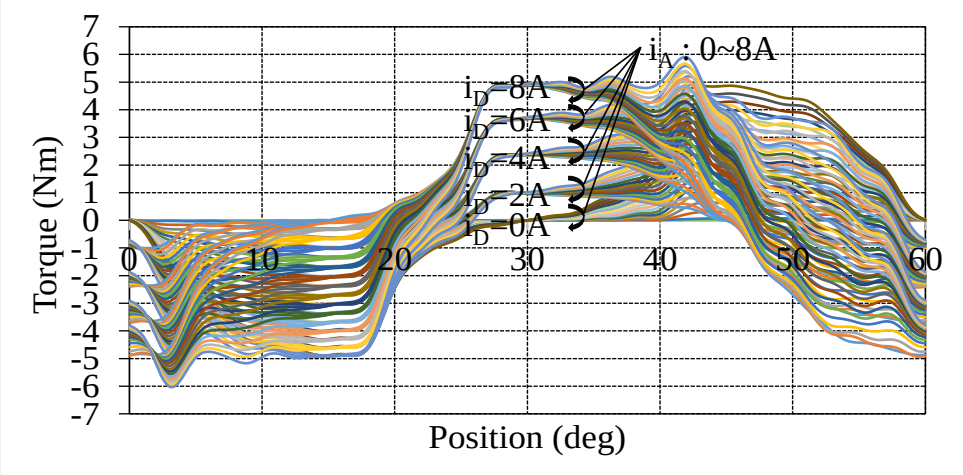

Figure 5.13 *T-θ-i* curves considering the mutual coupling effect between A- and D-phase derived from the calculation using the measured magnetizing curves.

contour function. Figure 5.14 shows the torque calculated from the current reference profiles under the conventional method and the proposed method. It is found from the figure that the torque ripple is reduced effectively by the proposed method under both 100% and 200% of the rated torque conditions. At these conditions, the mutual coupling effect is relatively small because the current overlapping region is finished before the stator teeth of A-phase and rotor poles start to overlap. In other words, the current overlap finish angle θ_{fo} is 42 degrees which is same with the teeth overlapping start angle.

In this study, to evaluate the torque ripple reduction performance when the mutual coupling effect is strong, the experiments in control parameters with θ_{fo} = 44deg. and θ_{lap} = 6deg. are conducted later. Figure 5.15 shows the corresponding instantaneous torque profile calculated from the current reference profiles under the conventional method and the proposed method. It is confirmed that the torque ripple is reduced effectively by the proposed method under both 100% and 200% of the rated torque conditions. As a result, regardless of the degree of mutual coupling, it is safely to say that the torque ripple can be minimized effectively by the proposed method.

Now, again repeating the author's pointed out in Ref. (54) that *"the accuracy of this method for practical SRM, depends on how close to the FEA data, matches with the real SRM"*[54]. From this viewpoint, it can be observed from the figure 5.16 that the direction of torque fluctuation in the current overlapping region under some load condition computed by 2D-FEA is completely different from that calculated by using the measured magnetizing curves, i.e., that in the real test motor. For example, under the rated torque condition, the direction of torque fluctuation of the real test motor is positive with respect to the target

torque, but that computed by 2D-FEA is negative. Therefore, how to close to the FEA data so as to match well with the real motor is still indispensable task.

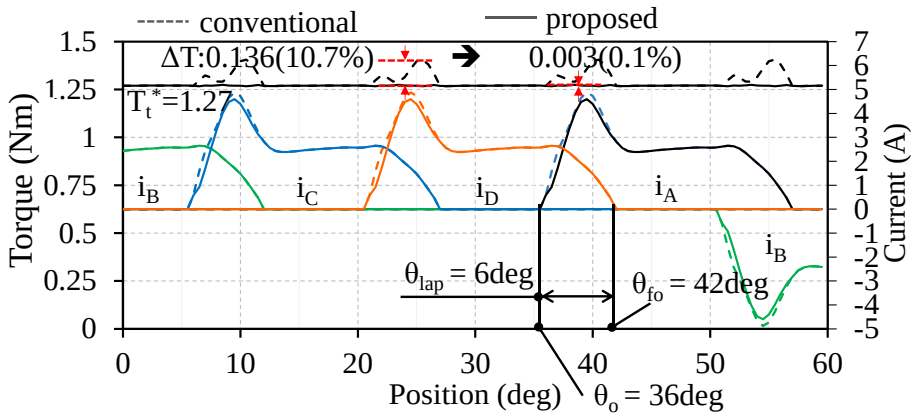

(a) 100% (1.27Nm) load

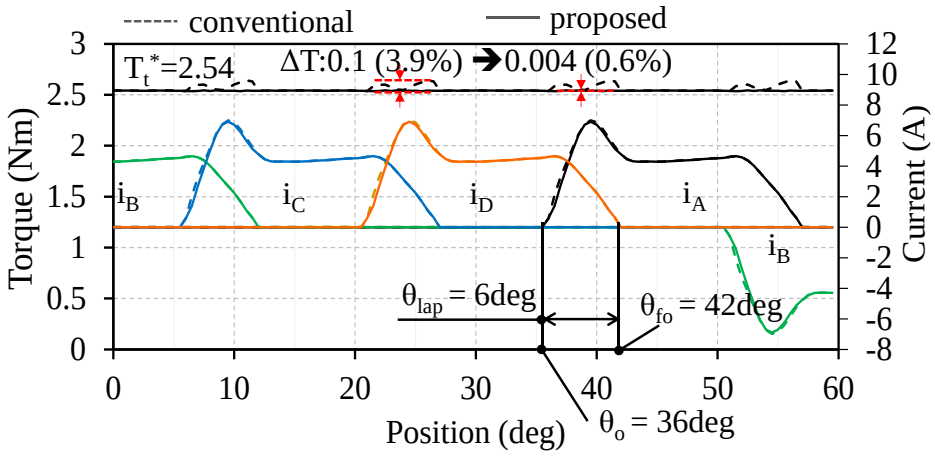

(b) 200% (2.54Nm) load

Figure 5.14 Calculated torque for current reference profiles obtained from the conventional and the proposed methods under different load conditions at θ_o = 36[deg], θ_{fo} = 42[deg].

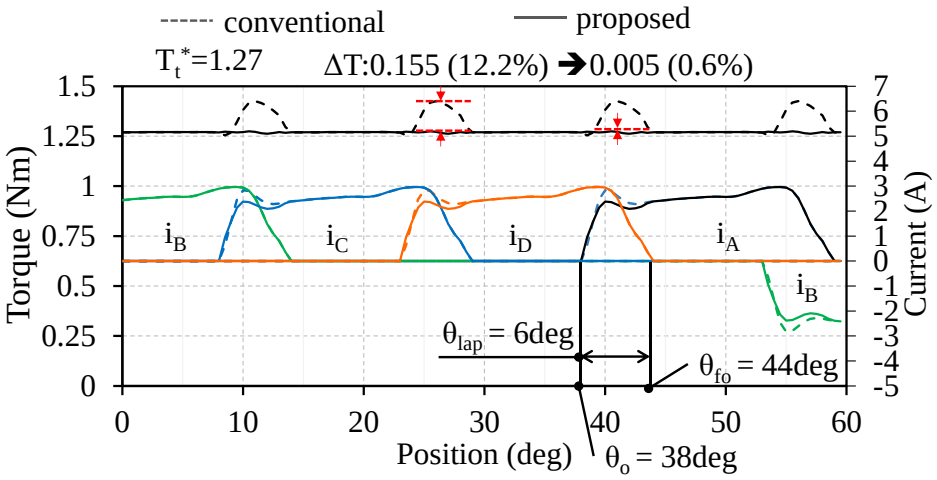

(a) 100% (1.27Nm) load

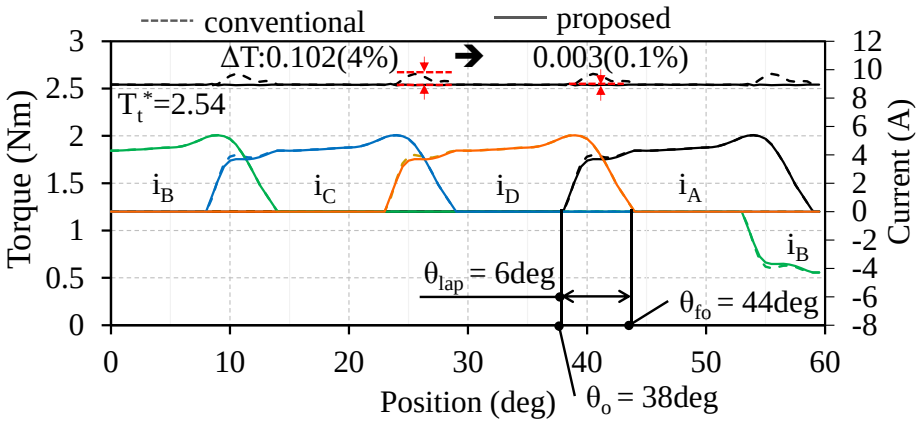

(c) 200% (2.54Nm) load

Figure 5.15 Calculated torque for current reference profiles obtained from the conventional and the proposed methods under different load conditions at θ_o = 38[deg], θ_{fo} = 44[deg].

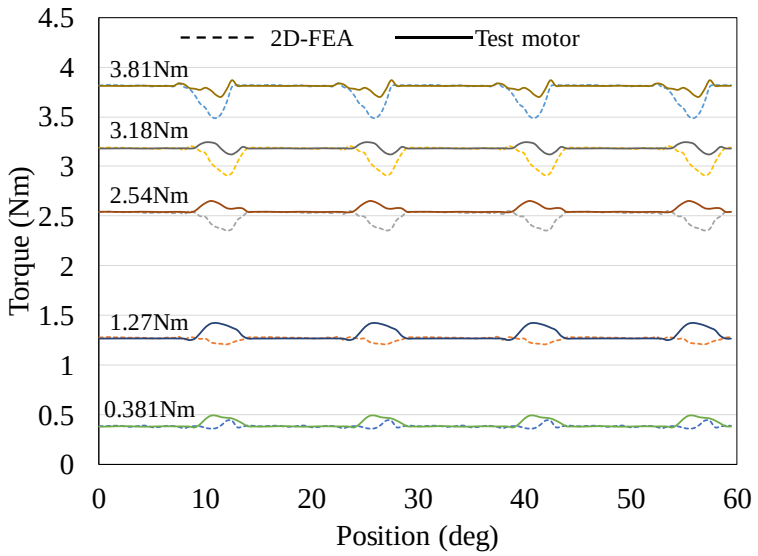

Figure 5.16 Comparison of torque ripple waveforms computed by 2D-FEA simulation and calculated from the measured magnetizing data of the test motor for different load conditions under the conventional current profiling control with θ_{fo} = 44[deg] and θ_{lap} = 6[deg].

5.4 Experimental results

In this section, the effectiveness of the proposed method based on the modified i-T-θ model obtained from the measured magnetizing curves for torque ripple minimization is verified through experiments using the test motor.

5.4.1 Experimental setup

To evaluate a performance of torque ripple minimization, experimental equipment is set up as can be seen figure 5.17. This equipment consists of test motor, dynamo, torque sensor, and controller. For the test motor control, the PE-Expert III (Myway Plus Corporation) was used to generate gate signals for the symmetric full bridge converter using 10kHz PWM. For position sensing, rotary encoder (Tamagawa Seiki, TS5667N420, 131072 ppr, 0.0027deg/pulse) was attached. For torque measurement, torque sensor (SAN-E, MTS010NK) was coupled. As a load, a servo motor (Yaskawa Electric Corporation,

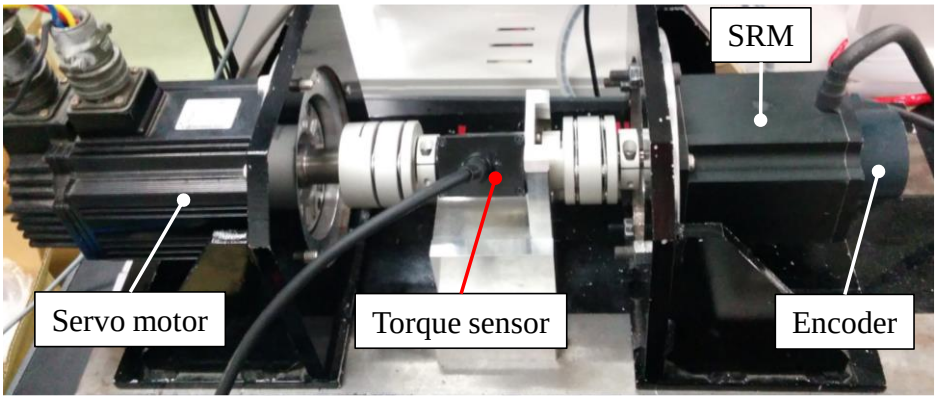

Figure 5.17 Equipment for torque ripple test

SGMSH-15A) was coupled to the tested SRM and used as a constant speed dynamo.

5.4.2 Comparisons of torque ripple minimization test results

Experimental studies using the test motor under the proposed method described in prior section are conducted for 100% and 200% of the rated torque condition. To control the actual current profiles well following the target current profiles, the current tracking controller explained in chapter 4 is employed.

Figure 5.18 shows a comparison between the reference and the actual current waveforms. It can be seen from the figure that the actual current profile is well controlled with small error. Figure 5.19 demonstrates instantaneous torque waveforms under the conventional control method and the proposed control method. It is confirmed that the torque ripples under both load conditions are well suppressed by the proposed method compared with the conventional method. Figure 5.20, the θ_{fo} is changed from 42deg. to 44deg. to increase the affection of the

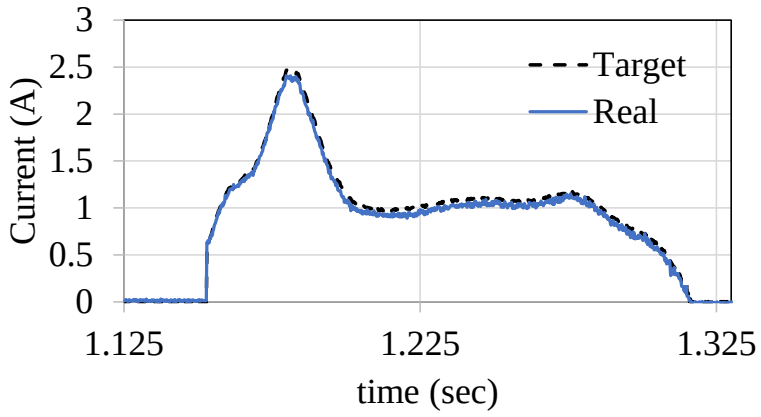

Figure 5.18 Experimental result of current controlled with target value

mutual coupling intentionally. In this experimental condition, it can be also found that the torque ripple minimization algorithm in the proposed method works well in both load conditions.

To evaluate how much torque ripple is reduced, spectrum analysis on the instantaneous torque data of one revolution (360 degrees mechanical angle) is executed by DFT. As a number of commutations per revolution is 24 as shown in figures 5.19 and 5.20, the 24^{th} and the 48^{th} order harmonics become dominant components. Figure 5.21 illustrates the result of spectrum analysis for different control methods and different load conditions when θ_o = 36[deg] and θ_{fo} = 42[deg]. Figure 5.22 is the result of spectrum analysis for different control methods and different load conditions when θ_o = 38[deg] and θ_{fo} = 44[deg]. From the both results, the 24^{th} and the 48^{th} components included in the torque waveforms under the proposed control method are greatly reduced compared with those under the conventional control method in spite of operating conditions. Figures 5.23 and 5.24 demonstrate enlarged instantaneous torque waveforms under 100% load condition shown in figures 5.19 and 5.20. From the figures, it is revealed that the torque ripple is minimized by the proposed control method less than ± 5% of the target average torque. Table 5.1 summarizes the experiment results. T^*, T_{ave} is the target torque and the average torque measured in one mechanical revolution, respectively. Δ/T_{ave} means the torque ripple factor for the average torque. All of the 24^{th} and 48^{th} harmonic components are well suppressed by the proposed control method. At this point, important thing is that the copper loss in case of θ_{fo} =44[deg] is lower than that in case of θ_{fo} = 42[deg]. This means that high efficiency control while keeping low torque ripple is possible by changing θ_{fo} to optimal value. In the conventional method, to minimize

the affection of the mutual coupling effect, the current overlapping region have to be start before the rotor position at which the stator teeth begins to overlap with rotor poles. In this case, as the conduction of A-phase occurs at low inductance region, the A-phase current at the current overlapping region increases, resulting the increase in copper loss. In the proposed method, the torque ripple minimization control is possible no matter where the current overlapping occurs and therefore, the operation angle parameters can be selected with more degree of freedom to minimize the copper loss while keeping torque ripple minimum.

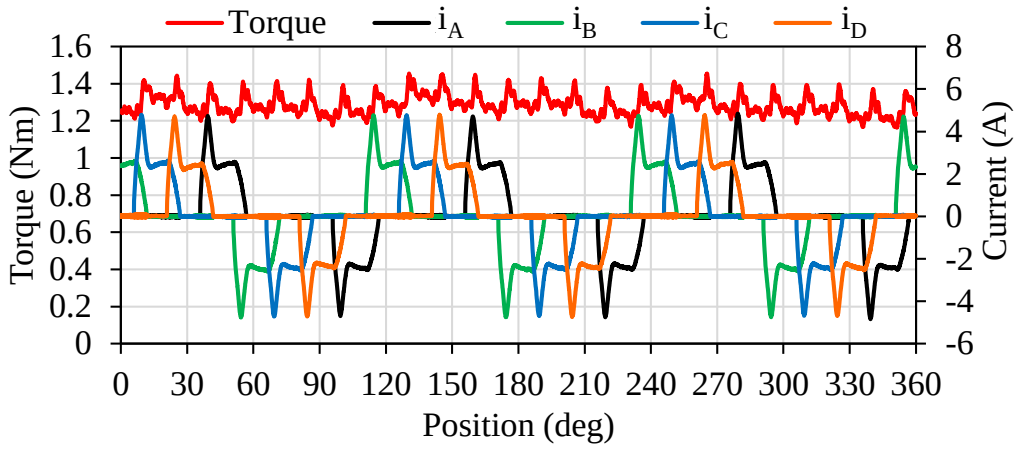

(a) 100% (1.27Nm) load under the conventional method

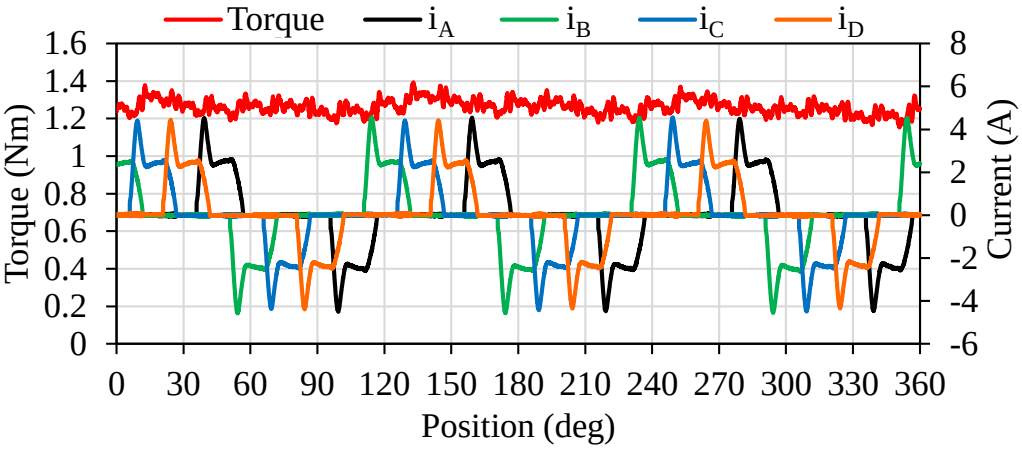

(b) 100% (1.27Nm) load under the proposed method

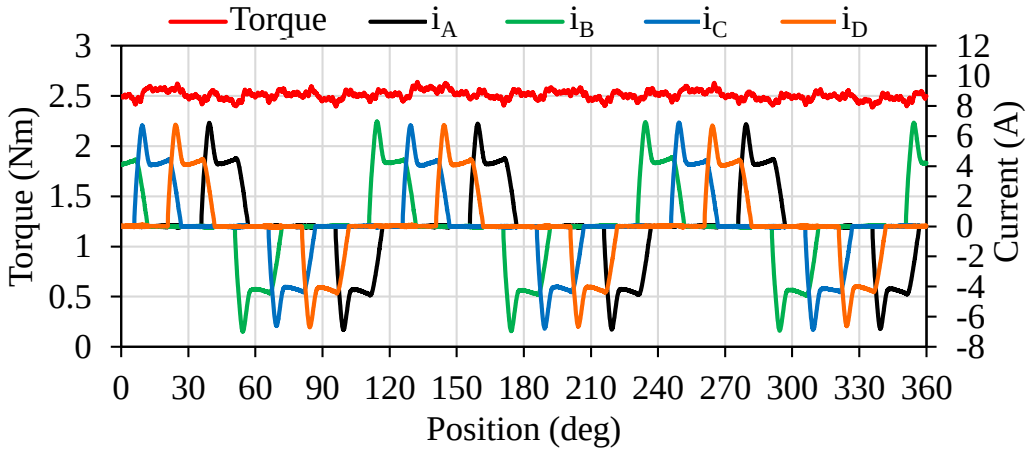

(c) 200% (2.54Nm) load under the conventional method

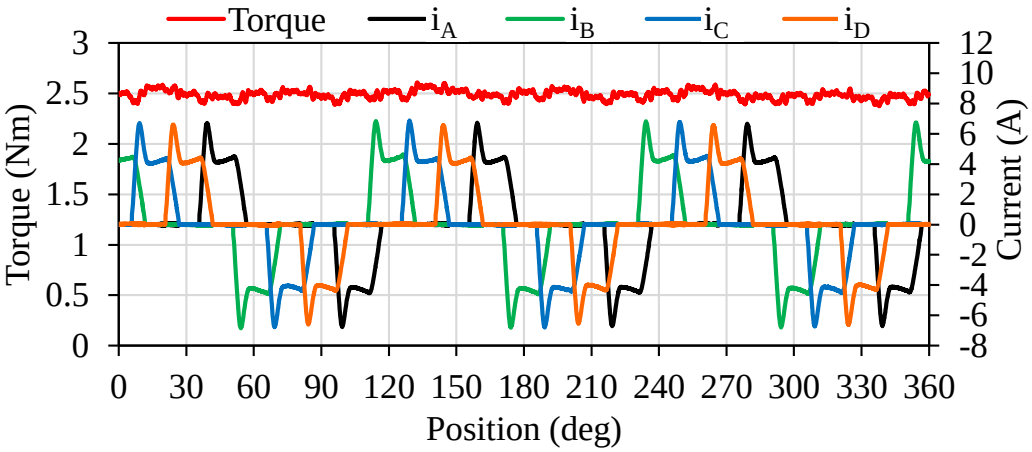

(d) 200% (2.54Nm) load under the proposed method

Figure 5.19 Measured instantaneous torque waveforms and current waveforms under the conventional and proposed control methods for different load conditions. (θ_o = 36[deg], θ_{fo} = 42[deg], speed 20[r/min])

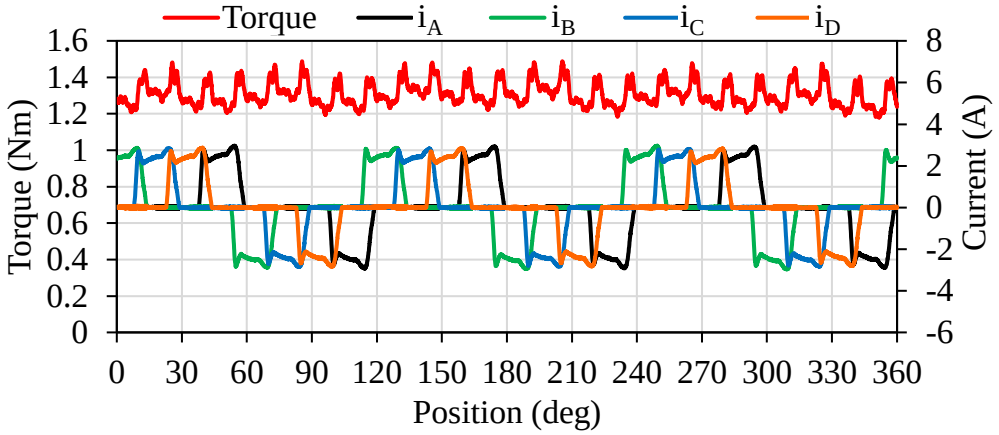

(a) 100% (1.27Nm) load, conventional method

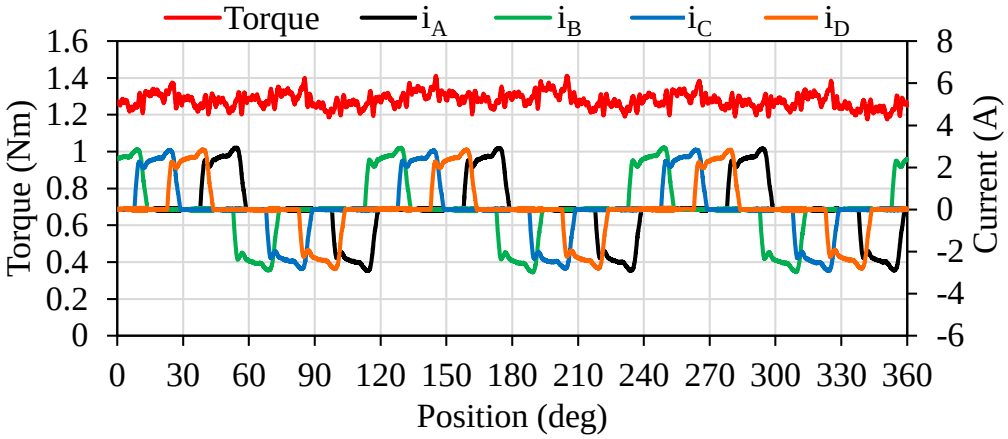

(b) 100% (1.27Nm) load, proposed method

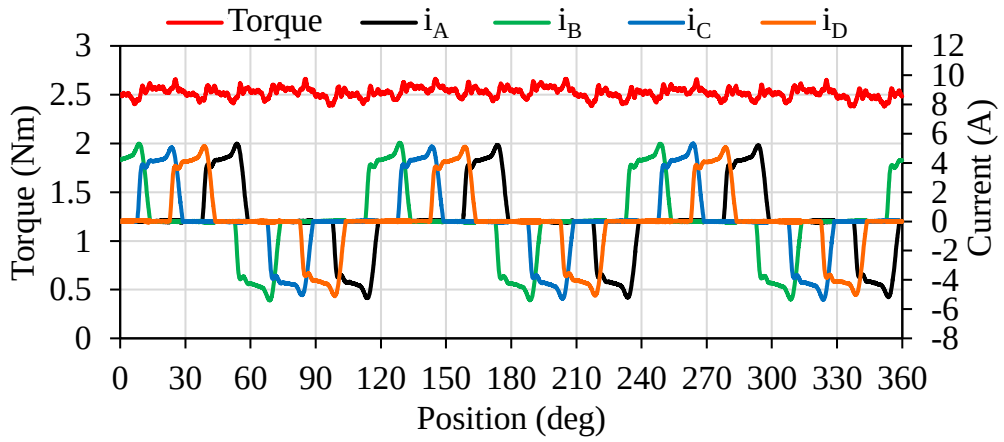

(c) 200% (2.54Nm) load, conventional method

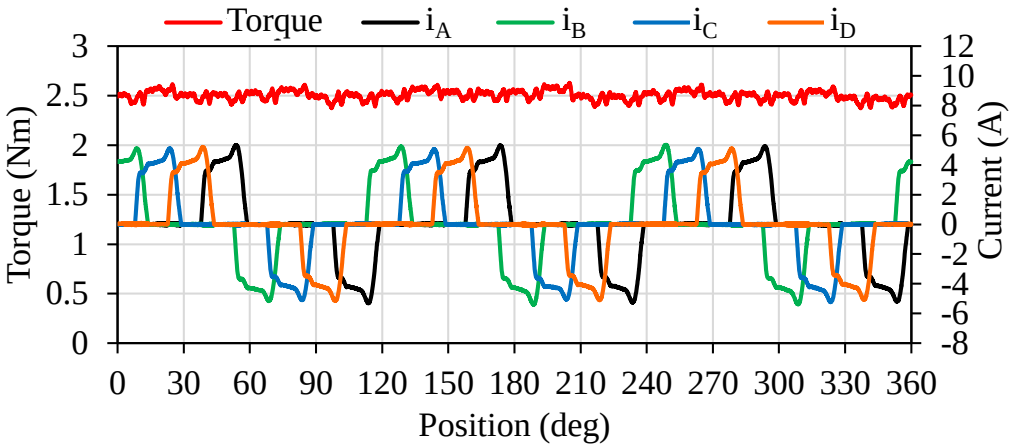

(d) 200% (2.54Nm) load, proposed method

Figure 5.20 Measured instantaneous torque waveforms and current waveforms under the conventional and proposed control methods for different load conditions. (θ_o = 38[deg], θ_{fo} = 44[deg], speed 20[r/min])

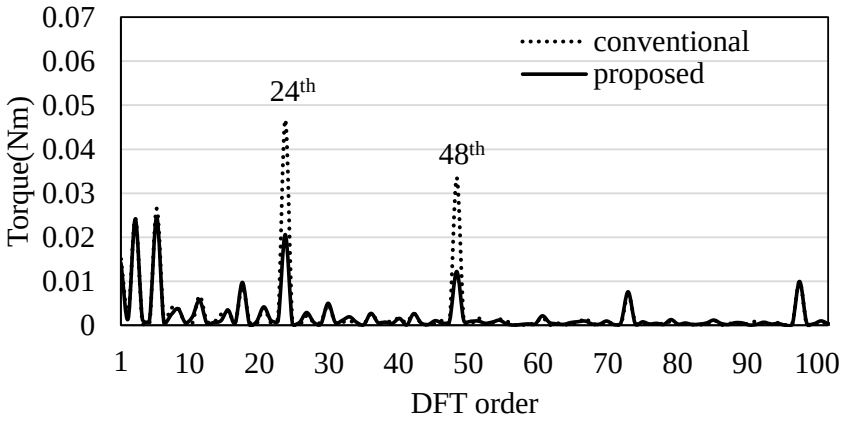

(a) 100% (1.27Nm) load

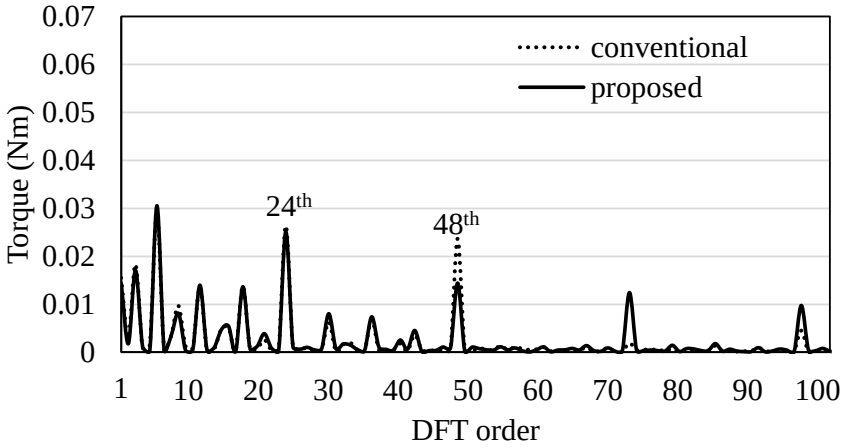

(b) 200% (2.54Nm) load

Figure 5.21 DFT result of torque under different load conditions at θ_o = 36[deg], θ_{fo} = 42[deg], speed 20[r/min]

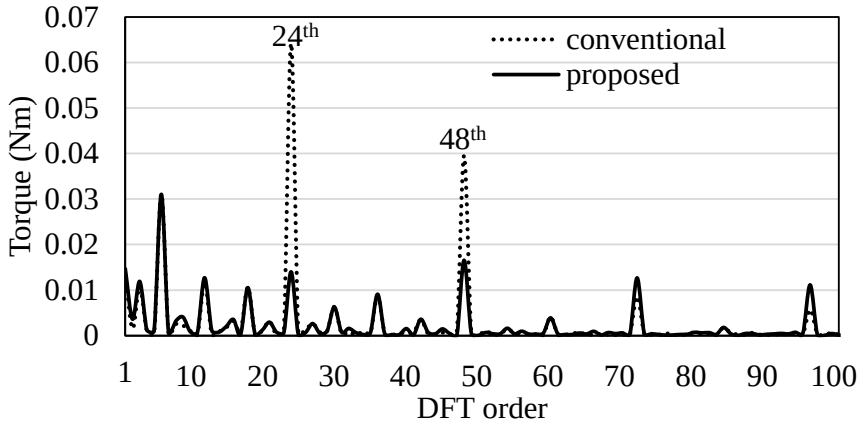

(a) 100% (1.27Nm) load

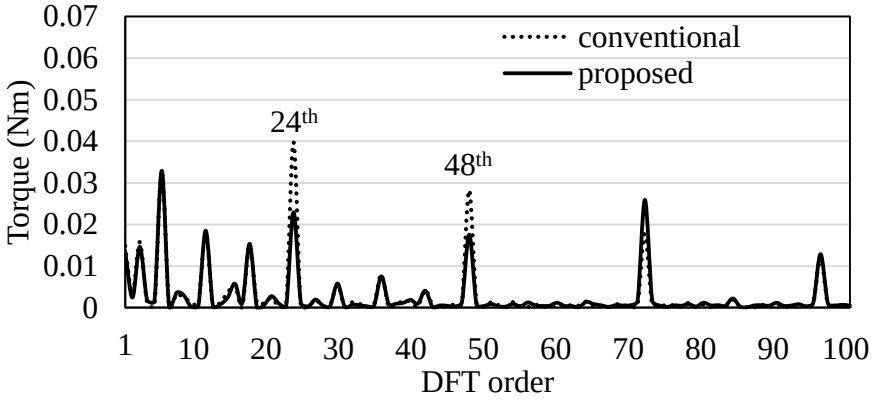

(b) 200% (2.54Nm) load

Figure 5.22 DFT result of torque under different load conditions at θ_o = 38[deg], θ_{fo} = 44[deg], speed 20[r/min]

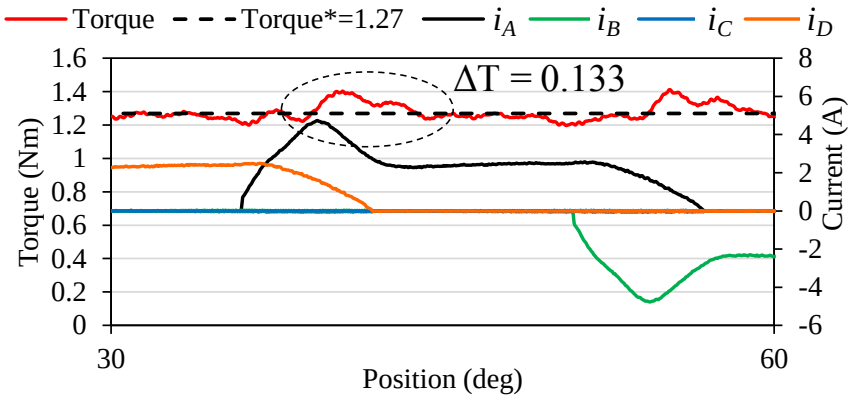

(a) conventional method

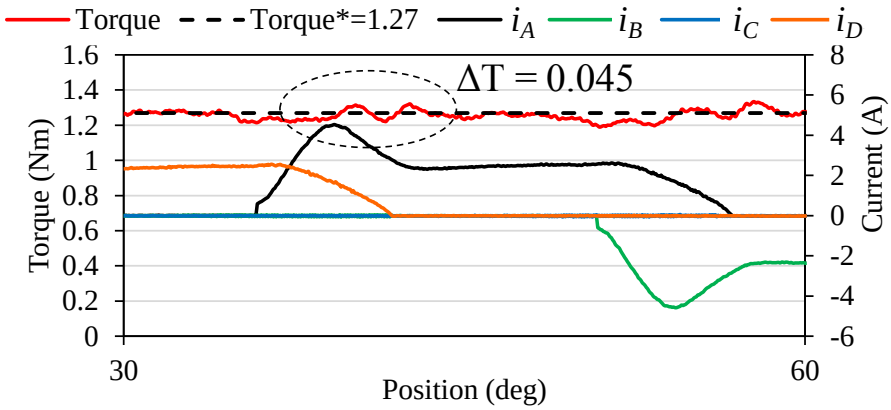

(b) proposed method

Figure 5.23 Enlargement of the angle 30 to 60 [deg] of figure 5.17-the results under the 100% load condition, θ_o = 36[deg], θ_{fo} = 42[deg]

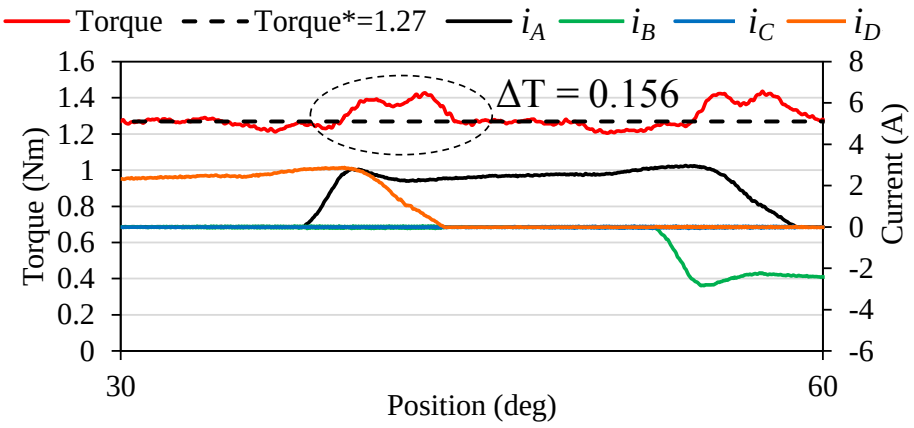

(a) conveitional method

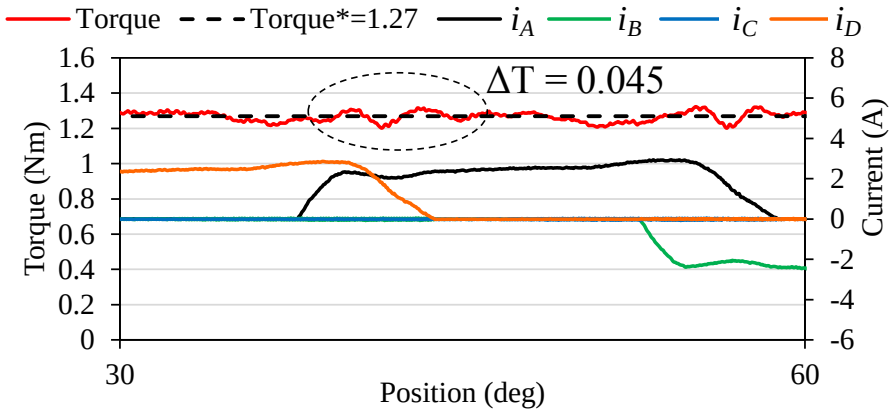

(b) proposed method

Figure 5.24 Enlargement of the angle 30 to 60 [deg] of figure 5.20-the results under the 100% load condition, θ_o = 38[deg], θ_{fo} = 44[deg]

Tabel 5.1 Summary of experimental results

θ_{fo} (deg)	T_t^* (Nm)	method	T_{ave} (Nm)	DFT 24th		DFT 48th		P_C (W)
				(Nm)	Δ/T_{ave}	(Nm)	Δ/T_{ave}	
42	1.27	conventional	1.29	0.047	3.6%	0.034	2.6%	50.8
		proposed	1.26	0.021	1.6%	0.012	1.0%	47.7
	2.54	conventional	2.51	0.026	1.1%	0.024	0.9%	133.3
		proposed	2.49	0.025	1.0%	0.014	0.6%	130.0
44	1.27	conventional	1.31	0.064	4.9%	0.040	3.0%	38.9
		proposed	1.28	0.014	1.1%	0.017	1.3%	37.5
	2.54	conventional	2.52	0.040	1.6%	0.028	1.1%	114.2
		proposed	2.50	0.023	0.9%	0.018	0.7%	112.7

5.5 Epilogue

In this chapter, the modified current profiling control method considering mutual coupling was proposed as the improved torque ripple minimization control. Through experiments, it was verified that the torque ripple was minimized in ±5% of the average target torque under 100% and 200% load condition. As a result, it was able to contribute to achieving more precise position control. In the future, the control parameters θ_{fo} and θ_{lap} must be optimized for further high efficiency control with copper loss minimization while keeping torque ripple minimum.

Chapter 6
Sensorless position estimation for SRM using phase voltage and voltage rate

6.1 Prologue

For high performance control of SRM, accurate rotor position information is necessary thing. A position sensor with high resolution is available for SRM, but it needs other space for installation and is burden in cost and reliability terms. So, to eliminate the position sensor, the many studies for rotor position estimation have been proposed to date. In this chapter, the estimation methods are classified into from a viewpoint of their applicable operating speed range and their drawbacks are explained. In order to compensate these drawbacks, an economic and simple position estimation method that has small position error for wide operating speed range is proposed. In this method, instead of an use of expensive current sensors with high frequency band width and accuracy, three voltage sensors that can be configured as economic shunt resistors are employed. In the proposed method, since linear gradient of phase voltage and voltage rate changed with respect to position displacement are focused on, neither complicate calculation of inductance/flux linkage or memory to save data table of inductance/flux linkage are necessary. As a result, the proposed method promises to provide an economic position estimation applicable for wide operating speed range. The proposed position estimation algorithm is explained and its effectiveness is evaluated through experiments.

6.2 Classification of earlier researches on position estimation algorithm for SRM

According to speed and torque, it is important to accurately apply a phase voltage with proper control parameters such as commutation angle θ_c and turn-on angle θ_o because efficiency, output power and vibration characteristic of SRM depend on them and therefore, an exact position information is necessary. Generally, for position sensing of SRM, an encoder or a resolver or a hall sensor is used. However, these sensors are not rigid and need another space for installation. To solve these problems, many kinds of sensorless control method have been studied. These studies can be classified into their applicable operating speed range of motor and some of the classified methods is explained from a viewpoint of their weak and strong points. Then, the position estimation algorithm to overcome the drawbacks based on the analysis of these weak and strong points is summarized.

6.2.1 Definition of voltage equation used for position estimation in accordance with operating speed range

Generally, the position estimation methods of SRM are based on the voltage equation of SRM. The voltage equation can be expressed like below[57].

$$V_x = Ri_x + \frac{d}{dt}\sum_{y=1}^{m}\lambda_{xy} = Ri_x + \frac{d}{dt}\sum_{y=1}^{m}\left(L_{xy}(i_y,\theta)\cdot i_y\right)$$

$$V_x = Ri_x + \sum_{y=1}^{m}\left\{\overset{(1)}{\boxed{i_y\frac{\partial L_{xy}}{\partial i_y}\frac{di_y}{dt}}} + \overset{(2)}{\boxed{L_{xy}\frac{di_y}{dt}}} + \overset{(3)}{\boxed{i_y\frac{\partial L_{xy}}{\partial\theta}\omega}}\right\} \tag{6.1}$$

Where x and y are phase number, R is phase resistance, V_x and i_x are phase voltage and current,

λ_{xy} is flux linkage of x phase by y phase current, L_{xy} is inductance between x and y phases (e.g. L_{aa} is self-inductance of A-phase, L_{ad} is mutual-inductance between A- and D-phases), ω and θ are angular speed and rotor position, respectively. In equation (6.1), (1) represents the voltage drop by inductance variation by current change. (2) represents the voltage drop by inductance. (3) represents back EMF. All of the above terms contain the inductance value that is a function of current i and rotor position θ. As a result, the rotor position can be estimated based on inductance calculated from three terms of equation (6.1) by using measured phase voltage and current.

6.2.2 Algorithms classification into their applicable operating speed range[57][58]

Based on the voltage equation explained in prior subsection, the voltage equation can be simplified in accordance with operating speed. As shown in figure 6.1, the speed ranges for various sensorless control are classified into five regions. The voltage equation can be simplified at each region based on the assumptions shown in table 6.1. All of sensorless methods in SRM use one of the simplified models in table 6.1. In the table, V, i, θ, ω, ω_{base}, L, R and M_j are phase voltage, phase current, motor angular speed, base angular speed, phase inductance, phase resistance and mutual inductance by adjacent j phase respectively. This

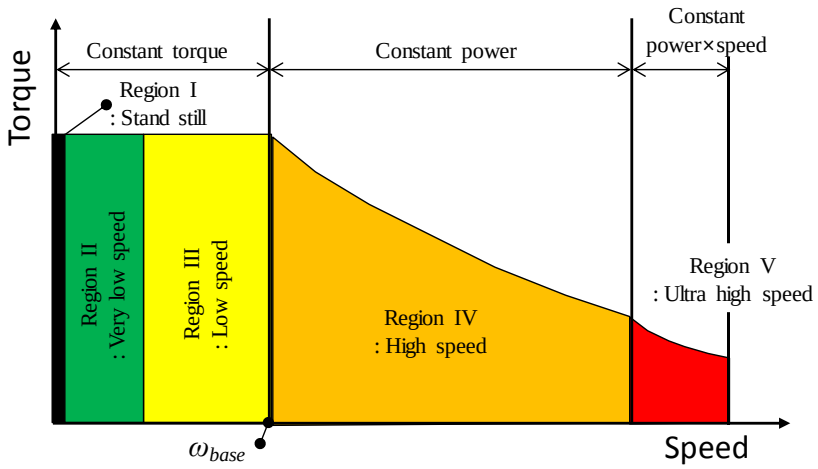

Figure 6.1 Classification of operating speed range in sensorless control of SRM [57][58].

Table 6.1 Simplification of voltage equation in accordance with operating speed[58].

Region	Speed	Criteria	Assumption	Simplified voltage equation
I	Standstill ($\omega = 0$)	Constant Torque	1. Small effect of magnetic mutual flux 2. Back EMF is zero 3. L^* means that $L(i,\theta)$ becomes $L(\theta)$ by small diagnostic pulse current	$V = Ri + \left(L^* + i\frac{dL^*}{di} \right)\frac{di}{dt}$
II	Very Low		1. Weak Back EMF	$V = Ri + \left(L(i,\theta) + i\frac{dL}{di} \right)\frac{di}{dt}$
III	Low ($\omega \le \omega_{base}$)		2. Strong Back EMF	$V = \left(R + \omega\frac{dL}{d\theta} \right)i + \left(L(i,\theta) + i\frac{dL}{di} \right)\frac{di}{dt}$
IV	High	Constant Power	1. No magnetic flux saturation (input current is low) 2. One pulse control	$V = \left(R + \omega\frac{dL}{d\theta} \right)i + L(\theta)\frac{di}{dt}$
V	Ultra High	Constant Power ×speed	1. Small iR drop voltage compared with Back EMF 2. High effect of magnetic mutual flux	$V = \omega\frac{dL}{d\theta}i + L(\theta)\frac{di}{dt} + \sum M_j\frac{di_j}{dt}$

was summarized by professor Fahimi in the references (57) and (58). Because the voltage equation is simplified differently in accordance with running speed, different estimation

algorithm can be selected for the speed range. In standstill state, almost position estimation algorithms [59)-(61)] are conducted, based on the voltage equation described in table 6.1 and the *voltage probing* injecting the voltage pulse(hereafter, named as diagnostic pulse) into *unexcited* phase[(36)], except for the *Feed-forward open loop method* that the pulse train with initial frequency is excited to each phases in a commutation sequence of a rotating direction while the frequency is linearly accelerating until target speed from zero speed or the *align method* starting after locking the rotor along with phase axis [(62)]. By using the current and voltage measured through diagnostic pulse injection, the position is estimated by comparing with calculated inductance and pre-measured inductance table[(59)(60)], or by using directly the variation of phase current or voltage according to position change[(61)].

In low speed region, the voltage equation un-considering Back EMF and mutual magnetic flux linkage, is mainly used. Representative one is AM(amplitude modulation), PM(phase modulation), FM(frequency modulation), active phase vector method. In AM/PM method, through specific hardware, the sinusoidal diagnostic pulse is injected into unexcited phase coil and current is measured[(63)]. And then, the magnitude or phase angle of current waveform is changed by inductance variation, therefore, by comparing inductance value with pre-measured inductance data, position can be estimated. In FM method, after diagnostic pulse injection to un-excited phase through also additional circuit, the rectangular wave with the frequency changed by inductance variation is produced from circuit[(64)]. By using this frequency variation, position is estimated. In active phase vector method, through the measured voltage and current of active (conducting) phase, the inductance is calculated assuming that the Back EMF and inductance variation by current variation-dL/di is small[(65)].

Then, by comparing calculated inductance and pre-measured inductance table, position is estimated.

The method considering Back EMF in low speed range also exist[66]. Especially in CCC (constant current control) mode by hysteresis control, *di/dt* will be zero. Then, the component of (*v-iR*) is just concerned with Back EMF term. After calculation of Back EMF, through inputting Back EMF into voltage equation, the inductance $L(i, \theta)$ varied by current and position variation can be calculated. By comparing calculated inductance value and the value obtained from inductance model, position is estimated.

The method using mutual voltage induced by mutual inductance in low speed range also was proposed[67]. In this method, assuming that incremental inductance by current variation *dL/di* can be neglected and motor is controlled to constant current control (CCC) mode, from the voltage equation considering Back EMF, the current variation *di/dt* is deduced. If this *di/dt* is inputted into mutual voltage equation of apposite phase induced by active phase (C phase when A phase is active at four-phase SRM), the C-phase mutual voltages by A-phase is calculated. Through comparison measured mutual voltage with the conversion table of mutual voltage with respect to position variation, rotor position is estimated. However, for calculation of mutual voltage conversion table, pre-measured self-inductance *L* and mutual-inductance *M* with respect to position variation are necessary.

In observer method in low speed range, both Back EMF and incremental inductance by current change *dL/di* are considered for exact SRM model[68]. This method is also suitable for high speed region theoretically, however, this method only had been used in low speed region because of a calculation time problem. Now a days, this method also has become

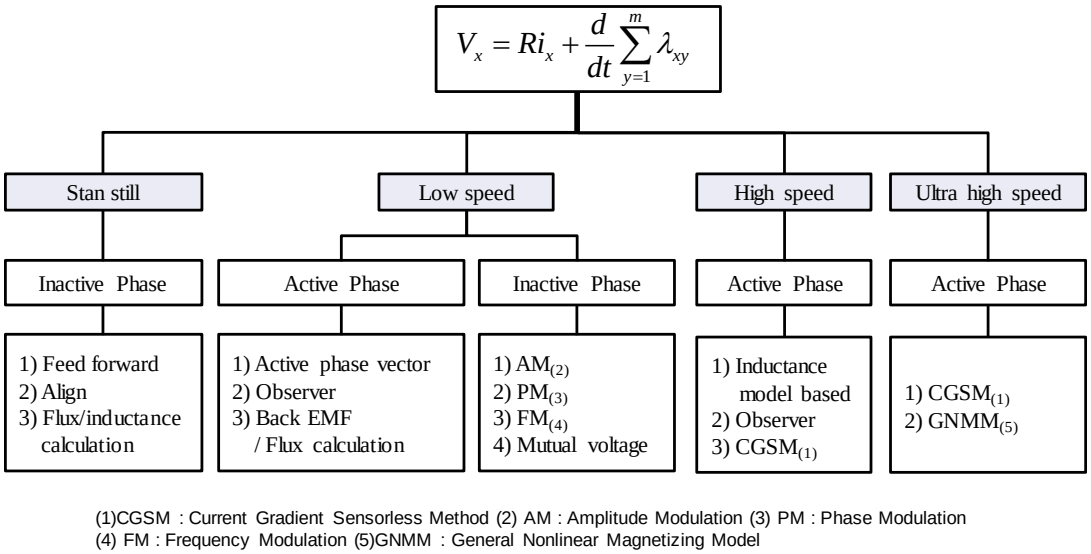

Figure 6.2 Classification of position estimation methods in accordance with speed range[57].

available in high speed region by the development of high-speed processor. The inductance model based method also consider both Back EMF and incremental inductance dL/di[69]. Specific explanation is omitted.

In high speed and ultra-high speed (over 20,000[r/min]) region, CGSM (current gradient sensorless method)[70] and GNMM (general nonlinear magnetizing model)[71] method are used. The CGSM uses the characteristic which the gradient of current is changed from positive to negative at teeth overlap by rapid Back EMF change. For sensing of the differential of current with respect to time, specific hardware is used.

All methods are summarized in the figure 6.2. As the operating speed region, the estimation algorithms were distributed, and in same speed region, the algorithms were divided into the methods using measured voltage and current of active phase, and the methods using measure voltage and current of inactive phase produced by diagnostic pulse injection into inactive

phase, or induced by mutual coupling of active phase. Active phase means the current conducting phase, and inactive phase means the non-conducting phase.

6.2.3 Analysis of advantages and disadvantages about various estimation algorithms

About each position estimation method of figure 6.2, the advantages and disadvantages are represented as can be seen in table 6.2. As can be known through this table, all methods need some additional circuit or the data table / model of magnetic flux linkage λ or inductance L with respect to position and/or current. And to calculate λ or L from the simplified voltage equation in accordance with operating speed region, the measured voltage and current are necessary.

6.2.4 Drawbacks of general sensorless position estimation method in SRM

From the contents summarized in table 6.2, common drawbacks in general sensorless methods of SRM are explained like below.

1) For exact position estimation in every speed region, exact inductance (self-inductance L / mutual inductance M) data/model or flux linkage λ data/model is necessary. These require huge data memory to save or fast calculation to obtain from mathematical model of inductance or flux linkage.

Table 6.2 Analysis of advantages and disadvantage about estimation method.

Region	Estimate Method	Advantage	Disadvantage
I Standstill	Align	1. Algorithm is simple 2. No need L/λ table	1. Hesitation / vibration high 2. Misalign at equilibrium point 3. Need align time (start delay)
	Feed forward	1. Algorithm is simple 2. No need L/λ table	1. Hesitation / vibration / noise high 2. Need algorithm tuning as load change
	Flux computation	1. Exact position sensing 2. Fast position sensing (enable fast start) 3. Low hesitation	1. Need L/λ table 2. Need L/λ computation 3. Need current limitation for hesitation protection
II Very low speed & III Low speed	1. Active phase vector 2. Back EMF/flux calculation	1. Wide estimation region	1. Noise problem of active phase current 2. Need fast calculation 3. Need motor parameter(L,R,M)
	Observer control	1. Wide speed range estimation 2. Continuous rotor position estimation	1. Need fast calculation 2. Need L/R data for state observer model
	AM/PM/FM	1. Low estimation error by low current/voltage sensing noise 2. Unsaturated L table is enough	1. Need L/λ table 2. Need exterior circuit 3. Low accuracy on current overlap region 4. Narrow estimation region 5. Torque ripple and noise
	Mutual voltage at CCC	1. Sensing noise of current/voltage is low 2. Consider the effect by Back EMF	1. Not applicable at high speed (Not applicable except for CCC mode) 2. Need L & M table 3. Need voltage sensor
IV High speed	Inductance model based	1. Not need large data memory for L data (use polynomial eq. and DFT for L)	1. Need L model accordance with i, θ 2. Need Fast calculation to solve rearranged voltage equation
	CGSM	1. Not needs L/λ table and model 2. Implementation is simple 3. No extra computation	1. Not allowed at standstill and CCC mode, and large torque transient 2. Not suitable for low speed 3. Need external circuit
	Observer	Same characteristics with method used in II & III region	
V Ultra High Speed	GNMM	1. Simple and exact estimation using GNMM and motion equation	1. Low resolution due to short active phase conduction time 2. Need fast calculation 3. Error by Back EMF and mutual effect
	CGSM	Same characteristics with method used in IV region	

2) To calculate the inductance or flux linkage having position information, additional circuit or fast calculation through voltage equation is required. In addition, in the method based on observer, because the real current of test motor and the calculated current from SRM model are required, the fast calculation of the current through SRM model based

on voltage equation, is required.

3) To calculate inductance of magnetic flux linkage in 2), the measured voltage and current are necessary, and generally, the current sensor with high accuracy used for accurate position estimation is expensive.
4) According to speed range, different algorithm is necessary because the simplified voltage equations are different with speed range.

To solve above drawbacks, many kind of methods has been proposed in prior study. To solve the problems of 1), the methods to use the linear gradient of inductance before the magnetic saturation occurs, were proposed[59][60]. However, the problems that is needed inductance calculation still remains. To solve the drawbacks of 1), 2), and 3) spontaneously, the method using the phase voltage changed with respect to position variation was proposed[61]. In this method, just voltage sensor was used. And because rotor position was estimated by using linear gradient of the phase voltage changed by rotor position variation, no data table and calculation of inductance were required. However, this method can be used just in the standstill state, and estimation error is very high due to the too much approximation of voltage gradient. For position estimation in wide speed range containing a standstill, the reference (72) was proposed. However, as mentioned in the drawback 4), different algorithms with respect to operational speed region were used.

6.2.5 Purpose for this study and the proposed concept

This study focused on the algorithm that complements the drawbacks described in section 6.2.4. So, a simple and economic rotor position estimation method that makes it possible to

operate for wide speed range with small estimation error is to be the purpose of this study. In this method, expensive current sensors are not required, but just three voltage sensors are used. The rotor position can be estimated by using the linear slope of the distributed phase voltage obtained through diagnostic pulse injection into series connected phases. The concept to use voltage gradients for position estimation is similar with the pre-described method[61]. However, because accurate position estimation in the method using only phase voltage[61] is difficult at some position, the concept of voltage rate obtained from measured phase voltage is proposed. And, for position estimation in wide speed region from stand still state to running state, the estimation algorithm using gradient of voltage rate in running state, is proposed. Through the four phase 8/6 SRM with symmetric H-bridge converter for bipolar conduction, the effectiveness of proposed algorithm is verified.

6.3 Basic principle of proposed position estimation method

This method is based on the injection of diagnostic pulse into inactive phases, i.e. the non-energized phases. Figure 6.3 shows the sectional view of 400W four-phase 8/6 SRM used for experiment. And for diagnostic pulse injection, bipolar type converter is used as can be seen in figure 6.4. This converter topology is generally used to minimize the torque dip produced by the opposite magnetic flux polarity of adjacent phases when phase currents overlap. By using this converter, the magnetic flux of two phases is always made to flow in the same direction, i.e. always works as short flux mode in reference (53). In this study, by using switching composition of this converter, diagnostic pulse is injected into series connected

windings of A&C and B&D phases. To estimate position, the distributed phase voltage between series connected phase are utilized.

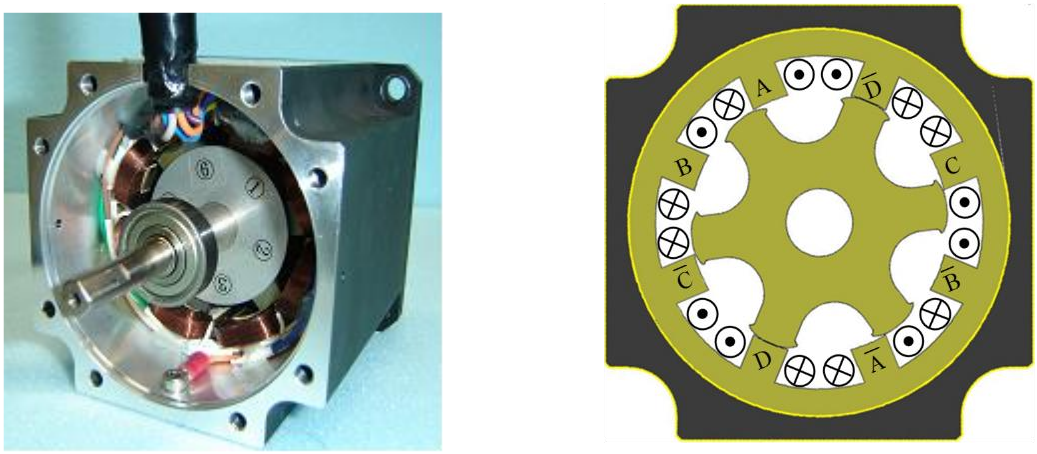

Figure 6.3 Picture and cross-sectional view of four-phase 8/6 SRM with fillet rotor pole.

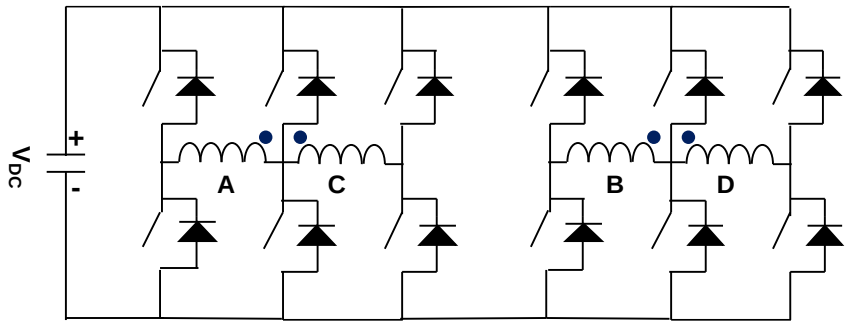

Figure 6.4 Structure of four-phase full bridge bipolar type converter.

6.3.1 Voltage diagnostic pulse injection and phase voltage profile

As is well known, the phase inductance of SRM varies with rotor position. Almost of the rotor position estimation algorithms for SRM are based on this variation of inductance. This study is also based on this inductance variation. As can be seen in figure 6.5, the self-inductance profiles obtained from 2D-FEA of test motor is changed with respect to rotor position and current. Especially, at phase current lower than 0.6[A], the inductance variation by current variation at same position has small difference because of no magnetic saturation. In this study, the maximum diagnostic pulse is limited phase current to less than 0.6[A] to utilize the same inductance variation for the position variation. In standstill state, because speed is zero and incremental inductance *dL/di* is negligible under current conditions lower than 0.6[A], the phase voltage equation can be represented like below from equation (6.1).

$$V_x = Ri_x + \sum_{y=1}^{m}\left(L_{xy}\frac{di_y}{dt} \right) \tag{6.2}$$

By using switching of the bipolar type converter, diagnostic pulse can be injected into series connected A- and C-, B- and D-phases independently as can be seen in figure 6.6. Hereafter, the names of each phase used in equations and figures, are expressed in lowercase letters, e.g. A ~ D is expressed as a ~ d. The voltage distributed over the A- and C-phase, and B- and D-phase can be given like below equation (6.3).

$$\begin{aligned} V_a &= R_a i_{ac} + L_a\frac{di_{ac}}{dt} + \sum_{y=b}^{d}\frac{d\lambda_{ay}}{dt}, \quad V_c = R_c i_{ac} + L_c\frac{di_{ac}}{dt} + \sum_{y=d}^{b}\frac{d\lambda_{cy}}{dt} \\ V_b &= R_b i_{bd} + L_b\frac{di_{bd}}{dt} + \sum_{y=c}^{a}\frac{d\lambda_{by}}{dt}, \quad V_d = R_d i_{bd} + L_d\frac{di_{bd}}{dt} + \sum_{y=a}^{c}\frac{d\lambda_{dy}}{dt} \end{aligned} \tag{6.3}$$

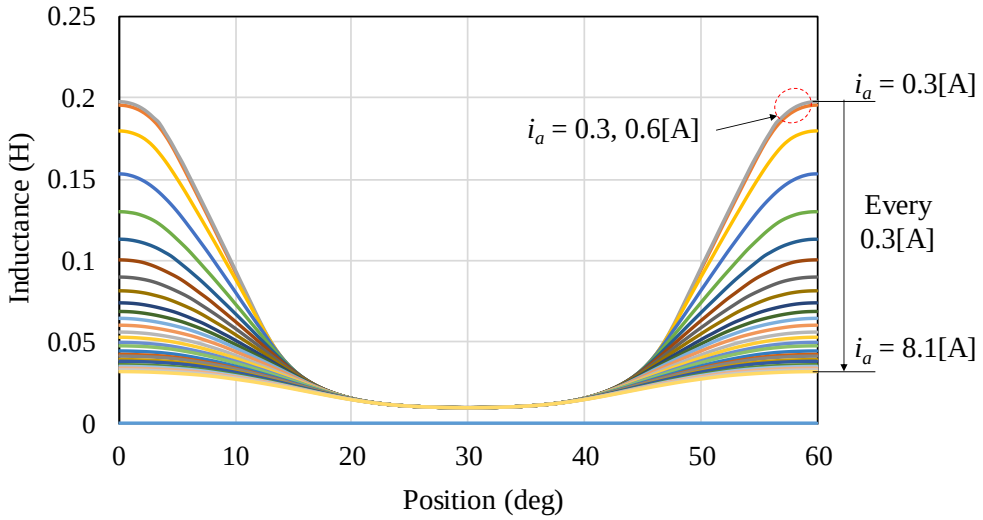

Figure 6.5 Phase inductance profile of SRM obtained from 2D-FEA.

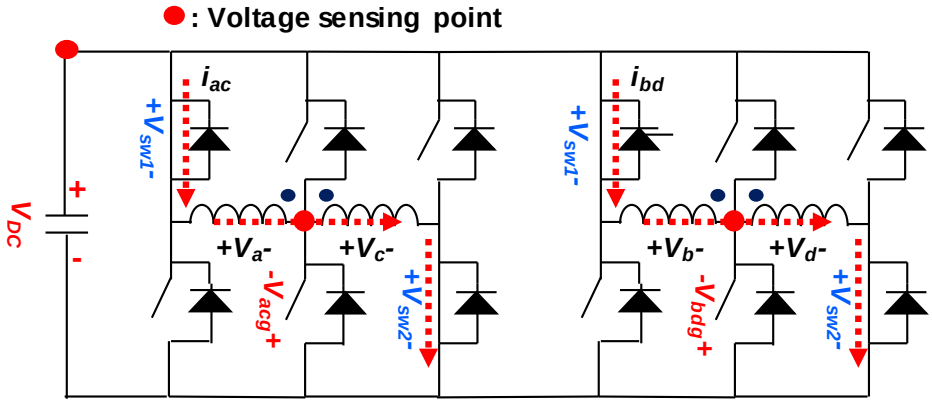

Figure 6.6 Switching state and distribution of phase voltage when diagnostic pulse is injected in four-phase full bridge bipolar type converter.

Where y is adjacent phase producing mutual flux. Because the diagnostic pulses are generally high frequency over 1[kHz], the drop voltage by resistance-R_x is very small compared with the drop voltage by self-inductance-L_x. And assuming that the effect of mutual magnetic flux linkage-λ_{xy} is small, each phase voltage can be approximated as follows.

$$V_a \approx L_a \frac{di_{ac}}{dt}, \quad V_c \approx L_c \frac{di_{ac}}{dt}$$
$$V_b \approx L_b \frac{di_{bd}}{dt}, \quad V_d \approx L_d \frac{di_{bd}}{dt} \tag{6.4}$$

As a result, assuming that the main value of phase impedance is by inductance, phase voltage can be expressed by using phase inductance L_x and dc-link voltage V_{DC} through the voltage distribution over series connected phases as follows.

$$V_a \approx \frac{L_a}{L_a + L_c} V_{DC}, \quad V_c \approx \frac{L_c}{L_a + L_c} V_{DC}$$
$$V_b \approx \frac{L_b}{L_b + L_d} V_{DC}, \quad V_d \approx \frac{L_d}{L_b + L_d} V_{DC} \tag{6.5}$$

Since the diagnostic pulse is injected for the current i_{ac} and i_{bd} to be less than 0.6[A], the inductance profile with respect to position variation will be similar with inductance profile at i_a=0.6[A] shown in figure 6.7. At this condition, the phase voltage by diagnostic pulse injection can be calculated from inductance and equation (6.5) as shown in figure 6.8. The dc-link voltage V_{DC} is set to 283[V]. The phase voltage is changed in accordance with rotor position and particularly, the phase voltage of the area (hereafter, called as blue box area) surrounded by blue dotted lines has linear slope as can be seen in figure 6.8. The reason is because the denominators in equation (6.5) are constant so that the phase voltage is proportional to linearly varying phase inductance. The figure 6.9 shows the simplified phase inductance and voltage profile in sub-region 1 between 0 and 3.75[deg]. In this simplified profile, the denominator-(L_b+L_d) of equation (6.5) about B- and D-phase is constant, therefore, the phase voltage is proportional to their phase inductance like $V_b \propto L_b$, $V_d \propto L_d$. And this phase inductance has linearity in accordance with position, as a result, phase voltage has

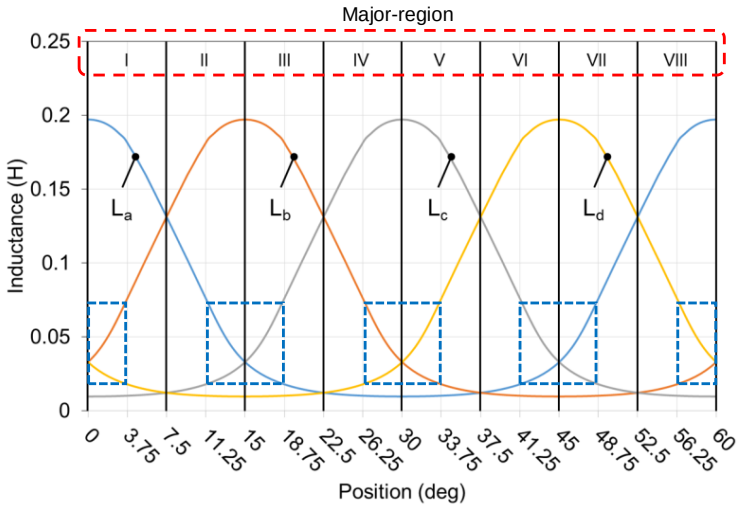

Figure 6.7 Phase inductance profile through 2D-FEA (current = 0.6 [A]), and blue box area with a phase voltage of linear gradient.

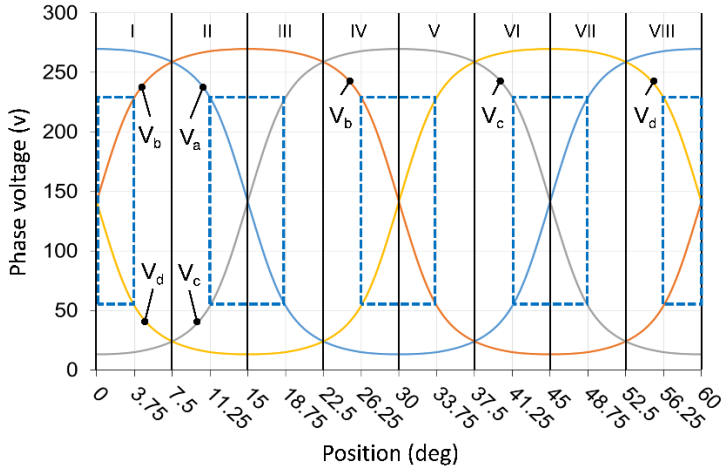

Figure 6.8 Phase voltage profile when diagnostic pulse is injected into A- and C-phases, and B- and D-phases.

linearity. In blue box area of figure 6.7 and 6.8, the phase inductance has below relationship.

$$\begin{aligned} &\text{At } 0\sim3.75 \;\&\; 26.25\sim33.75 \;\&\; 56.25\sim60[\text{deg}] : L_b + L_d \approx \text{constant} \\ &\text{At } 11.25\sim18.75 \;\&\; 41.25\sim48.75[\text{deg}] \quad : L_a + L_c \approx \text{constant} \end{aligned} \tag{6.6}$$

Then, the phase voltage is proportional to phase inductance from equation (6.5) and (6.6) as follows

$$\begin{aligned} &\text{At } 0\sim3.75 \,\&\, 26.25\sim33.75 \,\&\, 56.25\sim60[\text{deg}] : V_b \propto L_b, \quad V_d \propto L_d \\ &\text{At } 11.25\sim18.75 \,\&\, 41.25\sim48.75[\text{deg}] \quad\quad : V_a \propto L_a, \quad V_c \propto L_c \end{aligned} \tag{6.7}$$

In this study, as the motor with fillet rotor pole is used, the phase voltage profiles in blue box region are slightly different compared to the simplified profile of figure 6.9 with the same characteristics as the motor with rectangular rotor pole. There are small differences in linearity of phase voltage in accordance with rotor pole shape, however, those are negligible. Therefore, it is possible to estimate the position using linearity of the phase voltage. The details about difference of linearity of phase voltage by rotor pole shape will be explained later.

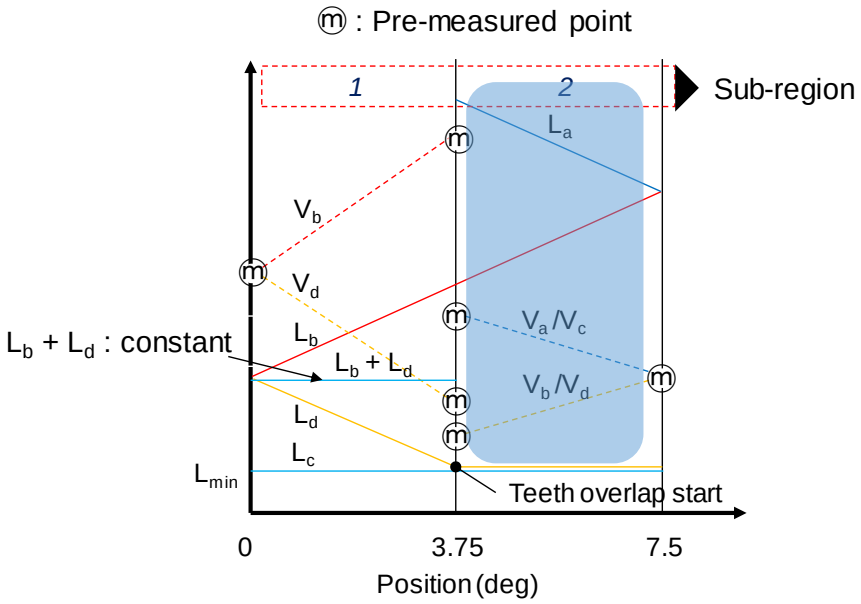

Figure 6.9 Simplified phase inductance and voltage profile between rotor position=0 and 3.75[deg].

6.3.2 Position estimation through the linearity of phase voltage and estimation error

Because the phase voltage in the blue box area has linear relationship with respect to position, the rotor position can be estimated simply by using the linear slope of phase voltage as can be seen in figure 6.10. For explanation, blue box area (B) between 41.25 and 48.75 [deg] is used. The phase voltages of other blue box areas have same relationship by structure symmetricity of SRM. The position θ_x is estimated by using measured voltage difference x of A- and C-phase, and pre-measured value G of A- and C-phase which is same with the voltage difference of B- and D-phase at position 3.75[deg]. Estimated position in box (B) of figure 6.10 is like below.

$$\theta_x = 45 + 3.75 \times \frac{x}{G} \tag{6.8}$$

However, since the voltage slopes outside blue box area in figure 6.10 are nonlinear, so high estimation error occurs as can be seen figure 6.11. When the real position is located at θ_{real} between 18.75 and 22.5[deg] in figure 6.10, the voltage difference will be Δv_{real}. The estimated position θ_{est} will be like below through estimation line.

$$\theta_{est} = 15 + 3.75 \times \frac{\Delta v_{real}}{G} \tag{6.9}$$

As a result, estimation error of (A) is produced. Figure 6.11 shows the experimental results of rotor position estimated by using the linear slope of phase voltage (named as conventional method) under the standstill state. There is high position estimation error between 3.75 and

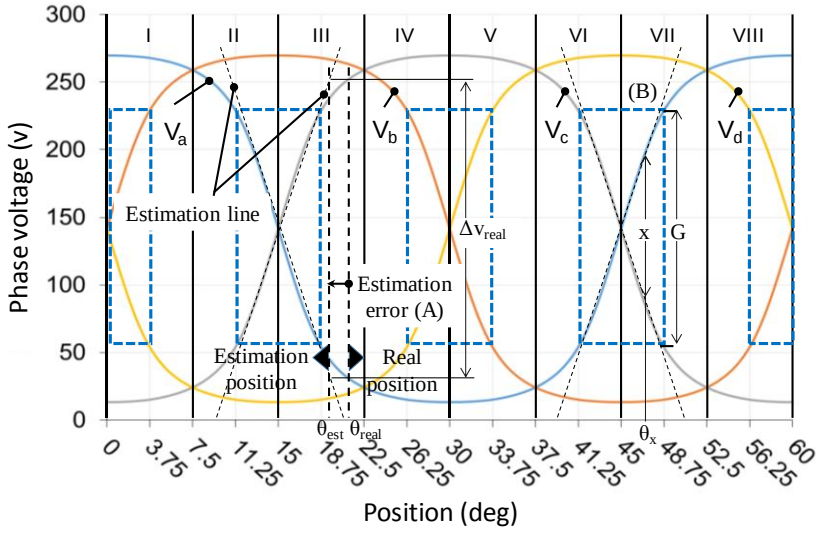

Figure 6.10 Position estimation and their error when linearity of phase voltage is used.

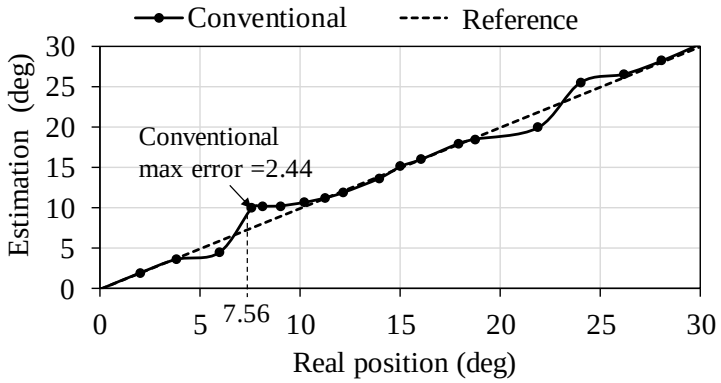

Figure 6.11 Position estimation results when linearity of phase voltage is used.

11.25[deg], and between 18.75 and 26.25[deg]. The maximum error in this area is about 2.44[deg]. In order to reduce this error, another estimation method is necessary.

6.3.3 Proposed method to reduce estimation error

As mentioned at prior subsection, position estimation through only phase voltage has big estimation error about 2.44[deg] at some position. In this subsection, for accurate position estimation, the voltage rate of phase voltage is focused on as a new factor. From equation (6.5), the voltage rate is expressed like below equation.

$$\frac{V_a}{V_c} \approx \frac{L_a}{L_c}, \quad \frac{V_b}{V_d} \approx \frac{L_b}{L_d}, \quad \frac{V_c}{V_a} \approx \frac{L_c}{L_a}, \quad \frac{V_d}{V_b} \approx \frac{L_d}{L_b} \tag{6.10}$$

As can be seen figure 6.13, the voltage rate V_x/V_y at the area (hereafter, called as red box area) surrounded by red line has linearity. For example, the voltage rate V_a/V_c between 3.75 and 11.25[deg] has linearity. That is because the denominator-L_c of the voltage rate-V_a/V_c from equation (6.10) is constant compared with numerator-L_a. As a result, V_a/V_c is proportional to linearly varying phase inductance-L_a, therefore, this voltage rate has a linearity. Another red box area, voltage rate has also linearity as follows,

$$\begin{aligned}
&\text{From } 3.75 \text{ to } 11.25 \text{ [deg]}, \ L_c \,\&\, L_d \text{ is constant} : \frac{V_a}{V_c} \propto L_a, \quad \frac{V_b}{V_d} \propto L_b \\
&\text{From } 18.75 \text{ to } 26.25 \text{ [deg]}, \ L_d \,\&\, L_a \text{ is constant} : \frac{V_b}{V_d} \propto L_b, \quad \frac{V_c}{V_a} \propto L_c \\
&\text{From } 33.75 \text{ to } 41.25 \text{ [deg]}, \ L_a \,\&\, L_b \text{ is constant} : \frac{V_c}{V_a} \propto L_c, \quad \frac{V_d}{V_b} \propto L_d \\
&\text{From } 48.75 \text{ to } 56.25 \text{ [deg]}, \ L_b \,\&\, L_c \text{ is constant} : \frac{V_d}{V_b} \propto L_d, \quad \frac{V_a}{V_c} \propto L_a
\end{aligned} \tag{6.11}$$

As shown at the sub-regions 2 and 3 between 3.75 and 11.25[deg] in figure 6.14 that shows more simplified profile, owing to that the inductances L_a and L_b are varied with linearity and L_c and L_d are constant, the voltage rates V_a/V_c and V_b/V_d have linearity. By using the linearity of voltage rate, the position can be estimated in the same manner as the equation

(6.8) to estimate rotor position by using linearity of phase voltage.

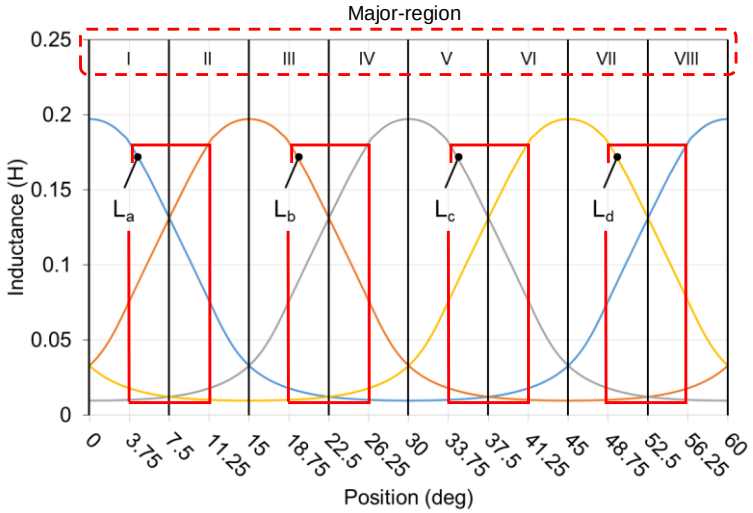

Figure 6.12 Phase inductance profiles obtained by 2D-FEA (current = 0.6 [A]), and red box area with a voltage rate of linear gradient.

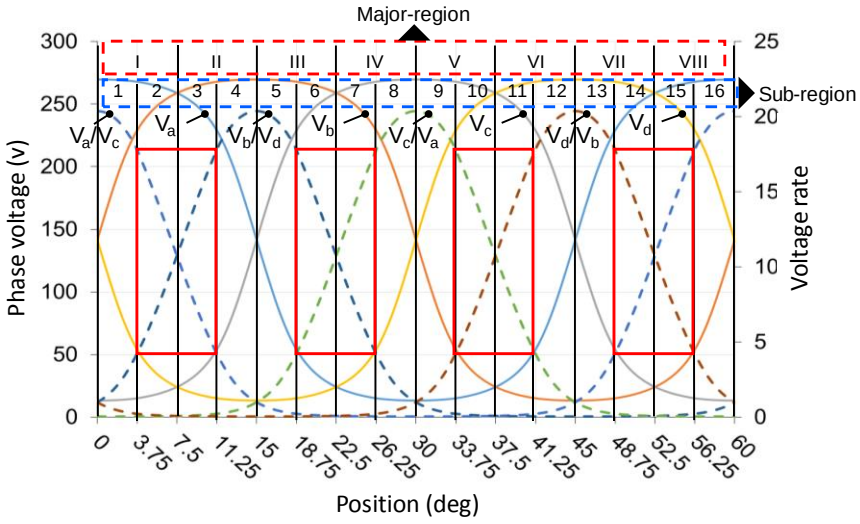

Figure 6.13 Phase voltage and voltage rate profiles when diagnostic pulses are injected into A- and C-phases, and B- and D-phases.

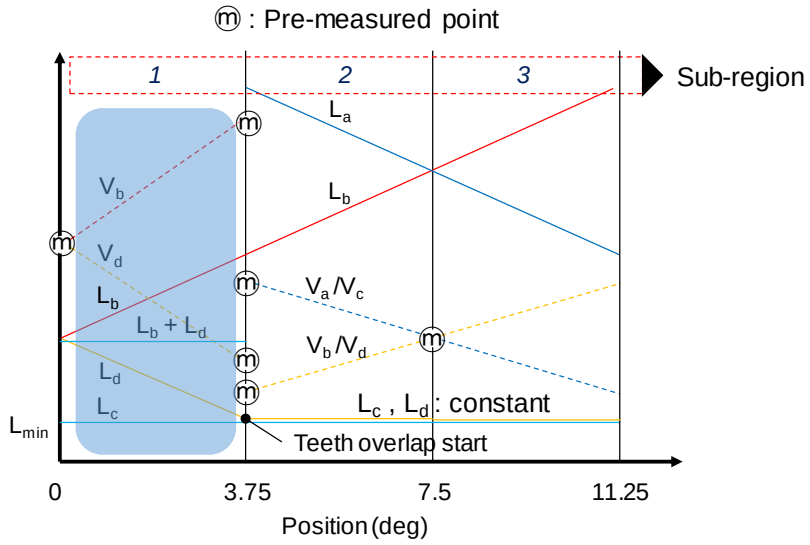

Figure 6.14 Simplified phase inductances and voltage rate profiles between 3.75 and 11.25[deg].

Consequently, by using the linear slope of the phase voltage and the voltage rate, the rotor position can be estimated simply for every rotor position. However, for the position estimation using the linear relationship of voltage and voltage rate, it must be firstly decided that which slope of phase voltage and voltage rate are used. To put how to decide simply, at first, the major region is selected through comparing of the phase voltages, then sub-region is selected through comparing the difference of measured phase voltage with pre-measured reference voltage difference at base position (0, 3.75 and 7.5 degrees). Depending on the found sub-region, the type of slope to be used for position estimation is selected. In detail, to select the slope to be used for position estimation, the sub-region (1-16) in figure 6.13 must be selected. For sub-region selection, the major-region (I-VIII) in figure 6.13 must be selected firstly. Major region can be selected by comparison of phase voltage. For example,

in major-region I, the relation in magnitude of phase inductance is as first line in equation (6.12), the magnitude order of inductance can be rearranged to equation (6.12).

$$\begin{aligned} & L_a \geq L_b \geq L_d \geq L_c \\ & \Rightarrow \frac{L_c}{L_a} \leq \frac{L_a}{L_c}, \quad \frac{L_b}{L_d} \geq \frac{L_d}{L_b}, \quad \frac{L_c}{L_a} \leq \frac{L_d}{L_b}, \quad \frac{L_a}{L_c} \geq \frac{L_b}{L_d} \\ & \Rightarrow \frac{L_c}{L_a} \leq \frac{L_d}{L_b} \leq \frac{L_b}{L_d} \leq \frac{L_a}{L_c} \quad \Rightarrow 1+\frac{L_c}{L_a} \leq 1+\frac{L_d}{L_b} \leq 1+\frac{L_b}{L_d} \leq 1+\frac{L_a}{L_c} \\ & \Rightarrow \frac{L_a}{L_a+L_c} \geq \frac{L_b}{L_b+L_d} \geq \frac{L_d}{L_b+L_d} \geq \frac{L_c}{L_a+L_c} \end{aligned} \tag{6.12}$$

From equation (6.5), equation (6.12) can be rewritten as follows,

$$V_a \geq V_b \geq V_d \geq V_c \tag{6.13}$$

The magnitude order of inductance is same as the thing of phase voltage. The relationship of magnitude of phase voltage at another major-region can be expressed as shown in table 6.3.

After selecting the major-region by using the voltage relationship in table 6.3, the sub-region is selected by comparing the phase voltage difference with reference value. For example, at major-region I, by comparing the phase voltage difference (V_b-V_d) of B- and D-phase with pre-measured phase voltage difference of B- and D-phase at 3.75[deg], sub-regions 1 and 2 are selected. Details about this will be explained in next section. Then the position can be estimated by using gradient of phase voltage difference (V_b-V_d) of B- and D-phase in sub-region 1, and using gradient of voltage rate difference (V_a/V_c-V_b/V_d) in sub-region 2.

In this study, the phase voltages and voltage rates at 0, 3.75, 7.5[deg] are informed as pre-measured value like ⓜ in figure 6.9 and 6.14. To measure the phase voltage for position

Table 6.3 The inductance and voltage relation according to major-region.

Major region	Sub region	Angle (degree)	Relation of inductance	Relation of phase voltage
I	1 to 2	0-7.5	$L_a>L_b>L_d>L_c$	$V_a>V_b>V_d>V_c$
		7.5	$(L_a=L_b)>L_c$ or $(L_c=L_d)<L_a$	$(V_a=V_b)>V_c$ or $(V_c=V_d)<V_a$
II	3 to 4	7.5-15	$L_b>L_a>L_c>L_d$	$V_b>V_a>V_c>V_d$
		15	$L_b>(L_a=L_c)>L_d$	$V_b>(V_a=V_c)>V_d$
III	5 to 6	15-22.5	$L_b>L_c>L_a>L_d$	$V_b>V_c>V_a>V_d$
		22.5	$(L_b=L_c)>L_d$ or $(L_a=L_d)<L_b$	$(V_b=V_c)>V_d$ or $(V_a=V_d)<V_b$
IV	7 to 8	22.5-30	$L_c>L_b>L_d>L_a$	$V_c>V_b>V_d>V_a$
		30	$L_c>(L_b=L_d)>L_a$	$V_c>(V_b=V_d)>V_a$
V	9 to 10	30-37.5	$L_c>L_d>L_b>L_a$	$V_c>V_d>V_b>V_a$
		37.5	$(L_c=L_d)>L_a$ or $(L_b=L_a)<L_c$	$(V_c=V_d)>V_a$ or $(V_b=V_a)<V_c$
VI	11 to 12	37.5-45	$L_d>L_c>L_a>L_b$	$V_d>V_c>V_a>V_b$
		45	$L_d>(L_c=L_a)>L_b$	$V_d>(V_c=V_a)>V_b$
VII	13 to 14	45-52.5	$L_d>L_a>L_c>L_b$	$V_d>V_a>V_c>V_b$
		52.5	$(L_d=L_a)>L_b$ or $(L_c=L_b)<L_d$	$(V_d=V_a)>V_b$ or $(V_c=V_b)<V_d$
VIII	15 to 16	52.5-60	$L_a>L_d>L_b>L_c$	$V_a>V_d>V_b>V_c$
		60	$L_a>(L_d=L_b)>L_c$	$V_a>(V_d=V_b)>V_c$

estimation, three voltage sensors are used at red sensing point as can be seen in figure 6.6. The measured voltage are dc-link voltage V_{DC}, the voltage between A- and C-phase V_{acg}, the voltage between B- and D-phase V_{bdg}. Subsequently, the phase voltages are calculated from below equations.

$$\begin{aligned} V_a &= V_{DC} + V_{acg} - V_{sw1}, \quad V_c = -V_{acg} - V_{sw2} \\ V_b &= V_{DC} + V_{bdg} - V_{sw1}, \quad V_d = -V_{bdg} - V_{sw2} \end{aligned} \tag{6.14}$$

Where V_{sw1}, V_{sw1} are the voltage drop across switching device as can be seen figure 6.6. About these values, the value described in the specification sheet of switching device can be utilized, however, in this study, the pre-measured values are used for exact position estimation.

6.3.4 Simplified phase voltage and voltage rate for position estimation

As mentioned earlier, by using the gradient of voltage or voltage rate decided in selected sub-region, the position can be estimated. Figure 6.15 illustrates the simplified voltage and voltage rate profiles with respect to position in major-region I and II. The value E, G, H and F are pre-measured values and X, Y are measured value at θ_x and θ_y, respectively. In next section, details of estimation procedure in accordance with speed condition will be explained.

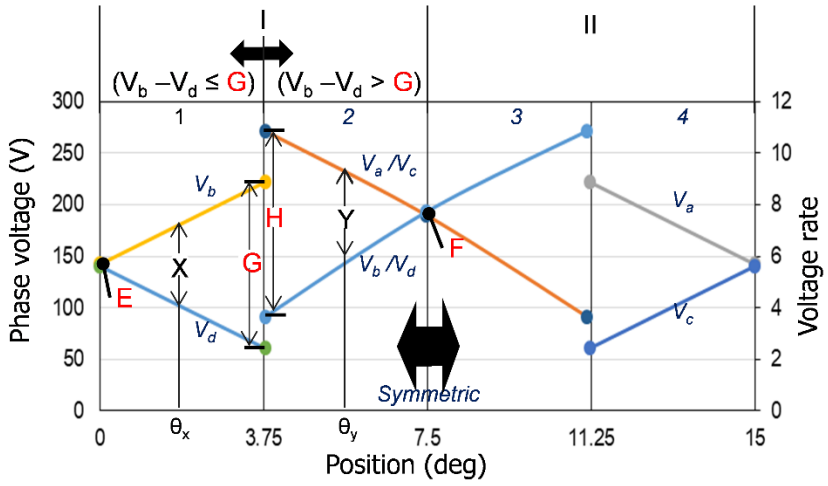

Figure 6.15 Simplified phase voltage and voltage rate in major-region I and II.

6.4 Procedure of rotor position estimation

The position estimation procedures at standstill and running state are explained. In addition, by using the estimation algorithm, a starting algorithm from the standstill state to running state is also presented.

6.4.1 Estimation procedure at standstill state

The procedure to find initial position at stand still state is explained. Estimation procedure consists of two stages. The first one is to find sub-region and the other is to calculate the rotor position based on the linear slope of the phase voltage or the voltage rate selected according to sub-region.

As can be seen in figure 6.13, the rotor position from 0 to 60 degrees is divided into eight

major regions (I-VIII). The major region, where the rotor is located at this moment, can be identified by comparing the phase voltage as shown in table 6.3. And then, the sub-region can be identified by comparing the phase voltage difference with reference value. As can be seen figure 6.15 depicting the simplified phase voltage and voltage rate in the major region I and II, the major region I can be divided into two sub-regions 1 and 2. According to sub-region, one of the phase voltage and voltage rate for position estimation is selected. For example, at the major region I, by comparing the voltage difference (V_b-V_d) of B and D phase with reference value G, the sub-region can be estimated easily as follows,

$$\begin{aligned} &if\ V_b - V_d \le G, \quad \text{sub-region} = 1 \\ &if\ V_b - V_d > G, \quad \text{sub-region} = 2 \end{aligned} \tag{6.15}$$

From figure 6.15, if the sub-region is selected, the rotor position can be estimated through linear relationship like below.

$$\begin{aligned} &if\ \text{sub-region} = 1, \quad \theta_x = 3.75 \times \frac{X}{G} \\ &if\ \text{sub-region} = 2, \quad \theta_y = 7.5 - 3.75 \times \frac{Y}{H} \end{aligned} \tag{6.16}$$

If sub-region is 1, the phase voltage is used for position estimation. If sub-region is 2, the voltage rate is used to estimate position. E and G are pre-measured phase voltages at 0 and 3.75[deg] and F and H are pre-measured voltage rate at 7.5 and 3.75[deg]. At other regions, the rotor position can be estimated by same procedures through the symmetricity of motor, assuming that the references value in other region have same value with E, F, G and H that is pre-measured values, e.g. in figure 6.15, the A- and C-phase voltages at 15[deg] are same with E, and the difference of voltage rate (V_b/V_d-V_a/V_c) at 11.25[deg] is same with H and etc.

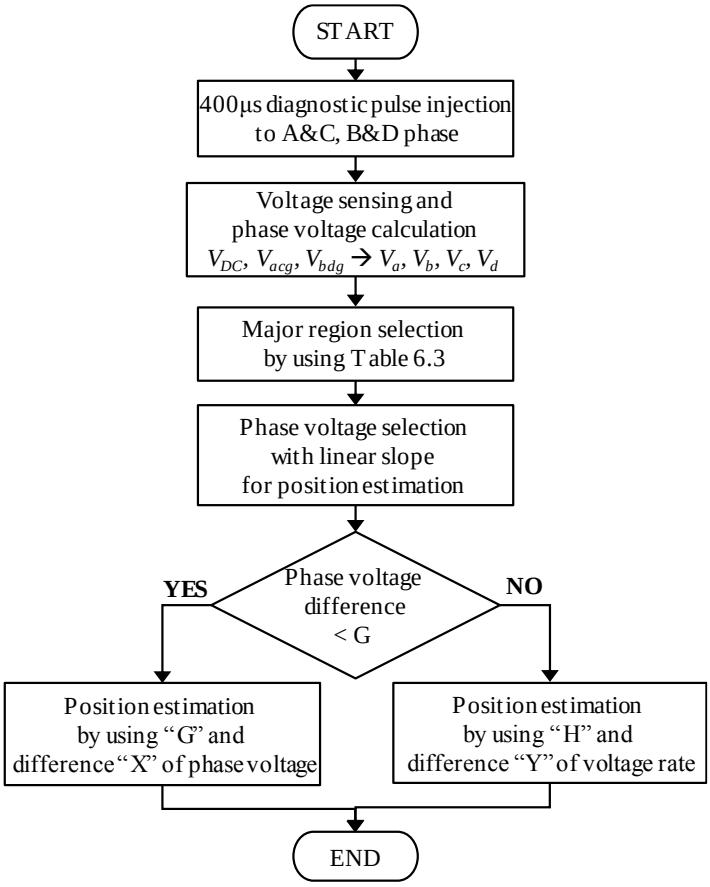

Figure 6.16 Flow chart for position estimation at standstill state.

Figure 6.16 shows the flow chart for position estimation at standstill state. In the standstill state, as all phases are inactive state, diagnostic pulse injection to all phases is possible. In addition, through pulse injection into all phases, the rotor fluctuation can be minimized. So, in the standstill state, the diagnostic pulse is injected into all phases. After injecting all phase pulses, V_{DC}, V_{acg} and V_{bdg} are measured, then the phase voltage V_a, V_b, V_c and V_d are calculated using equation (6.14). Through comparison of distributed phase voltage, major region is selected by considering table 6.3. Then, two phase voltages having linear slope at selected major region are selected. By comparing the difference of selected phase voltages with reference value G, sub-region is selected. For example, at major region III in figure 6.13, two phases voltages having linearity are V_a and V_c. if V_c-V_a is lower than G, the difference V_c-V_a of C- and A-phase in sub-region 5 is used for position estimation. And if V_c-V_a is higher than G, the difference (V_b/V_d - V_c/V_a) of voltage rate in sub-region 6 is used for position estimation. As shown in the flowchart, position estimation is conducted in accordance with sub-region. Table 6.4 summarizes the equations for calculation in accordance with sub-region.

6.4.2 Estimation procedure at running state

The procedure to find rotor position at running state is explained. As can be seen in figure 6.17, in the case of running state, one or two phases are turned on with respect to position.

Table 6.4 Position estimation equation according to region.

Major-region	Sub-region	Angle (degree)	Estimated position
I	1	0-3.75	$\theta = 3.75 \times \frac{(V_b - V_d)}{\mathrm{G}}$
	2	3.75-7.5	$\theta = 7.5 - 3.75 \times \frac{(V_a/V_c - V_b/V_d)}{\mathrm{H}}$
II	3	7.5-11.25	$\theta = 7.5 - 3.75 \times \frac{(V_a/V_c - V_b/V_d)}{\mathrm{H}}$
	4	11.25-15	$\theta = 15 + 3.75 \times \frac{(V_c - V_a)}{\mathrm{G}}$
III	5	15-18.75	$\theta = 15 + 3.75 \times \frac{(V_c - V_a)}{\mathrm{G}}$
	6	18.75-22.5	$\theta = 22.5 - 3.75 \times \frac{(V_b/V_d - V_c/V_a)}{\mathrm{H}}$
IV	7	22.5-26.25	$\theta = 22.5 - 3.75 \times \frac{(V_b/V_d - V_c/V_a)}{\mathrm{H}}$
	8	26.25-30	$\theta = 30 + 3.75 \times \frac{(V_d - V_b)}{\mathrm{G}}$
V	9	30-33.75	$\theta = 30 + 3.75 \times \frac{(V_d - V_b)}{\mathrm{G}}$
	10	33.75-37.5	$\theta = 37.5 - 3.75 \times \frac{(V_c/V_a - V_d/V_b)}{\mathrm{H}}$
VI	11	37.5-41.25	$\theta = 37.5 - 3.75 \times \frac{(V_c/V_a - V_d/V_b)}{\mathrm{H}}$
	12	41.25-45	$\theta = 45 + 3.75 \times \frac{(V_a - V_c)}{\mathrm{G}}$
VII	13	45-48.75	$\theta = 45 + 3.75 \times \frac{(V_a - V_c)}{\mathrm{G}}$
	14	48.75-52.5	$\theta = 52.5 - 3.75 \times \frac{(V_d/V_b - V_a/V_c)}{\mathrm{H}}$
VIII	15	52.5-56.25	$\theta = 52.5 - 3.75 \times \frac{(V_d/V_b - V_a/V_c)}{\mathrm{H}}$
	16	56.25-60	$\theta = 60 + 3.75 \times \frac{(V_b - V_d)}{\mathrm{G}}$

For example, in major-region I and II, phase B is turned on for torque production. And in major-region III and IV, phase C is turned on. As the phase is turned on in order of B→C→D→A, the series connected inactive phases that are possible to inject diagnostic pulse are changed A&C phase, B&D phase, C&A phase and D&B phase in order. In major-region I and II, since the A- and C-phase voltages V_a, V_c can be used, the linear gradients of the A- and C-phase voltages in the red box area of major-region II and the linear gradient of voltage rate V_a/V_c outside red box area can be used for position estimation. In addition, as next conduction phase C is generally turned on before 12[deg] at which stator teeth and rotor pole starts overlap, motor is fully operable even by the estimated position from 0 to 12[deg]and therefore, with the rotor position estimated only by using the voltage rate V_a/V_c about the region between 0 and 12[deg] the motor control is possible. In other regions, the voltage rate is only used for position estimation. As an example, in major-region V and VI, the next phase to be conducted is A-phase, the position information from 30 to 42 degrees generally is required, which can be estimated by using voltage rate V_c/V_a. Table 6.5 appears the inactive phases that diagnostic pulse can be injected, and equations for position estimation. If the next phase to be conducted or current conducting phase is informed, the diagnostic pulse injection phases can be decided.

Figure 6.18 shows the voltage rate V_a/V_c of A- and C-phase having linearity between 3.75 and 11.25[deg]. In this figure, because a measurement of voltage rate of B- and D-phase impossible, V_b/V_d expressed as dotted line. After detecting the A- and C-phase voltage, the rotor position can be estimated by using the voltage rate of A- and C-phase and below equation.

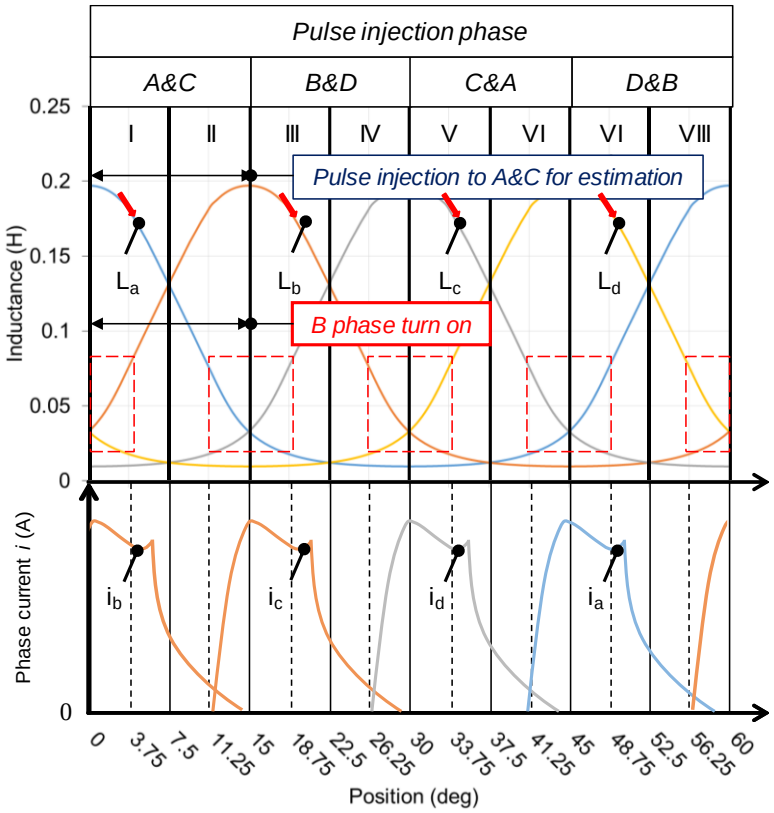

Figure 6.17 Current conduction and decision of pulse injection phase according to position.

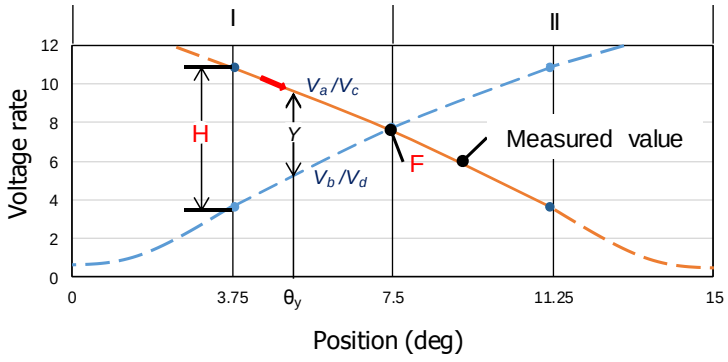

Figure 6.18 Simplified voltage rate profile when diagnostic pulse is injected into A- and C-phase in major-region I and II under running state.

Table 6.5 Phase selection for pulse injection and equations for position estimation.

Current turn-on phase	Next turn-on phase	Pulse injection phase	Position estimation
B	C	A&C	$\theta = 7.5 - 3.75 \times \frac{2(V_a/V_c - \mathrm{F})}{\mathrm{H}}$
C	D	B&D	$\theta = 22.5 - 3.75 \times \frac{2(V_d/V_b - \mathrm{F})}{\mathrm{H}}$
D	A	C&A	$\theta = 37.5 - 3.75 \times \frac{2(V_c/V_a - \mathrm{F})}{\mathrm{H}}$
A	B	D&B	$\theta = 52.5 - 3.75 \times \frac{2(V_d/V_b - \mathrm{F})}{\mathrm{H}}$

$$Y = 2 \times \left(\frac{V_a(\theta_y)}{V_c(\theta_y)} - F\right) \Rightarrow \theta_y = 7.5 - 3.75 \times \frac{Y}{H} \tag{6.17}$$

F and H is the pre-measured values at 3.75 and 7.5[deg]. Assuming that the difference Y of voltage rate is two times of (V_a/V_c - F), the rotor position is calculated using same equation used in stand-still state. In table 6.5, the position estimation equation is expressed in accordance with region. Figure 6.19 is the flow chart for position estimation at running state. The phase for pulse injection is selected by next turn-on phase. The phase voltage is detected after pulse injection. By using the detected voltage rate, pre-measured value F and H, position estimation can be conducted.

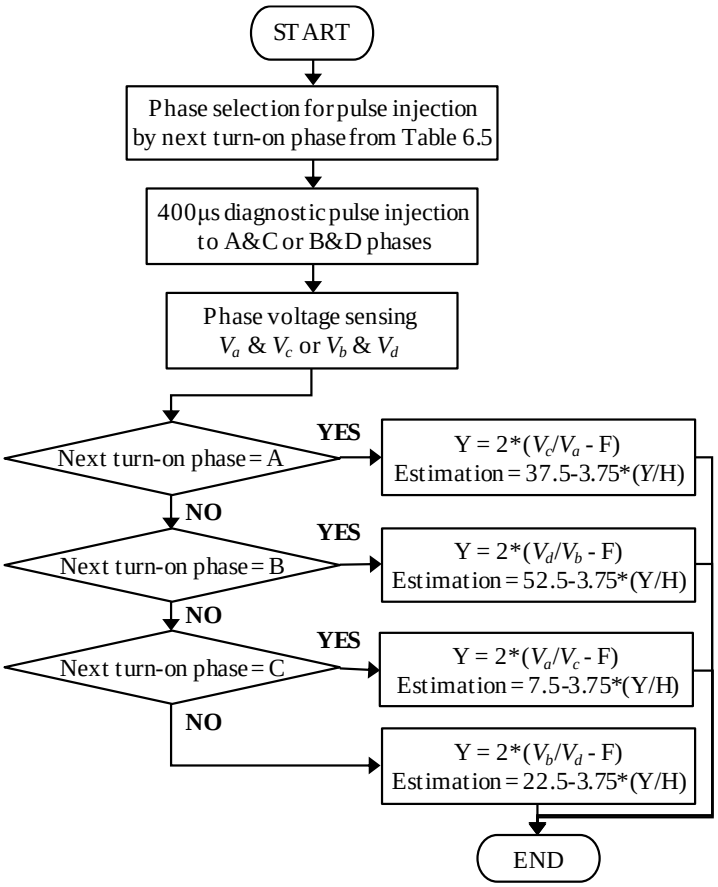

Figure 6.19 Flow chart for position estimation at running state.

6.4.3 Starting algorithm from zero to running state

In order to drive test motor from stand still state to running state, the starting algorithm is figured out. As can be seen in figure 6.20, at the state lower than 5[r/min], through the algorithm of figure 6.16, the initial position $\theta_{est\_initial}$ is estimated. Then corresponding phase is conducted after 20msec delay. At running state (over than 5[r/min]), the instant position $\theta_{est\_running}$ is estimated by using the algorithm of figure 6.19. In running state, the number of

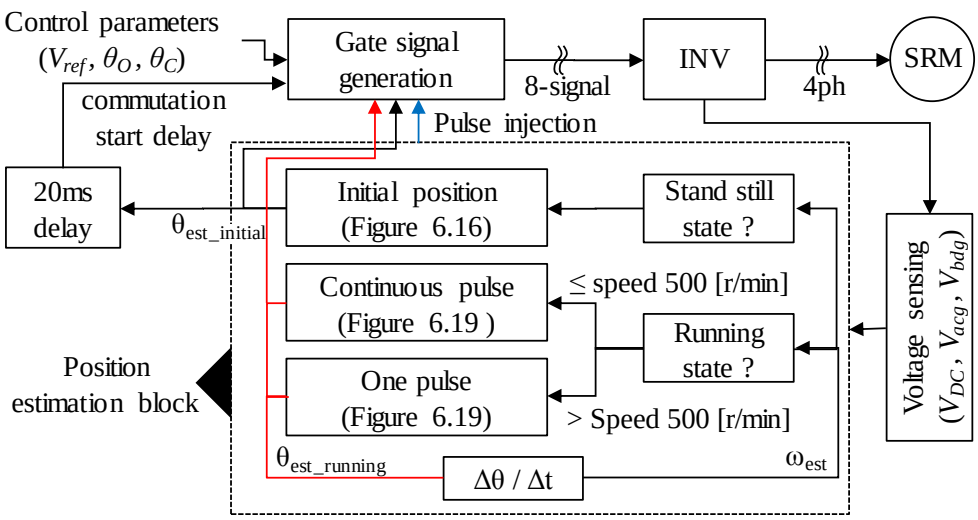

Figure 6.20 Block diagram of starting algorithm.

diagnostic pulse is changed according to the speed. If the speed is beyond reference speed (500[r/min]), injected pulse is changed from continuous pulses to one pulse. In high speed, because of long tail current, the time for pulse injection is not enough. the diagnostic pulse must be injected at zero current state to prevent inductance variation by magnetic saturation. As a result, as the time required for current to be zero becomes shorter by long tail current in high speed, in the worst case, only one pulse in one electrical cycle may be allowed for position estimation. To verify the sensorless performance in this worst case, one pulse injection was considered.

In one pulse injection, for continuous position estimation every PWM, the estimated angular speed ω_{est} calculated by using estimated position variation $\Delta\theta$ and time variation Δt between diagnostic pulses is used. The position at each PWM between estimated position and next position to be estimated can be estimated by,

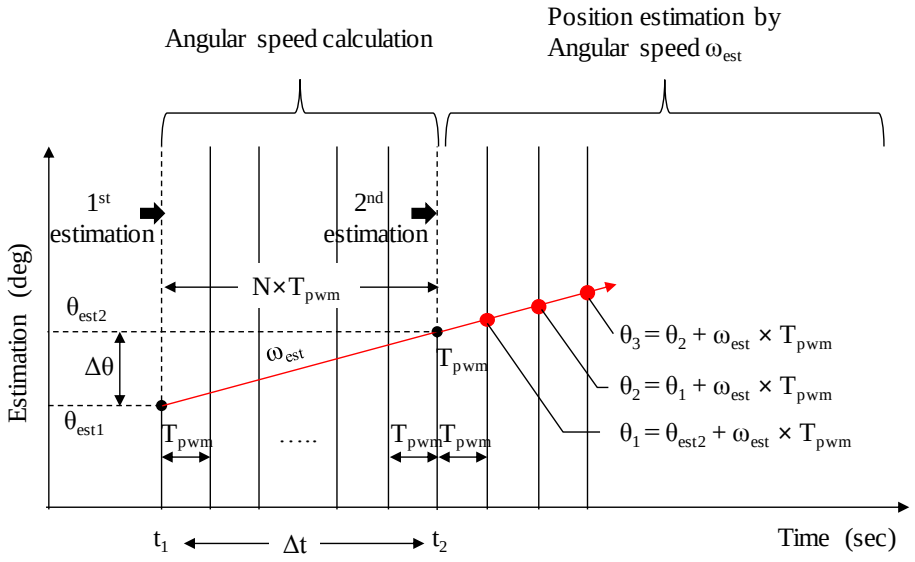

Figure 6.21 Position estimation at each PWM using angular speed ω_{est}.

$$\omega_{est} = \frac{\Delta\theta}{\Delta t} = \frac{\theta_{est\_2} - \theta_{est\_1}}{N \cdot T_{pwm}}$$
$$\Rightarrow \ \theta_0 = \theta_{est\_2}, \quad \theta_{n+1} = \theta_n + \omega_{est} \cdot T_{pwm} \tag{6.18}$$

where, θ_{est_2} is the estimated location by the last pulse injection as can be seen in figure 6.21. θ_{est_1} is the estimated position by the previous pulse of the last pulse. N is PWM count between θ_{est_1} and θ_{est_2}. After θ_{est_2}, the position θ_{n+1} is calculated by using above equation. The PWM control with constant voltage reference is used in this study. Current feed-back control is not used. Current sensor is used just for protection of current limit.

6.5 Experiment results

To verify the effectiveness of sensorless algorithm, experimental studies using the test motor are conducted. Firstly, experimental equipment is explained. Subsequently, the

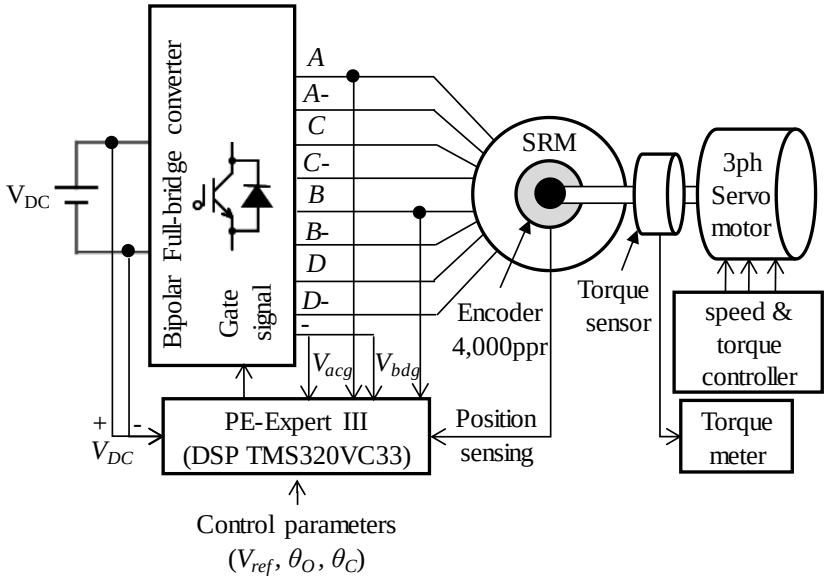

Figure 6.22 Block diagram of experimental equipment.

position estimation through the diagnostic pulse with ON period of 400[usec] is conducted under the standstill and under the running state at 300[r/min] with the rated torque. Finally, through starting algorithm, it is verified that test motor safely starts from zero to running state with small estimation error.

6.5.1 Experimental equipment configuration

Figure 6.22 is the configuration of experimental system. For driving the motor, a bipolar full bridge converter controlled by PE-Expert III (Myway Plus Corporation) is used. To get real position information for comparing with estimated rotor position, the incremental encoder (OM Corporation) with resolution of 4000 [ppr] is used. As a load, a servo motor (SGMSH-15A, Yaskawa Corporation) is connected to the SRM and controlled as constant

torque or speed mode. The voltage sensor (LV-25P, LEM Corporation) is attached on converter for voltage sensing of V_{DC}, V_{acg}, V_{bdg}. Current sensor is used just for protection of current limit.

6.5.2 Estimation performance according to operating condition

Experimental studies on position estimation ability of the proposed method is firstly conducted at standstill and 300 [r/min] running state. Diagnostic pulse with magnitude 283[V] and ON period 400[μsec] is injected in both cases. Figure 6.23 demonstrates the voltage and current waveforms when diagnostic pulse is turned on and off with 400[μsec] ON period at rotor position θ=11.25[deg]. For exact position estimation, measurement point (data pickup) is very important. Because 10[kHz] PWM is used for control, control period is 100[usec] and four measurable point (#1~#4) of voltage is considered as shown in figure 6.23. If the current is higher than 0.6[A], magnetic saturation occurs and current will be nonlinear and voltage has some error like point A. So, measurements at #2, #3 have some error due to inductance variation by magnetic saturation due to high current more than 0.6[A]. In point B, ringing is produced by switch capacitance, line resistance and inductance at switching instant. In point C, there are some delay between real voltage (V_{acg}, V_{dc}, V_c) and measured voltage (V_{acgs}, V_{dcs}, V_{cs}) due to the time constant of filter circuit and voltage sensor response delay. Total delay time of sensing circuit from input to output considering 5τ(5 times of time constant) of low pass filter is about 128[μsec]. As a result, measurement at point #1 has also some error with real value due to time delay of voltage sensor. As a result, of four measurable points, #4 has small measurement error. From now, the voltages measured at

point #4 that is 700[μsec] after applying the pulse voltage is used for position estimation. In this case, note that equation (6.14) to calculate phase voltage must be modified as following fashion because the point #4 is switch off state.

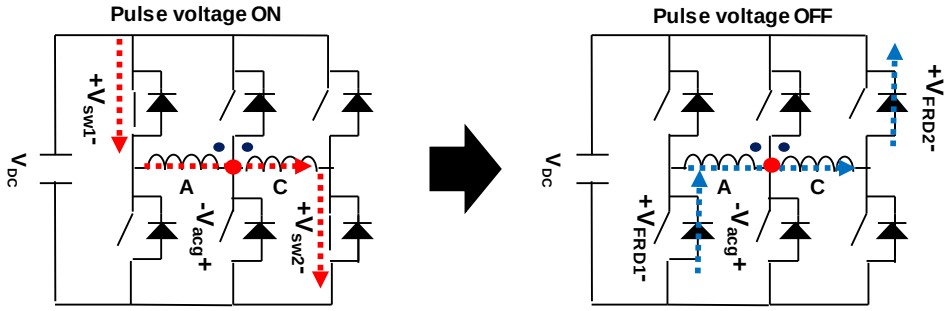

[Switching status variance]

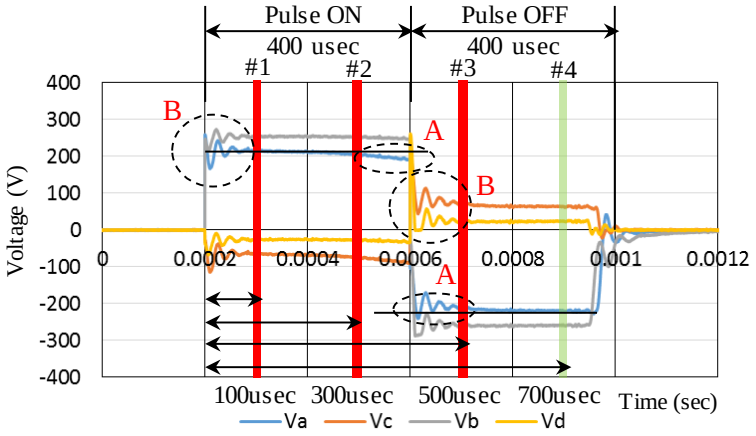

[Phase voltage]

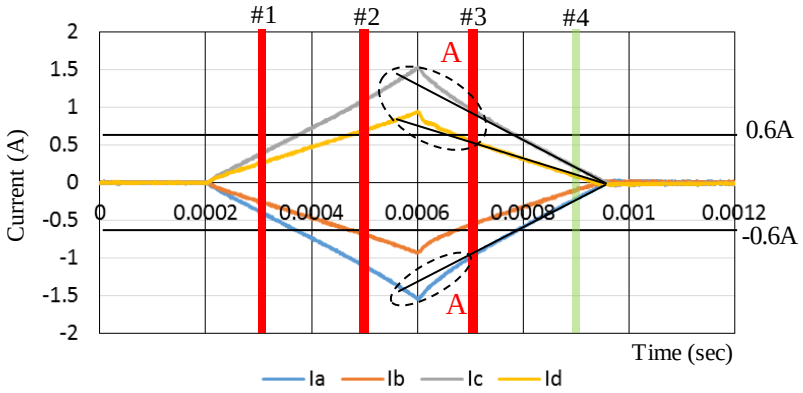

[Phase current]

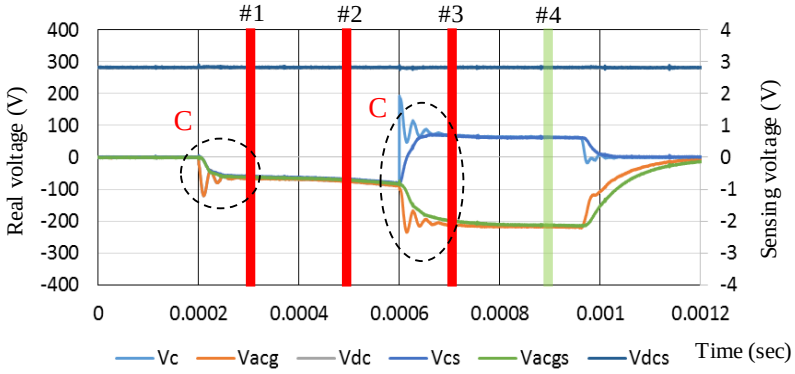

[Real and Sensing voltage]

Figure 6.23 Voltage and current at the pulse injection instant on rotor position 11.25[deg] for decision of measurement point.

$$V_a = -V_{acg} - V_{FRD1}, \quad V_c = V_{DC} + V_{acg} - V_{FRD2}$$
$$V_b = -V_{bdg} - V_{FRD1}, \quad V_d = V_{DC} + V_{bdg} - V_{FRD2} \tag{6.19}$$

Through experiment, the average value of V_{FRD1}, and V_{FRD2} in the current condition lower than 0.6[A] is measured as -0.26, -0.27[V]. When the voltage is measured at data sampling point #4, the moving average value for 20[μsec] is used to reduce the influence of

measurement noise. And the pre-measured value E, F, G and H are obtained from the measure phase voltage at 0, 3.75, 7.5[deg] as can be seen in figure 6.24. The average value of the measured values at 0 and 7.5[deg] will be taken as E and F value. So E = 141.3, F = 7.65, G = 161.2, H = 7.21 are selected as reference values.

As can be seen in figures 6.25 and 6.28, measurement is conducted at the data sampling point that is 700[μsec] after applying the diagnostic pulse and the phase voltage is calculated using the measured voltages V_{acg}, V_{bdg} and V_{DC}. At the data sampling point, the maximum phase current is lower than 0.6[A] to prevent from magnetic saturation.

1) Position estimation at standstill state

Figure 6.26 shows the estimation result under the standstill at the region between 0 and 30 [deg] as a mechanical angle. The maximum error of in this region is 0.33 [deg]. In

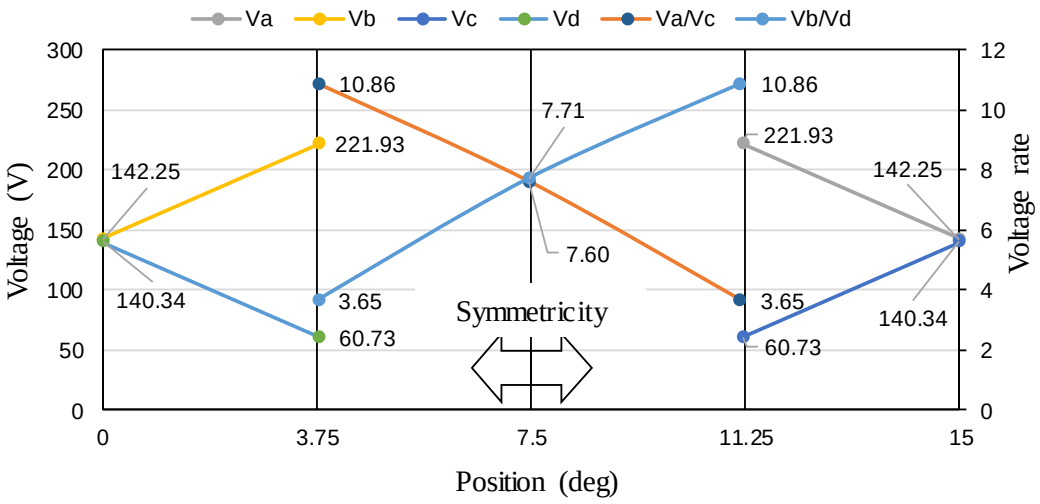

Figure 6.24 Pre-measured values at the position 0, 3.75, 7.5[deg].

conventional method using only the gradient of phase voltage, max error was 2.44[deg].

2) Position estimation at running state

Under the condition of 300[r/min] and the rated torque of 1.27[Nm], the same diagnostic pulse used in standstill state is injected at 3[deg] ahead of θ_O with 15 [deg] interval. The real

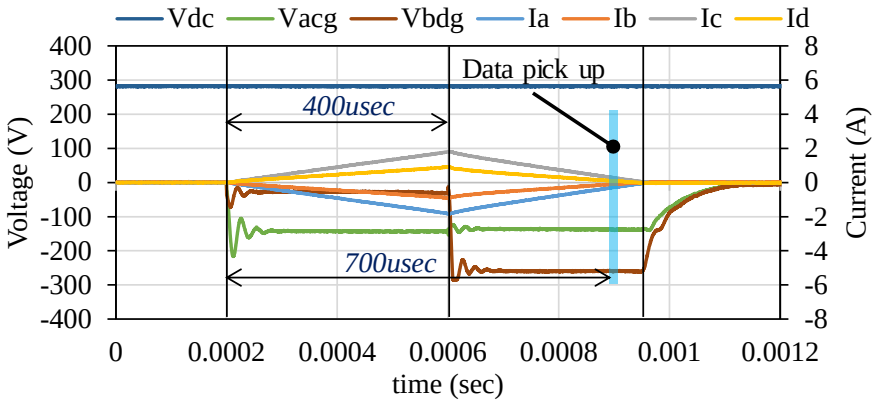

Figure 6.25 Injected voltage and current into A&C and B&D phase in standstill state at rotor position 15 [deg].

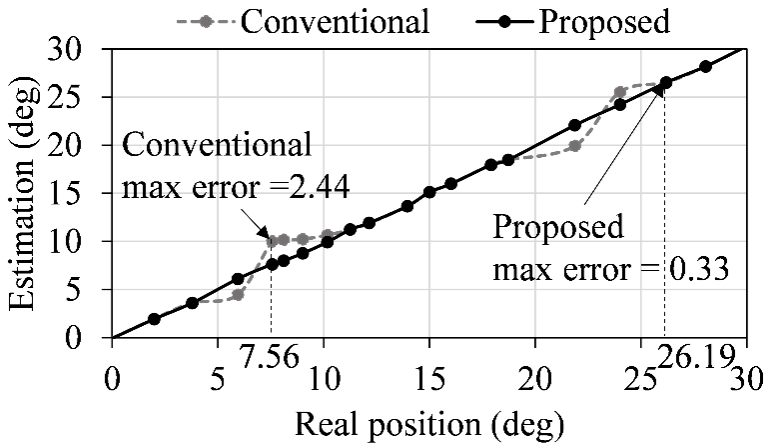

Figure 6.26 Position estimation results at standstill state from 0 to 30 mechanical degree.

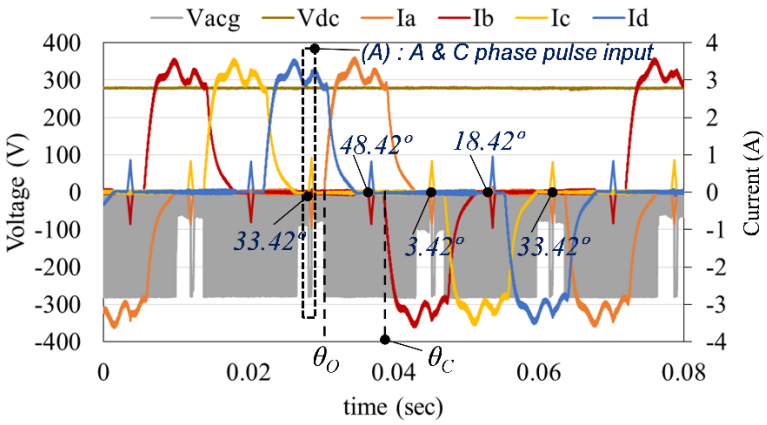

Figure 6.27 Voltage and current waveforms under pulse injection at 300 [r/min], 1.27[Nm] load, V_{ref}, = 39.6[V], θ_O = 38.14 [deg], θ_C = 54.03 [deg].

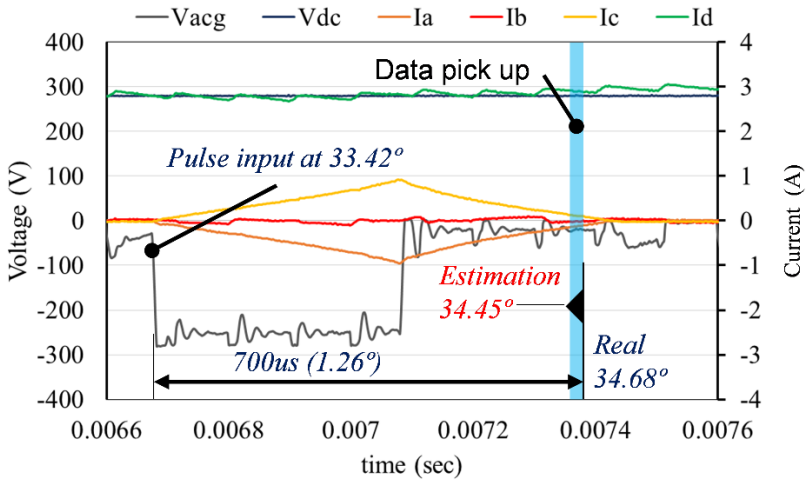

Figure 6.28 Enlargement of (A) in figure 6.27 – injected voltage and current into A and C phase at running state.

rotor position at the sensing point of position (A) in figure 6.27 is 34.68 [deg], the estimated position is 34.45 [deg]. The error of estimation is just 0.23 [deg]. As a result, in both states of stand-still and running state, the error of position estimation is minimized by using the

method using the gradient of phase voltage and voltage rate.

3) Verification of starting algorithm

Experiment to verify the proposed starting algorithm is conducted. The test is conducted under no load and rated torque condition. Figure 6.29 shows the result at no load condition.

The voltage reference V_{ref} is 30[V], on angle θ_O is set to 42 [deg] and commutation angle θ_C is set to 57 [deg]. The test motor runs well from zero to 680[r/min] with small average position estimation error 0.51 [deg] in the region having the voltage rate of linear gradient. As can be seen in figure 6.29 (c), at 20[msec] after initial position estimation, the test motor begins to start through conduction of proper phase based on estimated position. Simultaneously, through continuous pulse injection, continuous position estimation is conducted. Then, the injected pulse is changed from continuous pulse to one pulse after 500[r/min]. In the rated torque (1.27Nm) condition, the test motor starts well from zero to 200[r/min] with small average estimation error 1.21 [deg] in the region having the voltage rate of linear gradient as can be seen in figure 6.30. In this experiment, V_{ref} is 33[V], θ_O is 42 [deg], and θ_C is 57 [deg]. Like a no-load test, at 20[msec] after initial position estimation, the test motor begins to start through conduction of proper phase based on estimated position. However, position estimation using continuous pulse is only conducted as the speed is less than 500[r/min].

The table 6.6 summarizes the average estimation error at the initial acceleration region from the standstill state and the constant speed region under the different driving condition. The error in the region where the gradient of voltage rate is linear is measured. The position estimation error in the rated load condition become slightly larger than that measured under

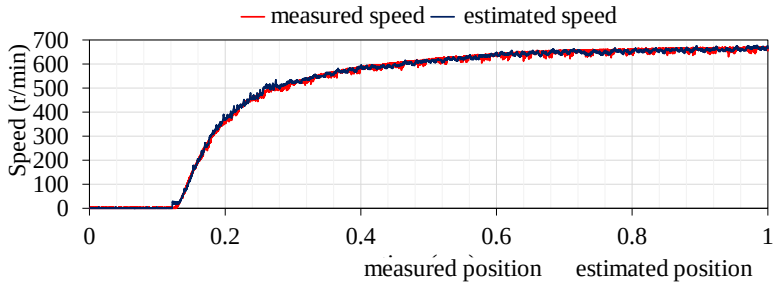

(a) measured and estimated speed profile

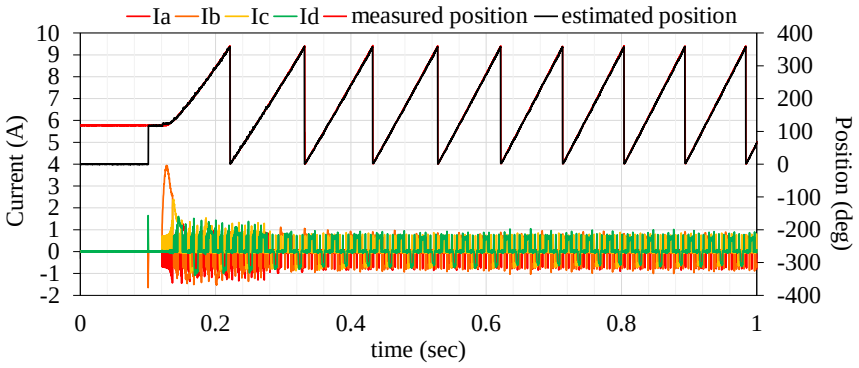

(b) measured and estimated position and real current profiles

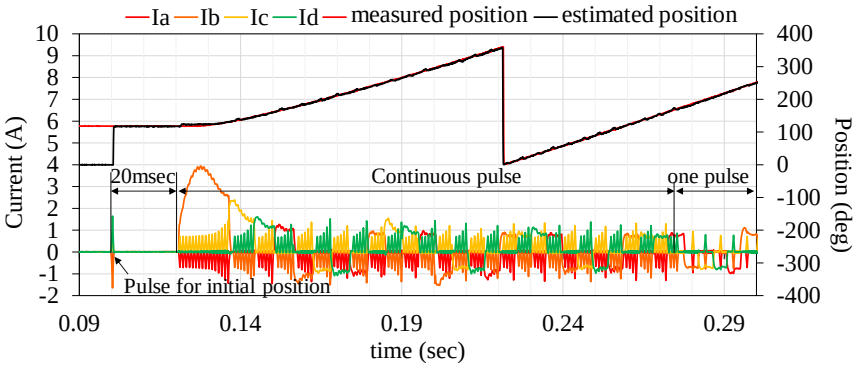

(c) enlargement of (b)

Figure 6.29 Starting up of test motor under no load condition, V_{ref} = 30[V], θ_O = 42 [deg], θ_C = 57 [deg].

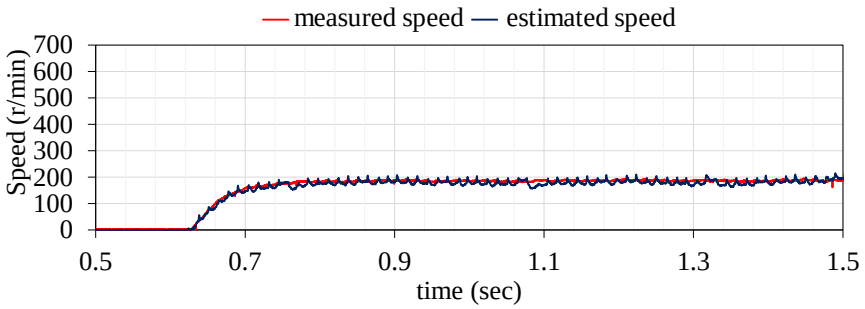

(a) measured and estimated speed profiles

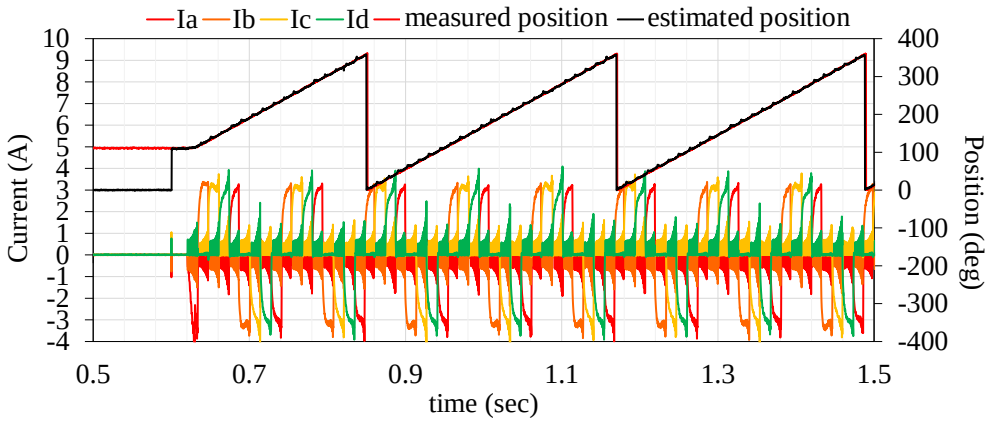

(b) measured and estimated position and real current profiles

Figure 6.30 Starting up of test motor under the rated load condition, V_{ref} = 33[V], θ_O = 42 [deg], θ_C = 57 [deg].

no load condition. The reason why the position estimation error under the rated torque condition in figure 6.28 is small is that the influence of mutual flux linkage by current conduction of active phase is small at 34.68[deg] near unaligned position. In addition, the reason is because the linearity error of the voltage rate is relatively small in 34.68[deg]. In

Table 6.6 Average position estimation error under different driving condition.

Driving condition		Average position error during 3[sec], (deg)	
Torque (Nm)	Speed (r/min)	Acceleration region	Constant speed region
No load	680	0.51	0.507
Rated (1.27)	200	1.21	1.16

overall range under rated torque condition, the estimation error increases. This is concerned with low estimation counts by diagnostic pulse with long period 400 [μsec], motor dimension tolerance and mutual coupling by active phase current. From a motor dimension point of view, if the SRM with rectangular shape rotor pole is used for position estimation, estimation accuracy can be improved. As can be seen in figure 6.31 (a), the gradient of inductance profile on area A of SRM with rectangular pole rotor has linearity compared with the test motor employing the fillet pole rotor. And in area B, inductance L_c and L_d is similar shape and linearity of L_a, L_c is same level in both motors. In the region from 0 to 3.75[deg], the linear region of L_a is more long in the case of motor using rectangular pole shape rotor.

As a result, in the region A, the phase voltage of the motor with rectangular pole rotor is more linear, resulting in small position estimation error. Owing to the long linearity of L_a in the motor with rectangular pole rotor as shown in region D of figure 6.31 (a), the measurable range in the motor with rectangular rotor is longer than the motor with fillet rotor and has small error like C of in figure 6.31 (b). in the region B, the estimation error is same level in both motor. After all, if the general motor with rectangular shape rotor pole is used, the estimation accuracy can be improved in both standstill and running state.

However, in other circumstances, there are still remaining the estimation error by motor

dimension tolerance and influence of mutual coupling effect by adjacent phase current. So, the study concerning above contents to reduce position estimation error under high load condition must be conducted in the future.

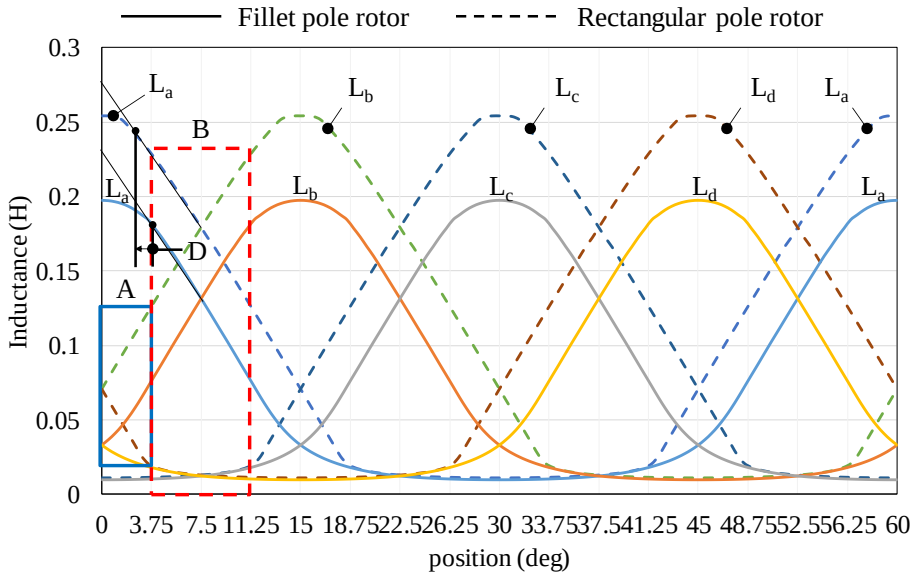

(a) inductance profile

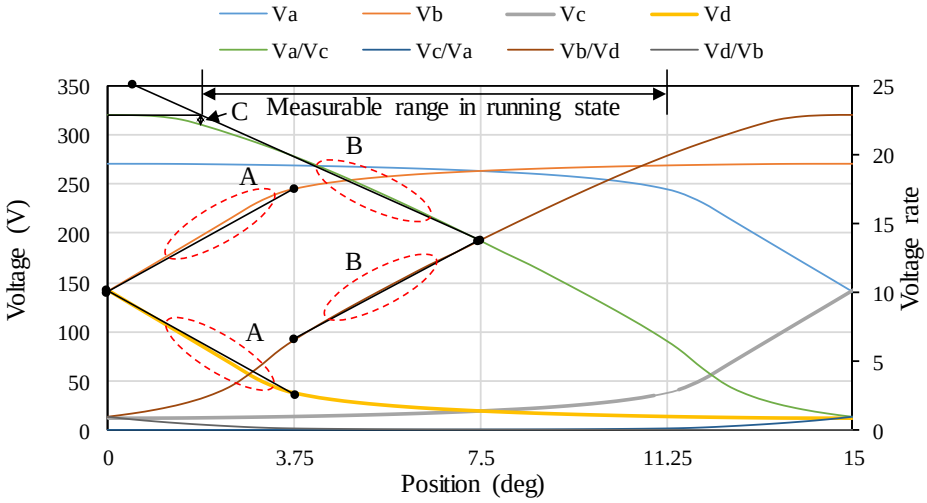

[Rectangular pole rotor]

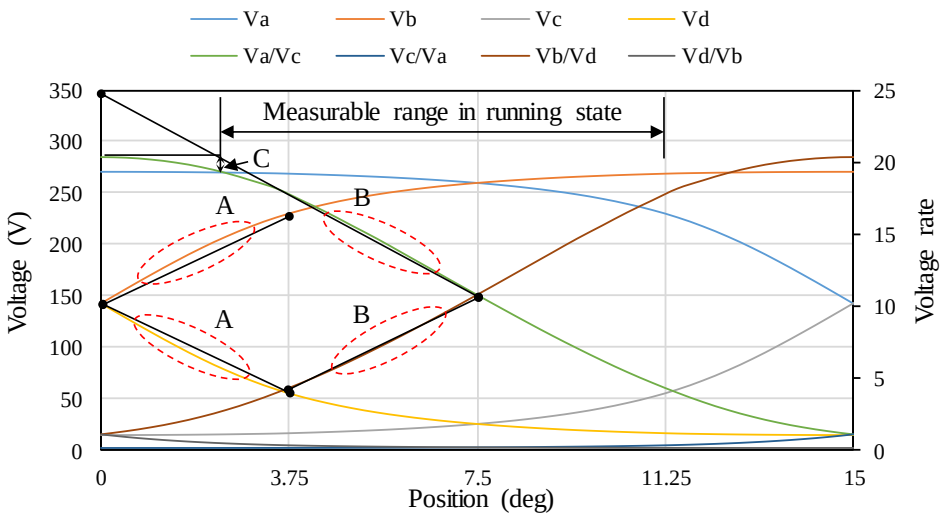

[Fillet pole rotor]

(b) phase voltage and voltage rate

Figure 6.31 comparison of inductance profile, phase voltage, and voltage rate in accordance with shape of rotor pole.

6.6 Epilogue

In this chapter, to solve the common drawbacks of general position estimation methods, the method that had no use of the current sensor, huge data table and complex calculation concerned with inductance or magnetic flux linkage was proposed as an economic and simple method. In the proposed method, the gradient of phase voltage and voltage rate obtained by using three voltage sensors were just used for the estimation. Therefore, this method was simple to implement with algorithm, economic. It was revealed by experimentally that in starting condition, this algorithm worked well from zero to running speed with small estimation error.

Chapter 7
Conclusion

7.1 Results obtained from this study

To reduce greenhouse gas emission, all electric motors have been forced to increase their efficiency. Therefore, the high-efficient PMSMs using rare-earth magnets have been used widely.

However, rare-earth magnets have the risk of supply anxiety and price increase. As a countermeasure against that, many kinds of rare-earth magnet free motors have been considered. At the center of that, SRM has emerged as an alternative. However, SRM is not widely used due to the aforementioned drawbacks. Of them, first one is large vibration and loud acoustic noise. Second one is high torque ripple. Last one is expensive and complicate position sensorless algorithm. To overcome these drawbacks, in this study, the following researches were carried out.

1) Improvement of vibration minimization performance of the conventional two-stage commutation method through the new modified method.
2) Torque ripple minimization through the modified current profiling control considering mutual coupling effect.
3) Simple and economic sensorless algorithm with small error in wide speed range.

The results of each theme are like below.

In chapter 1, Environmental issues about the supply problem of rare-earth materials were introduced. To overcome this circumstance, as the alternative motor without rare-earth magnets, SRM was introduced. However, SRM has drawbacks caused due to the nature of general driving methods. The drawbacks were explained and to overcome these, the purpose of this study was presented.

In chapter 2, the principle of vibration generation in SRM was explained through mathematical analysis. It was analyzed that the large vibration is generated when the spatial second order harmonics of radial force distributed along with airgap are matched with the circular 2^{nd} order vibration mode with the natural frequency of stator body. From this principle, the vibration production mechanism at commutation was explained. And then, the conventional two-stage commutation method to minimize this vibration was explained.

In chapter 3, the problem that the conventional two-stage commutation method does not work well under high speed and load condition, was explained. Through 2-D FEA and mathematical analysis, it was revealed that the problem was caused by the magnetic flux saturation in high load condition. To solve this problem, new modified two-stage commutation method was proposed. Through experiment, the effectiveness of vibration and acoustic noise reduction of proposed method was verified.

In chapter 4, the conventional torque ripple minimization method through instantaneous current profiling control that was proposed prior study, was explained. This conventional method was used for exact position control in all rotor position. However, because the target current profiles in the conventional method is calculated from the i-T-θ model obtained from the magnetizing curve un-considering mutual coupling effect by adjacent phase, the torque

ripple in the current overlapping region was increased as the load torque increases. Through 2-D FEA, the reason of this problem was revealed.

In chapter 5, to reduce the torque ripple produced by mutual coupling effect, the modified current profiling control method was proposed. The modified i-T-θ model considering mutual coupling effect was introduced for target current profile calculation. Through this method, it was verified that the torque ripple in the current overlapping region became lower than ±5% of average torque through experiment.

In chapter 6, the position sensorless algorithms of SRM that had been studied until now, were summarized. Through the analysis of the strong and weak points about representative methods, it was figured out that almost methods need huge data table and complex calculation about inductance or magnetic flux linkage that have position information. Also, for measurement of current and voltage required to calculate inductance or magnet flux linkage, the expensive current sensor with high performance is required. As a result, general position sensorless method is expensive and complicate. Therefore, the study for economic position estimation method with simple algorithm and small error in wide speed range, was set as a goal. To achieve the goal, the position estimation method using the linear slope of phase voltage and voltage rate was proposed. In this method, three voltage sensors were only used to calculate the phase voltage distributed by the diagnostic pulse injected into series connected phases. Because the linear gradient of voltage and their rate was only used for position calculation, any data table or complex calculation about inductance or flux linkage was not required. Through experiment, it was verified the proposed method has small estimation error lower than 1.21[deg] even under rated load condition when starting up from

zero speed.

7.2 Remaining challenges and prospects

In this chapter, the remaining challenges and prospects of SRM is explained.

In the case of vibration minimization using modified two-stage commutation method that was explained in chapter 3, only copper loss was considered as the power loss in the optimization. However, because the iron loss makes up big portion of power loss in SRM, the parameter optimization considering iron loss is required for high efficiency control. In addition, to get rid of the vibration produced before commutation interfering perfect vibration cancellation through two-stage commutation, the fillet shape rotor pole was designed in chapter 3. However, the rectangular shape pole rotor is generally used in SRM. Therefore, to use the proposed two-stage commutation method in SRM with rectangular shape rotor pole, the study of the two-stage commutation method to have the same vibration reduction performance without changing the rotor pols shape, e.g. the study to eliminate the total vibration combining the vibration produced at overlap point of stator and rotor tooth and the vibration produced at first commutation, is required.

In the case of torque ripple minimization, through the modified current profiling control considering mutual coupling effect, the torque ripple at current overlapping region was almost minimized. However, each torque profile of 24 strokes in one revolution varies with small variance. This variance is caused by the different magnetizing characteristics at each stroke due to the deviation of structural dimension of motor. In the study, it was assumed that all phases have same magnetizing characteristics with that of A-phase. However, the

magnetizing curves are different at each stroke. To solve this problem, the study about the method considering the magnetizing characteristics for every stroke is required. And as mentioned in chapter 5, in the proposed method, the torque ripple minimization control is possible no matter where the current overlapping occurs and therefore, the operation angle parameters can be selected with more degree of freedom to minimize the copper loss while keeping torque ripple minimum. By using this strong point, the optimization of control angle θ_{lap}, θ_{fo} for high efficiency torque ripple minimization is required.

Lastly, in the case of sensorless algorithm, by using the gradient of phase voltage and voltage rate calculated from the voltage measured by using three voltage sensors, rotor position was estimated simply and exactly in wide speed range. However, accuracy is not sufficient for precision control due to the inductance variance by dimensional deviation and the influence of mutual magnetic flux linkage, and the distortion of linearity in phase voltage by fillet shape of rotor pole. To minimize the estimation error by fillet shape, the study to compensate for the distortion of phase voltage caused by fillet shape is required. And The study to compensate the estimation error produced by mutual coupling effect is required.

Through the control method studied in each chapter, the problems with the conventional control methods were solved. As a result, the large vibration at high speed region and the high torque ripple at low speed region that were drawbacks of SR servo system were solved by using modified methods. And also, the economic and simple position sensorless algorithm usable in wide speed range was developed. In the end, through compensation for the drawbacks that have been an obstacle in competing against PMSM, the possibility of field application of SRM as an alternative motor that do not use rare-earth magnets, was increased.

Acknowledgments

First of all, i would like to thank Professor Kosaka Takashi who has helped me concentrate on my successful research in NITech for three and a half years, and it was a great honor for me to meet him. Whenever i run into difficulties, he always thinks together and gave me great suggestions or inspirations to solve problems quickly and actively. I appreciate about all his contribution of time, idea and passion for my work. I always admire him who try to think and solve problems scientifically and logically. In particular, i appreciate for his help in preparing this thesis to the last.

I would also like to thank assistant Professor Matsumori Hiroaki for kind teaching whenever i ask. Thank for your enthusiasm for the research. I wish him to be a great researcher and scientist.

I would like to thank Professor Iwasaki Makoto and Professor Morita Yoshifumi for their enthusiastic review about this thesis. I really appreciate their advice about contents of thesis as well as encouragement about my future during the review of this thesis.

And I'd like to thank Professor Matsui Nobuyuki for giving me lots of advice and sincere encouragement whenever i meet at the conference. I really wanted to meet him once in my life, and it was a great honor to meet him. I admire him academically and humanely. I still cannot forget the first meeting at the ICEMS 2017 conference in Australia.

I also would like to thank Professor Takemoto Shinji of Hokkaido University, Professor Akatsu Kan of Shibura Institute of Technology and Professor Kondo Keiichi of Waseda University as well. I appreciate for listening to my thesis and giving me a lot of advice and encouragement when I meet them at conference.

I would like to thank Professor Nam Kwang-Hee of Pohang University of Science and Technology for introducing me to Professor Kosaka Takashi when I was hesitating which school should i go. Thanks to you, I was able to make successful results with a respectful professor.

I also would like to thank all past and present member of Kosaka & Matsumori Lab. especially the SRM team, for their kind help and a passionate look in their studies. Let's everybody be the best engineers no matter where you are working.

I would like to say that “i love you” to my wife, Jeon In-Soon, and two daughters Yunseo

and Seoyeon who have lived well despite of difficult circumstance in Japan. Thank you very much for trusting me and following me even in difficult situations.

I would like to thank my parents who made me born and raised me. Thank you very much. I love you. I could be here thanks to mom and dad.

Finally, i would like to thank everyone who was important part of my life, and also to apology that i could not mention personally one by one.

June 17, 2019

Shin Sung Yong

References

(1) https://www.epa.gov/ghgemissions/global-greenhouse-gas-emissions-data ／ EPA (United States Environmental Protection Agency)

(2) https://www.globalcarbonproject.org/global/images/carbonbudget/Infographic_Emissions2018.pdf / Global Carbon Budget 2018 of Global Carbon Progect.org

(3) Franck Betin, Gerard-Andre Capolino, Domenico Casadei, Basile Kawkabani, Radu Iustin Bojoi, Lennart Harnefors, Emil Levi, Leila Parsa, and Babak Fahimi, "Trends in Electrical Machines Control: Samples for Classical, Sensorless, and Fault-Tolerant Techniques", IEEE Industrial Electronics Magazine, Vol 8, No 2 ,pp. 43 - 55 (2014).

(4) P.P. Acarnley, and J.F. Watson, "Review of position-sensorless operation of brushless permanent-magnet machines", IEEE Transactions on Industrial Electronics, Vol 53, No 2, pp. 352 - 362 (2006).

(5) Hetal V. Patel, and Hina Chandwani, "Review paper on Torque Ripple Mitigation Techniques for PMBLDC Motor", Proc. of 2017 International Conference on Current Trends in Computer, Electrical, Electronics and Communication (CTCEEC), pp. 669 - 674 (2017).

(6) H.J. Kim, and S. M. Kim, "Rare Earth Dispute and Trend in Development of NdFeB anisotropic bonded Magnets", Journal of the Korean Magnetics Society, Vol 22, No 3 (June 2012).

(7) https://www.electronicdesign.com/analog/4-things-you-should-know-about-magnets-electric-vehicles / Electronic Design

(8) http://epsteinresearch.com/2019/03/12/roskill-rare-earth-elements-interview-with-david-merriman / Roskill's REE(Rare Earth Element) trend report

(9) Yoshiaki Kano, "Recent Technical Trends in SRM and FSM", Proc. of 2014 International Power Electronics Conference (IPEC-Hiroshima 2014 - ECCE ASIA), pp. 2004 - 2010 (2014).

(10) Hiroaki Hayashi, Kensaku Nakamura, Akira Chiba, Tadashi Fukao, Kanokvate Tungpimolrut, and David G. Dorrell, "Efficiency Improvements of Switched Reluctance Motors With High-Quality Iron Steel and Enhanced Conductor Slot Fill", IEEE Transactions on Energy Conversion, Vol. 24, No. 4, pp. 819 - 825 (2009).

(11) Shinji Nakano, Kyohei Kiyota, and Akira Chiba, “Design consideration of high torque-density switched reluctance motor for hybrid electrical vehicle”, Proc. of 2016 19th International Conference on Electrical Machines and Systems (ICEMS). pp. 1-6 (2016).

(12) Hisato Amano, Yuji Enomoto, Motoya Ito, Hiromitsu Itabashi, Sigeho Tanigawa, and Tyoso Masaki, “Examination of Applying Amorphous Rolled Core to Permanent Magnet Synchronous Motors”, IEEJ Transactions on Industry Applications, Vol. 130, No. 5, pp. 632-638 (2010) (in Japanese).

(13) Kazuki Ueta, and Kan Akatsu, “Study of high-speed SRM with amorphous steel sheet for EV”, Proc. of 2016 19th International Conference on Electrical Machines and Systems (ICEMS), pp. 1-6 (2016).

(14) T. Kosaka, A. Kume, T. Shikayama, and N. Matsui, “Development of High Torque Density and Efficiency Switched Reluctance Motor with 0.1mm Short Airgap”, Proc. of 12th European Conference on Power Electronics and Applications (EPE2007), No.834 (2007).

(15) Motoki Takeno, Nobukazu Hoshi, Akira Chiba, and Masastugu Takemoto, “A comparison of high power and high efficiency machines of 50kW SRM designed for HEVs”, Proc. of IEEJ Industry Applications Society Conference, Vol. III, pp. 407-412 (2011) (in Japanese).

(16) Shinichi Noda, and Huminori Ishibashi, “The vibration, acoustic noise of motor, and its reduction countermeasures”, NTS corporation (in Japanese)

(17) Hiroaki Makino, Takashi Kosaka, and Nobuyuki Matsui, “Natural Frequency Measurement of SRM by Applying Electromagnetically-Excited Mechanical Excitation”, National Convention record I.E.E. Japan, Vol. 5, No. 5-039, pp. 70-71 (2014) (in Japanese).

(18) Herbert H. Woodson, and James R. Melcher, “Electromechanical Dynamics, Part II: Fields, Forces, and Motion”, John Wiley & Sons, INC., 1968, chapter 8.

(19) Mohammadali Abbasian, Mehdi Moallem, and Babak Fahimi, “Double-Stator Switched Reluctance Machines (DSSRM): Fundamentals and Magnetic Force Analysis”, IEEE Transactions on Energy Conversion, Vol. 25, No. 3, pp. 589-597 (2010).

(20) Piyush C. Desai, Mahesh Krishnamurthy, Nigel Schofield, and Ali Emadi, “Novel Switched Reluctance Machine Configuration with Higher Number of Rotor Poles

than Stator Poles: Concept to Implementation", IEEE Transactions on Industrial Electronic, Vol. 57, No. 2, pp. 649-659 (2010).

(21) Kyohei Kiyota, Takeo Kakishima, Akira Chiba, and M. Azizur Rahman, "Cylindrical Rotor Design for Acoustic Noise and Windage Loss Reduction in Switched Reluctance Motor for HEV Applications", IEEE Transactions on Industry Applications, Vol. 52, No. 1, pp. 154-162 (2016).

(22) Arash Hassanpour Isfahani, and Babak Fahimi, "Comparison of Mechanical Vibration between a Double-Stator Switched Reluctance Machine and a Conventional Switched Reluctance Machine", IEEE Transactions on Magnetics, Vol. 50, No. 2 pp. 293-296 (2014).

(23) D. E. Cameron, J. H. Lang, and S. D. Umans, "The Origin and Reduction of Acoustic Noise in Doubly Salient Variable-Reluctance Motors", IEEE Transactions on Industry Applications, Vol. 28, No. 11, pp. 1250-1255 (1992).

(24) C. Y. Wu, and C. Pollock, "Time Domain Analysis of Vibration and Acoustic Noise in the Switched Reluctance Drive", Proc. of IET Conferences. 6th International Conference on Electrical Machines and Drives, pp. 558-563 (1993).

(25) B. Fahimi, G. Suresh, K. M. Rahman, and M. Ehsani, "Mitigation of Acoustic Noise and Vibration in Switched Reluctance Motor Drive Using Neural Network Based Current Profiling", Conference Record of 1998 IEEE Industry Applications Conference. Thirty-Third IAS Annual Meeting, Vol. 1, pp. 715-722 (1998).

(26) Noboru Kurihara, Jacob Bayless, Hiroya Sugimoto, and Akira Chiba, "Noise Reduction of Switched Reluctance Motor with High Number of Poles by Novel Simplified Current Waveform at Low Speed and Low Torque Region", IEEE Transactions on Industry Applications, Vol. 52, No. 4, pp. 3013-3021 (2016).

(27) Debiprasad Panda, and V. Ramanarayanan, "Reduced Acoustic Noise Variable DC-Bus-Voltage-Based Sensorless Switched Reluctance Motor Drive for HVAC Applications", IEEE Transactions on Industry Electronics, Vol. 54, No. 4, pp. 2065-2078 (2007).

(28) C. Pollock, and C. Y. Wu, "Acoustic Noise Cancellation Techniques for Switched Reluctance Drives", Conf. Rec. of the IEEE 30th IAS Annual Meeting, Vol. I, pp. 448-455 (1995).

(29) Daniel Scharfenstein, Bernhard Burkhart, and Rik W. De Doncker, "Influence of an FPGA-based Switching Angle Dithering on Acoustics in Single-Pulse Controlled

Switched Reluctance Machines", Proc. of IEEE 11th International Conference on Power Electronics and Drive Systems, pp. 754-761 (2015).

(30) C-Y. Wu, and C. Pollock, "Analysis and Reduction of Vibration and Acoustic Noise in the Switched Reluctance Drive", IEEE Trans. on Industry Applications, Vol. 31, No. 1, pp. 91-98 (1995).

(31) A. Michaelides, and C. Pollock, "Reduction of Noise and Vibration in Switched Reluctance Motors: New Aspects", Conf. Rec. of the IEEE 31st IAS Annual Meeting, Vol. II, pp. 771-778 (1996).

(32) Hiroaki Makino, Takashi Kosaka, and Nobuyuki Matsui, "Digital PWM-Control-Based Active Vibration Cancellation for Switched Reluctance Motors", IEEE Transactions on Industry Applications, Vol. 51, pp. 4521-4530 (2015).

(33) Sungyong Shin, Naoki Kawagoe, Takashi Kosaka, and Nobuyuki Matsui, "Study on Commutation Control Method for Reducing Noise and Vibration in SRM", Proc. of 20th International Conference on Electrical Machines and Systems (ICEMS), pp. 1-6 (2017).

(34) S. Y. Shin, H. Naruse, T. Kosaka, and N. Matsui, "Design Study on Salient Pole Shape of Rotor in SR Motor for Vibration Suppression Under 2-Stage Commutation Control", Proc. of 2018 XIII International Conference on Electrical Machines (ICEM 2018), pp. 1478-1484 (2018).

(35) T. Kosaka, T. Nakagami, Y. Kano, T. Shikayama, N. Matsui, and C. Pollock, "GA-based Computer Aided Autonomous Electromagnetic Design of Switched Reluctance Servomotor Drives", Conf. Rec. of the IEEE 39th IAS Annual Meeting, Vol. I, pp. 416-423 (2004).

(36) T. J. E. Miller, "Switched Reluctance Motors and their Control", Magna Physics Publishing and Clarendon Press Oxford (1993).

(37) Y. Sozer, I. Husain, and David A. Torrey, "Guidance in Selecting Advanced Control Techniques for Switched Reluctance Machine Drives in Emerging Applications", IEEE Transactions on Industry Applications, Vol. 51, No. 6, pp. 4505-4514 (2015).

(38) H. Makino, T. Kosaka, and N. Matsui, "Control Performance Comparisons among Three Types of Instantaneous Current Profiling Technique for SR Motor", Proc. of 7th international conference on Power Electronics, Machines and Drives (PEMD2014), pp. 1-6 (2014).

(39) I. Husain, "Minimization of torque ripple in SRM drives", IEEE Trans. on PE, Vol.

49, No.1, pp.28-39 (2010).

(40) I. Husain, and M. Ehsani, “Torque Ripple Minimization in Switched Reluctance Motor Drives by PWM Current Control”, IEEE Trans. on PE, Vol.11, No.1(Jan/Feb 1996).

(41) S. Mir, M. Elbuluk, and I. Husain, “Torque Ripple Minimization in Switched Reluctance Motors using Adaptive Fuzzy Control”, IEEE Trans. on IA., Vol. 35, pp. 461–468 (Mar/Apr 1999).

(42) H. Ishikawa, Y. Kamada and H. Naito, “Instantaneous Current Profile Control for Flat Torque of Switched Reluctance Motors”, T. IEE Japan, Vol. 125-D, No. 12, pp.1113-1121 (2005, in Japanese).

(43) C. Ma, L. Qu, R. Mitra, P. Pramod, and R. Islam, “Vibration and torque ripple reduction of switched reluctance motors through current profile optimization,” Proc. IEEE Appl. Power Electron. Conf. Expo. 2016, pp. 3279–3285 (2016).

(44) B.S. Lee, Z. Q. Zhu, and Liren R. Huang, “Torque Ripple Reduction for 6-Stator/4-Rotor-Pole Variable Flux Reluctance Machines by Using Harmonic Field Current Injection”, IEEE Transactions on Industry Applications, Vol. 53, No. 4, pp. 3730-3737 (2017).

(45) Y. Niwa, T. Abe and T. Higuchi, “A Study of Rotor Position Control for Switched Reluctance Motor”, Proc. of 10th IEEE International Conference on Power Electronics and Drive Systems (PEDS), pp.1039-1044 (2013).

(46) K. M. Rahman, A. V. Rajarathnam, and M. Ehsani, “Optimized Instantaneous Torque Control of Switched Reluctance Motor by Neural Network”, Conf. Rec. of IEEE-IAS Annual Meeting, Vol. I, pp.556-563 (1997).

(47) T. Husain, A. Elrayyah, Y. Sozer, and I. Husain, “Flux-Weakening Control of Switched Reluctance Machines in Rotating Reference Frame”, IEEE Transactions on Industry Applications, Vol. 52, No. 1, pp. 267-277 (2016).

(48) H. Makino, T. Kosaka, N. Matsui, M. Hirayama and M. Ohoto, “PWM-based Instantaneous Current Profile tracking control for Torque Ripple Suppression in Switched Reluctance Servomotors”, Proc. of 10th IEEE International Conference on Power Electronics and Drive Systems (PEDS), pp. 1055-1060 (2013).

(49) H. Makino, T. Kosaka, S. Morimoto, M. Ohto and N. Matsui, “Instantaneous Current Profile Control of Four-Phase SR Motor for Industrial Serve Drives”, T. IEE Japan, Vol. 135-D, No. 6, pp.711-717 (2015)(in Japanese).

(50) H. Makino, S. Nagata, T. Kosaka, and N. Matsui, “Instantaneous Current Profiling Control for Minimizing Torque Ripple in Switched Reluctance Servo Motor”, Proc. of IEEE Energy Conversion Congress and Expo (ECCE), pp. 3941-3948, (2015).

(51) K. Mhatli, and B. B. Salah, “Improved Modeling of Switched Reluctance Motor Including Mutual and Saturation Effects”, Proc. of 2010 15th IEEE Mediterranean Electrotechnical Conference, pp. 1470-1475 (2010).

(52) G. J. Li, and Z. Q. Zhu, “Comparative Study of Torque Production in Conventional and Mutually Coupled SRMs Using Frozen Permeability”, IEEE Transactions on Magnetics, Vol 52, No.6, pp. 1-8 (2016).

(53) B. Qu, J. Song, T. Liang, and H. Zhang, “Mutual Coupling and Its Effect on Torque Waveform of Even Number Phase Switched Reluctance Motor”, Proc. of 2008 International Conference on Electrical Machines and Systems, pp. 3405-3410 (2008).

(54) N. Bhiwapurkar, Ted K. A. Brekken, and N. Mohan, “Torque Ripple Optimization of Switched Reluctance Motor Using Two-phase Model and Optimization Search Techniques”, Proc. of the 37th IEEE Power Electronics Specialists Conference (PESC), pp. 1-6 (2006).

(55) P. Pillay, Y. Liu, W. Cai, and T. Sebastian, “Multiphase operation of switched reluctance motor drives”, Proc. of IAS '97. Conference Record of the 1997 IEEE Industry Applications Conference Thirty-Second IAS Annual Meeting, Vol 1, pp. 310 – 317 (1997).

(56) Akiya Kume, Takashi Kosaka, and Nobuyuki Matsui, “A Suppression Measure against Torque Ripple Caused by Mutual Coupling in 4-phase SRM”, National Convention record I.E.E. Japan, Vol. 4, No. 4-121, pp. 207-208 (2009) (in Japanese).

(57) Mehrdad Ehsani, and Babak Fahimi, “Elimination of Position Sensors in switched reluctance motor drives : state of the art and future trends” IEEE Transactions on Industrial Electronics, Vol 49, No 1, pp. 40-47 (2002).

(58) B. Fahimi, A. Emadi, and B. Sepe, “Position sensorless control” IEEE Industry Applications Magazine, Vol 10, No 1, pp. 40-47 (2004).

(59) M. Krishnamurthy, C.S. Edrington, and B. Fahimi, “Prediction of Rotor Position at Standstill and Rotating Shaft Conditions in Switched Reluctance Machines” IEEE Transactions on Power Electronics, vol.21, pp. 225-233 (2006).

(60) Lei Shen, Jianhua Wu, and Shiyou Yang, “Initial Position Estimation in SRM Using Bootstrap Circuit Without Predefined Inductance Parameters”, IEEE Transactions

on Power Electronics, vol.26, No9 pp. 2449-2456 (2011).

(61) Pakasit Somsiri, Ruchao Pupadubsin, Prapon Jitkreeyan, Seubsuang Kachapornkul, Kanokvate Tungpimolrut, Nattapon Chayopitak, and Pichai Aree, "Simple Initial Rotor Position Estimation Method for Three-Phase Star-Connected Switched Reluctance Machine" Proc of 2009 ICCAS-SICE (ICROS-SICE International Joint Conference 2009), pp.5285-5290 (2009).

(62) Oshaba Ahmed, Kazuhiro Ohyama, Yousuke Narumoto, Hiroaki Fujii, and Hitoshi Uehara, "Sensorless operation of SRM drives from starting to steady state", Proc. of 2009 IEEE International Symposium on Industrial Electronics, pp. 1269–1274 (2009).

(63) M.Ehsani, I.Husain, S.Mahajan, and K.Ramani, "New modulation encoding techniques for rotor position sensing in switched reluctance motors", IEEE Transactions on Industry Applications, vol. 30, no. 1, pp. 85–91 (1994).

(64) M. Ehsani, I. Husain, and A.B. Kulkarni, "Elimination of Discrete Position Sensor and Current Sensor in Switched Reluctance Motor Drives", IEEE Transactions on Industry Applications, vol.28, No 1 pp. 128-135 (1992).

(65) K.R. Ramani, and M. Ehsani, "New commutation methods in switched reluctance motors based on active phase vectors", Proc. of 1994 Power Electronics Specialist Conference - PESC'94, Vol.1, pp.493-499 (1994).

(66) F.R. Salmasi, B. Fahimi, H. Gao, and M. Ehsani, "Sensorless control of switched reluctance motor drive based on BEMF calculation", Proc of APEC Seventeenth Annual IEEE Applied Power Electronics Conference and Exposition, vol. 1, pp 293-298 (2002).

(67) M. Ehsani, and Iqbal Husain, "Rotor Position Sensing in Switched Reluctance Motor Drives by Measuring Mutually Induced Voltages", IEEE Transactions on Industry Applications, vol.30, No 3 pp. 665-672 (1994).

(68) Wenzhe. Lu, and A. Keyhani, "Sensorless Control of Switched Reluctance Motors Using Sliding Mode Observers", Proc of IEMDC 2001. IEEE International Electric Machines and Drives Conference, pp. 69-72 (2001).

(69) G. Suresh, B. Fahimi, K.M. Rahman, and M. Ehsani, "Inductance Based Position Encoding for Sensorless SRM Drives", Proc. of 30th Annual IEEE Power Electronics Specialists Conference. Record. (Cat. No.99CH36321), Vol.2, pp. 832-837 (1999).

(70) G. Gallegos-Lopez, P.C. Kjaer, and T.J.E. Miller, "A New Sensorless Method for

Switched Reluctance Motor Drives", IEEE Transactions on Industry Applications, vol.34, No 4 pp. 832-840 (1998).

(71) C. Wang, and L. Xu, "Accurate Rotor Position Detection and Sensorless Control of SRM for Super-High Speed Operation", IEEE Transactions on Power Electronics, Vol 17, No 5, pp. 757-763 (2002).

(72) Babak Fahimi, Ali Emadi, and Raymond B. Sepe, "Four-Quadrant Position Sensorless Control in SRM Drives Over the Entire Speed Range", IEEE Transactions on Power Electronics, Vol 20, No 1, pp. 154-163 (2005).

List of publications

1. Journal

[1] **S. Y. Shin**, N. Kawagoe, T. Kosaka, and N. Matsui, "Study on Commutation Control Method for Reducing Noise and Vibration in SRM", IEEE Transactions on Industry Applications, vol. 54, no.5 pp. 4415-4424 (2018)

2. International conference

[2] **S. Y. Shin**, N. Kawagoe, T. Kosaka, and N. Matsui, "Study on Commutation Control Method for Reducing Noise and Vibration in SRM", Proc. of 20th International Conference on Electrical Machines and Systems (ICEMS) pp. 1-6 (2017)
This paper received Best Paper Award (The First Prize) in the 20th International Conference on Electric Machines and Systems (ICEMS2017).

[3] **S. Y. Shin**, H. Naruse, T. Kosaka, and N. Matsui, "Torque Ripple Minimization Control of SRM Based on Novel Motor Model Considering Mutual Coupling Effect", Proc of 2018 International Power Electronics Conference (IPEC-Niigata 2018 -ECCE Asia), pp. 3418-3425 (2018)

[4] **S. Y. Shin**, T. Kosaka, and N. Matsui, "Indirect Position Sensing at Stand-Still and Running State in SRM by Using Distributed Voltage and Voltage Rate for Injected Pulse", Proc of 2018 XIII International Conference on Electrical Machines (ICEM 2018), pp. 1558-1564 (2018)

[5] **S. Y. Shin**, H. Naruse, T. Kosaka, and N. Matsui, "Design Study on Salient Pole Shape of Rotor in SR Motor for Vibration Suppression Under 2-Stage Commutation Control", Proc of 2018 XIII International Conference on Electrical Machines (ICEM 2018), pp. 1478-1484 (2018)